Alma Mater Studiorum – Università di Bologna

DOTTORATO DI RICERCA IN

CHIMICA

Ciclo XXVIII

Settore Concorsuale di afferenza: 03/C1

Settore Scientifico disciplinare: CHIM/06

Preparation and Applications of Pseudopeptide-Based Nanomaterials

Presentata da: Lorenzo Milli

Coordinatore Dottorato	**Relatore**
Prof Aldo Roda	Prof.ssa Claudia Tomasini

Esame finale anno 2016

Dott. Lorenzo Milli
Supervisore: Prof. Claudia Tomasini
Curriculum: Scienze Chimiche
Indirizzo: Chimica Organica
Titolo della tesi: Preparation and Applications of Pseudopeptide-Based Nanomaterials

During the three years of his PhD, Lorenzo Milli focused his research project on the synthesis, characterization and application of pseudopeptide foldamers.
During this period, he collaborated with my research group in the field of synthetic organic chemistry and he gained experience in all the techniques needed for the synthesis and analysis of organic molecules. Quickly he understood all the problems related to his research project that dealt with the preparation and application of new seudopeptides that behave as low molecular weight gelators. Moreover he prepared pseudopeptides capped with electrodonor and electroacceptor for energy transfer, then he made gold nanoparticles containing pseudopeptide foldamers and finally pseudopeptides capped with fluorescent tags. He is versatile and collaborative and he is able to find solution for problems, demonstrating excellent skills in organizing the work. Moreover he collaborates optimally with colleagues in the laboratory and other research groups involved in collaborative projects.
The main results achieved during the period of his PhD are documented by 7 scientific articles published in important peer-reviewed international journals.

1) N. Castellucci, G. Falini, L. Milli, M. Monari, S. Abbate, G. Longhi, E. Castiglioni, G. Mazzeo, C. Tomasini – "Solid-State Properties and Vibrational Circular Dichroism Spectroscopy in Solution of Hybrid Foldamers Stereoisomeric Mixtures" ChemPlusChem, 2014, 79, 114–121.
2) L. Milli, M. Larocca, M. Tedesco, N. Castellucci, E. Ghibaudi, A. Cornia, M. Calvaresi, F. Zerbetto, C. Tomasini – "α,ε-Hybrid Foldamers with 1,2,3-Triazole Rings: Order versus Disorder", Journal of Organic Chemistry, 2014, 79, 5958–5969.
3) L. Milli, N. Castellucci, C. Tomasini – "Turning Around the L-Phe-D-Oxd Moiety for a Versatile Low Molecular Weight Gelator", Eur. J. Org. Chem., 2014, 5954–5961.
4) C. Tomasini, N. Castellucci, V. C. Caputo, L. Milli, G. Battistelli, S. Fermani, G. Falini – "Shaping calcite crystals by customized self-assembling pseudopeptide foldamers", CrystEngComm, 2015, 17, 116–123.
5) L. Milli, E. Marchi, N. Castellucci, M. T. Indelli, M. Venturi, P. Ceroni, C. Tomasini – "Pseudopeptide Foldamers Designed for Photoinduced Intramolecular Electron Transfer", RSC Advances, 2015, 5, 10809-10815.
6) R. Fanelli, L. Milli, A. Cornia, A. Moretto, N. Castellucci, N. Zanna, G. Malachin, R. Tavano, C. Tomasini – "Chiral Gold Nanoparticles Decorated with Pseudopeptides, Eur. J. Org. Chem., 2015, 6243-6248.
7) N. Zanna, A. Merlettini, G. Tatulli, L. Milli, M. L. Focarete, C. Tomasini - Hydrogelation Induced by Fmoc-Protected Peptidomimetics, Langmuir, 2015, 31, 12240-12250.

In addition, one manuscript has been submitted and three manuscripts are in preparation and will be soon submitted.
He has been the co-supervisor of two 2nd level degrees thesis in Chemistry and 4 1st level degree thesis in Chemistry and 2 1st level degree thesis in Biological Sciences proving a great ability in coordination of the activities of the students. He has also been tutor for the incoming students of the Scuola di Farmacia, Biotecnologie e Scienze Motorie for two years demonstrating great teaching skills.
He took actively part in 1 international congress and 2 national congress with oral or poster presentations showing excellent knowledge of the presented subjects, ability of organize the information in a slide presentation, and effective communication skills.
Moreover he attended the National School of Photochemistry in 2013 and the XL International Summer School on Organic Synthesis in 2015.
My overall evaluation of the Candidate is excellent.

The Board expresses a score of excellence on the activity carried out by the candidate during the whole cycle of doctorate and considers him worthy to attain the PhD in Chemistry.

Acronyms

2D	Two Dimensional
3D	Three Dimensional
A	Acceptor
Ala	Alanine
AuNPs	Gold Nanoparticles
Bn	Benzyl
Boc	*tert*-Butyloxycarbonyl
Carboxy-H2DCFDA	6-Carboxy-2',7'-dichlorodihydrofluorescein diacetate
CD	Circular Dichroism
CT	Charge transfer
CuAAC	Copper-Catalysed Azide Alkyne Cycloaddition
D	Donor
DBU	1,8-Diazabicyclo[5.4.0]undec-7-ene
DCC	N,N'-dicyclohexylcarbodiimide
DCM	Dichloromethane
DFT	Density Functional Theory
DIEA	N,N-Diisopropylethylamine
DLS	Dynamic Light Scattering
DMAP	4-Dimethylaminopyridine
DMF	Dimetilformammide
ECD	Electronic Circular Dichroism
ECM	Extracellular Matrix
EDTA	ethylenediaminetetraacetic acid disodium salt
ET	Electron Transfer
EtOH	Ethanol
EY	Eosin Y
Fmoc	9-Fluorenylmethoxycarbonyl
FT-IR	Fourier Transform – Infra Red
G'	Storage Modulu
G''	Loss Modulu
GdL	glucono-δ-lactone
Gly	Glycine
GO	Graphene Oxide
HATU	1-[Bis(dimethylamino)methylene]-1H-1,2,3-triazolo[4,5-b]pyridinium 3-oxid hexafluorophosphate
HBTU	N,N,N′,N′-Tetramethyl-O-(1H-benzotriazol-1-yl)iranium hexafluorophosphate
HeLa	Henrietta Lacks
L	Linker
LMWG	low molecular weight gelator
LVE	Linear Viscoelastic
MB	Methylene Blue
MeOH	Methanol
MTS	3-(4,5-dimethylthiazol-2-yl)-5-(3-carboxymethoxyphenyl)-2-(4-sulfophenyl)-2Htetrazolium
NMR	Nuclear Magnetic Resonance
NOE	Nuclear Overhauser Effect
NOESY	Nuclear Overhauser Effect Spectroscopy
NPs	Nanoparticles
Oxd	4-carboxy-5-methyl-oxazolidin-2-one
PAs	Peptide amphiphiles
PBS	Phosphate Buffered Saline
Pd/C	Palladium on carbon
PEG	Poly Ethylene Glycol

p-Glu	Pyroglutammic acid or 5-oxo-Proline
Ph	Phenyl
Phe	Phenylalanine
Pro	Proline
ROESY	Rotating frame nuclear Overhauser Effect Spectroscopy
ROS	Reacting Oxygen Species
RuAAC	Ruthenium-Catalysed Azide Alkyne Cycloaddition
SEM	Scanning Electron Microscopy
tBu	tert-Buthyl
TEA	Triethylamine
TEM	Transmission Electron Microscopy
TFA	Trifluoroacetic acid
THF	Tetrahydrofuran
Thr	Threonine
Tri	1,2,3 Triazole
Trp	Tryptophan
TsCl	4-Toluenesulfonyl chloride
Tyr	Tyrosine
Val	Valine
Xaa	General Amino Acid
XRD	X-Ray Diffraction

Summary

1. Introduction

1.1. Foldamers

Samuel H. Gellman coined in 1996 the word "Foldamers" [1,2], that means "folding molecules" and is used to describe any polymer with a strong tendency to adopt a specific compact conformation [3,4]. The first step in foldamer design must therefore be to identify new backbones with well-defined secondary structural preferences (helices, sheets, and turns). "Well-defined" in this case means that the conformational preference should be displayed in solution by oligomers of modest length (500-5000 Dalton). Gellman defined in his "Manifesto" [2] the path to creating useful foldamers involves several daunting steps:

One must identify new polymeric backbones with suitable folding propensities. This goal includes developing a predictively useful understanding of the relationship between the repetitive features of monomer structure and conformational properties at the polymer level.

One must endow the resulting foldamers with interesting chemical functions, by design, by randomization and screening ("evolution"), or by some combination of these two approaches.

For technological utility, one must be able to produce a foldamer efficiently, which will generally include preparation of the constituent monomers in stereochemically pure form and optimization of heteropolymer synthesis.

Before the term ''foldamer'' was coined, many nucleic acid analogues and peptide analogues had already been successfully designed to mimic the structures and, potentially, the biological properties of their natural counterparts. Typical examples are peptide nucleic acids (PNAs) [5] and N-substituted oligoglycines (peptoids) [6].

Later on, Moore [7] proposed in 2001 a new definition of foldamer: any oligomer that folds into a conformationally ordered state in solution, the structures of which are stabilized by a collection of noncovalent interactions between nonadjacent monomer units. There are two major classes of foldamers: single-stranded foldamers that only fold and multiple-stranded foldamers that both associate and fold.

Over the last twenty years, this field has rapidly expanded, in fact the investigation on these new structural scaffolds has blossomed in many laboratories as they hold promise for

---

[1] Appella, D. H.; Christianson, L. A.; Karle, I. L.; Powell, D. R.; Gellman, S. H., β-Peptide Foldamers: Robust Helix Formation in a New Family of β-Amino Acid Oligomers. *Journal of the American Chemical Society* **1996,** *118* (51), 13071-13072.

[2] Gellman, S. H., Foldamers: A Manifesto. *Accounts of Chemical Research* **1998,** *31* (4), 173-180.

[3] Hecht, S.; Huc, I., *Foldamers: Structure, Properties, and Applications*. **2007**; p 1-434.

[4] Tomasini, C.; Castellucci, N., Introduction to Unnatural Foldamers. In *Metallofoldamers: Supramolecular Architectures from Helicates to Biomimetics*, **2013**; pp 51-89.

[5] Nielsen, P.; Egholm, M.; Berg, R.; Buchardt, O., Sequence-selective recognition of DNA by strand displacement with a thymine-substituted polyamide. *Science* **1991,** *254* (5037), 1497-1500.

[6] Simon, R. J.; Kania, R. S.; Zuckermann, R. N.; Huebner, V. D.; Jewell, D. A.; Banville, S.; Ng, S.; Wang, L.; Rosenberg, S.; Marlowe, C. K., Peptoids: a modular approach to drug discovery. *Proceedings of the National Academy of Sciences of the United States of America* **1992,** *89* (20), 9367-9371.

[7] Hill, D. J.; Mio, M. J.; Prince, R. B.; Hughes, T. S.; Moore, J. S., A Field Guide to Foldamers. *Chemical Reviews* **2001,** *101* (12), 3893-4012.

addressing chemical, physical-chemical, and biological problems and represent a new frontier in research [8]. To have an idea of the steady increase of this research topic, Figure 1 shows the number of papers published in the period 1996 to 2015.

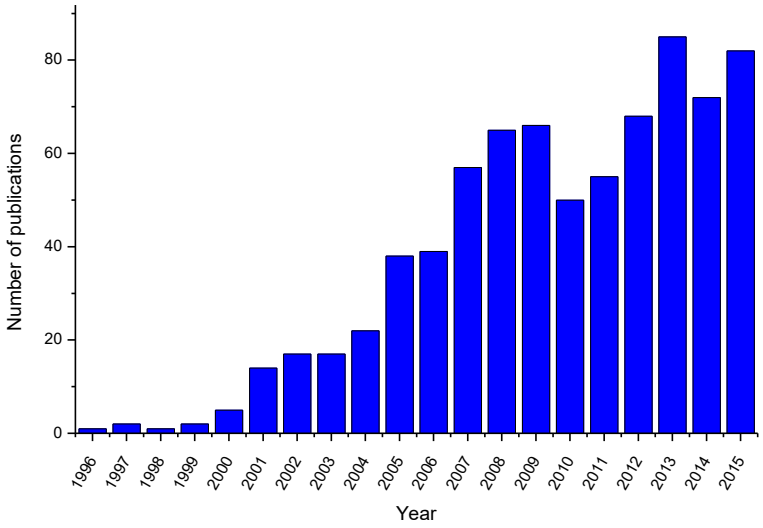

Figure 1. Number of publication with Title, Abstract and Keynote "Foldamers" (Scopus from 1996 to 2015).

The research was directed towards the mimic of α-peptidic secondary structures, to prepare compounds that retain their biological functions without having to cope with hydrolytic and metabolic instability, typical of α-peptides. The foldamers that have been developed have any sort of skeleton and differ both for structures and for applications. Synthetic foldamers are far too numerous to be presented or even simply mentioned here, thus in this introduction we will describe only some recent examples.

The foldamers scaffolds have been classified by Guichard and Huc and divided into two large families: “biotic” foldamers and “abiotic” foldamers [9,10].

“Biotic” foldamers are molecules whose synthesis has been guided by analogy to biopolymers with which they share comparable folding principles. They are peptoids, β-peptides, α/β-peptides, γ-peptide, oligoureas, etc. (Figure 2). In contrast, “abiotic” foldamers are molecules with aromatic backbones: [11] for example oligo-phenylene-ethynylenes, sequences of alternating aromatic electron donors and acceptors, aryl-oligomers (in particular those based on aza-heterocycles as pyridines, pyrimidines, pyridazines, etc.), aromatic tertiary amide, imide or urea oligomers, and aromatic oligoamides (Figure 3).

[8] Cheng, R. P., Beyond de novo protein design — de novo design of non-natural folded oligomers. *Current Opinion in Structural Biology* **2004,** *14* (4), 512-520.
[9] Guichard, G.; Huc, I., Synthetic foldamers. *Chemical Communications* **2011,** *47* (21), 5933-5941.
[10] Goodman, C. M.; Choi, S.; Shandler, S.; DeGrado, W. F., Foldamers as versatile frameworks for the design and evolution of function. *Nat Chem Biol* **2007,** *3* (5), 252-262.
[11] Haldar, D.; Schmuck, C., Metal-free double helices from abiotic backbones. *Chemical Society Reviews* **2009,** *38* (2), 363-371.

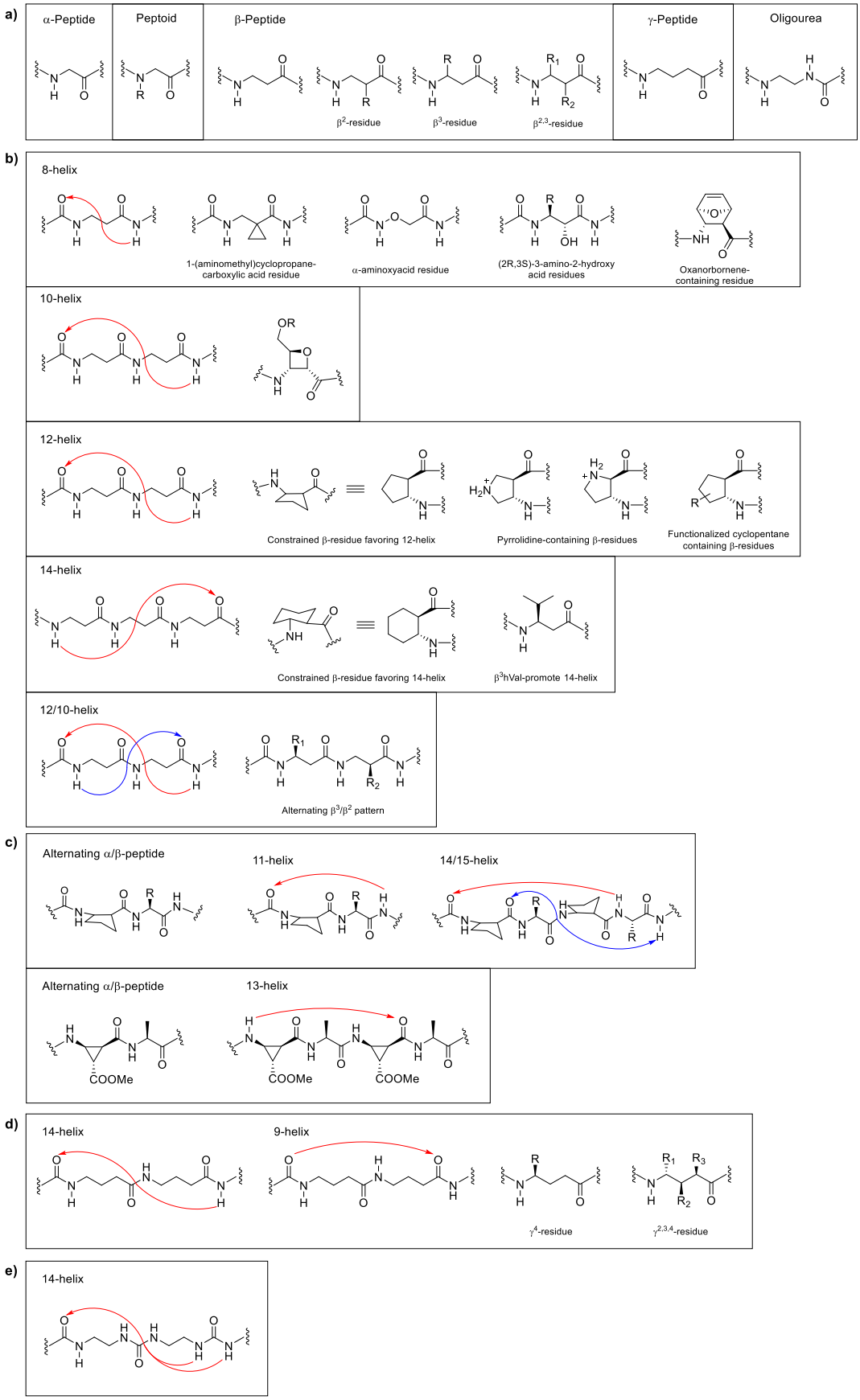

Figure 2. Chemical representations of "biotic foldamers": a) Monomeric units; b) Secondary structure of β-peptide; c) Secondary structure of alternating α/β-peptide; d) Secondary structure of γ-peptide; e) Helix formed by oligoureas.

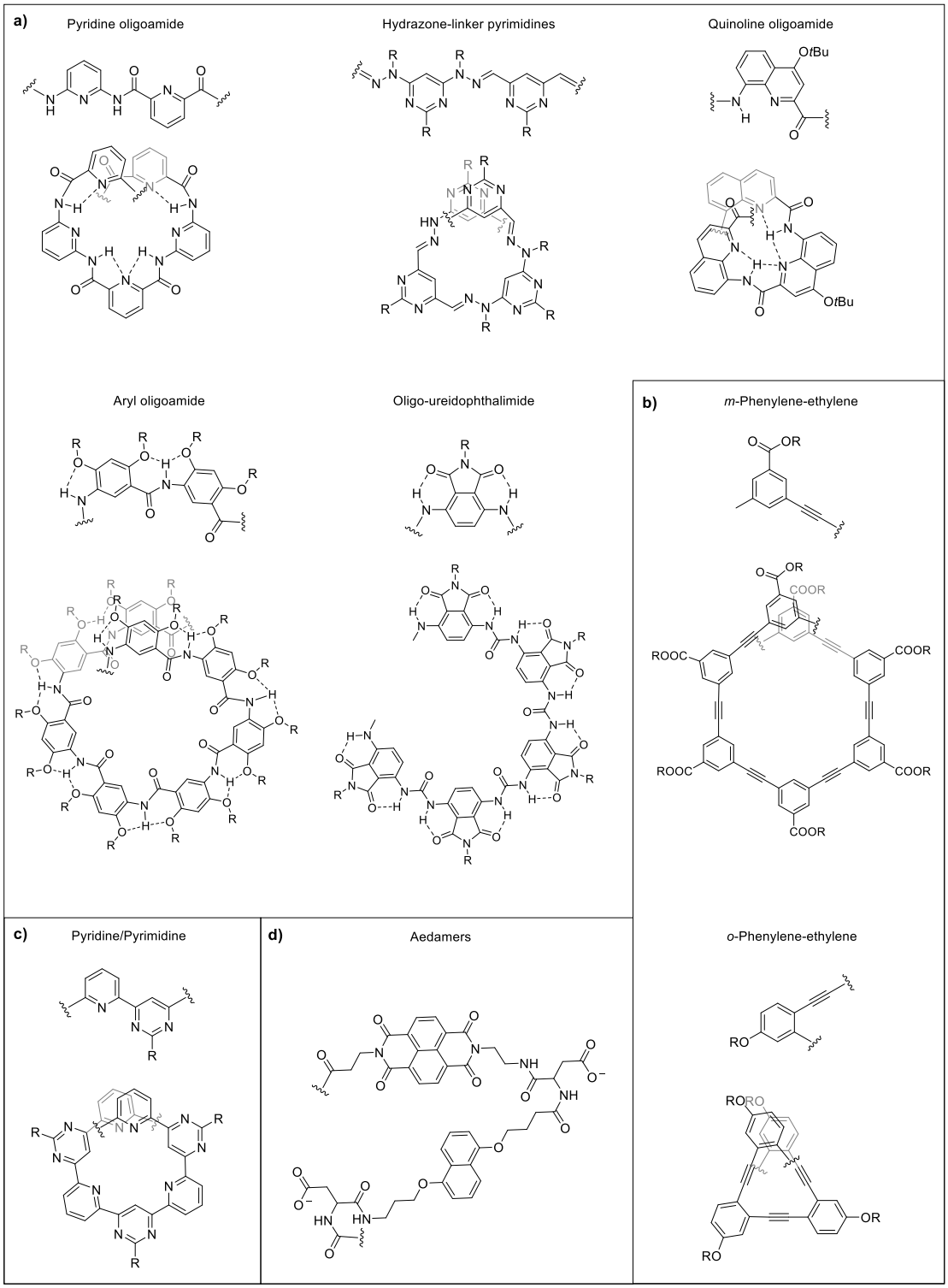

Figure 3. Chemical representations of “abiotic foldamers”: a) Oligoamides and Oligoureas; b) Phenylene ethylene; c) Oligoheterocyclic; d) Aedamers.

1.1.1. Biotic Foldamers

1.1.1.1. Peptoids

Peptoids (Figure 2a) are poly-*N*-substituted glycines. Analogous to polyproline, peptoids lack backbone hydrogen-bond donors. The helical 'handedness' of peptoids is dictated by the stereochemistry of the sidechains; achiral aromatic and aliphatic sidechains have both been shown to support the polyproline type I helix [12]. With the aim of creating peptoids with tertiary structures, Zuckermann and co-workers [13] generated a 15-mer amphiphilic peptoid library using a 'mix-and-split' strategy. The sidechains of four hydrophobic positions and three hydrophilic positions were varied randomly using twelve hydrophobic and two hydrophilic sidechains, respectively.

1.1.1.2. β-Peptides

β-Peptides (Figure 2a,b) are oligo(β-amino acids) and can assume a wide variety of secondary structures, including helices, sheets and turns [14,15]. The sidechain substitution pattern of the constituting β-amino acids can bias the local backbone conformational preference and thus the overall secondary structure [16].

Among the β-peptide helical conformations, the 14-helix is the best studied [14,15]. The 14-helix has 14 atoms in the hydrogen-bonded ring N–H•••O = C (Figure 2b) and an approximately three-residue repeat. The 14-helix is stabilized by placing complementary charged residues to interact favorably with the helix macrodipole. Unprotected termini also stabilize the 14-helix conformation by interacting with the helix macrodipole. Gellman [17] and Schepartz [18] showed independently that γ-branched β^3-amino acids (such as β^3-hVal and β^3-hIle) can be used to promote the formation of the 14-helix.

---

[12] Wu, C. W.; Kirshenbaum, K.; Sanborn, T. J.; Patch, J. A.; Huang, K.; Dill, K. A.; Zuckermann, R. N.; Barron, A. E., Structural and Spectroscopic Studies of Peptoid Oligomers with α-Chiral Aliphatic Side Chains. *Journal of the American Chemical Society* **2003,** *125* (44), 13525-13530.

[13] Burkoth, T. S.; Beausoleil, E.; Kaur, S.; Tang, D.; Cohen, F. E.; Zuckermann, R. N., Toward the Synthesis of Artificial Proteins: The Discovery of an Amphiphilic Helical Peptoid Assembly. *Chemistry & Biology* **2002,** *9* (5), 647-654.

[14] Cheng, R. P.; Gellman, S. H.; DeGrado, W. F., β-Peptides: From Structure to Function. *Chemical Reviews* **2001,** *101* (10), 3219-3232.

[15] Seebach, D.; L. Matthews, J., [small beta]-Peptides: a surprise at every turn. *Chemical Communications* **1997,** (21), 2015-2022.

[16] Martinek, T. A.; Fülöp, F., Side-chain control of β-peptide secondary structures. *European Journal of Biochemistry* **2003,** *270* (18), 3657-3666.

[17] Raguse, T. L.; Lai, J. R.; Gellman, S. H., Evidence that the β-Peptide 14-Helix is Stabilized by β3-Residues with Side-Chain Branching Adjacent to the β-Carbon Atom. *Helvetica Chimica Acta* **2002,** *85* (12), 4154-4164.

[18] Hart, S. A.; Bahadoor, A. B. F.; Matthews, E. E.; Qiu, X. J.; Schepartz, A., Helix Macrodipole Control of β3-Peptide 14-Helix Stability in Water. *Journal of the American Chemical Society* **2003,** *125* (14), 4022-4023.

The β-peptide 12-helix had previously been formed only with constrained cyclic residues containing five-membered rings [14,15]. Various pyrrolidine-containing [19] and functionalized cyclopentane-containing [20] cyclic β-amino acids were incorporated into 12-helical β-peptides to improve solubility in aqueous solution and to provide sequence diversity [21,22].

β-Peptides with alternating β^2- and β^3-monosubstituted amino acids can adopt the 10/12-helix conformation [14]. The 10/12-helix consists of an intertwined network of 10- and 12-membered hydrogen-bonded rings [23].

Oligomers formed by 1-(aminomethyl)cyclopropanecarboxylic acid and α-aminoxy acids, (2R,3S)-3-amino-2-hydroxy acids and cyclic oxanorbornene β-amino acid is organized in 8-helix [24,25].

β-peptides prepared by Fleet et al. from monomers with a four-membered ring constraint stabilized 10-helix secondary structure (Figure 2b) [26]. The constitutent β-amino acids contain an oxetane ring (four-membered ring ether). The amino and carboxyl substituents are *cis* on the four-membered ring, in contrast to the *trans* relationship for pyrrolidine-, cyclohexane- and cyclopentane- constrained residues discussed above.

1.1.1.3. Alternating α/β-Peptides

The emergence of β-peptides has raised curiosity about mixed α/β-peptides (Figure 2c) [27]. Gellman and co-workers [28] studied the conformational preferences of alternating α/β-peptides in which the β-residues contained conformationally constraining five-membered rings. As both

[19] Lee, H.-S.; Syud, F. A.; Wang, X.; Gellman, S. H., Diversity in Short β-Peptide 12-Helices: High-Resolution Structural Analysis in Aqueous Solution of a Hexamer Containing Sulfonylated Pyrrolidine Residues. *Journal of the American Chemical Society* **2001,** *123* (31), 7721-7722.

[20] Woll, M. G.; Fisk, J. D.; LePlae, P. R.; Gellman, S. H., Stereoselective Synthesis of 3-Substituted 2-Aminocyclopentanecarboxylic Acid Derivatives and Their Incorporation into Short 12-Helical β-Peptides That Fold in Water. *Journal of the American Chemical Society* **2002,** *124* (42), 12447-12452.

[21] LePlae, P. R.; Fisk, J. D.; Porter, E. A.; Weisblum, B.; Gellman, S. H., Tolerance of Acyclic Residues in the β-Peptide 12-Helix: Access to Diverse Side-Chain Arrays for Biological Applications. *Journal of the American Chemical Society* **2002,** *124* (24), 6820-6821.

[22] Park, J.-S.; Lee, H.-S.; Lai, J. R.; Kim, B. M.; Gellman, S. H., Accommodation of α-Substituted Residues in the β-Peptide 12-Helix: Expanding the Range of Substitution Patterns Available to a Foldamer Scaffold. *Journal of the American Chemical Society* **2003,** *125* (28), 8539-8545.

[23] Rueping, M.; Schreiber, J. V.; Lelais, G.; Jaun, B.; Seebach, D., Mixed β2/β3-Hexapeptides and β2/β3-Nonapeptides Folding to (P)-Helices with Alternating Twelve- and Ten-Membered Hydrogen-Bonded Rings. *Helvetica Chimica Acta* **2002,** *85* (9), 2577-2593.

[24] Gademann, K.; Häne, A.; Rueping, M.; Jaun, B.; Seebach, D., The Fourth Helical Secondary Structure of β-Peptides: The (P)-28-Helix of a β-Hexapeptide Consisting of (2R,3S)-3-Amino-2-hydroxy Acid Residues. *Angewandte Chemie International Edition* **2003,** *42* (13), 1534-1537.

[25] Doerksen, R. J.; Chen, B.; Yuan, J.; Winkler, J. D.; Klein, M. L., Novel conformationally-constrained [small beta]-peptides characterized by 1H NMR chemical shifts. *Chemical Communications* **2003,** (20), 2534-2535.

[26] Claridge, T. D. W.; Goodman, J. M.; Moreno, A.; Angus, D.; Barker, S. F.; Taillefumier, C.; Watterson, M.P.; Fleet, G. W. J., 10-Helical conformations in oxetane β-amino acid hexamers. *Tetrahedron Letters* **2001,** *42* (25), 4251-4255.

[27] Cubberley, M. S.; Iverson, B. L., Models of higher-order structure: foldamers and beyond. *Current Opinion in Chemical Biology* **2001,** *5* (6), 650-653.

[28] Hayen, A.; Schmitt, M. A.; Ngassa, F. N.; Thomasson, K. A.; Gellman, S. H., Two Helical Conformations from a Single Foldamer Backbone: "Split Personality" in Short α/β-Peptides. *Angewandte Chemie International Edition* **2004,** *43* (4), 505-510.

the 14/15-helix and the 11-helix were consistent with the NMR data, more studies are necessary to specify one predominant conformation. Additionally, Reiser and co-workers [29] studied an alternating α/β peptide in which the β-residues contained conformationally constrained three-membered rings. NMR studies showed that a 13-helix is formed in CD_3OH, but not in water.

1.1.1.4. γ-Peptide

There have been several studies on γ-peptides, revealing helix and turn conformations [7]. Whereas γ^4-peptides form a 14-helix in solution (Figure 2d), $\gamma^{2,4}$-disubstituted residues with the appropriate stereochemistry form a reverse turn. Seebach et al. [30] performed NMR and crystallography studies on oligomers of $\gamma^{2,3,4}$-trisubstituted residues, revealing a 14-helix in methanol.

1.1.1.5. Oligoureas

Guichard and co-workers [31] studied oligoureas that also form the 14-helix (Figure 2e), similar to γ-peptides. The C = O*i* on urea is not equidistant from $N'H_{i+2}$ and NH_{i+3}, and statistics performed on the calculation suggest that the 14-membered H-bonded rings are more populated than the corresponding 12-membered rings, at least in the inner part of the helix. NMR and crystallography studies revealed a more sophisticated pattern of hydrogen-bonded rings involving 12 and 14 atoms due to the urea functionality.

1.1.2. Abiotic Foldamers

Abiotic foldamers with helical conformations have been designed using oligoarylamides and ureas, oligoaromatics and phenylene ethynylene oligomers (Figure 3). The helix radius and repeat are determined by the collective curvature of the constituting monomers and the linking functionality (amide or urea). The curvature/bend of the monomers can be modulated by several factors: substitution patterns on the aromatic ring (ortho, meta, para), placement of hydrogen-bond donor/acceptor for backbone rigidification and use of the aromatic ring such as benzene, pyridine, pyrimidine, naphthalene and so on [32].

---

[29] De Pol, S.; Zorn, C.; Klein, C. D.; Zerbe, O.; Reiser, O., Surprisingly Stable Helical Conformations in α/β-Peptides by Incorporation of cis-β-Aminocyclopropane Carboxylic Acids. *Angewandte Chemie International Edition* **2004,** *43* (4), 511-514.

[30] Seebach, D.; Brenner, M.; Rueping, M.; Jaun, B., γ2-, γ3-, and γ2,3,4-Amino Acids, Coupling to γ-Hexapeptides: CD Spectra, NMR Solution and X-ray Crystal Structures of γ-Peptides. *Chemistry – A European Journal* **2002,** *8* (3), 573-584.

[31] Semetey, V.; Rognan, D.; Hemmerlin, C.; Graff, R.; Briand, J.-P.; Marraud, M.; Guichard, G., Stable Helical Secondary Structure in Short-Chain N,N′-Linked Oligoureas Bearing Proteinogenic Side Chains. *Angewandte Chemie International Edition* **2002,** *41* (11), 1893-1895.

[32] Huc, I., Aromatic Oligoamide Foldamers. *European Journal of Organic Chemistry* **2004,** *2004* (1), 17-29.

1.1.2.1. Oligoarylamides and Oligoarylureas

Lehn [33], Huc [34] and co-workers performed NMR and CD studies on different protonation states of oligoamides containing 2,6-disubstituted pyridines (Figure 3a). Diamino and dicarbonyl substitution of alternating pyridine rings resulted in varying pKa values for the pyridine nitrogens. This caused conformational change in a two-stage manner upon protonation. Whereas the non-protonated form and the fully protonated form exhibited helical conformations in solution, the partially protonated form was proposed to adopt an extended conformation. Huc et al. [35] also appended benzyloxy, hydroxyl and hydroxylate functionalities onto the pyridine-containing oligomer; the hydroxylate derivative was fully soluble in water. NMR and crystallography studies confirmed the helical conformation. Lehn and co-workers [36] also devised helical oligomers composed of hydrazone-linked pyrimidines. NMR and crystallography studies revealed that aromatic sidechains promoted more regular helices with better pyrimidine ring stacking, most probably due to sidechain aromatic stacking (Figure 3a).

Gong and co-workers [37] have studied oligoamides composed of 1,3-disubstituted benzene rings (Figure 3a). A three center hydrogen bond rigidifies the local conformation to generate a bend in the backbone. Nonamers exhibited one helical turn, as characterized by crystallography and NMR.

Huc and co-workers [38] studied a helical oligomer of quinolone derived amino acids by NMR and crystallography (Figure 3a). Meijer and co-workers [39] designed an aromatic helix using para-substituted aromatic units in an oligo ureidophthalimide (Figure 3a). The phthalimide functionality hydrogen bonds to the backbone urea and rigidifies the backbone conformation. Also, the incorporation of chiral amines into the phthalimide induced helical handedness. Molecular modeling and CD studies showed that there are 6–8 repeating units in each helical turn. Interestingly, the helical conformation is observed in THF, but not in chloroform.

---

[33] Kolomiets, E.; Berl, V.; Odriozola, I.; Stadler, A.-M.; Kyritsakas, N.; Lehn, J.-M., Contraction/extension molecular motion by protonation/deprotonation induced structural switching of pyridine derived oligoamides. *Chemical Communications* **2003,** (23), 2868-2869.

[34] Dolain, C.; Maurizot, V.; Huc, I., Protonation-Induced Transition between Two Distinct Helical Conformations of a Synthetic Oligomer via a Linear Intermediate. *Angewandte Chemie International Edition* **2003,** *42* (24), 2738-2740.

[35] Huc, I.; Maurizot, V.; Gornitzka, H.; Leger, J.-M., Hydroxy-substituted oligopyridine dicarboxamide helical foldamers. *Chemical Communications* **2002,** (6), 578-579.

[36] Schmitt, J.-L.; Stadler, A.-M.; Kyritsakas, N.; Lehn, J.-M., Helicity-Encoded Molecular Strands: Efficient Access by the Hydrazone Route and Structural Features. *Helvetica Chimica Acta* **2003,** *86* (5), 1598-1624.

[37] Gong, B., Crescent Oligoamides: From Acyclic “Macrocycles” to Folding Nanotubes. *Chemistry – A European Journal* **2001,** *7* (20), 4336-4342.

[38] Jiang, H.; Léger, J.-M.; Huc, I., Aromatic δ-Peptides. *Journal of the American Chemical Society* **2003,** *125* (12), 3448-3449.

[39] van Gorp, J. J.; Vekemans, J. A. J. M.; Meijer, E. W., Facile synthesis of a chiral polymeric helix; folding by intramolecular hydrogen bonding. *Chemical Communications* **2004,** (1), 60-61.

1.1.2.2. Phenylene Ethylene

m-Phenylene ethynylene oligomers exhibit helical conformations in a solvent-dependent manner (Figure 3b). In polar solvents, such as acetonitrile, each helical turn consists of six repeating units [40]. Although the helix is mainly stabilized by π-stacking and solvophobic effects, Moore and co-workers [41] independently showed that hydrogen-bonding interactions can be used to restrict bond rotation of the ethynylene unit and favor the helical conformation by 1.2 kcal/mol. Water-soluble m-phenylene ethynylene oligomers were obtained by substituting the triethylene glycol sidechains with hexaethylene glycol sidechains [42].
Tew and co-workers [43] synthesized alkoxy-substituted o-phenylene ethynylene oligomers, which may form helices with three units per turn (Figure 3b). The alkoxy substituents make the oligomers soluble in common organic solvents such as chloroform, enabling future solution studies of o-phenylene ethynylene oligomers.

1.1.2.3. Oligoheterocyclic Strands

Lehn and co-workers [44] have studied helical oligoheterocyclic strands, composed of alternating pyridine and pyrimidine rings, by molecular modeling, NMR and crystallography (Figure 3c). Upon binding Pb^{2+} in acetonitrile or chloroform, the original helical oligomer adopted an extended conformation. The conformational change was readily reversed by introducing cryptands [2,2,2], which sequestered the Pb^{2+} from the extended oligomer. Upon the addition of Ag^{+}, the monomeric helical oligomers dimerized to give a double helix. The Ag^{+} bound the terminal bipyridyl moieties to give an $Ag_2(oligomer)_2$ complex. The double helix was stabilized by favorable face-to-face stacking of the aromatic rings involving dipole–dipole or dipole–complexation-induced dipole interactions. Dimerization was also reversed by subjecting the double-helical complex to cryptands [2,2,2], which sequestered the Ag^{+} ion from the double helix.

1.1.2.4. Aedamers

Aedamers are molecules that form a pleated secondary structure based on the stacking of alternating electron rich (1,5-dialkoxynaphthalene) and electron deficient (1,4,5,8-

---

[40] Hill, D. J.; Moore, J. S., Helicogenicity of solvents in the conformational equilibrium of oligo(m-phenylene ethynylene)s: Implications for foldamer research. *Proceedings of the National Academy of Sciences* **2002,** *99* (8), 5053-5057.
[41] Cary, J. M.; Moore, J. S., Hydrogen Bond-Stabilized Helix Formation of a m-Phenylene Ethynylene Oligomer. *Organic Letters* **2002,** *4* (26), 4663-4666.
[42] Stone, M. T.; Moore, J. S., A Water-Soluble m-Phenylene Ethynylene Foldamer. *Organic Letters* **2004,** *6* (4), 469-472.
[43] Jones, T. V.; Blatchly, R. A.; Tew, G. N., Synthesis of Alkoxy-Substituted ortho-Phenylene Ethynylene Oligomers. *Organic Letters* **2003,** *5* (18), 3297-3299.
[44] Barboiu, M.; Vaughan, G.; Kyritsakas, N.; Lehn, J.-M., Dynamic Chemical Devices: Generation of Reversible Extension/Contraction Molecular Motion by Ion-Triggered Single/Double Helix Interconversion. *Chemistry – A European Journal* **2003,** *9* (3), 763-769.

naphthalene-tetracarboxylic diimide) aromatic units [45] (Figure 3d). Folding is driven by hydrophobic effect coupled with electrostatic complementarity for face-centered stacking. Based on chemical shift data, the linkers determined the aromatic stacking geometry (center versus off-center), indicating conformational modularity for aedamers.

[45] Zych, A. J.; Iverson, B. L., Conformational Modularity of an Abiotic Secondary-Structure Motif in Aqueous Solution. *Helvetica Chimica Acta* **2002,** *85* (10), 3294-3300.

1.2. Pseudoproline Foldamers Based on 5-Carboxy-Oxazolidin-2-ones or Pyroglutamic Acids

Proline is the only amino acid that has a cyclic side chain; this characteristic provides to proline an exceptional rigidity and a considerably restricted conformational space. It has been noted that *cis-trans* isomerization of Xaa-Pro peptide groups is one of the rate-determining steps for folding and unfolding of various proteins (Figure 4a). In fact, poly-proline is known to form helical structures with two well-characterized conformations. The first is a left-handed poly-proline helix (PPII) that is formed when all the sequential residues adopt prolyl bonds in the *trans*-isomer conformation with three residues per turn (Figure 4b). The second is a compact right-handed polyproline helix (PPI), which is characterized by all sequential residues forming prolyl bonds in the *cis*-isomer conformation with 3.3 residues per turn (Figure 4c). The probability distribution for *cis-trans* prolyl bonds is affected by neighboring amino acids, pH and ionic strength, solvent and chain length.

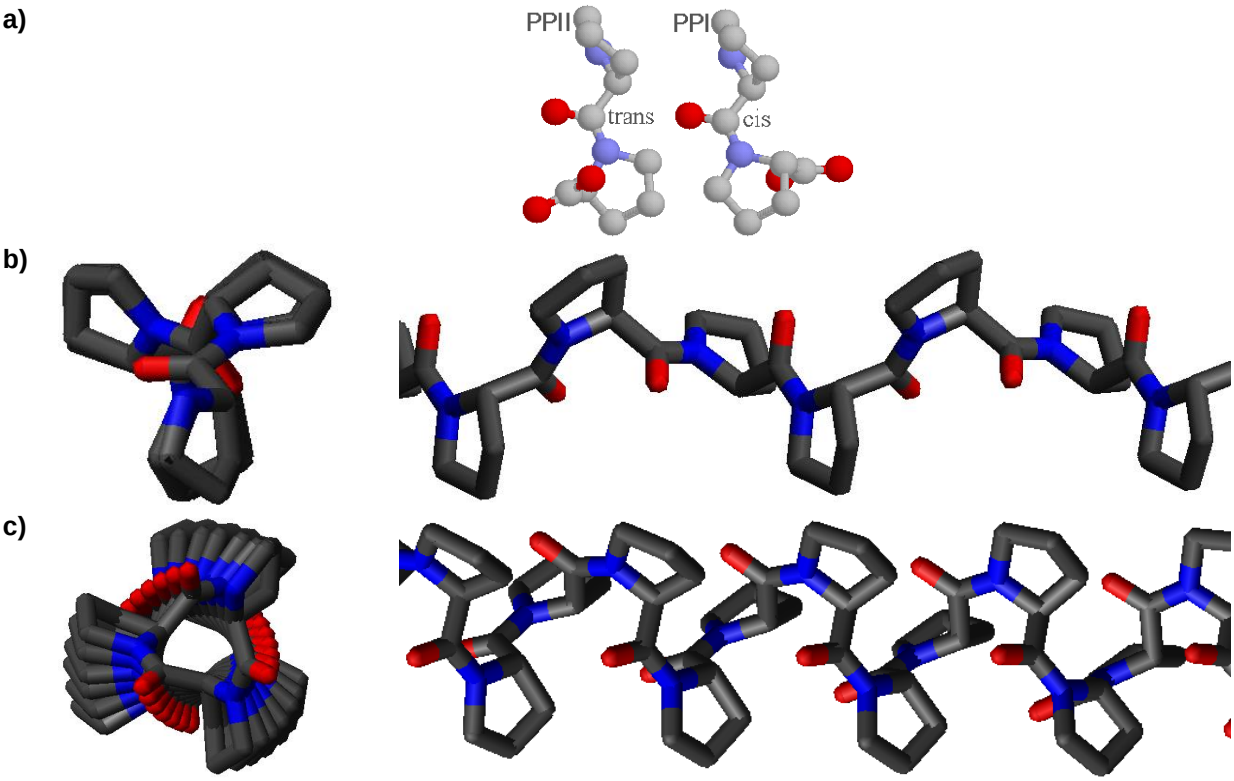

Figure 4. Poly-L-Proline: a) *cis-trans*-Isomer of Proline; b) Top-view and Slide-view of PPII; c) Top-view and Slide-view of PPI.

It has been noted experimentally that the PPII structure is favored in water, trifluoroethanol and methanol, while the PPI structure is favored in the presence of aliphatic alcohols like *n*-propanol.

New structures may be prepared by replacing the proline moieties with pseudoproline (ψ-Pro) units. The term pseudoproline was introduced recently to indicate synthetic proline analogues

usually obtained by cyclocondensation of the amino acids cysteine, threonine or serine with aldehydes or ketones [46].

Five-membered cycles that contain a nitrogen and a carboxy unit adjacent to one another in the ring may be assigned to the family of pseudoprolines. The research group of professor Claudia Tomasini [47] demonstrated that the presence of pseudoproline units like L-pyroglutamic acid (L-pGlu) and *trans*-(4*S*,5*R*)-4-carboxy-5-methyl oxazolidin-2-one (L-Oxd) (Figure 5) in more complex molecular architectures can lead to the formation of stable conformations, both in solution and in solid state.

The acylation product of those pseudoprolines leads to a particular backbone, in which the nitrogen atom of the ring is adjacent to both an exocyclic and an endocyclic carbonyl group, forcing them to a strict *trans* conformation (Figure 5).

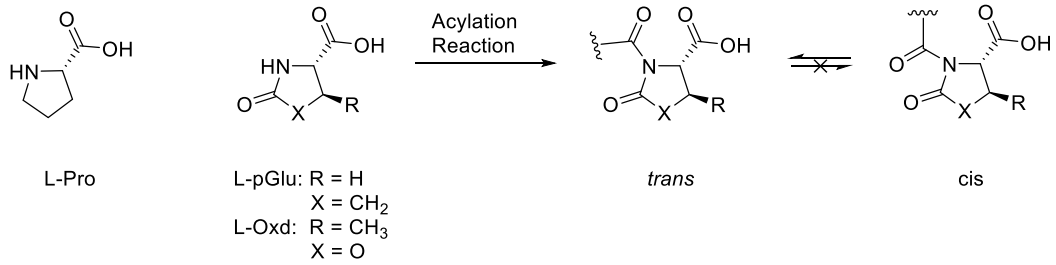

Figure 5. Chemical formula of L-Pro and *ψ*-Pro like L-Oxd and L-pGlu. The figure show the preferential *trans* conformation of the N-acylated form.

Tomasini and co-workers [48] synthetized the homo-oligomers of L-pGlu from monomer to tetramer (Figure 6). Interesting results were obtained from the analysis of the ^{1}H-NMR spectra, as the oligomers show a very deshielded signal of the CH_α compared with the monomer. This outcome should be ascribed to the presence of the carbonyl of the γ-lactam which strongly deshields CH_α that is nearby to the carbonyl, as the peptide bond is in the *trans* conformation (Figure 6a). X-ray crystallography confirms this preferential conformation (Figure 6a).

CD analysis show that poly-(L-pGlu)$_n$ formed a helical structure, similar to that adopted by poly-(L-Pro)$_n$ with *trans* tertiary peptide bonds (type II) (Figure 6b).

[46] Keller, M.; Sager, C.; Dumy, P.; Schutkowski, M.; Fischer, G. S.; Mutter, M., Enhancing the Proline Effect: Pseudo-Prolines for Tailoring Cis/Trans Isomerization. *Journal of the American Chemical Society* **1998,** *120* (12), 2714-2720.

[47] Tomasini, C.; Angelici, G.; Castellucci, N., Foldamers Based on Oxazolidin-2-ones. *European Journal of Organic Chemistry* **2011,** *2011* (20-21), 3648-3669.

[48] Bernardi, F.; Garavelli, M.; Scatizzi, M.; Tomasini, C.; Trigari, V.; Crisma, M.; Formaggio, F.; Peggion, C.; Toniolo, C., Pseudopeptide Foldamers: The Homo-Oligomers of Pyroglutamic Acid. *Chemistry – A European Journal* **2002,** *8* (11), 2516-2525.

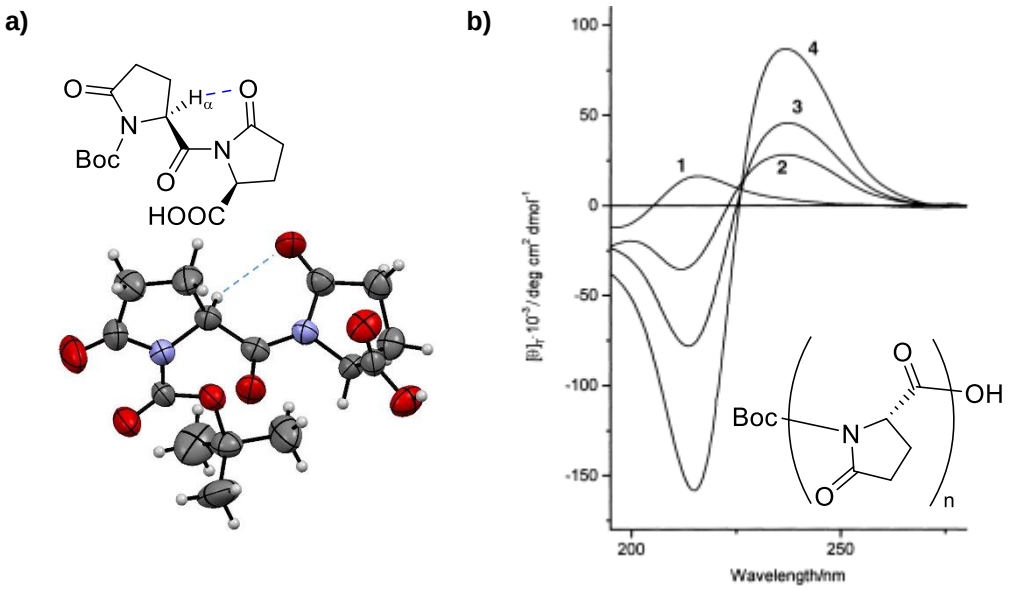

Figure 6. a) Chemical formula and X-ray of Boc-(L-pGlu)$_2$-OH; b) ECD spectra of Boc-(L-pGlu)$_n$-OH (n = 1-4) series in methanol.

Tomasini et al. studied also the conformational properties of the L-Oxd homo-oligomers (Figure 7). Unfortunately it was not possible to obtained a single crystal to determine the secondary structure by X-ray diffraction, so the research group determined the preferential conformation of the oligomers through DFT calculations implemented by ^{1}H NMR analysis.

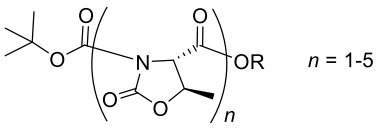

Figure 7. Chemical structure of the Boc-(L-Oxd)$_n$-OBn species investigated.

The lowest energy minimum for trimer, tetramer and pentamer was optimized, thus it was shown that for each homo-oligomer there are *n*–1 (where *n* is the number of monomers in each molecule) downfield-shifted protons and, as a consequence, that there are also *n*–1 αC–H•••O = C hydrogen bonds. These interactions, although weak, stabilize the overall secondary structure, allowing the molecule to adopt a robust poly-(L-Pro)$_n$ II-type helix (Figure 8a). The experimental CD spectra shown in Figure 8b confirm these conclusion obtained from DFT optimization. This result is in agreement with the results obtained with the L-*p*Glu series.

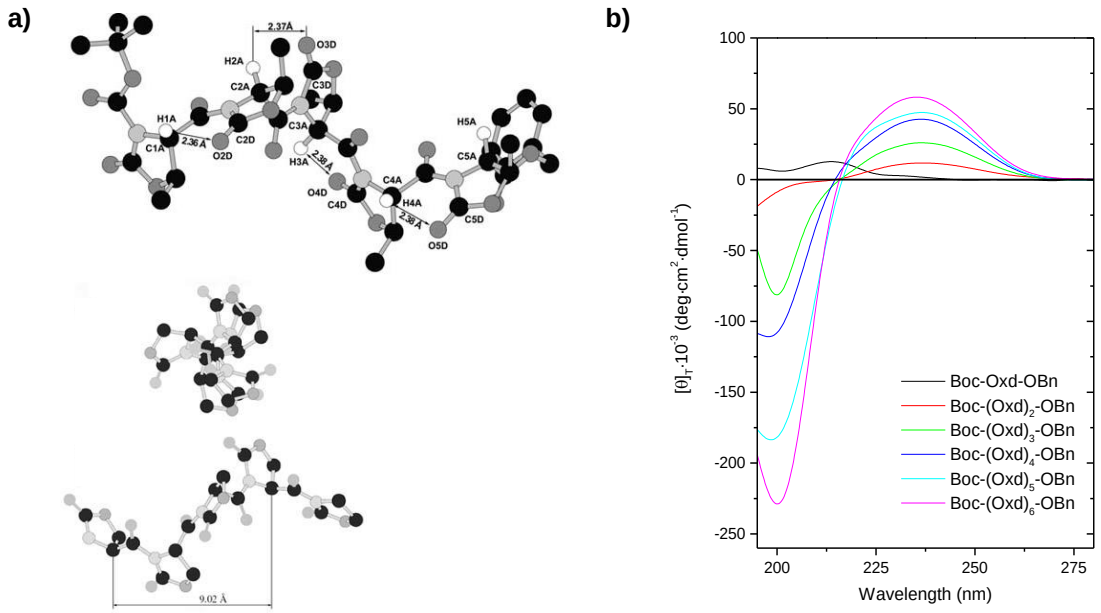

Figure 8. a) DFT optimization of poly-(L-Oxd)$_5$-OBn and Top-view and Slide-view of pentamer helix. b) ECD spectra of Boc-(L-Oxd)$_n$-OBn (n = 1-6) series in methanol.

Later Tomasini and co-worker [49] synthetized hybrid oligomers starting from Boc-Gly-OH and H-L-Oxd-OH in order to obtain Boc-(Gly-L-Oxd)$_n$-OBn (Figura 9).

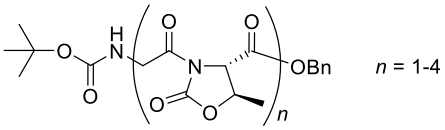

Figure 9. Chemical structure of the Boc-(Gly-L-Oxd)$_n$-OBn species investigated.

To establish if these molecules have a stable secondary structure, Tomasini and co-workers have analyzed these compounds by FT-IR, ^{1}H-NMR and CD spectra (Figure 10). The outcomes show that the regular increase in C = O•••H-N hydrogen bonds from n = 1 to n = 4 suggested by the IR analysis (Figure 10a) was also detected on investigation of the DMSO-d_6 dependence of the NH proton chemical shift (Figure 10b).

The per-residue CD signals change on going from n = 1 to n = 4 with a dramatic increase in absorbance, thus showing that an extra effect besides the chromophore absorption is present (Figure 10c). This can be attributed to the formation of hydrogen bonds and, as a result, of a secondary structure.

[49] Luppi, G.; Soffrè, C.; Tomasini, C., Stabilizing effects in oxazolidin-2-ones-containing pseudopeptides. *Tetrahedron: Asymmetry* **2004,** *15* (10), 1645-1650.

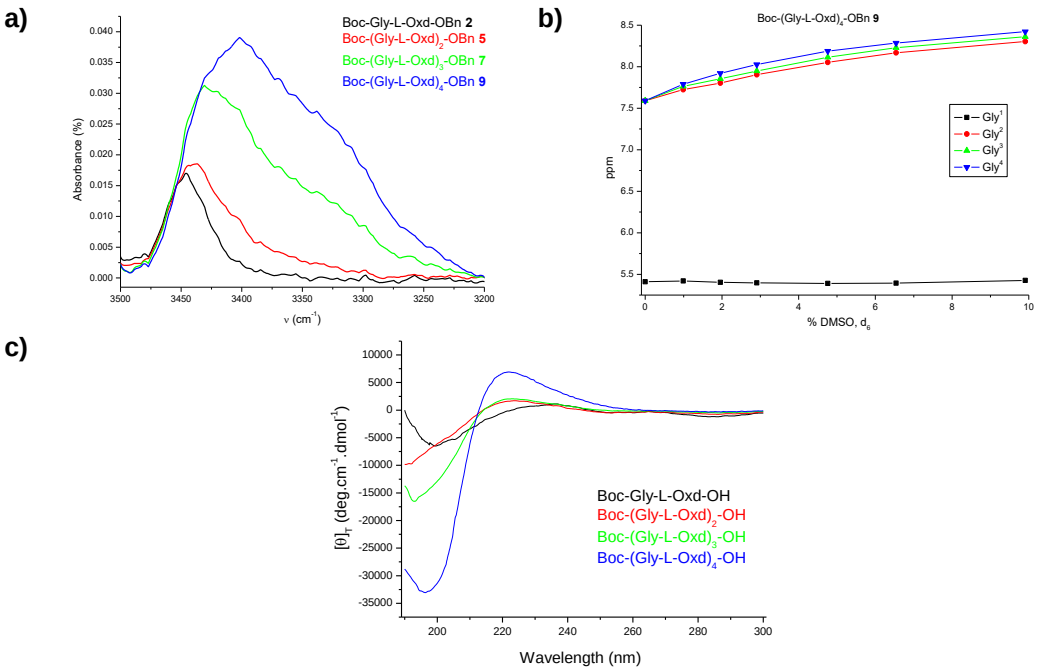

Figure 10. a) FT-IR of Boc-(Gly-L-Oxd)$_n$-OBn in chloroform; b) Variation of NH proton chemical shift (ppm) of tetramer a fuction of increasing percentages of DMSO-d_6 to the $CDCl_3$ solution; c) CD spectra of Boc-(Gly-L-Oxd)$_n$-OH in methanol.

To investigate further the preferred conformations of oligomers of the Boc-(Xaa-Oxd)$_n$-OBn series, Gly was replaced with Ala, thus introducing a methyl group as a side chain. Oligomers of both the Boc-(L-Ala-L-Oxd)$_n$-OBn and the Boc-(L-Ala-D-Oxd)$_n$-OBn series (Figure 11) were therefore synthesized, in order to check whether the Gly pro-S hydrogen or the pro-R hydrogen should be replaced [50].

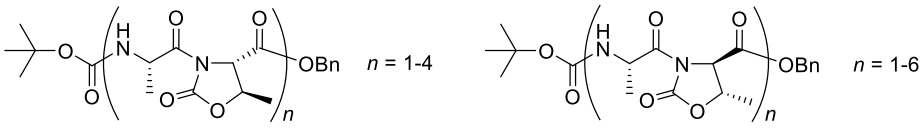

Figure 11. Chemical structure of Boc-(L-Ala-L-Oxd)$_n$-OBn and Boc-(L-Ala-D-Oxd)$_n$-OBn.

The FT-IR absorption spectra of the two series were obtained (Figure 12a): the results show that the two series behave in very different ways. Indeed, the compounds of the series Boc-(L-Ala-L-Oxd)$_n$-OBn show no propensity to form intramolecular C = O•••H–N hydrogen bonds, whereas those of the Boc-(L-Ala-D-Oxd)$_n$-OBn series form strong hydrogen bonds in oligomers longer than the trimer.

[50] Tomasini, C.; Luppi, G.; Monari, M., Oxazolidin-2-one-Containing Pseudopeptides That Fold into β-Bend Ribbon Spirals. *Journal of the American Chemical Society* **2006,** *128* (7), 2410-2420.

To further validate these results, the two sets of oligomers were analyzed by ^{1}H NMR spectroscopy, as the formation of a C_{i+1} = O•••H–C_i intramolecular hydrogen-bond can be spotted simply by checking the chemical shift of the α-proton and the carbonyl proximity involves a marked deshielding of the proton. Unfortunately, the oligomers of both sets follow this trend, regardless of the absolute configurations of carbons 4 and 5 of the Oxd moiety, which in contrast are crucial for the formation of intramolecular O = C•••H–N hydrogen bonds, as deduced by IR absorption spectra analysis. However, the occurrence of intramolecular C = O•••H–N H-bonds in oligomers of the two sets was further determined by investigation of the DMSO-d_6 dependence of the NH proton chemical shifts (not show). The outcomes of these titrations are in perfect agreement with the results obtained from FT-IR absorption.

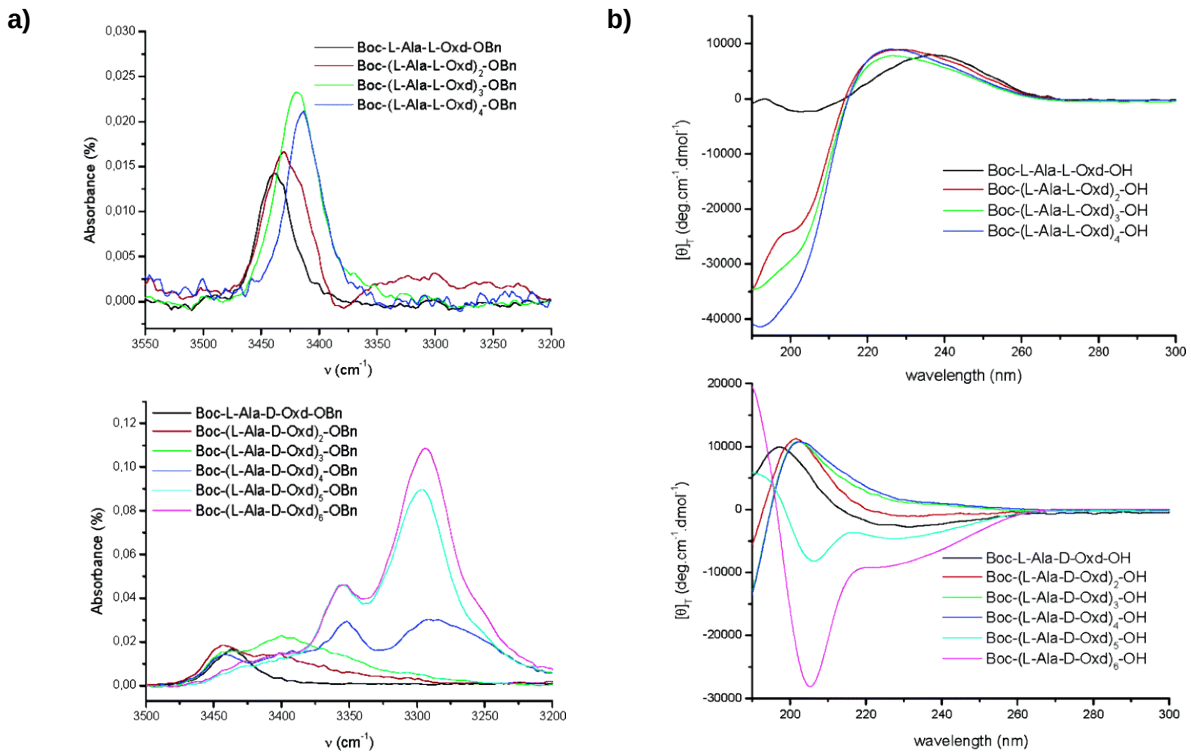

Figure 12. a) FT-IR of Boc-(L-Ala-L-Oxd)$_n$-OBn and Boc-(L-Ala-D-Oxd)$_n$-OBn in chloroform; b) CD of of Boc-(L-Ala-L-Oxd)$_n$-OH and Boc-(L-Ala-D-Oxd)$_n$-OH in metanol.

The per-residue CD spectra of the Boc-(L-Ala-L-Oxd)$_n$-OH sets (Figura 12b) do not exhibit any significant change from the monomers to longer oligomers, thus showing that no configuration-based effect takes place. The per-residue CD spectra of the Boc-(L-Ala-D-Oxd)$_n$-OBn series (Figure 12b) show a reversal of the Cotton effect for Boc-(L-Ala-D-Oxd)$_5$-OBn and, more dramatically, for Boc-(L-Ala-D-Oxd)$_6$-OBn, thus suggesting the formation of ordered secondary structures. The CD data meet all of the requirements for a 3_{10} helix (Figure 13).

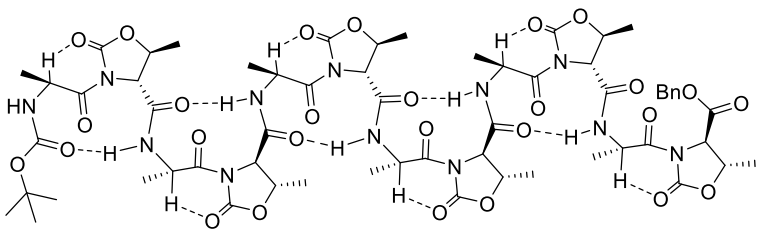

Figure 13. Conformation of Boc-(L-Ala-D-Oxd)$_6$-OBn, with the stabilizing effects.

Finally Tomasini et al [51] synthetized hybrid oligomers of the Boc-(L-Phe-D-Oxd)$_n$-OBn series with n from 1 to 5 (Figure 14). The compounds of Boc-(L-Phe-D-Oxd)$_n$-OBn (n = 2-5) were investigated both in solution and in solid state.

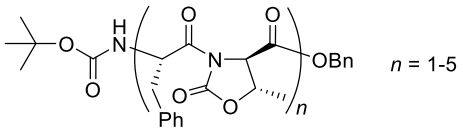

Figure 14. Chemical structure of the Boc-L-Phe-D-Oxd-OBn series.

The information about the preferred conformation of the oligomers in solution was obtained by analysis of FT-IR, ^{1}H NMR and X-ray crystallography. The results obtained from single-crystal X-ray diffraction of the dimer (Figure 15a) show that in this compound exists only a single intermolecular NH•••CO hydrogen bond between the dimeric units in the crystal packing, and these single hydrogen bonds generate an infinite antiparallel β-sheet structure running along the crystallographic *a* axis (Figure 15b).

[51] Angelici, G.; Falini, G.; Hofmann, H.-J.; Huster, D.; Monari, M.; Tomasini, C., Nanofibers from Oxazolidi-2-one Containing Hybrid Foldamers: What is the Right Molecular Size? *Chemistry – A European Journal* **2009,** *15* (32), 8037-8048.

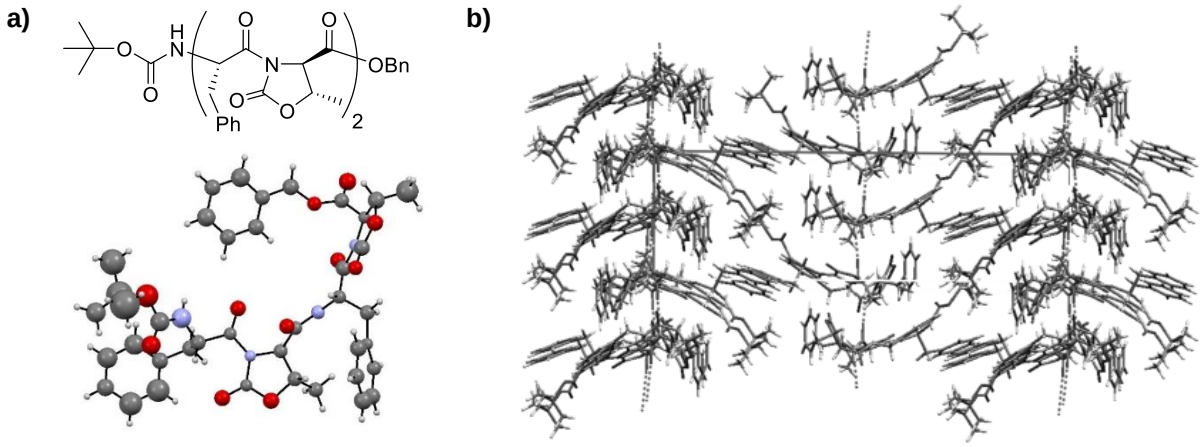

Figure 15. a) chemical structure and X-ray structure of Boc-(L-Phe-D-Oxd)$_2$-OBn; b) View down the crystallographic *b* axis of the crystal packing diagram of Boc-(L-Phe-D-Oxd)$_2$-OBn showing the intermolecular NH•••CO hydrogen bonds running along the *a* axis.

NOESY experiments on a 10 mM solution of Boc-(L-Phe-D-Oxd)$_5$-OBn in DMSO-d_6 give additional structural information. $N_iH \rightarrow N_{i+1}H$ Cross-peaks between the H^N amide hydrogen atoms (δ = 8.91, 8.93, 8.99, and 9.11 ppm) and the H^N carbamate hydrogen (δ~7.25 ppm) account for the formation of a folded structure. In addition, a cross-peak between the H^N amide proton and only one of the two phenylalanine H^β atoms (δ~2.6 ppm) was observed, together with several cross-peaks between the H^N amide hydrogen atoms and the phenylalanine H^α (δ~6 ppm), the Oxd CHN and CHO hydrogen atoms (δ~4.5 ppm), and the methyl hydrogen atoms (δ~1.3 ppm).

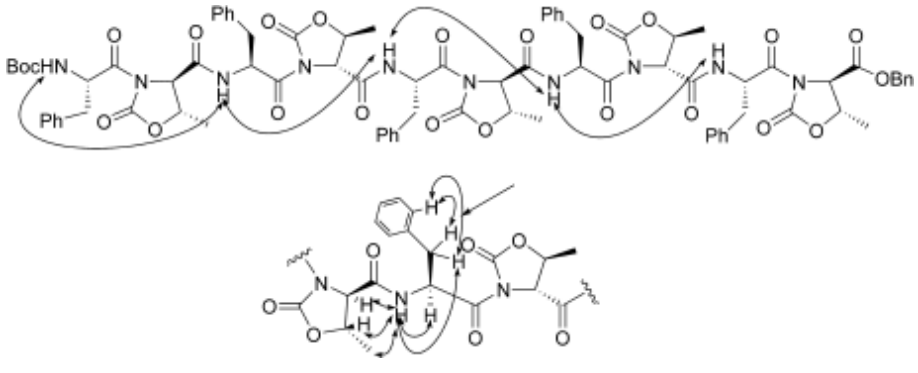

Figure 16. Results for the NOESY experiments of Boc-(L-Phe-D-Oxd)$_5$-OBn performed on a 10 mM DMSO-*d6* solution.

2. Base Studies

2.1. Conformational Studies

2.1.1. 1,2,3-Triazole as Peptidomimetics

The biological function of peptides and proteins is defined by their ability to adopt well-defined conformations that complement those of their corresponding binding partner or receptor. The access to peptidomimetics that mimic and/or stabilize such secondary structures (e.g., α-helices and β-turns) allows the study of the associated biological processes, with an opportunity for drug design and development. However, a major obstacle to this endeavor is the lack of general methods for the synthesis of specific classes of peptidomimetics that are active under physiological conditions. 1,2,3-Triazoles offer an appealing structural motif in peptidomimetic research because their structural and electronic characteristics are similar to those of a peptide bond and because general methods are now available for their synthesis (Figure 17) [52,53]. Historically, 1,2,3-triazoles are synthesized by a thermal Huisgen cycloaddition reaction which generally produces mixtures of 1,4- and 1,5-substituted triazoles [54,55].

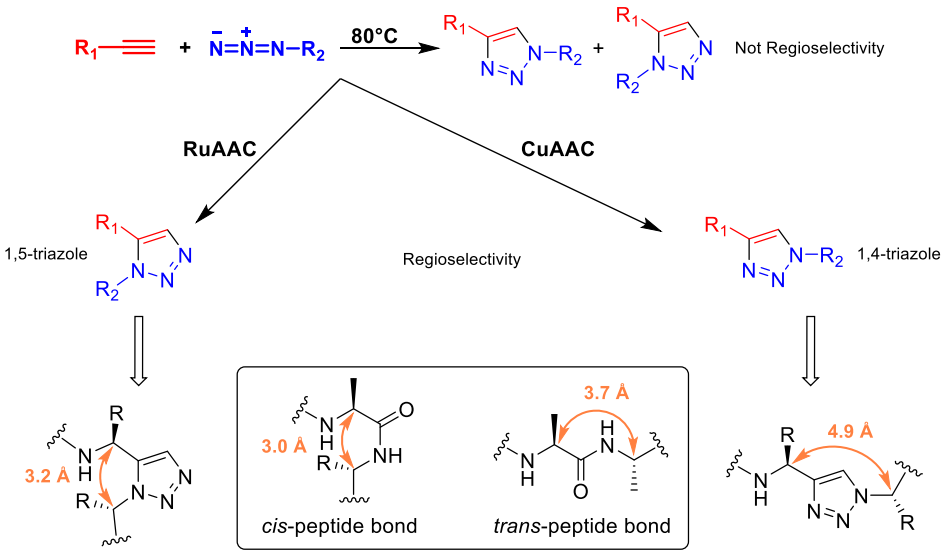

Figure 17. General method of triazoles synthesis and comparison of 1,4- and 1,5-substituted triazoles with *cis*- and *trans*-peptide bond.

[52] Angell, Y. L.; Burgess, K., Peptidomimetics via copper-catalyzed azide-alkyne cycloadditions. *Chemical Society Reviews* **2007,** *36* (10), 1674-1689.
[53] Pedersen, D. S.; Abell, A., 1,2,3-Triazoles in Peptidomimetic Chemistry. *European Journal of Organic Chemistry* **2011,** *2011* (13), 2399-2411.
[54] Huisgen, R., 1.3-Dipolare Cycloadditionen Rückschau und Ausblick. *Angewandte Chemie* **1963,** *75* (13), 604-637.
[55] Huisgen, R., Kinetik und Mechanismus 1.3-Dipolarer Cycloadditionen. *Angewandte Chemie* **1963,** *75* (16-17), 742-754.

The group of Meldal [56,57] reported that copper(I) can catalyse azide alkyne cycloaddition (CuAAC, also known as the copper-catalysed Huisgen cycloaddition), thus providing a selective access to 1,4-substituted 1,2,3-triazoles. More recently Sharpless and co-workers [58] reported a ruthenium catalysed azide alkyne cycloaddition (RuAAC) that allows the synthesis of 1,5-substituted triazoles. Several research groups have reported the formation of 1,4-triazoles that are mimics of *trans* peptide bonds [52,53,59,60,61,62,63] and few groups have reported the preparation of 1,5-triazoles that are mimics of *cis* peptide bonds [64,65,66].

As 1,4-triazoles mimic *trans* peptide bonds, they are interesting compounds in combinatorial and/or high throughput synthesis of peptidomimetics of potential value in medicinal chemistry. In fact, the triazole ring has several attributes that are highly attractive:

1) the 1,2,3-triazole nucleus is a good candidate for small molecule drugs;
2) it can be prepared in high yields with few by-products;
3) it is compatible with the side chains of all the amino acids, at least in the protected form;
4) the molecular dimensions of 1,2,3-triazoles are somewhat similar to amide bonds in terms of distance and planarity (Figure 16);
5) the 1,2,3-triazole nucleus is a strong dipole and has hydrogen-bond accepting and donating properties similar to peptides.

[56] Tornøe, C. W.; Christensen, C.; Meldal, M., Peptidotriazoles on Solid Phase: [1,2,3]-Triazoles by Regiospecific Copper(I)-Catalyzed 1,3-Dipolar Cycloadditions of Terminal Alkynes to Azides. *The Journal of Organic Chemistry* **2002,** *67* (9), 3057-3064.

[57] Meldal, M.; Tornøe, C. W., Cu-Catalyzed Azide−Alkyne Cycloaddition. *Chemical Reviews* **2008,** *108* (8), 2952-3015.

[58] Zhang, L.; Chen, X.; Xue, P.; Sun, H. H. Y.; Williams, I. D.; Sharpless, K. B.; Fokin, V. V.; Jia, G., Ruthenium-Catalyzed Cycloaddition of Alkynes and Organic Azides. *Journal of the American Chemical Society* **2005,** *127* (46), 15998-15999.

[59] Angelo, N. G.; Arora, P. S., Solution- and Solid-Phase Synthesis of Triazole Oligomers That Display Protein-Like Functionality. *The Journal of Organic Chemistry* **2007,** *72* (21), 7963-7967.

[60] Wu, C.-F.; Zhao, X.; Lan, W.-X.; Cao, C.; Liu, J.-T.; Jiang, X.-K.; Li, Z.-T., A 1,4-Diphenyl-1,2,3-Triazole-Based β-Turn Mimic Constructed by Click Chemistry. *The Journal of Organic Chemistry* **2012,** *77* (9), 4261-4270.

[61] Zhang, Z.; Fan, E., Solid phase synthesis of peptidotriazoles with multiple cycles of triazole formation. *Tetrahedron Letters* **2006,** *47* (5), 665-669.

[62] Oh, K.; Guan, Z., A convergent synthesis of new [small beta]-turn mimics by click chemistry. *Chemical Communications* **2006,** (29), 3069-3071.

[63] Angell, Y.; Burgess, K., Ring Closure to β-Turn Mimics via Copper-Catalyzed Azide/Alkyne Cycloadditions. *The Journal of Organic Chemistry* **2005,** *70* (23), 9595-9598.

[64] Pokorski, J. K.; Miller Jenkins, L. M.; Feng, H.; Durell, S. R.; Bai, Y.; Appella, D. H., Introduction of a Triazole Amino Acid into a Peptoid Oligomer Induces Turn Formation in Aqueous Solution. *Organic Letters* **2007,** *9* (12), 2381-2383.

[65] Tam, A.; Arnold, U.; Soellner, M. B.; Raines, R. T., Protein Prosthesis: 1,5-Disubstituted[1,2,3]triazoles as cis-Peptide Bond Surrogates. *Journal of the American Chemical Society* **2007,** *129* (42), 12670-12671.

[66] Horne, W. S.; Olsen, C. A.; Beierle, J. M.; Montero, A.; Ghadiri, M. R., Probing the Bioactive Conformation of an Archetypal Natural Product HDAC Inhibitor with Conformationally Homogeneous Triazole-Modified Cyclic Tetrapeptides. *Angewandte Chemie* **2009,** *121* (26), 4812-4818.

Sharpless and his co-workers published many high quality papers to alert the scientific community to the value of CuAAC as a Click Chemistry Reaction [67]. He coined the term ‘‘Click Chemistry’’ [68] to describe a reaction that is modular and wide in scope, gives very high yields, generates only inoffensive by-products that can be removed easily and is stereospecific (but not necessarily enantioselective). The required process characteristics include simple reaction conditions (ideally, the process should be insensitive to oxygen and water), readily available starting materials and reagents, employing no solvent or a benign solvent (as water) and simple conditions for product isolation. Purification (if required) must be made by non-chromatographic methods, such as crystallization or distillation, and the product must be stable under physiological conditions. Unfortunately, the RuAAC method for the synthesis of 1,5-substituted triazoles is not compatible with the Click Chemistry concept.

2.1.2. Synthesis of the L-Oxd-Tri Scaffold and Preliminary Conformational Analysis

We have prepared some new compounds containing both the oxazolidin-2-one and 1,2,3-triazole rings (Figure 18) that are pseudo-dipeptide units and mimic a α,β-dipeptide. Both heterocycles impart a rigid *trans* conformation to the chain, but they differ in their spatial arrangements, as the Oxd moiety is chiral and 3,4-disubstituted, whereas the Tri moiety is flat, achiral and 1,4-disubstituted.

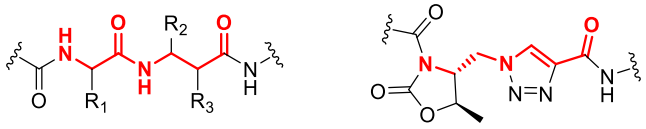

Figure 18. General structure of the L-Oxd-Tri-CO scaffords compared to a general structure of α,β-dipeptide.

Tomasini and Castellucci [69] synthetized Boc-D-Phe-L-Oxd-Tri-CO-D-Val-OMe in several step with a good overall yield. They have obtained interesting conformational informations by ^{1}H NMR spectroscopy. They found that the ROESY spectrum of Boc-D-Phe-L-Oxd-Tri-CO-D-Val-OMe shows a cross-peak between the C–H of the triazole ring and the *tert*-butyl group of the Boc moiety (Figure 19a).

[67] Kolb, H. C.; Sharpless, K. B., The growing impact of click chemistry on drug discovery. *Drug Discovery Today* **2003,** *8* (24), 1128-1137.
[68] Kolb, H. C.; Finn, M. G.; Sharpless, K. B., Click Chemistry: Diverse Chemical Function from a Few Good Reactions. *Angewandte Chemie International Edition* **2001,** *40* (11), 2004-2021.
[69] Castellucci, N.; Tomasini, C., Preorganised Dipeptide Mimics as Foldamer Building Blocks. *European Journal of Organic Chemistry* **2013,** *2013* (17), 3567-3573.

a) b)

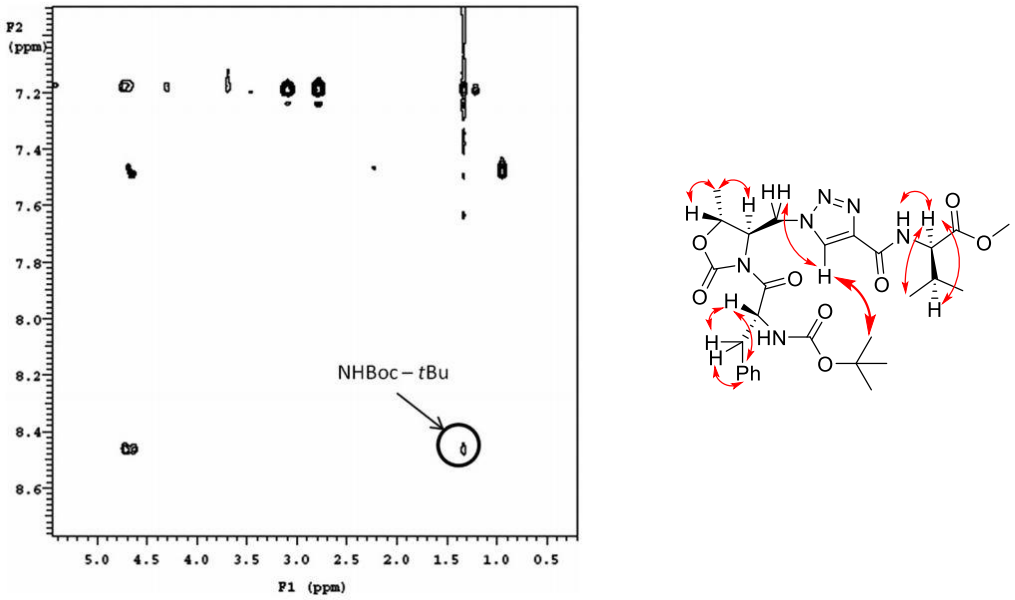

Figure 19. a) Enlargement of the ROESY spectrum of Boc-D-Phe-L-Oxd-Tri-CO-D-Val-OMe, showing the cross-peak between the triazole C–H and the Boc *tert*-butyl group; b) NOE enhancements obtained from ROESY spectrum.

The correlation between the triazole CH and the *tert*-butyl group in Boc-D-Phe-L-Oxd-Tri-CO-D-Val-OMe, suggests that the two rigid heterocycles are connected by a flexible methylene group and are organized in a bent conformation (Figure 19b). This moiety can mimic a turn if it is introduced into a polypeptide chain (Figure 20).

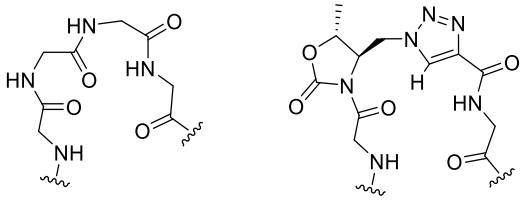

Figure 20. Proposed preferred conformation of Oxd-Tri (right), compared with a β-turn conformation (left).

This pseudo-dipeptide is an interesting scaffold for the formation of new foldamers. Moreover the ability of triazole-based pseudopeptide structures to interact with metals ions (e.g. copper, zinc, etc.) provides the interesting possibility to exploit these systems as building-blocks for

the fabrication of supramolecular materials [70], metal carriers [71], or metal-stabilized folded structures [72].

2.1.3. Synthesis of α,ε-Hybrid Oligomers

We have synthetized and studied the two series of oligomers [73] shown in Figure 21. The first series contains L-Ala and the D-Oxd-Tri moiety, while the other series contains L-Ala and the L-Oxd-Tri moiety. The two epimeric series of foldamers characterized by the presence of the repeating α,ε-dipeptide unit can be used to investigate which is the influence of asymmetric carbons and heterocycles on the secondary structure and the investigation of the tendency to form stable complexes with Cu^{2+} ions was also assessed.

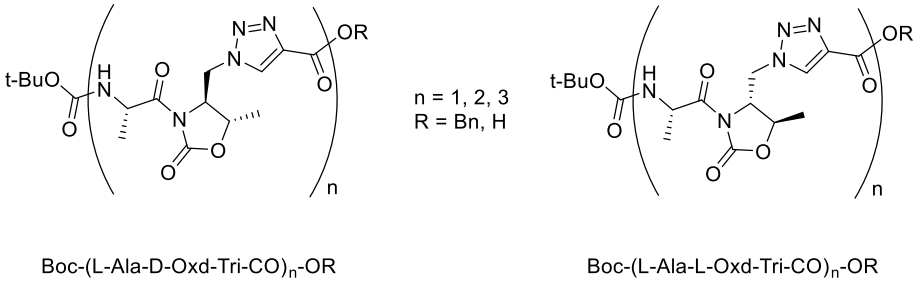

Figure 21. General formula of the investigated oligomers.

The preparation of the L-Oxd-Tri-CO moiety has been obtained following the recently described procedure,[69] but the synthesis of the key intermediates D- and L-4-azidomethyl-5-methyl–oxazolidin-2-one (D-**3** and L-**3**) on a multigram scale was optimized in terms of yield, times and costs. As compared with the known procedures [74], a convenient one-pot process was developed for the preparation of (4S,5S)-4-(hydroxymethyl)-5-methyloxazolidin-2-one D-**1** (Scheme 1).

D-Thr-OMe was cyclized with triphosgene at room temperature to give (4R-5S)–4–methylcarboxylate–5-methyl-oxazolidin-2-one. After removal of the volatiles, the methyl ester was directly reduced to D-**1** with sodium borohydride. The corresponding alcohol was

[70] Liu, Y.-Y., Synthesis, structure and characterization of copper(II) and zinc(II) complexes based on 3-carboxyl-1,2,4-triazole. *Journal of Coordination Chemistry* **2007,** *60* (23), 2597-2605.
[71] Lozano-Vila, A. M.; Luna-Giles, F.; Viñuelas-Zahínos, E.; Cumbrera, F. L.; Ortiz, A. L.; Barros-García, F. J.; Rodríguez, A. B., Synthesis and structural characterization of two new copper(II) complexes with thiazoline derivative ligands: Influence of the coordination on the phagocytic activity of human neutrophils. *Inorganica Chimica Acta* **2011,** *365* (1), 282-289.
[72] Nicoll, A. J.; Miller, D. J.; Fütterer, K.; Ravelli, R.; Allemann, R. K., Designed High Affinity Cu2+-Binding α-Helical Foldamer. *Journal of the American Chemical Society* **2006,** *128* (28), 9187-9193.
[73] Milli, L.; Larocca, M.; Tedesco, M.; Castellucci, N.; Ghibaudi, E.; Cornia, A.; Calvaresi, M.; Zerbetto, F.; Tomasini, C., α,ε-Hybrid Foldamers with 1,2,3-Triazole Rings: Order versus Disorder. *The Journal of Organic Chemistry* **2014,** *79* (13), 5958-5969.
[74] Lemen, G. S.; Wolfe, J. P., Pd-Catalyzed Carboamination of Oxazolidin-2-ones: A Stereoselective Route to trans-2,5-Disubstituted Pyrrolidines. *Organic Letters* **2010,** *12* (10), 2322-2325.

converted in the tosylate D-**2** with TsCl in high yield. Finally, the conversion of D-**2** to the corresponding azide D-**3** was complete in 25 minutes under microwave irradiation with an overall yield of 79%. The azide D-**3** was transformed into the corresponding 1,2,3-triazole by CuAAC with benzyl propiolate, affording D-Oxd-Tri-COOBn D-**4** in 78% yield. The compound was coupled with Boc-L-Ala-OH to synthesize Boc-L-Ala-D-Oxd-Tri-COOBn **5**.

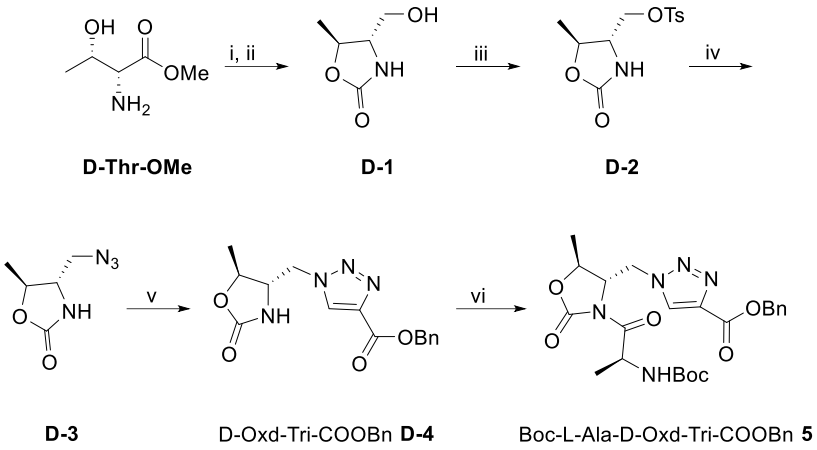

Scheme 1. Reagents and Conditions: (i) triphosgene (1.1 equiv), THF, r.t., 1 h; (ii) $NaBH_4$ (1.1 equiv.), EtOH, r.t., 1 h, NH_4Cl, 45 min; (iii) TsCl (1.1 equiv.), DMAP (10% w/w), pyridine, r.t., 18 h; (iv) NaN_3 (1.1 equiv.), dry DMF, MW - 150 Watt/s, 25 min; (v) benzyl propiolate (1.0 equiv.), DIEA (2.0 equiv.), lutidine (2.0 equiv.), CuI (0.1 equiv.), dry acetonitrile, r.t., 2 h; (vi) Boc-L-Ala-OH (1.0 equiv.), HBTU (1.1 equiv.), TEA (2.0 equiv.), dry acetonitrile, r.t., 50 min.

Compound **5** was used to generate the corresponding dimer Boc-(L-Ala-D-Oxd-Tri-CO)$_2$-OBn **7** and trimer Boc-(L-Ala-D-Oxd-Tri-CO)$_3$-OBn **9**, after deprotections and coupling reactions (Scheme 2). For the ECD analysis the benzyl protecting group was removed by hydrogenolysis, because the benzyl group have a strong adsorption in the region 180-220 and interferes with our analysis.

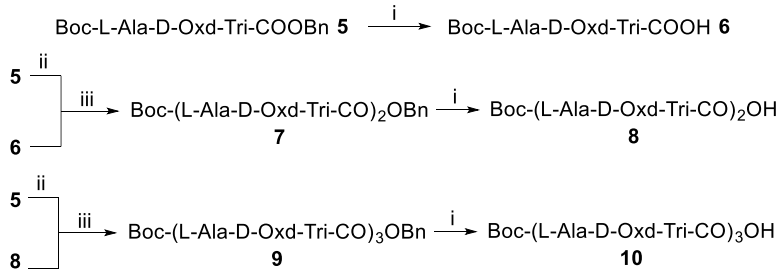

Scheme 2. Reagents and conditions: (i) H_2, Pd/C (10%) (0.1 equiv.), MeOH, r.t., 16 h; (ii) TFA (18 equiv.), dry CH_2Cl_2, r.t., 4 h; (iii) HBTU (1.1 equiv.), TEA (2.0 equiv.), dry acetonitrile, r.t., 50 min.

Following the same approach, we prepared a series of oligomers that have L,L configuration to compare their conformational preferences with the L,D series. Therefore, L-Oxd-Tri-COOBn L-**4** was prepared as previously described for D-**4**, starting from **L-Thr-OMe**, and it was further

derivatized with Boc-L-Ala-OH to yield Boc-L-Ala-L-Oxd-Tri-COOBn **11** (Scheme 3). In the same way, we synthetized the corresponding dimer Boc-(L-Ala-L-Oxd-Tri-CO)$_2$-OBn **13** and trimer Boc-(L-Ala-L-Oxd-Tri-CO)$_3$-OBn **15** by deprotections and subsequent coupling reactions, then we prepared the corresponding acids **12**, **14** and **16** by hydrogenolysis (Scheme 3).

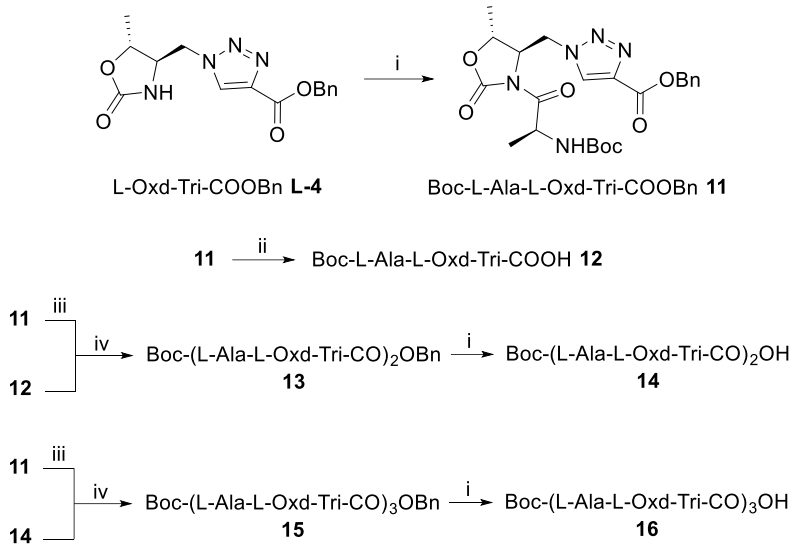

Scheme 3. Reagents and conditions: (i) Boc-L-Ala-OH (1.0 equiv.), HBTU (1.1 equiv.), TEA (2.0 equiv.), dry acetonitrile, r.t., 50 min; (ii) H_2, Pd/C (10%) (0.1 equiv.), MeOH, r.t., 16 h; (ii) TFA (18 equiv.), dry CH_2Cl_2, r.t., 4 h; (iv) HBTU (1.1 equiv.), TEA (2.0 equiv.), dry acetonitrile, r.t., 50 min.

2.1.4. Conformational Analysis

Preliminary information on the preferred conformation of the oligomers of both series was obtained by ^{1}H NMR and ECD absorption spectra in solution. Unfortunately the FT-IR spectroscopy in DCM solution gave no useful information, since we could not find any evidence for the formation of intramolecular N-H•••O = C hydrogen bonds, as no stretching bands below 3400 cm^{-1} were detected. The outcomes obtained by single-crystal X-ray diffraction and molecular dynamics calculations give information about the 3D disposition and the secondary structure of compounds.

2.1.4.1. ^{1}H NMR Spectroscopy

By ^{1}H NMR spectroscopy we confirmed the identity of all compounds. ROESY experiments on Boc-(L-Ala-D-Oxd-Tri-CO)$_3$-OBn **9** and Boc-(L-Ala-L-Oxd-Tri-CO)$_3$-OBn **15** gave information on the preferred conformation of the two oligomers. All experiments were recorded with a mixing time of 0.400 s for both samples (Figure 22).

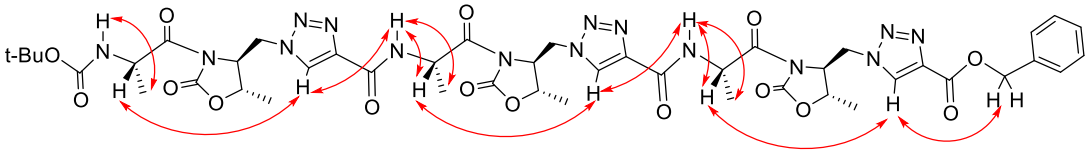

Boc-(L-Ala-D-Oxd-Tri-CO)$_3$-OBn **9**

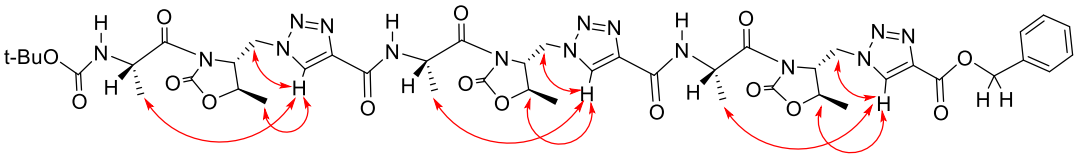

Boc-(L-Ala-L-Oxd-Tri-CO)$_3$-OBn **15**

Figure 22. NOE enhancements gathered from the ROESY spectrum analysis of **9** (top) and of **15** (bottom) (3 mM solution in $CDCl_3$, mixing time 0.400 s).

The ROESY spectrum of **9** in $CDCl_3$ shows cross peaks that have been attributed to the interaction of the triazole CH with the amide NH and with the alanine CH (Figure 23a). These outcomes suggest that the formation of a bent conformation is preferred. Unfortunately, the compound **15** was poorly soluble in $CDCl_3$, which forced us to record the ROESY spectrum in CD_3OD. The fast exchange between the NH of the amide moieties and the deuterated solvent prevented the analysis of cross peaks that involve the amide NH and we could analysed only the cross peaks between the triazole C-H and the alanine methylene groups (Figure 23b).

a)

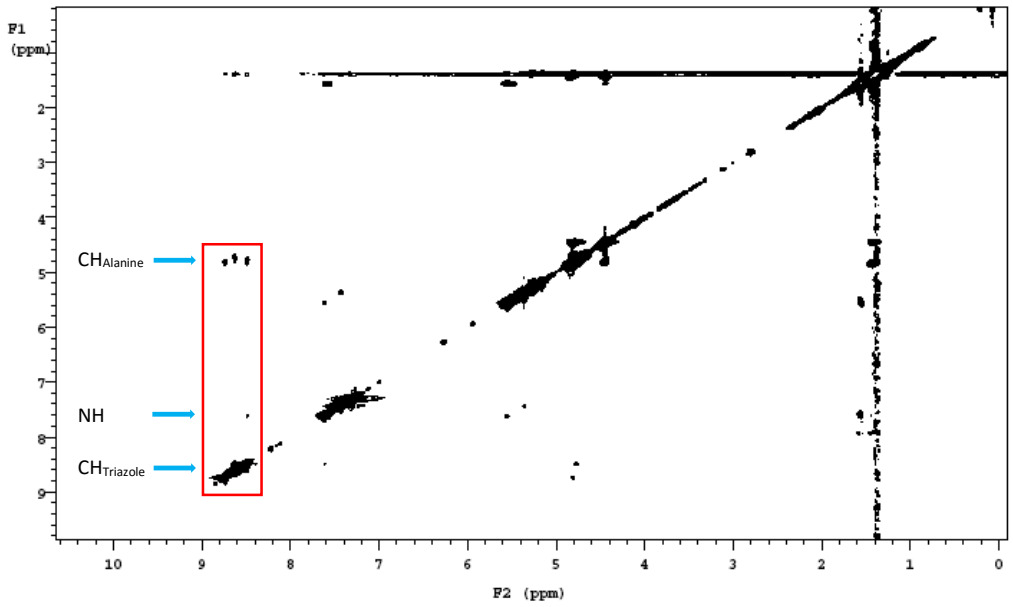

b)

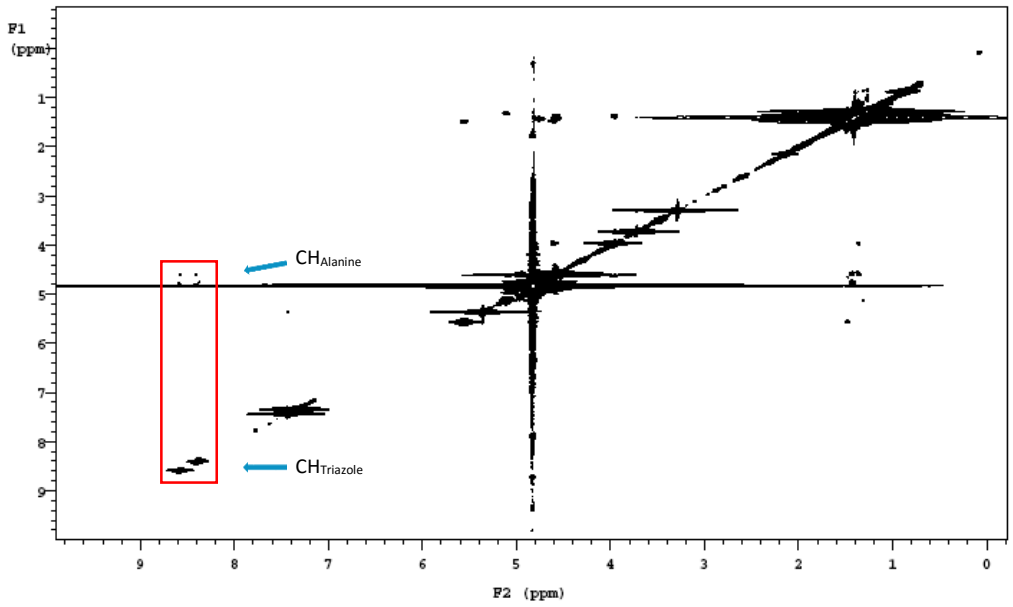

Figure 23. a) ROESY spectrum of Boc-(L-Ala-D-Oxd-Tri-CO)$_3$-OBn **9** in $CDCl_3$ (mixing time 0.150 s). b) ROESY spectrum of Boc-(L-Ala-L-Oxd-Tri-CO)$_3$-OBn **15** in CD3OD (mixing time 0.150 s).

2.1.4.2. ECD Spectroscopy

ECD spectroscopy was perfomed on the acids of both series, namely **6**, **8**, **10**, **12**, **14** and **16**. In Figure 8, the per-residue ECD spectra of the oligomers of both series are reported. The spectra were recorded for 5 mM solutions in a 8:2 methanol/water mixture. The analysis of the preferred conformation of these compounds is not straightforward. These oligomers contain unusual structures that cannot easily be compared with α-amino acid oligomers. Nevertheless some information can be obtained from the comparison of these ECD spectra: the spectra of the L,L series shown in Figure 24b are very similar and display a strong negative band at 200-

204 nm and a broad positive featureless band between 220 and 260 nm. These ECD spectra are strongly reminiscent of random coils.

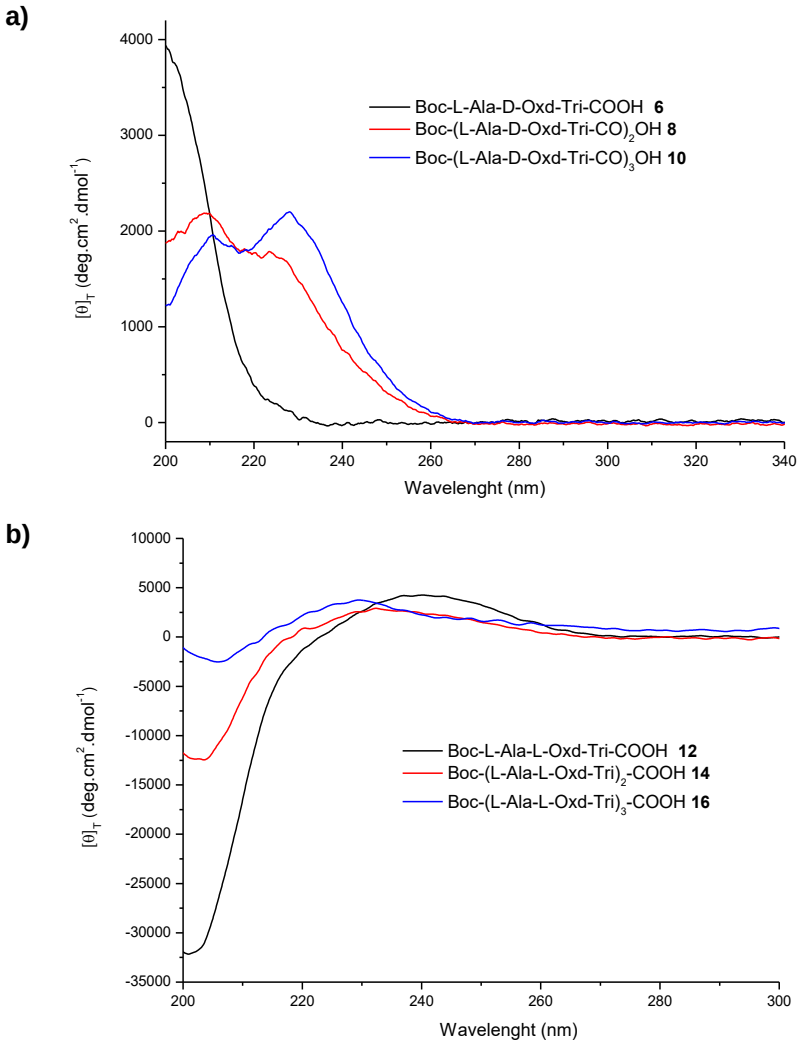

Figure 24. a) Per-residue CD spectra of the oligomers of the L,D series: **6**, **8** and **10**; b) Per-residue CD spectra of the oligomers of the L,L series: **12**, **14** and **16**.

Indeed, the ECD spectra of the L,D series (Figure 24a) differ from each other and suggest the appearance of a secondary structure in dimer **8** and trimer **10**. Comparison with previous data [75], as well as the analogy between triazole and proline rings, suggests the assignment of the ~200 nm band to a β-turn that may form by hydrogen bonding between the oxygen of the carbamate group (Boc) and the proton on the 1,2,3-triazole at position 5 of the ring. The CD spectra of compounds **8** and **10** display two positive bands of comparable intensity at ~210 and ~228 nm, that recall an atypical helical structure. In fact, apart from the sign of the Cotton effect, these features are typical of right-handed helix-3_{10} structures. On the other hand, the ratio between the intensities of the two bands does not fully correspond to such structures.

[75] Pokorski, J. K.; Miller Jenkins, L. M.; Feng, H.; Durell, S. R.; Bai, Y.; Appella, D. H., Introduction of a Triazole Amino Acid into a Peptoid Oligomer Induces Turn Formation in Aqueous Solution. *Organic Letters* **2007,** *9* (12), 2381-2383.

Taking into account the presence of a rigid triazole ring within the structure, by analogy with previous data, an atypical helix structure may be hypothesized, assuming that triazole is responsible for the inversion of the Cotton effect.

Based on the experimental evidence, we propose that the monomer (**6**), dimer (**8**) and trimer (**10**) of the L,D series, exhibit a β-turn responsible for the absorption at low wavelength. Chain elongation allows further structuring, stabilized by intramolecular hydrogen bonds.

2.1.4.3. Single-Crystal X-ray Diffraction

Crystals of **5** and **7**·0.5C_6H_6 suitable for X-ray diffraction were grown as long needles by slowly evaporating solutions of **5** and **7** in benzene and benzene/methyl *tert*-butyl ether 1:1 v/v, respectively. In compound **5**, the peptide folding mimics the β-turn structure of proteinogenic α-aminoacids (Figure 25).

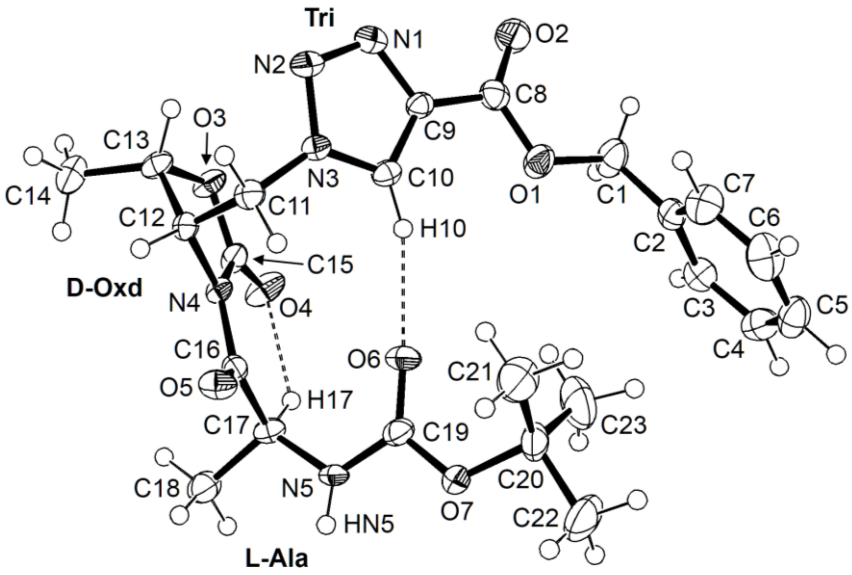

Figure 25. Ortep-3 [76] plot of **5** with thermal ellipsoids drawn at 50% probability and H atoms represented as spheres of arbitrary radius. For simplicity, only H atoms engaged in intra- or intermolecular interactions are labelled. The dashed lines highlight intramolecular hydrogen bonding interactions discussed in the text.

The carbon atom C10 of the triazole is engaged in a non-classical hydrogen interaction with the carboxyl oxygen O6 of the Boc group [d(H10•••O6) = 2.14(2) Å], resulting in an eleven-membered hydrogen-bonded turn (3_{11}-helical structure). By consequence, the two five-membered rings in the D-Oxd-Tri residue are forced in a *syn* conformation around the C11-C12 linkage. At the same time, the *t*Bu carbon atom C23 of the Boc terminus is found at 3.51 Å from the centre of the phenyl ring C2–C7, suggesting a CH/π interaction. The α-carbon

[76] Farrugia, L. J., ORTEP-3 for Windows - a version of ORTEP-III with a Graphical User Interface (GUI). *Journal of Applied Crystallography* **1997,** *30* (5-1), 565-565.

atom of the L-Ala residue (C17) has an intramolecular H-contact with the endocyclic carbonyl oxygen O4 of the D-Oxd fragment [d(H17•••O4) = 2.17(2) Å].

A similar pattern of intramolecular H-interactions, though with 0.2-Å longer H•••A distances, is present in the C(O)-L-Ala2-D-Oxd2-Tri2 residue of **7**·0.5C_6H_6, which also exhibits a turn structure (Figure 26).

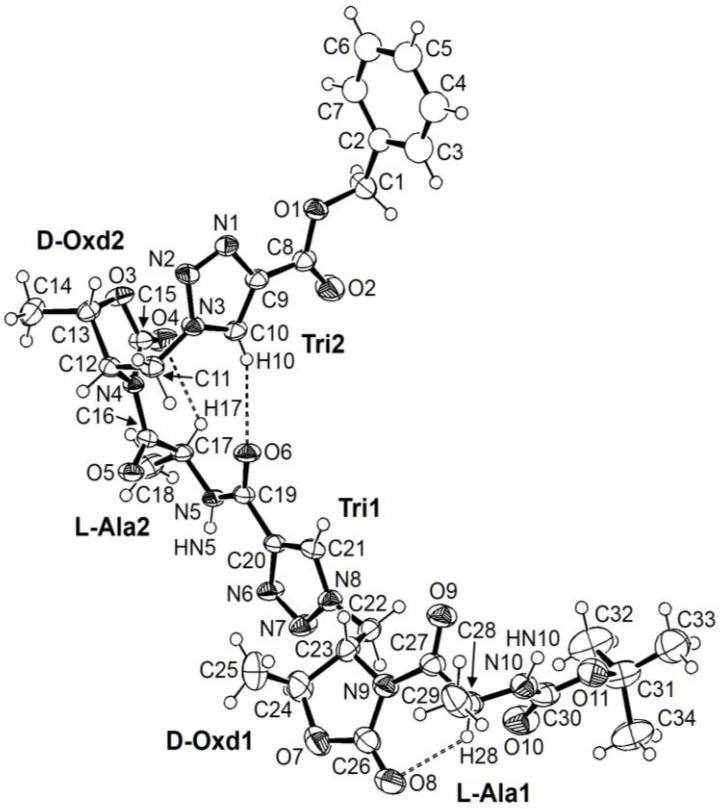

Figure 26. Ortep-3 [76] plot of **7** with thermal ellipsoids drawn at 50-% probability and H atoms represented as spheres of arbitrary radius. For simplicity, only H atoms engaged in intra- or intermolecular interactions are labelled. The dashed lines highlight intramolecular hydrogen bonding interactions discussed in the text.

Inspection of the backbone torsion angles for the two compounds (Table 1) indeed reveals a remarkable similarity between the conformation of L-Ala-D-Oxd-Tri in monomer **5** and of L-Ala2-D-Oxd2-Tri2 in dimer **7**; differences do not exceed 5° with the exception of the ψ angle for the L-Ala and L-Ala2 residues. The above-mentioned α-carbon/C = O contact is repeated also within the L-Ala1-D-Oxd1 unit (H28•••O8), which however does not adopt a turn structure. In fact, the two five-membered rings are rotated away from each other around the C22-C23 bond, as shown by the large N8-C22-C23-N9 torsion angle (172.6(3)). Moreover, D-Oxd1-Tri1 and D-Oxd2-Tri2 entail opposite rotations of the triazole moiety around the CH2-N bond (N-N-C-C = -101.0(3)° vs. 89.1(3)°). In the two compounds the torsion angles are presented in Table 1. Overall, the torsion angles at L-Ala residues (ϕ from -70.1 to -57.2° and ψ from 136.3 to 147.5°) are close to those typical for a PPII helix (ϕ = -79° and ψ = 150°).

Table 1. Selected backbone torsional angles (in degrees) for compounds **5** and **7**·0.5C_6H_6.

	5		**7**·0.5C_6H_6	
C16-C17-N5-C19 (ϕ)	-60.1(3)	L-Ala	-57.2(3)	L-Ala2
N4-C16-C17-N5 (ψ)	136.3(2)		147.2(2)	
C11-C12-N4-C16	71.5(2)		72.2(3)	
N3-C11-C12-N4	69.4(2)	D-Oxd-Tri	64.8(3)	D-Oxd2-Tri2
N2-N3-C11-C12	90.1(2)		89.1(3)	
C27-C28-N10-C30 (ϕ)			-70.1(4)	L-Ala1-Tri1
N9-C27-C28-N10 (ψ)			147.5(3)	
C22-C23-N9-C27			70.7(4)	
N8-C22-C23-N9			172.6(3)	D-Oxd1-Tri1
N7-N8-C22-C23			-101.0(3)	

Turning now to crystal packing, the carbonyl C16-O5 and the amide N5-HN5 groups in **5** are involved in intermolecular hydrogen bonds directed approximately parallel to the b-axis [d(HN5•••O5I) = 2.15(2) Å; I = x-1/2, -y+1/2,-z+2]. These two H-bonds per molecule link the peptides into supramolecular zig-zag chains running along the a-axis. In the crystal lattice, molecules of **7** are linked by a H-bond between the amide (N5) and triazole (N1) nitrogen atoms, with d(HN5•••N1I) = 2.138(17) Å (I = x, y+1, z). The second amide nitrogen N10 is also engaged in a H-bond with triazole nitrogen atom N7 of a neighboring molecule, but with a significantly longer distance [d(HN10•••N7II) = 2.334(19) Å; II = -x, y-1/2, -z]. Both intermolecular contacts are directed approximately parallel to the b-axis of the unit cell. It is noteworthy that the only NH•••CO hydrogen bonds found in these structures are of intermolecular type and occur in **5**, in agreement with the results of FT-IR spectroscopy in solution. Detailed geometrical parameters for hydrogen interactions are gathered in Table 2 and Table 3.

Table 2. Geometry of hydrogen bonding interactions in **5** (distances in Å, angles in degrees).

D-H•••A	*d*(D-H)	*d*(H•••A)	*d*(D•••A)	∠(DHA)
C10-H10•••O6	0.95(2)	2.14(2)	3.058(3)	163.5(18)
C17-H17•••O4	0.98(2)	2.17(2)	2.945(3)	134.5(16)
N5-HN5•••O5^{I}	0.83(2)	2.15(2)	2.959(2)	164(2)

I = x-1/2, -y+1/2,-z+2.

Table 3. Geometry of hydrogen bonding interactions in **7**·0.5C_6H_6 (distances in Å, angles in degrees).

D-H•••A	*d*(D-H)	*d*(H•••A)	*d*(D•••A)	∠(DHA)
C10-H10•••O6	0.87	2.30	3.066(4)	147.1
C17-H17•••O4	0.88(3)	2.35(3)	2.900(4)	121(2)
C28-H28•••O8	0.89(3)	2.29(3)	2.912(5)	127(3)
N5-HN5•••N1^{I}	0.855(14)	2.138(17)	2.970(4)	164(3)
N10-HN10•••N7^{II}	0.884(14)	2.334(19)	3.178(4)	160(3)
C22-H22A•••O9^{III}	1.05(4)	2.33(4)	3.323(4)	157(3)

I = x, y+1, z. II = -x, y-1/2, -z. III = -x, y+1/2, -z.

2.1.4.4. Molecular Dynamics

The inability to grow crystals of the trimers **9**, **10**, **15** or **16** suggested the use of alternative approaches to gain insight in their structures. Molecular dynamics simulations for 1 μs of the trimers Boc-(L-Ala-D-Oxd-Tri-CO)$_3$-OBn **9** and Boc-(L-Ala-L-Oxd-Tri-CO)$_3$-OBn **15** were carried out in an explicit methanol box, reproducing the conditions in which NMR spectra are registered. Principal component analysis (PCA) of the MD trajectories generated the free-energy landscapes of the two peptides. This approach proved effective in reproducing the NMR and crystallographic data and provides insight into the free energy landscape [77].

The energy landscape of **9** is characterized by well-separated minima corresponding to specific conformational structures (Figure 27a). The most populated conformer, Conf A, has a well-defined hydrogen-bond pattern that folds the peptide in a structurally stable turn structure. This eleven-membered hydrogen-bonded turn corresponds to the motif identified in the solid state by the crystallographic analysis of the monomer **5** and dimer **7** (Table 4).

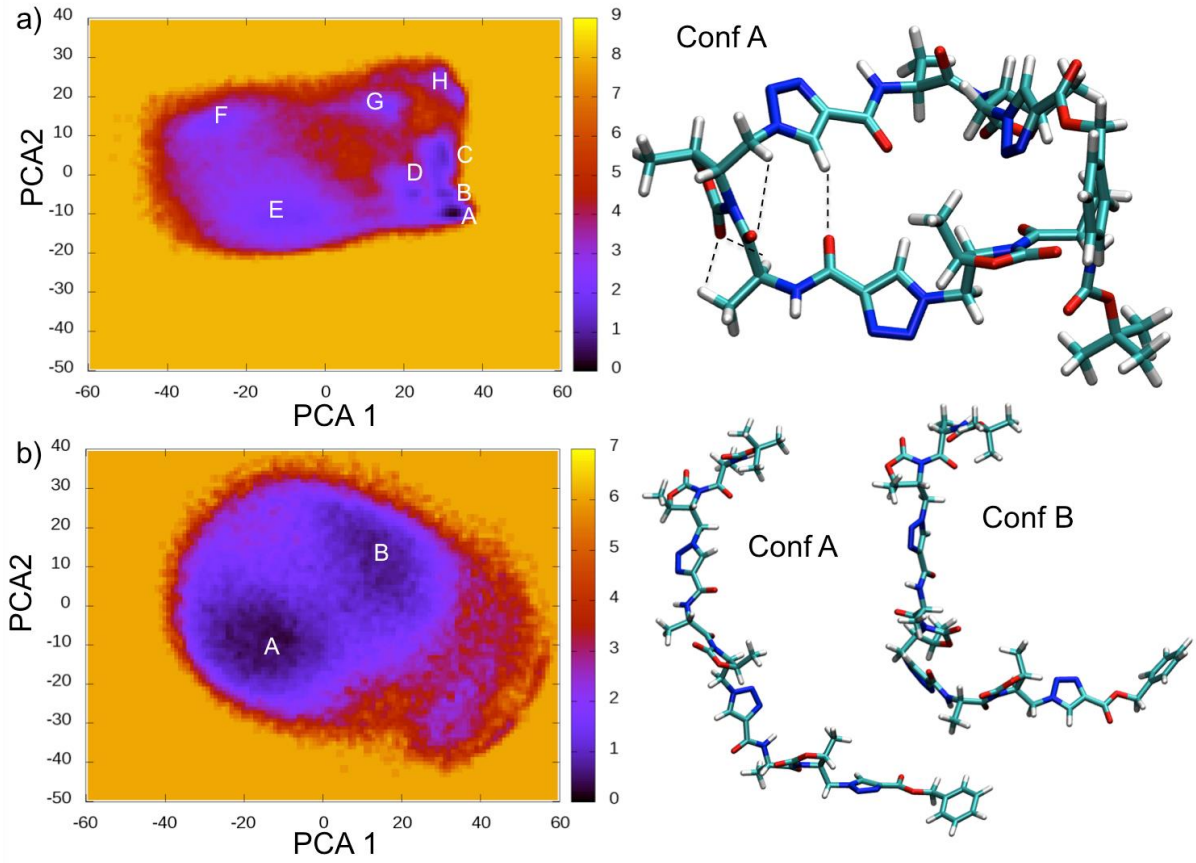

Figure 27. Conformational analysis of trimers **9** (a) and **15** (b). On the left, 2D free-energy landscape of the peptides (the values are in kcal mol^{-1}). The letters identify the most populated conformations. PCA1 and PCA2 are the two eigenvectors with the lowest eigenvalues of the principal component analysis

[77] Fermani, S.; Trivelli, X.; Sparla, F.; Thumiger, A.; Calvaresi, M.; Marri, L.; Falini, G.; Zerbetto, F.; Trost, P., Conformational Selection and Folding-upon-binding of Intrinsically Disordered Protein CP12 Regulate Photosynthetic Enzymes Assembly. *Journal of Biological Chemistry* **2012,** *287* (25), 21372-21383.

calculated from the analysis of the MD trajectory. On the right, representative structures of the conformational states corresponding to the most prominent minima of the free energy landscape

Table 4. Comparison between the backbone torsion angles (in degrees) for the conserved structural motif of the eleven-membered hydrogen-bonded turn in **5** and **7**·0.5C_6H_6 (from crystallographic structures), in **9** (most populated conf A from molecular dynamics simulations) and in the theoretical 3_{11}-helical structure [78].

	5	**7**·0.5C_6H_6	**9**	**Ref 78**
C16-C17-N5-C19 (ϕ)	-60.1	-57.2	-69.9	-60
N4-C16-C17-N5 (ψ)	136.3	147.2	139.0	150
C11-C12-N4-C16	71.5	72.2	77.5	77
N3-C11-C12-N4	69.4	64.8	60.7	60
N2-N3-C11-C12	90.1	89.1	99.4	100

The other stable minima Conf B, Conf C and Conf D maintain this structural motif, even if the other regions of the peptide show considerable conformational freedom (Figure 28). This area of the peptide energy landscape, characterized by the presence of the turn, is around 2-7 kcal mol^{-1} more stable than any other conformation (extended, helix-like, twist-like, Figure 29). The non-standard C-H•••O = C hydrogen bonds, represented by dashed lines in Figure 27a, govern the structural stability of this motif.

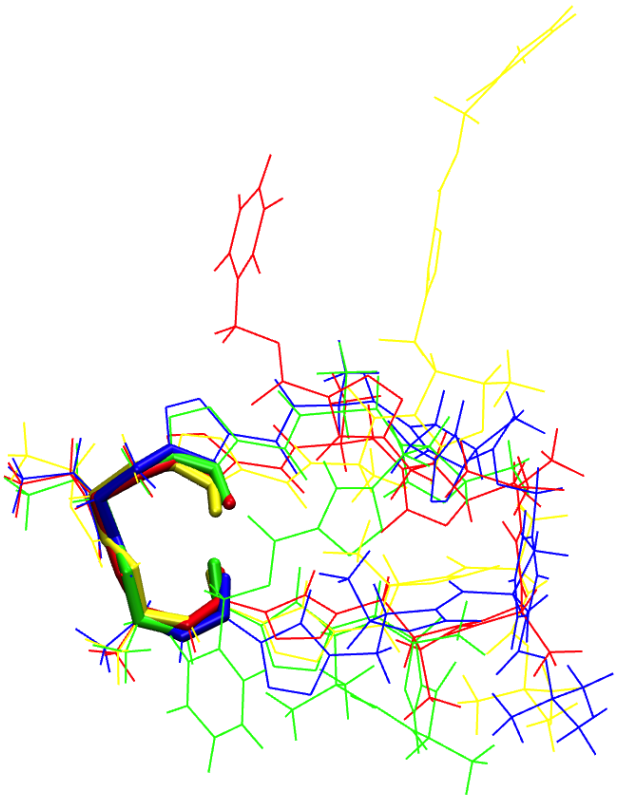

Figure 28. Superposition of the representative structures of the conformational states corresponding to Conf A (Blue), Conf B (Red), Conf C (Yellow) and Conf D (Green). In licorice the conserved structural motif of the eleven-membered hydrogen-bonded turn.

[78] Baldauf, C.; Günther, R.; Hofmann, H.-J., Theoretical prediction of the basic helix types in α,β-hybrid peptides. *Peptide Science* **2006,** *84* (4), 408-413.

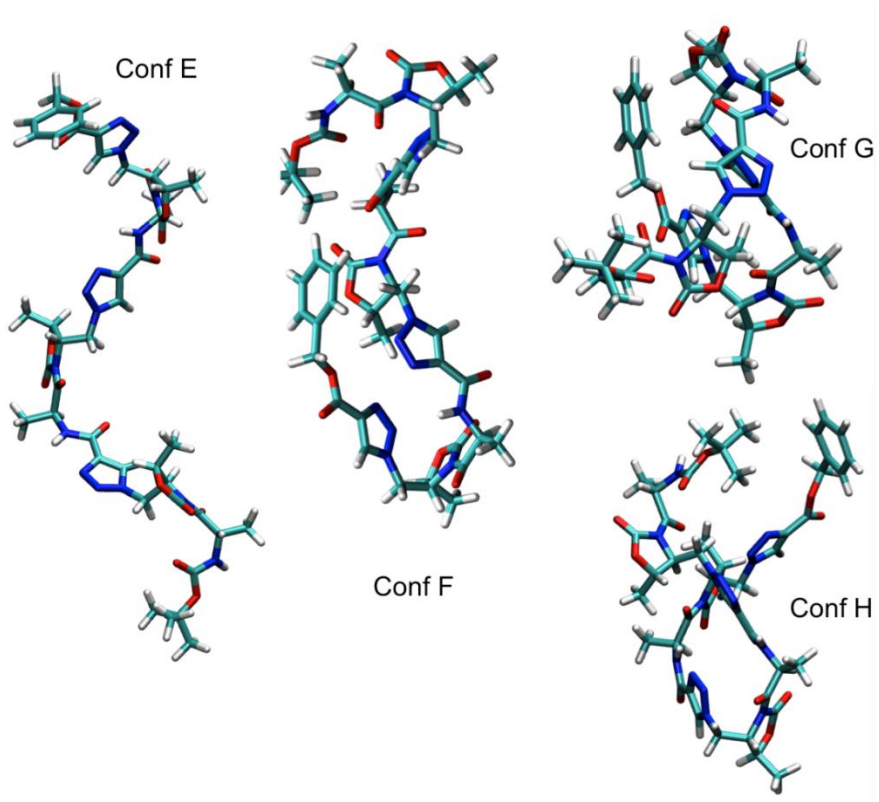

Figure 29. Representative structures of the conformational states corresponding to Conf E, Conf F, Conf G and Conf H of the trimer **9**.

On the contrary, in the energy landscape of **15** (Figure 27b) the local minima are broad and there is no significant basin of attraction indicative of a folded conformation. The most populated Conf A and Conf B (Figure 27b) represent non folded extended conformations of the peptide that undergoes practically free rotation in the solvent. A turn structure can still be identified (Figure 30). It is located the region of PCA1 that ranges between 37-40 and its energy is more than 2 kcal/mol higher than the more stable minima. The β-turn structure of **9** is replaced by a γ-turn structure in **15**, with a 7-membered hydrogen bonded ring. This structure usually competes with its 10-membered analogue (here 11 because of the presence of a ε-amino acid) typical of a β-turn. Steric hindrance and/or chirality stabilize/destabilize the two competing ring-structures.

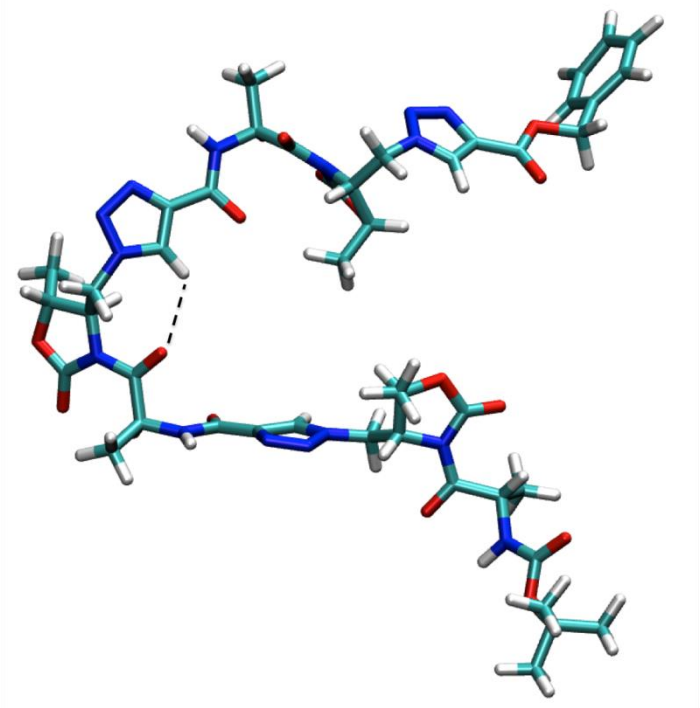

Figure 30. γ-turn structure in **15**, characterized by a 7-membered ring hydrogen bond (dashed line).

2.1.5. Complexation with Cu^{2+}

Triazole rings tend to interact with Cu^{2+} ions and form complexes. The extra stabilization energy provided by the interaction with Cu^{2+} could in principle be used to impart an ordered structure to both series of oligomers.

2.1.5.1. UV-Vis Spectroscopy

UV-Vis complexometric titrations show that oligomers **6**, **8** and **10** interact with copper, giving rise to complexes. Table 5 presents the average K_D values for the L,D series. The saturation threshold (i.e. the metal concentration corresponding to system saturation) increases with elongation of the pseudo-peptide chain, due to the increase of putative metal-binding sites. The absence of absorption bands in the λ~600 nm region suggests that we are dealing with type-II copper centers.

Table 5. K_D (mM) values for the Cu^{2+}-complexes with **6**, **8** and **10** in MeOH/H_2O 8:2 v/v. The λ values corresponding to the peak and trough in the difference spectra as well as the Cu^{2+}-equivalents at system saturation are reported.

Compound		λ*p* (nm)	λ*t* (nm)	K_D (mM)	Cu^{2+}-equivalents at saturation
Boc-L-Ala-D-Oxd-Tri-COOH	**6**	411	213	0.270	2
Boc-(L-Ala-D-Oxd-Tri-CO)$_2$-OH	**8**	264	235	0.406	2-3
Boc-(L-Ala-D-Oxd-Tri-CO)$_3$-OH	**10**	267	230	0.341	3

2.1.5.2. ECD Spectroscopy

Complexometric titrations of compounds **6**, **8** and **10**, monitored by ECD spectroscopy (Figure 31a, 31b and 31c) showed that in all cases Cu^{2+}-addition affects the intensity of the absorption bands without changing the spectral pattern. This outcome suggests that copper leaves the folding unchanged as compared to the free ligand and is confirmed by the lack of meaningful changes upon addition of an EDTA excess. Analogous titrations with **12**, **14**, and **16** oligomers did not produce significant variations of the spectra (Figures 31d, 31e and 31f). We conclude that Cu^{2+} is not able to induce extra-folding in either series of oligomers.

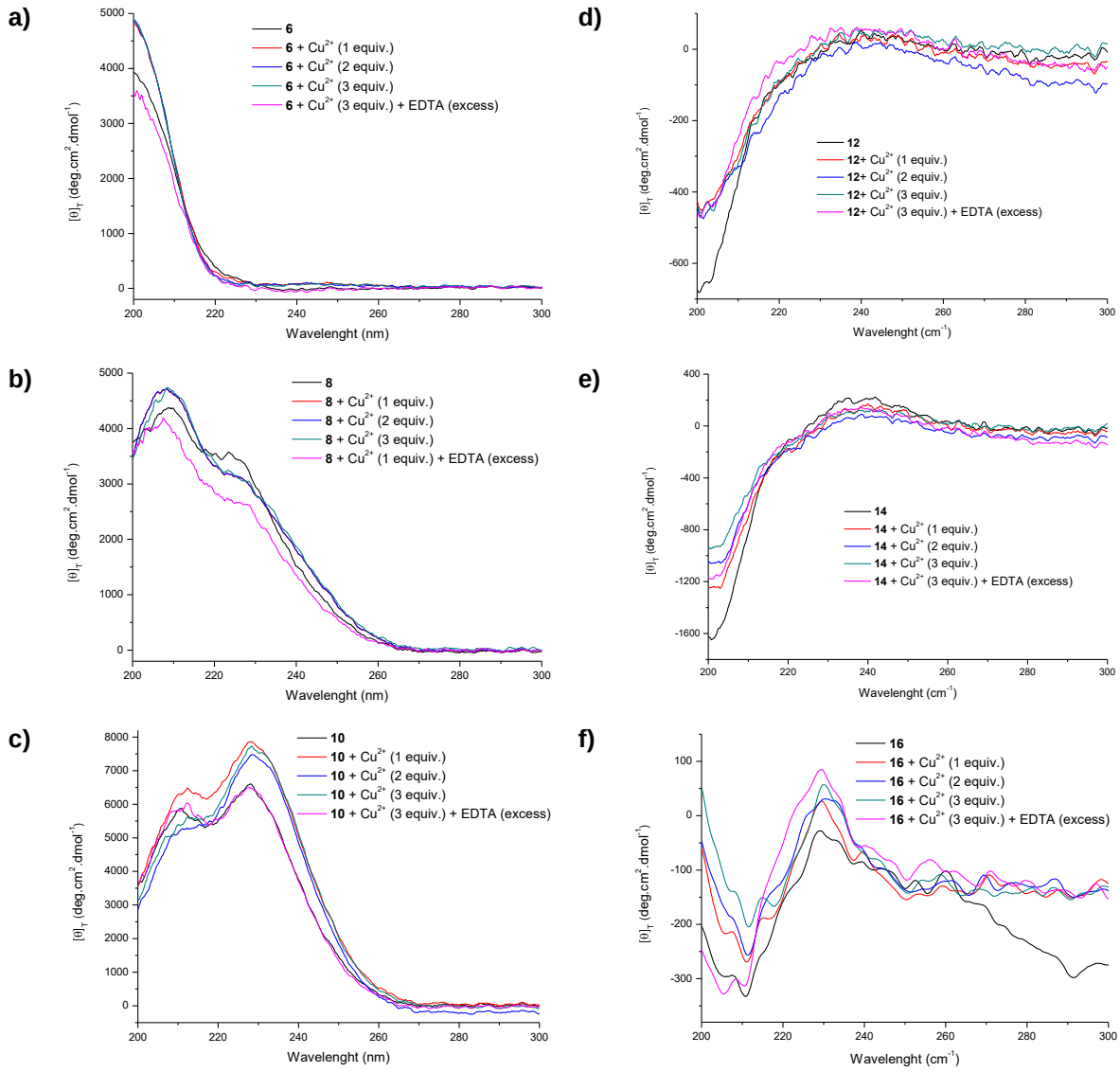

Figure 31. CD spectra of compounds **6**, **8**, **10**, **12**, **14** and **16** dissolved in MeOH/H_2O 8:2 v/v, in the absence and presence of Cu^{2+} and after addition of a molar excess of EDTA a) **6** (0.419 mM); b) **8** (0.246 mM); c) **10** (0.174 mM); d) **12** (0.419 mM); e) **14** (0.246 mM); c) **16** (0.174 mM).

2.1.5.3. EPR Spectroscopy

The interaction of Cu^{2+} with ligands **6**, **8** and **10** in MeOH/H_2O 8:2 (v/v) was further characterized by EPR spectroscopy and the corresponding spin-Hamiltonian parameters are summarized in Table 6. In all cases, two distinct complexation modes were highlighted: these correspond to at least two distinct metal binding sites, called a and b in the Table 6.

Table 6. Spin-Hamiltonian parameters calculated from simulation of the EPR spectra of Cu^{2+}-complexes of compounds **6**, **8** and **10** recorded in MeOH/H_2O 8:2 (v/v) at 77K.

Ligand	Center	Contribution %	$g_\perp$	$g_\parallel$	$A_\parallel$ (10^4 cm^{-1})	$A_\parallel$ (G)	$g_\parallel/A_\parallel$ (cm)
6	a	82	2.085	2.427	106.5	113.9	227.88
	b	18	2.069	2.364	125.7	134.4	188.06
8	a	70	2.085	2.425	109.1	116.7	222.27
	b	30	2.069	2.356	127.5	136.4	184.78
10	a	84	2.085	2.427	108.2	115.8	224.30
	b	16	2.070	2.362	133.3	142.6	177.19

The EPR parameters, with values of $A_\parallel > 100 \cdot 10^{-4}$ cm^{-1}, and the absence of absorption bands in the visible region of the electronic spectra suggest that, in all cases, the metal center is a type-II copper site. Center a shows lower $A_\parallel$ values ($106\text{-}109 \cdot 10^{-4}$ cm^{-1}) as compared to center b ($125\text{-}133 \cdot 10^{-4}$ cm^{-1}). Based on these spectral parameters, center a was assigned to a nitrogen-coordinated copper (i.e. copper interacting with the triazole ring). Due to the similarity of its EPR parameters with those of $Cu(H_2O)_6^{2+}$, center b was assigned to an oxygenated ligand (i.e. a carboxylate). $g_\perp < g_\parallel$ is typical of a distorted tetragonal geometry, with the unpaired electron located in the dx2 - y2 orbital. The tetragonal distortion is further supported by the following evidence:

$g_\parallel/A_\parallel$ ratios $>222 \cdot 10^{-4}$ cm^{-1} for center a and $>177 \cdot 10^{-4}$ cm^{-1} for center b. Square planar complexes exhibit much lower values ($105\text{-}135 \cdot 10^{-4}$ cm^{-1}) [79,80]. This also indicates that center a is more distorted than center b.

The absence of electronic absorption bands in the visible region as, for complexes with strong tetragonal distortion, these bands shift towards the IR [81].

The lower degree of distortion of center b as compared to center a is consistent with its assignment to the carboxy-terminal site, since it is reasonable to expect a less conformationally constrained complex as compared to the triazole.

Finally, according to Sakaguchi et al.[79], $g_\parallel$ values >2.30 are consistent with predominantly ionic interactions and corroborate the assignments of binding sites a and b to a triazole and a carboxylate, respectively.

In all cases, the addition of a 10-fold molar excess of EDTA caused the formation of a pale blue solution. The EPR spectral pattern of the pale blue solutions was typical of Cu^{2+}-EDTA complexes. This indicates the complete disruption of the Cu^{2+}-complexes by EDTA.

[79] Sakaguchi, U.; Addison, A. W., Structural implications for blue protein copper centers from electron spin resonance spectra of copper sulfide (CuIIS4) chromophores. *Journal of the American Chemical Society* **1977,** *99* (15), 5189-5190.

[80] Romanowski, S. M. d. M.; Tormena, F.; Santos, V. A. d.; Hermann, M. d. F.; Mangrich, A. S., Solution studies of copper(II) complexes as a contribution to the study of the active site of galactose oxidase. *J. Braz. Chem. Soc.* **2004,** *15* (6).

[81] Hathaway, B. J., The correlation of the electronic properties and stereochemistry of mononuclear {CuN4-6} chromophores. *Journal of the Chemical Society, Dalton Transactions* **1972,** (12), 1196-1199.

3. Applications

3.1. Photochemistry and Photophysics

Photochemistry and photophysics are natural phenomena and our life depends on photosynthesis, a natural photochemical and photophysical process [82]. Currently, it represents a modem branch of science, at the interface between light and matter and at the crossroads of several disciplines including chemistry, physics, material science, ecology, biology and medicine. This field continues to expand with development of new molecules, new materials and new processes [83].

3.1.1. Supramolecular Photochemistry

A supramolecular system [84] can be preorganized to favor the occurrence of electron and energy transfer processes. The molecule D (donor) that has to be excited can indeed be placed in the supramolecular structure nearby a suitable molecule A (acceptor). We consider the case of the D-L-A supramolecular system, where D is the light adsorbing molecular unit, A is the other molecular unit involved with D in the light induced processes and L is a connecting unit called linker. In such a system, after light excitation of D, there is no need to wait for a diffusion controlled encounter between *D and A, as in molecular photochemistry, since the two reaction partners can already be at an interaction distance suitable for electron and energy transfer (Figure 32).

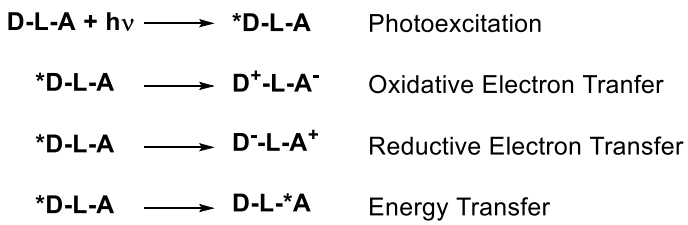

Figure 32. Schematic reaction of electron and energy transfer.

In absence of chemical complications (as fast decomposition of the oxidized and/or reduced species), photoinduced electron transfer processes are followed by spontaneous back electron transfer reactions that regenerate the starting ground state system, and photoinduced energy transfer is followed by radiative and/or nonradiative deactivation of the excited acceptor (Figure 33).

[82] Balzani, V.; Ceroni, P.; Juris, A., Photochemistry and Photophysics: Concepts, Research, Applications. Wiley-VCH, Weinheim: 2014.
[83] Balzani, V.; Credi, A.; Venturi, M., Molecular Devices and Machines: Concepts and Perspectives for the Nanoworld: Second Edition. 2008; p 1-546.
[84] Lehn, J.-M., Supramolecular Chemistry, Concepts and Prespectives. Wiley-VCH, Weinheim: 1995.

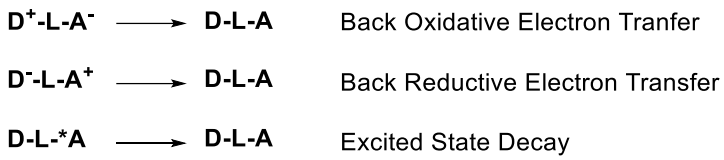

Figure 33. Deactivation mechanism of electron transfer

In supramolecular systems, electron and energy transfer processes are no longer limited by diffusion and take place by first order kinetics. As a consequence, in suitably designed supramolecular systems, these processes can involve even very short lived excited states.

3.1.2. Electron Transfer with Peptide Linker

In Nature, 20 common amino acids are the fundamental building blocks of functional peptides and proteins. Understanding charge transfer and electron transfer (ET) processes in proteins is of fundamental importance to the unravelling of key biological processes [85,86,87,88].

Schlag and co-workers [89] suggest that peptides possess near ideal conduction in the isolated state. Amongst the various mechanisms of ET, he suggested that charge transport in peptides is highly efficient and that it proceeds in a stepwise fashion. Charge transfer is found to be a through-bond mechanism involving energetically accessible electronic states along the path of charge flow. Because of the complexity of peptides, the importance of individual amino acids in controlling ET is not yet understood in details. More recently, the dynamic properties of protein folding have begun to attract attention. A quantum mechanical generalized master equation was used to treat protein folding processes ranging from picoseconds to a second or longer. Petrov and May [90,91], a solid theoretical foundation was laid for a hopping model of ET in peptides, a mechanism, which is now recognized for charge transport in DNA, but which is still controversial for peptides.

In a series of photophysical studies of well-behaved peptide model systems, the ET through the peptide spacer is greatly influenced by the separation between acceptor (A) and the donor

[85] Isied, S. S.; Ogawa, M. Y.; Wishart, J. F., Peptide-mediated intramolecular electron transfer: long-range distance dependence. Chemical Reviews 1992, 92 (3), 381-394.
[86] Stubbe, J.; Nocera, D. G.; Yee, C. S.; Chang, M. C. Y., Radical Initiation in the Class I Ribonucleotide Reductase: Long-Range Proton-Coupled Electron Transfer? Chemical Reviews 2003, 103 (6), 2167-2202.
[87] Long, Y.-T.; Abu-Irhayem, E.; Kraatz, H.-B., Peptide Electron Transfer: More Questions than Answers. Chemistry – A European Journal 2005, 11 (18), 5186-5194.
[88] Cordes, M.; Giese, B., Electron transfer in peptides and proteins. Chemical Society Reviews 2009, 38 (4), 892-901.
[89] Sheu, S.-Y.; Schlag, E. W.; Yang, D.-Y.; Selzle, H. L., Efficiency of Charge Transport in a Polypeptide Chain: The Isolated System. *The Journal of Physical Chemistry A* **2001,** *105* (26), 6353-6361.
[90] Petrov, E. G.; Shevchenko, Y. V.; Teslenko, V. I.; May, V., Nonadiabatic donor–acceptor electron transfer mediated by a molecular bridge: A unified theoretical description of the superexchange and hopping mechanism. *The Journal of Chemical Physics* **2001,** *115* (15), 7107-7122.
[91] Petrov, E. G.; Shevchenko, Y. V.; May, V., On the length dependence of bridge-mediated electron transfer reactions. *Chemical Physics* **2003,** *288* (2–3), 269-279.

(D), the nature of the peptide backbone, the amino acids sequence and the resulting flexibility. The mechanistic interpretations for these observations are still highly controversial. Two major mechanisms are currently debated to rationalize the distance dependence of ET in peptide models: a bridge-assisted superexchange and an electron-hopping mechanisms. In the hopping mechanism, the electron temporarily resides on the bridge for a short time during its passing from one redox centre to the other, while in the superexchange mechanism the conjugated bridge only serves as a medium to pass the electron between the donor and the acceptor. In a superexchange mechanism, the ET rate exhibits an exponentially distance dependence, whereas a linear distance relationship is expected for a hopping mechanism (Figure 34) [92,93,94,95].

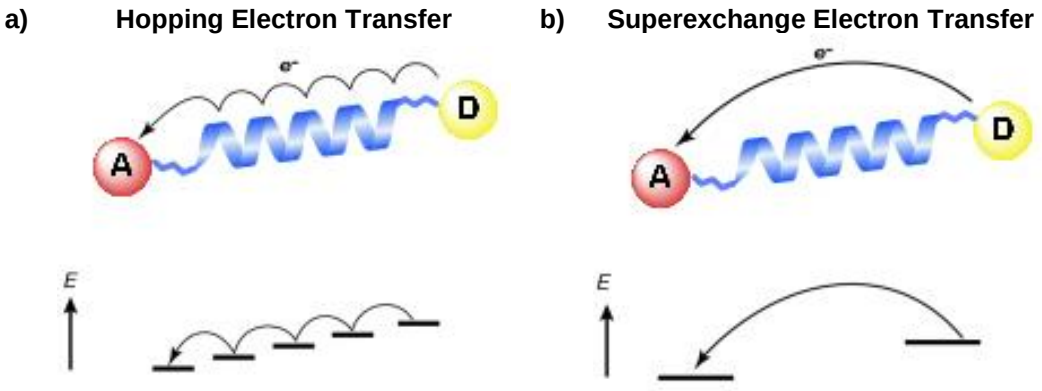

Figure 34. a) Mechanism of Hopping electron transfer, b) Superexchange eòectron transfer.

Isied [96,97] have reported a series of peptide-bridged diruthenium systems in which the length of the oligoproline spacer was varied. His results indicated that short oligomers (n = 0-3) had predominantly superexchange ET, indeed longer oligomers (n = 4-9) ha predominantly hopping ET.

3.1.3. Dyads

[92] Benniston, A. C.; Harriman, A., Charge on the move: how electron-transfer dynamics depend on molecular conformation. Chemical Society Reviews 2006, 35 (2), 169-179.
[93] Bhosale, S.; Sisson, A. L.; Talukdar, P.; Fürstenberg, A.; Banerji, N.; Vauthey, E.; Bollot, G.; Mareda, J.; Röger, C.; Würthner, F.; Sakai, N.; Matile, S., Photoproduction of Proton Gradients with π-Stacked Fluorophore Scaffolds in Lipid Bilayers. Science 2006, 313 (5783), 84-86.
[94] Sakai, N.; Sisson, A. L.; Bhosale, S.; Furstenberg, A.; Banerji, N.; Vauthey, E.; Matile, S., Rigid-rod push-pull naphthalenediimide photosystems. Organic & Biomolecular Chemistry 2007, 5 (16), 2560-2563.
[95] Bhosale, S.; Sisson, A. L.; Sakai, N.; Matile, S., Synthetic functional [small pi]-stack architecture in lipid bilayers. Organic & Biomolecular Chemistry 2006, 4 (16), 3031-3039.
[96] Malak, R. A.; Gao, Z.; Wishart, J. F.; Isied, S. S., Long-Range Electron Transfer Across Peptide Bridges: The Transition from Electron Superexchange to Hopping. Journal of the American Chemical Society 2004, 126 (43), 13888-13889.
[97] Vassilian, A.; Wishart, J. F.; Van Hemelryck, B.; Schwarz, H.; Isied, S. S., Electron transfer across polypeptides. 6. Long-range electron transfer in osmium-ruthenium binuclear complexes bridged with oligoproline peptides. Journal of the American Chemical Society 1990, 112 (20), 7278-7286.

Intramolecular electron-transfer reactions between donor and acceptor sites separated by a synthetic peptide or a protein fragment provided a deep insight into the role played by the bridge in mediating electron transfer. To carry out these studies, the supramolecular chemistry and photochemistry approach can be very useful because it enables to assemble prefabricated molecular components that carry the desired photophysical and redox properties. Indeed, in a suitably designed supramolecular species A-L-D (where the electron acceptor A and electron donor D units are covalently bound with a linker L) light excitation can cause an intramolecular electron transfer from the excited state of D to A. This approach offers the advantage that the properties of the supramolecular system can be predicted by knowing the properties of the isolated components or of suitable model molecules.

Tomasini and co-worker extensively studied the conformational behavior of foldamers containing the 4-carboxy-5-methyl-oxazolidin-2-one (Oxd) moiety. The relative configuration of Oxd and the alternated amino acid is very important, as the L-Ala-D-Oxd series tends to form β-bend ribbon spirals. Using these rigid spacers, we have synthetized some hybrid oligomers called dyads (Figure 35). They contain a derivative of pyromellitic diimide as electron acceptor group and a derivative of 1,5-dihydroxynaphthalene as the electron donor group. These two moieties are linked by one, two, or three L-Ala-D-Oxd units in dyads [98]. Then we analysed the conformational behaviour and we measured the photophysical proprieties of the dyads.

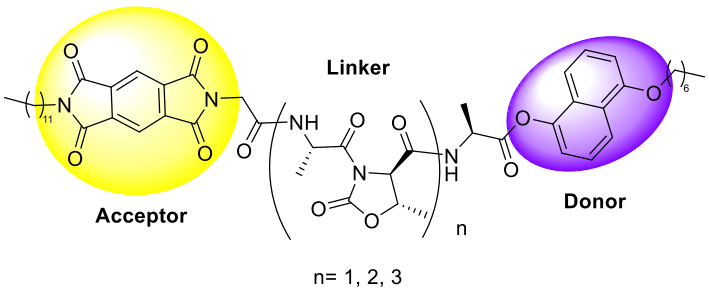

Figure 35. Dyads.

3.1.4. Synthesis of Dyads

The acceptor group **17** is a pyromellitic diimide, it has been prepared in one step with a reaction between pyromellitic dianhydride, dodecylamine and glycine in refluxing DMF as 28% yield. The compound **17** was used for the dyads preparation and the corresponding methyl ester **18** was synthesized as acceptor model for the photophysical analysis, by reaction of **17** with $SOCl_2$ in methanol (Scheme 4).

[98] Milli, L.; Marchi, E.; Castellucci, N.; Indelli, M. T.; Venturi, M.; Ceroni, P.; Tomasini, C., Pseudopeptide Foldamers designed for photoinduced intramolecular electron transfer. *RSC Advances* **2015,** *5* (14), 10809-10815.

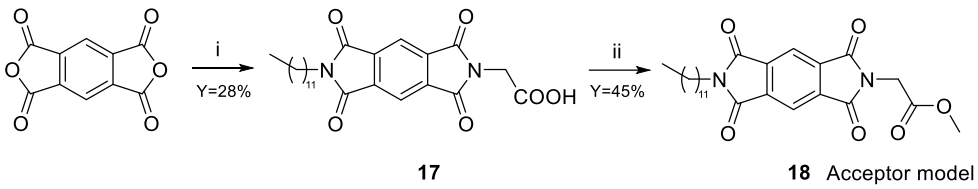

Schema 4. Reagents and conditions: (i) H-Gly-OH (1.0 equiv.), dodecylamine (1.0 equiv.), DMF, 120 °C, 6h; (ii) $SOCl_2$ (excess), MeOH, r.t., 24h.

The donor **21** was prepared in two steps starting from the commercially available 1,5-dihydroxynaphthalene (Scheme 5). By reaction with potassium carbonate, potassium iodide and n-heptyl bromide in acetone, we obtained a mixture of the desired 5-(heptyloxy)naphthalen-1-ol **19** and 1,5-bis(heptyloxy)naphthalene **20**. After purification, compounds **19** and **20** were obtained in 37% and 30% yield respectively. While **19** was used for the dyad preparation, **20** was used as donor model for the photophysical analysis. Finally the compound **19** was coupled with Boc-L-Ala-OH in the presence of DCC and DMAP to give the final product **21** in 55% yield (Scheme 2).

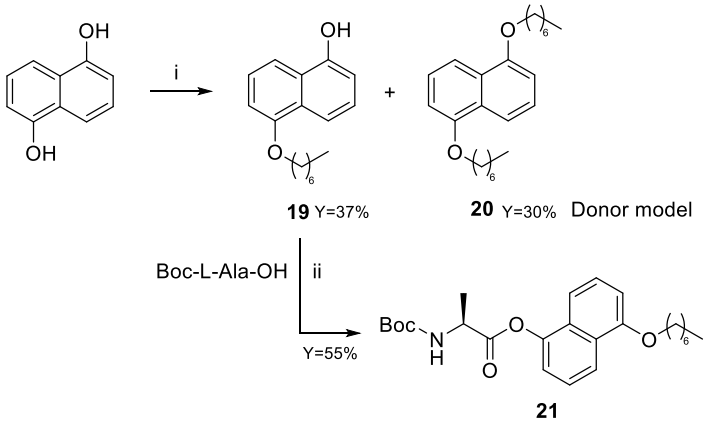

Scheme 5. Reagents and conditions: (i) 1-bromoheptane (1.0 equiv.), K_2CO_3 (2.1 equiv.), KI (1.0 equiv.), acetone, reflux, 10h; (ii) DCC (1.1 equiv.), DMAP (0.1 equiv.), DCM, r.t., 24h.

After the donor and the acceptor synthesis, these units were linked together by coupling with $(L\text{-}Ala\text{-}D\text{-}Oxd)_n$ moieties (n = 1, 2, 3). The preparation of dyads **23**, **24** and **25** was obtained by peptide coupling reactions with the acceptor group followed by coupling with the donor group (Scheme 6). The first step was the deprotection of Boc group with TFA in dichloromethane and the second step was the coupling reaction between free acid and TFA salt of amine assisted by HBTU or HATU and DIEA in acetonitrile.

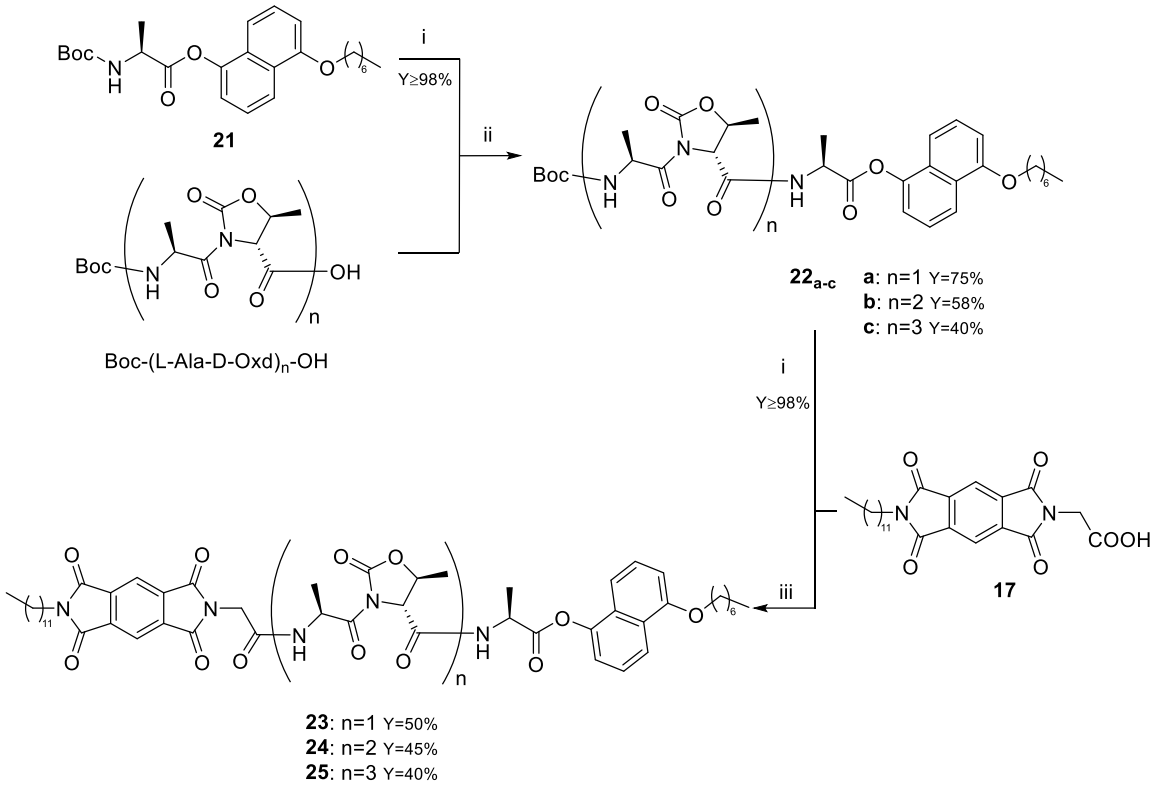

Scheme 6. Reagents and conditions: (i) TFA (18 equiv.), dry CH_2Cl_2, r.t., 4 h; (ii) HATU (1.1 equiv.), DIEA (3.0 equiv.), dry CH_3CN, r.t., 1h; (iii) HBTU (1.1 equiv.), DIEA (3.0 equiv.), dry DMF, r.t., 2h.

3.1.5. Conformational Analysis

Information on the preferred conformations of dyads **23**, **24** and **25** in solution was obtained by the analysis of FT-IR and ^{1}H NMR spectra.

The analysis of the N-H stretching regions enables to detect if intramolecular N-H•••O = C hydrogen bonds are formed, because non-hydrogen-bonded amide NH groups exhibit a stretching signal above 3400 cm^{-1}, while hydrogen-bonded amide NH ones produce a stretching band below 3400 cm^{-1}. The FT-IR spectra were recorded in DCM at a compound concentration of 3 mM; such a concentration was chosen to avoid compound self-aggregation. The spectrum of compound **23** shows two bands at 3420 and 3340 cm^{-1}, suggesting the presence of a hydrogen-bonded and a non-hydrogen-bonded amide NH group (Figure 36). The stretching band at 3340 cm^{-1} becomes weaker for **24** and totally disappears in the case of **25**. This finding suggests that a folded conformation is strongly favored in the case of the shortest dyad **23**, whereas it occurs only partially in dyad **24** and it does not take place at all in dyad **25**.

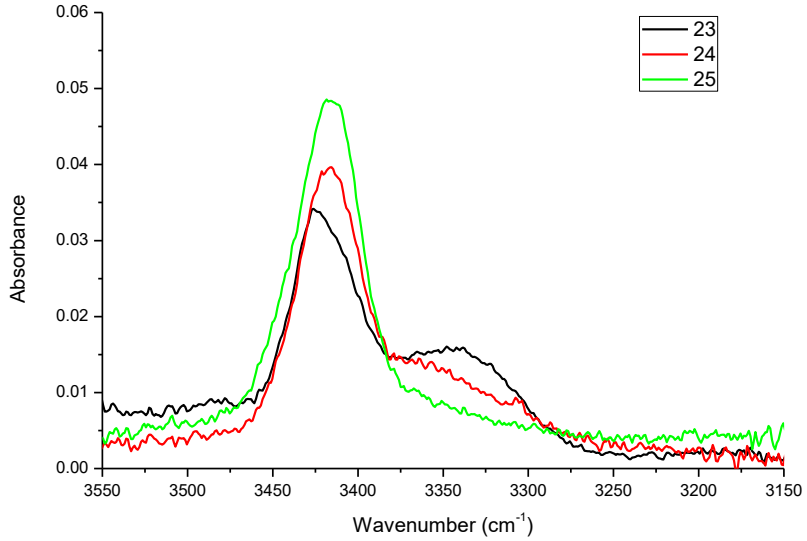

Figure 36. N-H stretching regions of the FT-IR absorption spectra in pure CH_2Cl_2 at room temperature for 3 mM concentration of dyads **23**, **24** and **25**.

The ^{1}H NMR analysis of the NH chemical shifts supports the interpretation of the IR spectroscopy results, as the NH of dyad **23** resonates at 7.45 ppm, while the NH's of dyads **24** and **25** resonate between 7.18 and 7.32 ppm, thus showing that NH is more deshielded for **23** (Table1). In contrast, compounds **22a-c** show the opposite behaviour as the NH's chemical shifts resonate at 7.35 for **22a**, increasing to 7.35-7.57 for **22b** and 7.50-7.60 for **22c** and the FT-IR showing that **22c** have a strong band at 3390 cm^{-1} indeed **22a** have a week band at 3410 cm^{-1} (Figure 37).

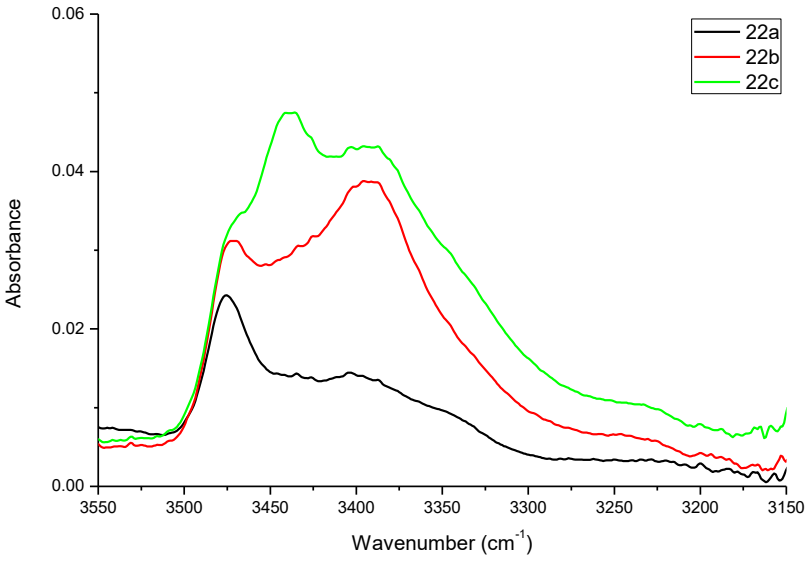

Figure 37. N-H stretching regions of the FT-IR absorption spectra in pure CH_2Cl_2 at room temperature for 3 mM concentration of **22a**, **22b** and **22c**.

A further confirmation of the preferred bent conformation assumed by **23** was obtained by analyzing the chemical shifts of the pyromellitic diimide and 1,5-dihydronaphthalene hydrogens. These chemical shifts for dyads **23**, **24** and **25** together with those found for the model compound **18** and compound **21** are reported in Table 7.

Table 7. Proton chemical shifts (ppm) of aromatic hydrogens for compounds **23**, **24**, **25**, **18** and **21** in different solvents.

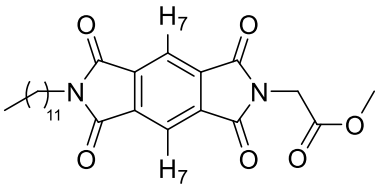

18

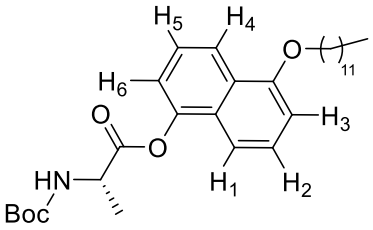

21

Compound	Solvent	δ_{H1} (ppm)	δ_{H2} (ppm)	δ_{H3} (ppm)	δ_{H4} (ppm)	δ_{H5} (ppm)	δ_{H6} (ppm)	δ_{H7} (ppm)
23	$CDCl_3$	8.02	7.26	7.13	6.74	7.22	7.02	7.85
24	$CDCl_3$	8.18	7.36	7.20	6.79	7.36	7.32	8.25
25	$CDCl_3$	8.17	7.39	7.18	6.79	7.36	7.31	8.27
18	$CDCl_3$	-	-	-	-	-	-	8.33
21	$CDCl_3$	8.21	7.44	7.23	6.83	7.38	7.42	-
23	DMSO,d_6	8.02	7.46	7.20	6.99	7.38	7.32	8.15
18	DMSO,d_6	8.03	7.47	7.22	6.97	7.38	7.44	-
21	DMSO,d_6	-	-	-	-	-	-	8.22

We can notice that H_7 resonates as a singlet for both hydrogens at 8.33 ppm in the spectrum of **18** (Figure 38). In dyads **23**, **24** and **25** there is no skeleton modification that could be responsible for the variation of this chemical shift. In fact, both **24** and **25** spectra show a singlet at 8.25 and 8.27 ppm respectively. In contrast, in the dyad **23** spectrum, the chemical shift of the pyromellitic diimide hydrogens resonates at 7.85 ppm, suggesting that these hydrogens are shielded by an aromatic ring (Figure 7). The same effect was observed for the chemical shifts of the 1,5-dihydronaphtalene hydrogens (compound **21**), that are all shielded only in the case of dyad **23**. This outcome suggests that all the aromatic hydrogens of dyad **23** suffer from the shielding effect of a nearby aromatic ring.

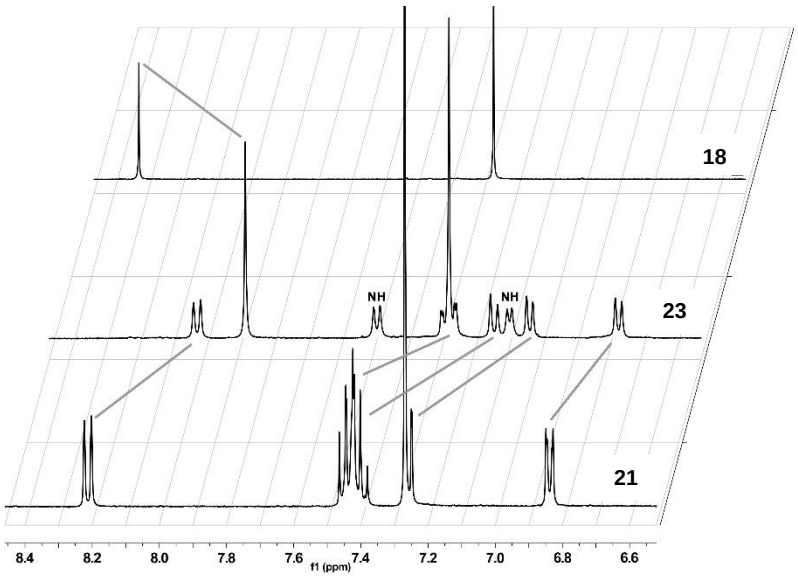

Figure 38. Superimposition of the ^{1}H NMR spectra in $CDCl_3$ of **23**, **18** and **21** in the aromatic region. All hydrogens of dyad **23** are shielded compared with **18** and **21**, as the two aromatic moieties suffer mutually from a shielding effect.

Interestingly, when the ^{1}H NMR spectra of compounds **18**, **21** and **23** are registered in DMSO-d_6, the chemical shifts variations are negligible as Δδ ranges from 0 to 0.12 ppm, while in $CDCl_3$ it ranges between 0.09 and 0.47 ppm (Table 1 and Figure 39). Thus the bent conformation of **1** is favoured by $CHCl_3$, that is a structure supporting solvent and is disfavoured by DMSO, that is a competitive solvent for N-H•••O = C bonds [99].

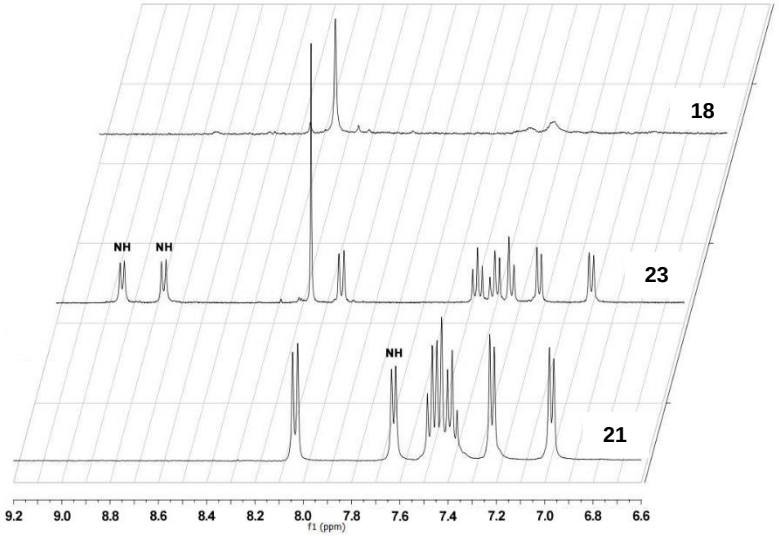

Figure 39. Superimposition of the ^{1}H NMR spectra in DMSO-d_6 of **18**, **21** and **23** in the aromatic region.

[99] Kopple, K. D.; Ohnishi, M.; Go, A., Conformations of cyclic peptides. IV. Nuclear magnetic resonance studies of cyclo-pentaglycyl-L-leucyl and cyclo-diglycyl-L-histidyldiglycl-L-tyrosyl. *Biochemistry* **1969,** *8* (10), 4087-4095.

ROESY experiments performed on dyads **23** and **24** (as a model of the unfolded dyads), in $CDCl_3$ using a mixing time of 0.400 s, proved this hypothesis.

Besides the trivial couplings, in the ROESY spectrum of **23** in $CDCl_3$, several cross peaks accounting for the interactions between the pyromellitic diimide and 1,5-dihydronaphthalene hydrogens and NH are visible and are highlighted (Figure 40).

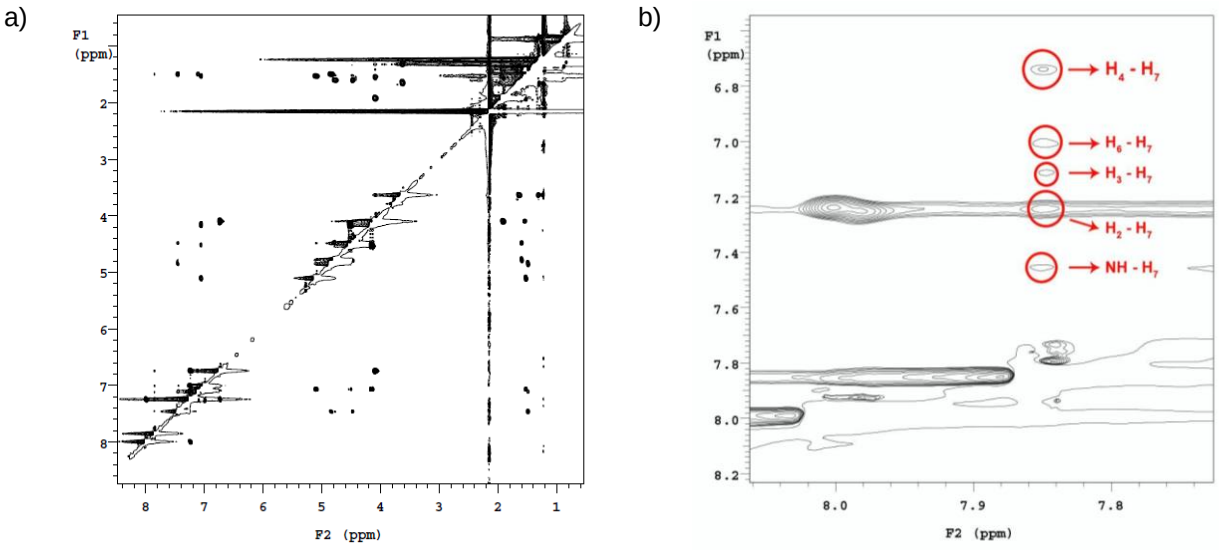

Figure 40. a) ROESY spectrum of dyad **23** in $CDCl_3$ (mixing time 0.400 s). b) Enlargement of the ROESY spectrum of Dyad **23**, showing the cross-peak between the C-H aromatic.

In contrast, in the ROESY spectrum of **24** or **25** these signals are totally absent (Figure 41). This finding is in agreement with a preferred bent conformation of **23**, that favours the proximity between the donor and the acceptor groups in a range of about 4 Å. The preferred conformation of dyad **23**, together with all the cross peaks registered in the ROESY spectrum, is summarized in Figure 42.

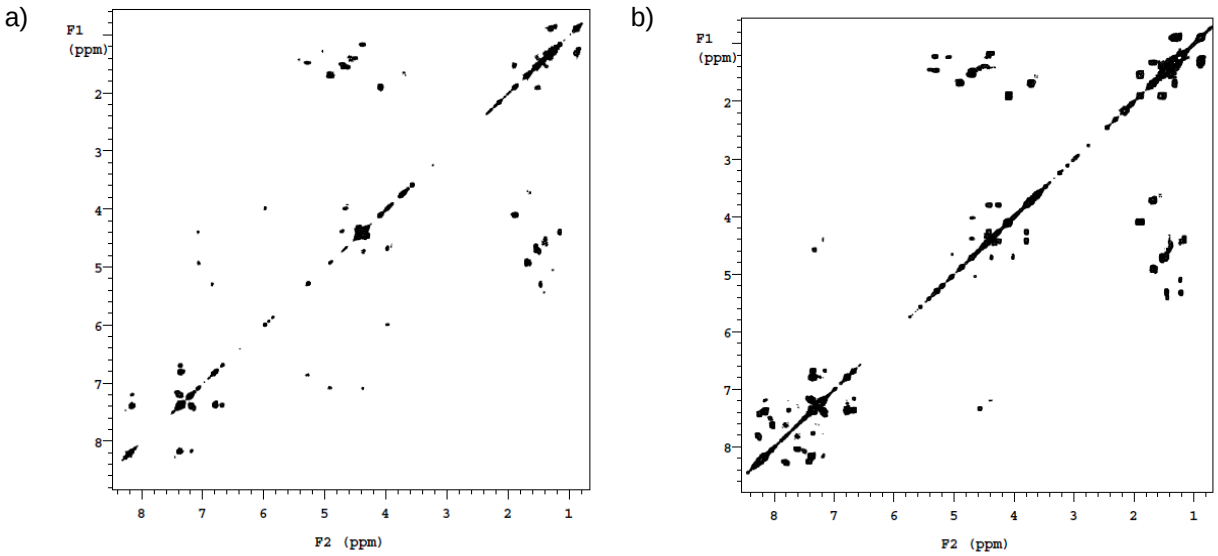

Figure 41. a) ROESY spectrum of dyad **24** in $CDCl_3$ (mixing time 0.400 s). b) ROESY spectrum of dyad **25** in $CDCl_3$ (mixing time 0.400 s).

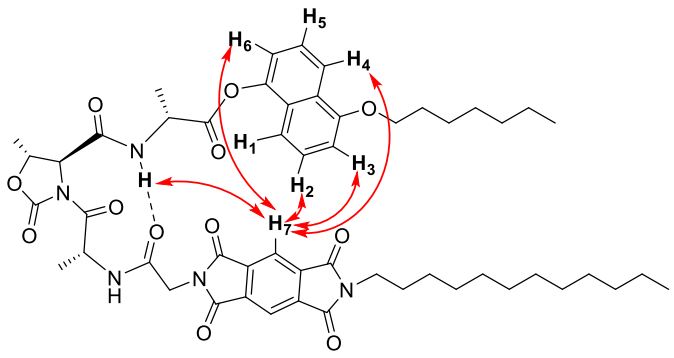

Figure 42. Preferential conformation of dyad **23**, that accounts for the formation of a NH hydrogen bond and for the NOE enhancements as gathered from the analysis of its ROESY spectrum (10 mM solution in $CDCl_3$, mixing time 0.400 s).

3.1.6. Photophysical Characterization

The photophysical properties of the three donor-acceptor dyads **23**, **24** and **25** are compared to those of the compounds **18** and **20** taken as models for the electron acceptor and donor units respectively (Table 8).

Table 8. Photophysical data for dyads **23**, **24** and **25** and model compounds **18** and **20** in air equilibrated CH_2Cl_2 solution at room temperature.

Comound	Absorption		Emission[b]			η_q[d]
	λ (nm)	ε ($M^{-1}cm^{-1}$)	λ (nm)	ϕ	τ (ns)[c]	
23	300 308[a] 410	10200 9300 150	330	0.002	0.12 (0.73) 5.30 (0.02)	0.99
24	299 308[a]	10400 9600	330	0.013	0.31 (0.41) 5.30 (0.03)	0.95
25	300 308[a]	11600 10400	330	0.027	0.52 (0.31) 5.30 (0.03)	0.91
18	309 319	1950 2000	447	0.003	9.45	-
20	298 313 327	9950 8200 6100	330	0.25	6.30	-

[a] Shoulder of the absorption band. [b] For the three dyads data are reported only for the residual emission of the donor subunit (λ_{ex} = 280 nm). No sensitized or residual emission of the acceptor subunit is observed. [c] The fitting equation is $I = A_1\exp(-t/\tau_1) + A_2\exp(-t/\tau_2) + B$. The values in brackets are the pre-exponential factors. [d] Donor excited state quenching efficiency.

3.1.7. Absorption Properties

The absorption spectra of **23**, **24** and **25** (Figure 43, Table 8) in CH_2Cl_2 solution are similar but not exactly superimposable to that obtained by the sum of the acceptor and donor model compounds **18** and **20** (Figure 43, Table 8). These spectra show the characteristic band of the naphthalene derivative [19] donor compound (280-320 nm). However, the vibronic structure is less pronounced, likely because of the different substituents of the naphthalene chromophore in the dyads compared to compound **20**, which bring about a decrease of the symmetry.

In addition, the spectrum of **23** is characterized by an unstructured, large and weak band centered at 410 nm (Figure 12) that is not present in the spectra of dyads **24** and **25**. This band can be assigned to a CT transition between donor and acceptor units, as previously reported for similar donor-acceptor components [100,101]. The presence of this CT band only in **23** is in line with the previously reported results showing that only for the shortest dyad the donor and acceptor units undergo a noticeable interaction because of their close proximity. This band is not sensitive to concentration (the molar absorption coefficient does not change in the range 3.7×10^{-7} – 3.7×10^{-4}), thus excluding intermolecular interactions, but it is sensitive to the solvent nature. In fact, the CT band disappears upon dissolution of dyad **23** in DMSO (Figure 43), a competitive solvent that promote the unfolding of the pseudopeptide. [99]

[100] Hamilton, D. G.; Davies, J. E.; Prodi, L.; Sanders, J. K. M., Synthesis, Structure and Photophysics of Neutral π-Associated [2]Catenanes. *Chemistry – A European Journal* **1998,** *4* (4), 608-620.
[101] Iijima, T.; Vignon, S. A.; Tseng, H.-R.; Jarrosson, T.; Sanders, J. K. M.; Marchioni, F.; Venturi, M.; Apostoli, E.; Balzani, V.; Stoddart, J. F., Controllable Donor–Acceptor Neutral [2]Rotaxanes. *Chemistry – A European Journal* **2004,** *10* (24), 6375-6392.

This result evidences that the supramolecular structure of the pseudopeptide foldamers can be easily affected.

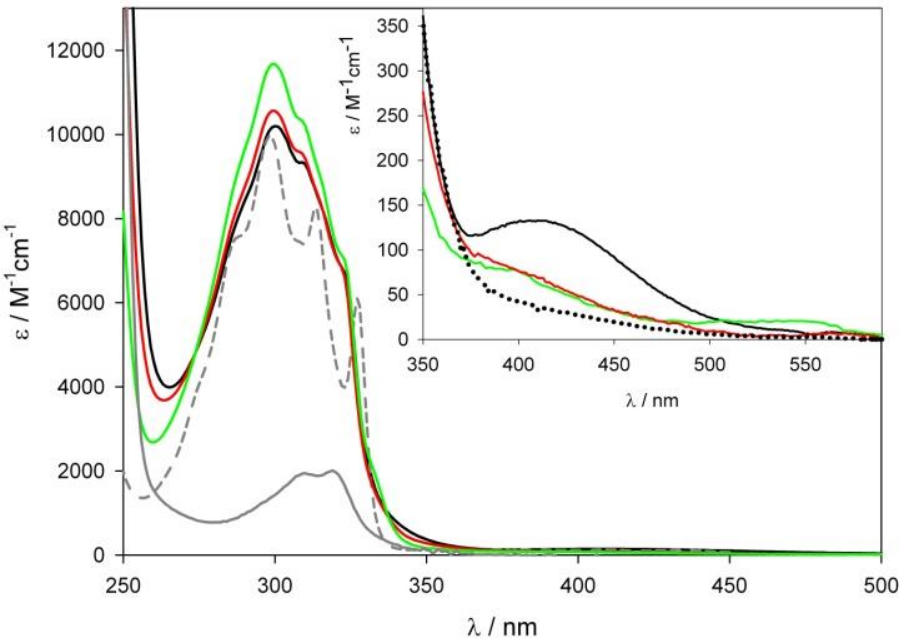

Figure 43. Absorption spectra of dyad **23** (black full line), dyad **24** (red full line) and dyad **25** (green full line) and of donor (**20**, grey dashed line) and acceptor (**18**, grey full line) model compounds in CH_2Cl_2 solution. In the inset an enlargement of the absorption spectra in the low energy part of the three dyads in CH_2Cl_2 solution and of the dyad **23** in DMSO solution (black dotted line) are shown.

3.1.8. Emission Properties and Evidence for Electron Transfer Quenching Mechanism

The emission properties of these systems were investigated upon excitation at 286 or at 320 nm, where the donor unit absorbs 90% and 70% of the light, respectively. From the emission spectra obtained by excitation of isoabsorbing CH_2Cl_2 solutions of **23**, **24**, **25** and **20** at 286 nm (Figure 44, left) we can estimate the quenching efficiency η_q of the luminescent excited state of the donor unit in the dyads, after correction for the amount of light directly absorbed by the acceptor (Table 8). The quenching efficiency is higher than 90% in all cases and is decreasing from **23** to **25** in agreement with a longer distance between the donor and the acceptor units. For dyad **23** and **24** in DMSO solution (**25** it is not soluble in this solvent) we observe, as expected, a stronger decrease of the quenching efficiency for dyad **23** (95%) than for dyad **24** (93%). These results are in accordance with the absence of the CT band in the absorption spectrum of **25** in DMSO. The lifetimes of the donor residual emission for the three dyads in CH_2Cl_2 solution are reported in Table 8. They are biexponential and characterized by a major short component (less than a ns) and a minor long component (ca. 5 ns) lifetime. The decay of the shorter lifetime is assigned to the donor molecules linked in the dyads, while the longer one is due to a small amount of free donor impurities present in solution.

The quenching efficiencies obtained comparing the corrected emission intensity are the same (within the experimental error) of those estimated by the analysis of the short component lifetime of the luminescent excited state of the donor in the dyads with respect to the one of **20** (Table 8). It is important to underline that, exciting the dyads at 286 nm, we are unable to see any emission of the acceptor unit. By excitation of isoabsorbing CH_2Cl_2 solutions of the dyads at 320 nm (where the 30% of the light is absorbed by the acceptor subunit), the emission spectra (Figure 44, right) are characterized only by a very weak tail due to the residual emission of the directly excited donor unit. These emissions are completely different from the one obtained exciting at 320 nm an isoabsorbing solution of the acceptor model **18** (Figure 44, black dashed-dotted line), demonstrating that in these systems also the luminescent excited state of the acceptor subunit is highly quenched.

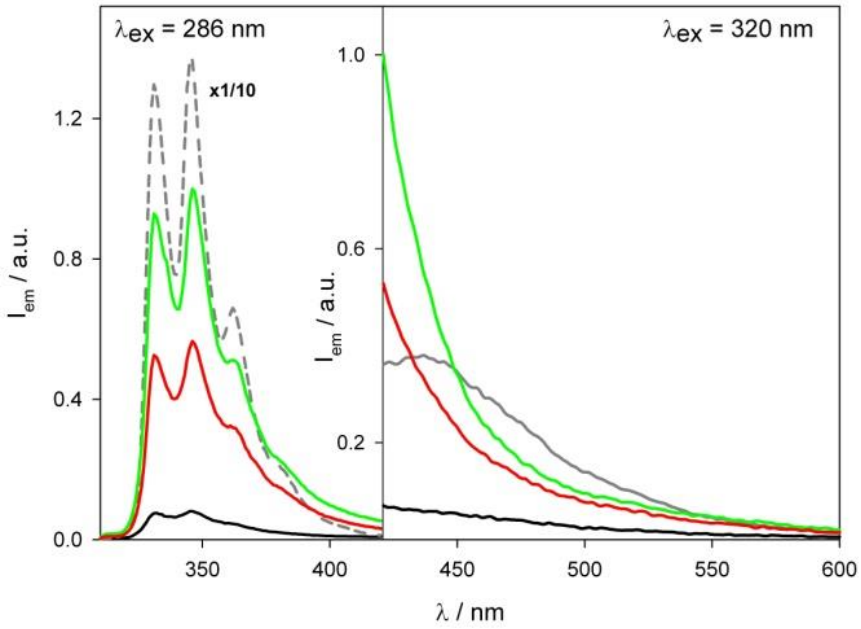

Figure 44. Emission spectra of dyad **23** (black full line), dyad **24** (red full line) and dyad **25** (green full line) and of donor (**20**, grey dashed line) and acceptor (**28**, grey full line) model compounds for optically matched CH_2Cl_2 solutions at the excitation wavelength: 286 nm (left) or 320 nm (right).

On the basis of the redox potentials of the donor and the acceptor model compounds, the energy of the charge transfer (CT) state, in which the donor is oxidized ($E_{p.a.}$ = + 1.23 V *vs* SCE) and the acceptor is reduced ($E_{1/2}$ = - 0.83 V *vs* SCE), is lower (ca 1.5 eV) than the energy of the excited state both of the donor and acceptor units (Table 9 and Figure 45). A schematic energy level diagram is reported in Figure 46. The presence of this low CT state suggests that the quenching mechanism of both the donor and the acceptor excited state is *via* electron transfer.

Table 9. Half-wave potentials ($E_{1/2}$ in V vs. SCE), unless otherwise noted, of acceptor **18** and donor **20** model compounds in CH_2Cl_2 solution at 298K. Working electrode: glassy carbon.

Compound	$E_{1/2}$ V vs. SCE				
18	-1.41	-0.83	+1.64[a]		
20			+1.22[a]	+1.64[a]	+1.97[a]

[a] Anodic peak potential, $E_{p.a.}$ at scan rate v = 0.2 Vs^{-1}.

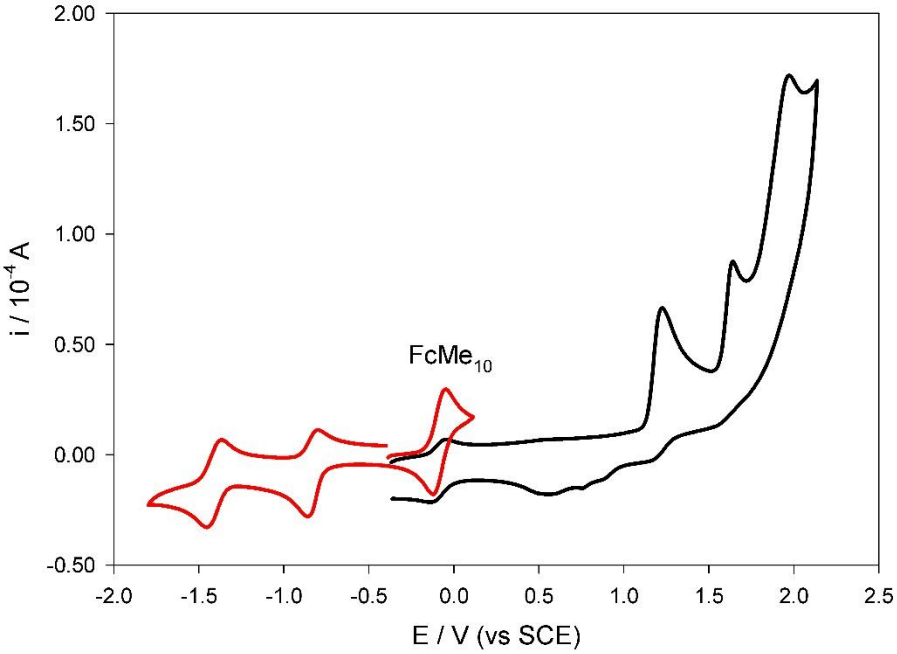

Figure 45. Cyclic voltammograms of a 1.0 mM solution of the acceptor **18** (red line) and donor **20** (black line) model compounds in CH_2Cl_2/$TBAPF_6$. T = 298 K; v = 0.2 V/s; working electrode: glassy carbon. Decamethylferrocene ($FcMe_{10}$) has been added as internal standard.

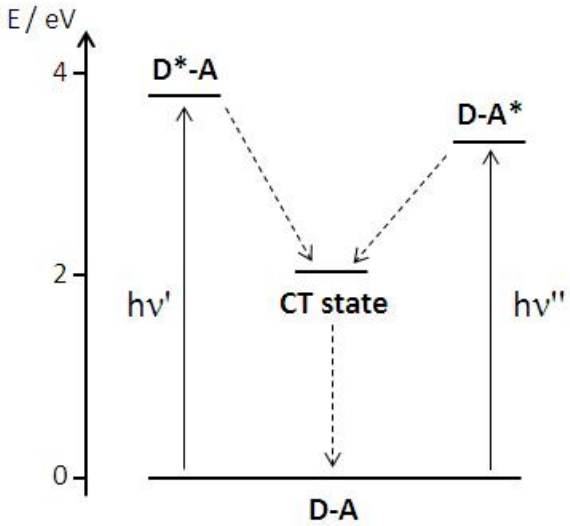

Figure 46. Schematic representation of the energy levels of model compounds **18** and **20** and for the charge transfer (CT) state of the dyads. Absorptions are indicated by full lines, non radiative transition are indicated by dashed lines.

In order to get a deeper insight into the electron transfer mechanism, ultrafast spectroscopic experiments in CH_2Cl_2 solution were performed by using 266 nm as excitation wavelength. No transient spectral changes with distinctive features of the formation of the charge separated product were observed in the 1-1000 ps time scale. We attribute this result to kinetic reasons: the charge recombination process to the ground state is faster than the photoinduced charge separation and, as a consequence, the charge separated product does not accumulate.

3.2. Nanoparticols

3.2.1. Gold Nanoparticols

Colorful aqueous solutions of gold colloids date back to Roman times and were known to the medieval alchemists “aurum potable” [102]. In most cases, the particles were charge stabilized in electrolyte solution, and hence it would not generally have been possible to isolate them as pure products without significant irreversible particle coalescence.

The deep-red color of AuNP sols in water and glasses reflects the surface plasmon band [103,104], indeed it have a broad absorption band in the visible region around 520 nm. The surface plasmon band is due to the collective oscillations of the electron gas at the surface of nanoparticles that is correlated with the electromagnetic field of the incoming light (i.e. the excitation of the coherent oscillation of the conduction band). Mie theory [105] attributes the plasmon band of spherical particles to the dipole oscillations of the free electrons in the conduction band occupying the energy states immediately above the Fermi energy level. All the numerous subsequent and recent reports correlate the spectroscopic behavior of AuNPs with the Mie theory. The main characteristics of the surface plasmon band are:

1) its position around 520 nm;
2) its sharp decrease with decreasing core size for AuNPs with 1.4-3.2 nm core diameters due to the onset of quantum size effects that become important for particles with core sizes less 3 nm in diameter and also cause a slight blue shift;
3) step-like spectral structures indicating transitions to the discrete unoccupied levels of the conduction band with monodispersed AuNPs with core diameters between 1.1 and 1.9 nm.

Thus, the surface plasmon band is absent for AuNPs with core diameter less than 2 nm, as well as for bulk gold (Figure 47).

[102] Mellor, J. W., *A comprehensive treatise on inorganic and theoretical chemistry. Longmans, Green and Co. London.* 1924.
[103] Daniel, M.-C.; Astruc, D., Gold Nanoparticles: Assembly, Supramolecular Chemistry, Quantum-Size-Related Properties, and Applications toward Biology, Catalysis, and Nanotechnology. *Chemical Reviews* **2004,** *104* (1), 293-346.
[104] Link, S.; El-Sayed, M. A., Spectral Properties and Relaxation Dynamics of Surface Plasmon Electronic Oscillations in Gold and Silver Nanodots and Nanorods. *The Journal of Physical Chemistry B* **1999,** *103* (40), 8410-8426.
[105] Mie, G., Beiträge zur Optik trüber Medien, speziell kolloidaler Metallösungen. *Annalen der Physik* **1908,** *330* (3), 377-445.

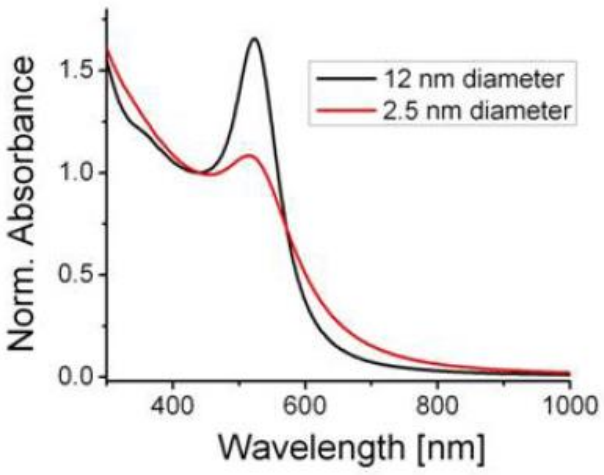

Figure 47. Plasmon band.

Apart from the control of optical properties, there are two other important aspects of modern nanoparticles research. The first one is the manipulation and study of individual particles and the second one is the assembly of 2D and 3D materials and structures in which the particles are closely packed without allowing the onset of uncontrolled aggregation.

In both cases, the chemical stability of the particles is crucial to avoid degradation processes such as partial oxidation or undesired sintering of particles. The lack of sufficient stability of many nanoparticle preparations could impede the development of real world applications of nanomaterials. The stability of such materials has been improved by the development of thiol-stabilized gold [103] and silver nanoparticles, from which new opportunities for fundamental and applied studies have arisen. Since nanocrystalline gold compounds have been the subject of intense research, scientist have found applications in areas such as catalysis, sensors, molecular electronics, or as bioconjugate probes for amplification tags in gene analysis, antibody or antigen detection, DNA sequencing or gene mapping [106,107,108,109,110,111,112,113].

---

[106] Lahav, M.; N. Shipway, A.; Willner, I., Au-nanoparticle-bis-bipyridinium cyclophane superstructures: assembly, characterization and sensoric applications. *Journal of the Chemical Society, Perkin Transactions 2* **1999,** (9), 1925-1931.

[107] Chen, W.; Grouquist, D.; Roark, J., Voltage Tunable Electroluminescence of CdTe Nanoparticle Light-Emitting Diodes. *Journal of Nanoscience and Nanotechnology* **2002,** *2* (1), 47-53.

[108] Shipway, A. N.; Katz, E.; Willner, I., Nanoparticle Arrays on Surfaces for Electronic, Optical, and Sensor Applications. *ChemPhysChem* **2000,** *1* (1), 18-52.

[109] Shipway, A. N.; Willner, I., Nanoparticles as structural and functional units in surface-confined architectures. *Chemical Communications* **2001,** (20), 2035-2045.

[110] Grieve, K.; Mulvaney, P.; Grieser, F., Synthesis and electronic properties of semiconductor nanoparticles/quantum dots. *Current Opinion in Colloid & Interface Science* **2000,** *5* (1–2), 168-172.

[111] Lue, J.-T., A review of characterization and physical property studies of metallic nanoparticles. *Journal of Physics and Chemistry of Solids* **2001,** *62* (9–10), 1599-1612.

[112] Trindade, T.; O'Brien, P.; Pickett, N. L., Nanocrystalline Semiconductors: Synthesis, Properties, and Perspectives. *Chemistry of Materials* **2001,** *13* (11), 3843-3858.

[113] Schwerdtfeger, P., Gold Goes Nano—From Small Clusters to Low-Dimensional Assemblies. *Angewandte Chemie International Edition* **2003,** *42* (17), 1892-1895.

3.2.2. Peptide-Functionalized Gold Nanoparticles

The combination of biotechnology and nanotechnology led to the development of hybrid nanomaterials that incorporate the highly selective catalytic and recognition properties of biomaterials, such as proteins/enzymes and DNA, with the unique electronic, photonic, and catalytic features of nanoparticles [114].

Enzymes, antigens and antibodies, and biomolecular receptors have dimensions in the range of 2–20 nm, similar to those of nanoparticles, thus the two classes of materials are structurally compatible. Moreover biomaterials display specific and strong complementary recognition interactions, for example, antigen–antibody, nucleic acid–DNA, and hormone–receptor interactions. The functionalization of nanoparticles with biomolecules could lead to biomolecule–nanoparticle recognition interactions.

Peptide-functionalised gold nanoparticles are intriguing supramolecular systems for their aptitude to mimic natural proteins or DNA. In particular, it is possible to designate a supramolecular as a well-defined complex of molecules (1 – 200 nm) held together by noncovalent bonds. A cluster of gold atoms, which is surrounded of copies of a peptide, forms a nanosystem that resembles a protein in size (2 - 20 nm), shape (globular) and, possibly in function. Gold nanoparticles are an interesting model system for several reasons:

1) The size of the gold core can be precisely controlled between one and several tens of nanometer by using various synthetic procedures.
2) Gold surfaces are readily functionalized by using thiolated ligands, which form covalent bonds with the gold atoms.
3) Gold nanoparticle solutions are colored due to the nanoparticle plasmon band. Therefore, the formation of nanoparticle aggregates leads to a color change that offers a visual insight into nanometer-scale processes.

Often, nanoparticles are prepared with “wet chemistry” procedures, in which clusters of metal atoms or semiconductor molecules are formed in the presence of a surface-capping ligand. This capping ligand binds to the metal/semiconductor clusters, preventing aggregation and controlling the final dimensions of the nanoparticles. Examples of capping systems are hydrophobic monolayers, positively or negatively charged hydrophilic monolayers, and polymer layers. The aggregation of molecular units to nanoparticles provides the appropriate structure, which also enables to desired 2D and 3D architectures on surfaces.

The design strategy for the synthesis of a peptide-capping ligand requires some specific characteristics. As peptides should have a strong gold affinity and should be able to self-assemble into a dense layer that excludes water, a hydrophilic terminus is requested to achieve solubility and stability in water.

---

[114] Katz, E.; Willner, I., Integrated Nanoparticle–Biomolecule Hybrid Systems: Synthesis, Properties, and Applications. *Angewandte Chemie International Edition* **2004,** *43* (45), 6042-6108.

The first example for thiols stabilized nanoparticles was prepared by Brust and co-workers [115] : $AuCl_4^-$ was solubilized in toluene using tetraoctylammonium bromide as the phase-transfer reagent and reduced by sodium borohydride in the presence of dodecanethiol. The organic phase changes color from orange to deep brown within a few seconds upon addition of sodium borohydride.

The interface between the core of the cluster and the thiolate ligands is a bridged binding motif (Figure 48a): an Au(I) atom is stabilized between the sulfur atoms of two neighboring ligands [116]. The binding motif was found in several crystal structures and was observed in scanning tunnelling microscopy studies of self-assembled monolayers (Figure 48b).

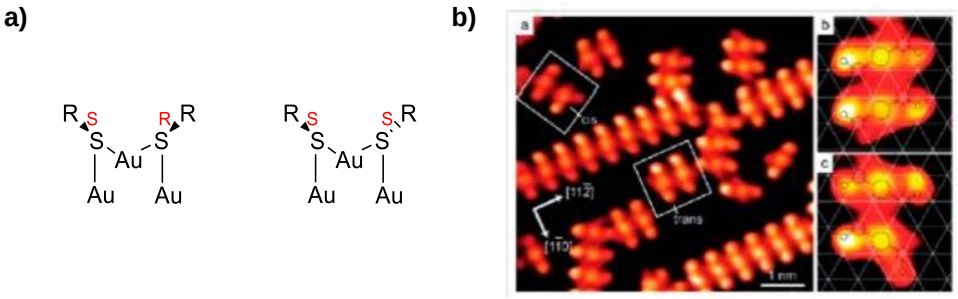

Figure 48. a) Stereochemistry of sulphur ligand; b) Scanning tunnerlung microscopy of methylthiolate on Au(111) surface.

Thiolate-protected gold clusters can show chirality at different levels: (1) protection with chiral thiolate ligands, (2) arrangement of the ligands on the surface of the cluster, (3) inherent chirality of the cluster core and (4) *cis/trans* isomerism in the bridged Au−S binding motifs.

The bridged binding motifs RS-Au-SR form semi rings on the cluster surface, and the organic rests of the ligands can adopt *cis* and *trans* geometries. For near sp^3 hybridization, the sulfur atoms have four different substituents in tetrahedral coordination geometry. This renders them as stereogenic centers, and the absolute configuration can be assigned for the monomeric units RS-Au-SR (Figure 48a). The *cis/trans* isomerism of the protecting units is hard to experimentally assess. Computations showed the influence of the orientation of the ligands with respect to the units, leading to different energy and CD spectra [117].

In 2010, Hamm et al. [118] designed and characterised spherical gold nanoparticles functionalised with 3_{10}-helical peptides. They used two octapeptides as capping agents: Trt-S-

[115] Brust, M.; Walker, M.; Bethell, D.; Schiffrin, D. J.; Whyman, R., Synthesis of thiol-derivatised gold nanoparticles in a two-phase Liquid-Liquid system. *Journal of the Chemical Society, Chemical Communications* **1994,** (7), 801-802.

[116] Knoppe, S.; Bürgi, T., Chirality in Thiolate-Protected Gold Clusters. *Accounts of Chemical Research* **2014,** *47* (4), 1318-1326.

[117] Dolamic, I.; Varnholt, B.; Burgi, T., Chirality transfer from gold nanocluster to adsorbate evidenced by vibrational circular dichroism. *Nat Commun* **2015,** *6*.

[118] Schade, M.; Moretto, A.; Donaldson, P. M.; Toniolo, C.; Hamm, P., Vibrational Energy Transport through a Capping Layer of Appropriately Designed Peptide Helices over Gold Nanoparticles. *Nano Letters* **2010,** *10* (8), 3057-3061.

$(CH_2)_2$-O-CO-Aib-L-Ala*-$(Aib)_6$-OMe and Trt-S-$(CH_2)_2$-O-CO-$(Aib)_3$-L-Ala*-$(Aib)_4$-OMe that have a strong tendency to favour 3_{10}-helical conformations. In 2013 Scrimin, Moretto and co-workers [119] found out that the chiroptical properties of the peptide-functionalized nanoparticles change as a function of the peptide sequence, the main chain length and the temperature of analysis in the regions of plasmon band.

3.2.3. Synthesis of Gold Nanoparticols Containing Pseudopeptide Foldamers

We have synthetized, studied the conformation and evaluated the biological properties of AuNPs capped by pseudopeptide foldamers containing the L-Ala-D-Oxd moiety and functionalized with a trytil mercaptopropanoic linker (Figure 49) [120].

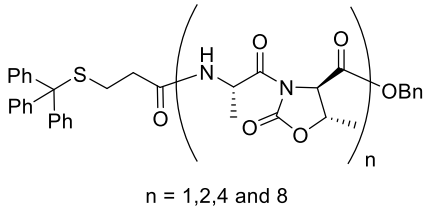

Figure 49. General structure of the pseudopeptide foldamers functionalised with trytil mercaptopropanoic units.

We prepared a series of oligomers Boc-(L-Ala-D-Oxd)$_n$-OBn (n = 1, 2, 4, 8) showed in Scheme 7 by conventional peptide synthesis methods in solution, starting from L-Ala and D-Oxd, as previously described.

[119] Longo, E.; Orlandin, A.; Mancin, F.; Scrimin, P.; Moretto, A., Reversible Chirality Control in Peptide-Functionalized Gold Nanoparticles. *ACS Nano* **2013,** *7* (11), 9933-9939.
[120] Fanelli, R.; Milli, L.; Cornia, A.; Moretto, A.; Castellucci, N.; Zanna, N.; Malachin, G.; Tavano, R.; Tomasini, C., Chiral Gold Nanoparticles Decorated with Pseudopeptides. *European Journal of Organic Chemistry* **2015,** (28), 6243-6248.

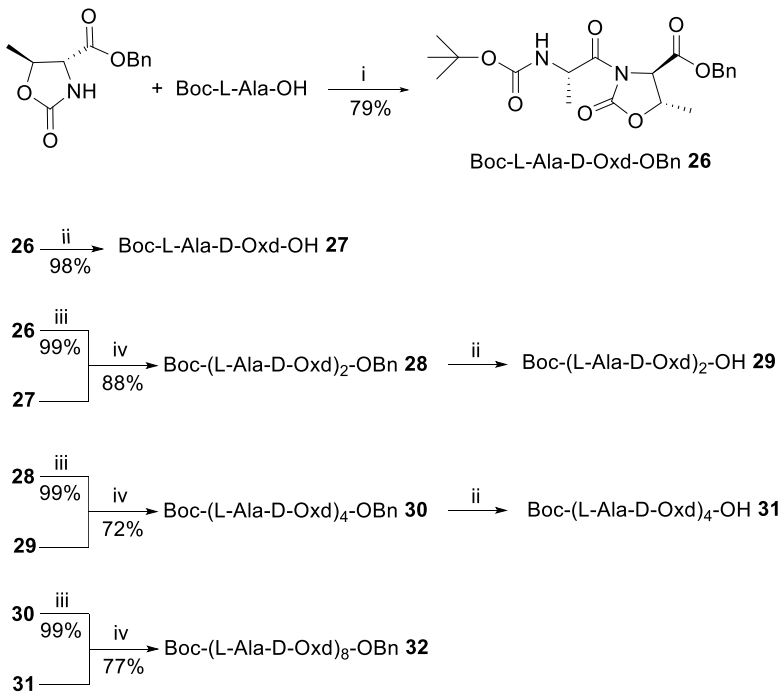

Scheme 7. Reagents and Conditions: (i) HBTU (1.1 equiv.), DBU (2.1 equiv.), dry acetonitrile, 1 h, r.t.; (ii) H_2, Pd/C (10%), MeOH, r.t., 16 h; (iii) TFA (18 equiv.), dry CH_2Cl_2, r.t., 4 h; (iv) HBTU (1.1 equiv.), Et_3N (3 equiv.), dry acetonitrile, 1 h, r.t..

Compounds **33**, **34**, **35** and **36** were prepared by cleavage of the *N*-terminal Boc moieties with anhydrous TFA in dichloromethane followed by coupling with trityl mercaptopropionic acid in the presence of HBTU and TEA in acetonitrile at room temperature under nitrogen atmosphere (Scheme 8). The reaction was complete after 1 hour and the desired compounds were obtained with a yield ranging between 52 and 63%.

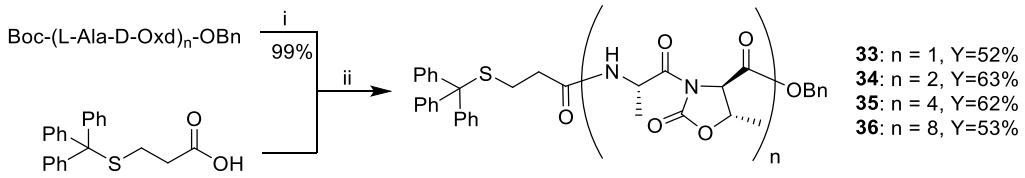

Scheme 8. Reagents and Conditions: (i) TFA (18 equiv.), dry CH_2Cl_2, r.t., 4 h; (ii) HBTU (1.1 equiv.), TEA (2 equiv.), dry acetonitrile, 1 h, r.t.

3.2.4. Conformational Analysis of Pseudopeptide Foldamers 33-36

The adoption of a well-defined secondary structure of compounds **33**, **34**, **35** and **36** was investigated by IR and NMR spectroscopies and by single-crystal X-Ray diffraction. The FT-IR spectra were recorded in CH_2Cl_2 at a compound concentration of 3 mM, so as to avoid compound self-aggregation (Figure 50 and Table 10).

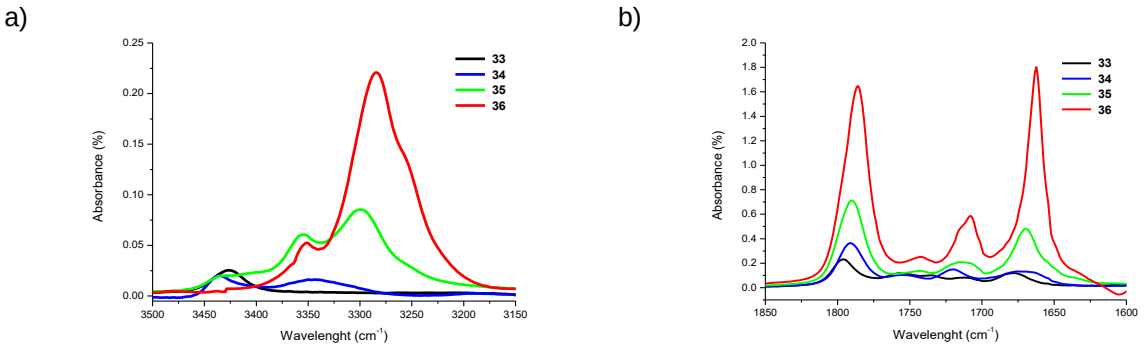

Figure 50. a) N-H Stretching regions of the FT-IR absorption spectra in pure DCM at room temperature for 3 mM concentration of compounds **33**, **34**, **35** and **36**; b) C = O stretching regions of the FT-IR absorption spectra in pure CH_2Cl_2 at room temperature for 3 mM concentration of **33**, **34**, **35** and **36**.

Table 10. NH and amide CO stretching bands of compounds **33-36** in CH_2Cl_2 (3 mM solution).

Compound	IR stretching bands	
	NH	CO (amide band)
33	3419	1679
34	3436, 3347	1672
35	3355, 3299	1669
36	3351, 3284	1663

The spectrum of **33** clearly shows the presence of only one band at 3419 cm^{-1} attributed to free amide groups. By contrast, two bands at 3436 and 3347 cm^{-1} are seen in the spectrum of **34**, indicating that both free and hydrogen-bonded amide NH groups are present in solution. Significantly, the stretching band above 3400 cm^{-1} totally disappears in **35** and **36**, suggesting that these compounds adopt a folded conformation, as could be anticipated from the analysis of their N-Boc protected counterparts. A similar trend was observed for the C = O stretching band of the amide groups that shifts from 1679 cm^{-1} in **33** to 1663 cm^{-1} in **36**.

^{1}H NMR analysis supports the foregoing interpretation of IR spectroscopy results. The NH of **33** resonates at 6.08 ppm, while the NH's of **34** resonate at 5.94 and 7.35 ppm and the NH's of **36** are very deshielded, ranging between 7.9 and 8.5 ppm: these pronounced downfield shifts are usually indicative of hydrogen-bonded NH's. The occurrence of intramolecular C = O···H-N hydrogen bonds in oligomers **34** and **36** was further confirmed by following the dependence of NH proton chemical shifts upon addition of DMSO-d_6. This solvent is a strong hydrogen-bond acceptor and, when bound to a NH proton, it is expected to have a dramatic deshielding effect. The results of DMSO-d_6/$CDCl_3$ titrations of the NH protons in pseudopeptides **34** and **36** are presented in Figure 51.

Of the two NH protons in **34**, one is totally free (Δδ = 1.40 ppm over the explored range of DMSO concentration), while the other one is quite H-bonded (Δδ = 0.34 ppm). The former is most likely the one closer to S terminus, as its chemical shift in $CDCl_3$ solution is virtually the same as found in compound **33**. By contrast, all NH protons in **36** are DMSO insensitive, confirming that **36** is fully organized in a secondary structure supported by C = O•••H-N interactions.

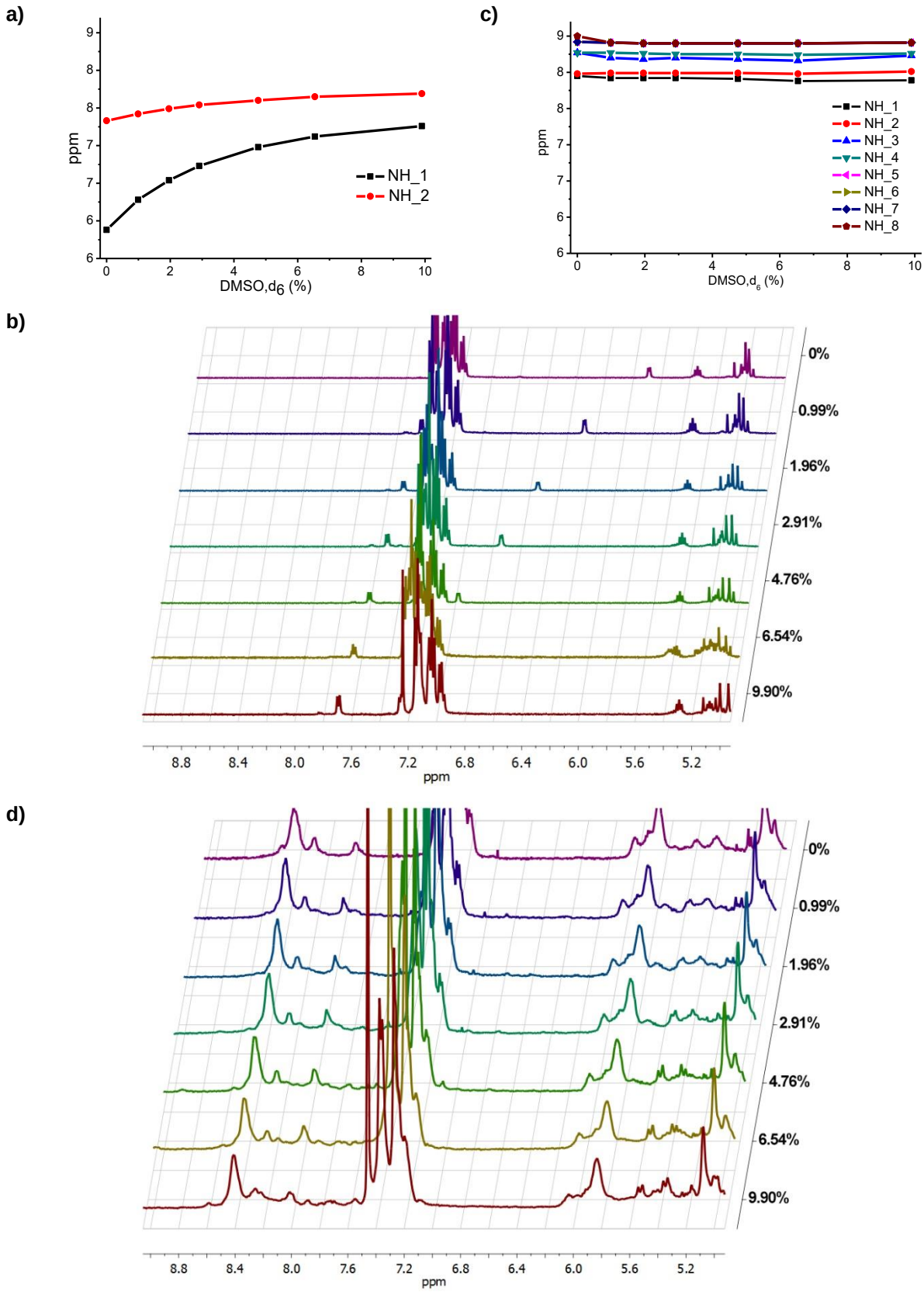

Figure 51. Variation of NH proton chemical shifts (ppm) of **34** (a), and **36** (b) as a function of increasing percentages of DMSO-d_6 added to the $CDCl_3$ solution (v/v) (concentration: 3 mM). Superposition of the ^1H NMR spectra in $CDCl_3$ of **34** (b) and **36** (d) in the NH region, as a function of an increasing percentage of DMSO-d_6.

X-ray quality crystals of **34** were grown as long colorless needles by slow evaporation of a toluene solution. Unfortunately we were not able to grow crystals of oligomers **33**, **35** and **36**. Crystal data and refinement parameters for **34** are given in Table 11, the geometry of hydrogen-bond interactions is detailed in Table 12 while conformational data are gathered in Table 13. The crystals are monoclinic, space group $P2_1$, and the unit cell comprises two molecules related by the twofold screw axis (Figure 52).

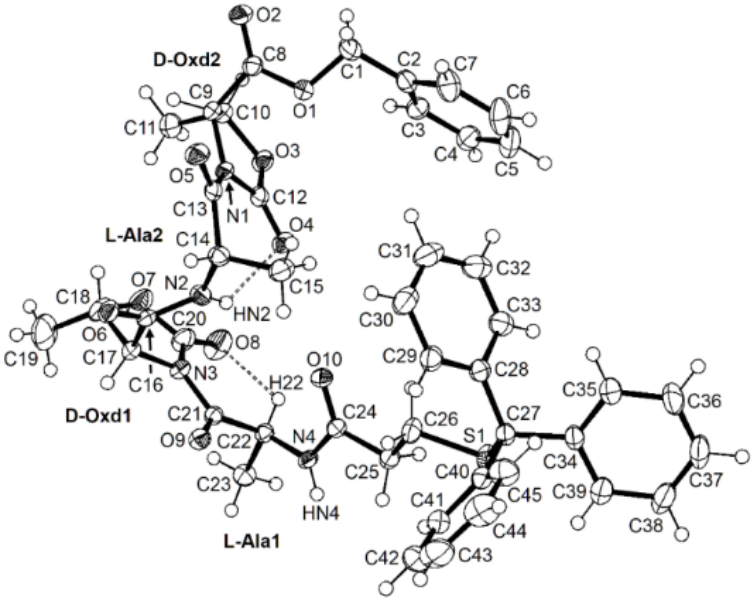

Figure 52. Partially labelled ORTEP-3 [76] plot of **34** with displacement ellipsoids at 50% probability level and H atoms drawn as spheres with arbitrary radius. Dashed lines indicate intramolecular hydrogen bonding interactions discussed in the text. For simplicity, only H atoms engaged in intra- or intermolecular hydrogen bonds have been labelled.

Table 11. Crystal data and refinement parameters for compound **34**

Formula	$C_{45}H_{46}N_4O_{10}S$
Formula weight	834.92
T, K	140(2)
λ, Å	0.71073
Crystal size, mm^3	0.53×0.40×0.12
Crystal system	monoclinic
Space group	*P* 2_1 (No. 4)
a, Å	15.2448(5)
b, Å	9.3221(3)
c, Å	15.8417(5)
α, deg	90.000
β, deg	110.8900(15)
γ, deg	90.000
V, Å^3	2103.33(12)
Z	2
D_{calcd}, g cm^{-3}	1.318
μ(MoK_α), mm^{-1}	0.141
F(000)	880
θ range, deg	3.19-31.03
Reflns collected	30727
R_{int}	0.0263
Data/restraints/parameters	12446/33/598
Goodness-of-fit on F^2	1.066
Final *R* indices [$I>2\sigma(I)$]	*R*1 = 0.0353, *wR*2 = 0.0875
R indices (all data)	*R*1 = 0.0442, *wR*2 = 0.0920
Flack parameter	0.01(4)
Largest diff. peak/hole, *e*Å^{-3}	0.268 / -0.186

Table 12. Hydrogen bond geometry (Å, °) in compound **34**

D*–H•••*A	***D*–H**	**H•••*A***	***D*•••*A***	**∠ *D*–H•••*A***
C22–H22•••O8	0.950(11)	2.300(13)	2.8858(16)	119.2(10)
N2–HN2•••O4	0.852(12)	2.141(18)	2.7370(14)	126.7(16)
C15–H15C•••O4	0.98	2.50	3.1685(18)	125.7
N4–HN4•••O4^{i}	0.842(11)	2.103(11)	2.9385(13)	171.9(15)
C23–H23C•••O10^{i}	0.98	2.40	3.3529(17)	164.2
C9–H9•••O6^{ii}	0.946(10)	2.327(11)	3.1983(15)	152.9(12)
C18-H18•••O2^{iii}	0.930(11)	2.434(12)	3.3419(17)	165.4(16)

Symmetry codes: (i) –*x*, –0.5+*y*, 1–*z*; (ii) = –1–*x*, 0.5+*y*, 1–*z*; (iii) = –1–*x*, –0.5+*y*, 1–*z*.

Table 13. Selected conformational parameters (°) in compound **34**

C21–C22–N4–C24 (ϕ)	-66.18(14)	L-Ala1
N3–C21–C22–N4 (ψ)	152.92(10)	
C16–C17–N3–C21 (ϕ)	71.43(14)	D-Oxd1
N2–C16–C17–N3 (ψ)	19.97(15)	
C13–C14–N2–C16 (ϕ)	-95.69(14)	L-Ala2
N1–C13–C14–N2 (ψ)	-36.94(16)	
C8–C9–N1–C13 (ϕ)	70.52(14)	D-Oxd2
O1–C8–C9–N1 (ψ)	23.55(14)	

The molecule exhibits a turn-like structure. As found in related foldamers, the L-Ala1 α-carbon atom C22 has a H-contact with the endocyclic C = O of the neighbouring D-Oxd1 residue [*d*(H22···O8) = 2.300(13) Å]. However, no significant H-bonding interaction is established

between the carbonyl oxygen O10 and the amide group N2-HN2 of L-Ala2 [*d*(HN2•••O10) = 2.808(16) Å], so that a ten-membered hydrogen-bonded turn (3_{10}-helical structure) is not formed. Instead, the strongest intramolecular H-bonding interaction involves amide nitrogen N2 and the D-Oxd2 carbonyl oxygen O4 [*d*(HN2•••O4) = 2.141(18) Å]. Notably, the amide group N4-HN4 of L-Ala1 is not engaged in intramolecular hydrogen bonds in the solid state and the resulting picture matches remarkably well the results of IR and ^{1}H NMR investigations in solution. Molecules related by the 2_1 axis are hydrogen bonded into chains via amide group N4–HN4 and carbonyl oxygen O4 [*d*(HN4•••O4^{i}) = 2.103(11) Å], but crystal packing also relies on a number of other short C–H•••O contacts (Table 12). The backbone conformational parameters gathered in Table 13 show that the torsion angles (ϕ and ψ) at the L-Ala1 residue are similar to those of poly-L-proline II helix, as in related foldamers. However, the L-Ala2 residue has quite different conformational parameters that fall in the right-handed α-helix region of Ramachandran plot.

The ECD spectra of compounds **33**, **34**, **35** and **36** were not recorded, as the spectral features related to the secondary structure are obscured around 200 nm by the very strong B transitions of trityl groups, that are removed when the **AuNPs** are formed. Strong support to the formation of a well built secondary structure for the longer oligomers of the (L-Ala-D-Oxd)$_n$ series comes from the analysis of the Boc-(L-Ala-D-Oxd)$_n$-OH oligomers [49]. We could demonstrate that when n ≥ 5, a stable 3_{10} helix is formed.

3.2.5. Synthesis and Analysis of Gold Nanoparticols

Pseudopeptide-functionalised gold nanoparticles **AuNPs1**, **AuNPs2**, **AuNPs3** and **AuNPs4** have been obtained by reduction of $HAuCl_4$ with $NaBH_4$ in the presence of compounds **33**, **34**, **35** and **36**, respectively.

Structural information on the NPs has been obtained using several techniques (Table 14).

Table 14. Chemical Structure Data for **AuNPs1-4**.

Entry	Core diameter (nm)[a]	No. of Au atoms for NP[b]	No. of foldamers for NP[c]	Footprint (nm^2)[d]
AuNPs1	2.1± 0.3	289	167	0.10
AuNPs2	2.3 ± 0.3	376	156	0.11
AuNPs3	2.3 ± 0.4	376	135	0.15
AuNPs4	2.5 ± 0.3	508	97	0.56

[a] Calculated by averaging the size of at least 200 NPs. [b] Calculated assuming a spherical model. [c] Determined combining TEM and TGA analysis. [d] Defined as the area occupied by the projection of the foldamer ligand onto the gold cluster surface.

The average number of Au atoms per NP was calculated assuming spherical particles and using the diameter of the metallic core observed in TEM (transmission electron microscopy) images and the density of bulk metal (55 atoms/nm^3) (Figure 53).

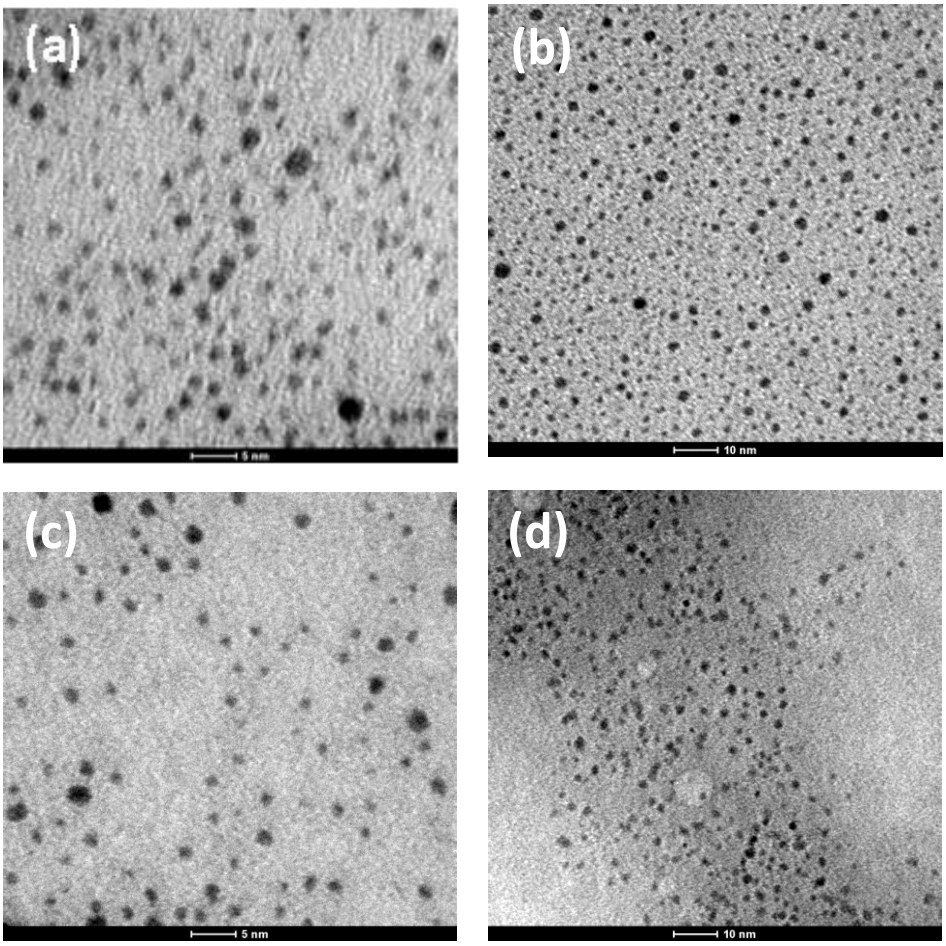

Figure 53. TEM images of gold nanoparticles in water solution: (a) **AuNPs1**, (b) **AuNPs2**, (c) **AuNPs3**, (d) **AuNPs4**

The number of foldamers conjugated to the inorganic core was calculated using the TGA (thermogravimetric analysis) weight loss (corresponding to the weight fraction of the organic coating monolayer on the inorganic cluster) and the molecular weight of the appropriate oligomer (Figure 54).

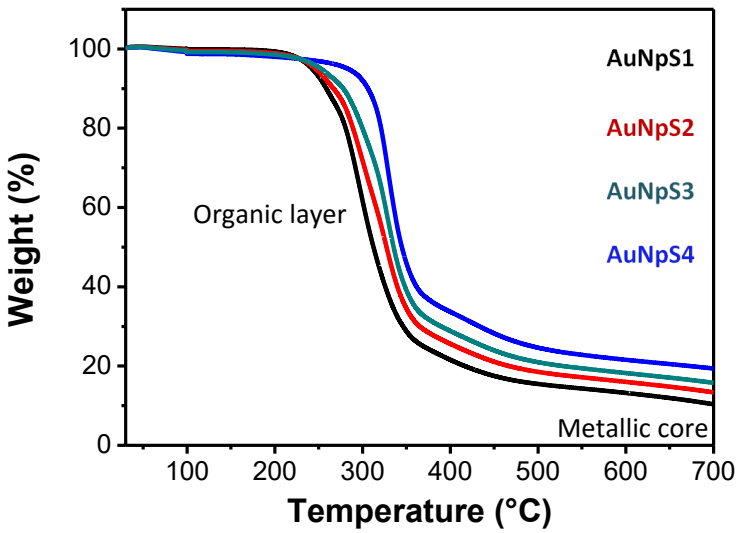

Figure 54. TGA analysis of **AuNPs1-4**.

Finally, the foldamer footprints were calculated by relating the number of oligomers linked to the gold surface with the dimensional information obtained by TEM analysis (Figure 55).

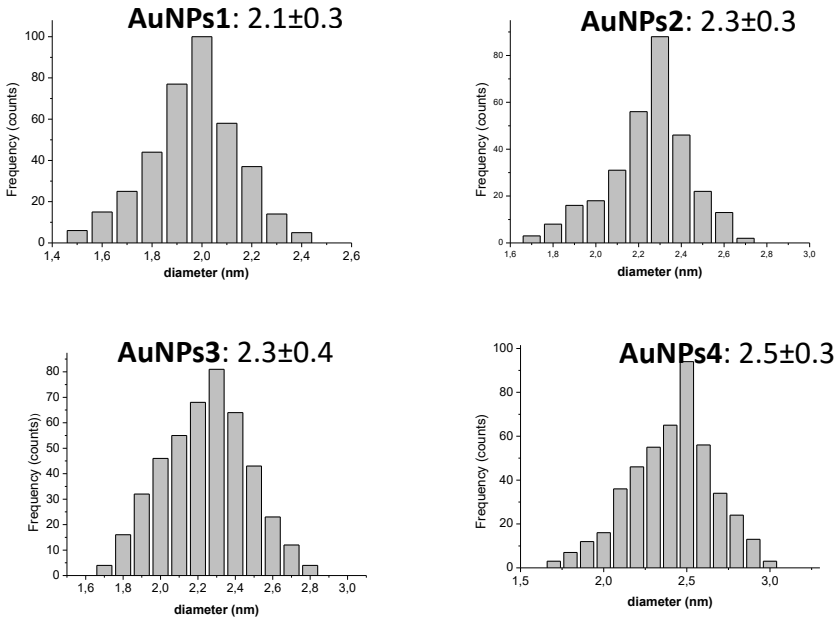

Figure 55. Histograms showing the core size distributions of **AuNPs1-4** series.

The UV-Vis absorption spectra (Figure 56) are consistent with the results gathered in Table 14, as a plasmonic band (~520 nm) indicative of a NP diameter ≥ 2.5 nm was observed only for **AuNPs4** [121].

[121] Alvarez, M. M.; Khoury, J. T.; Schaaff, T. G.; Shafigullin, M. N.; Vezmar, I.; Whetten, R. L., Optical Absorption Spectra of Nanocrystal Gold Molecules. *The Journal of Physical Chemistry B* **1997,** *101* (19), 3706-3712.

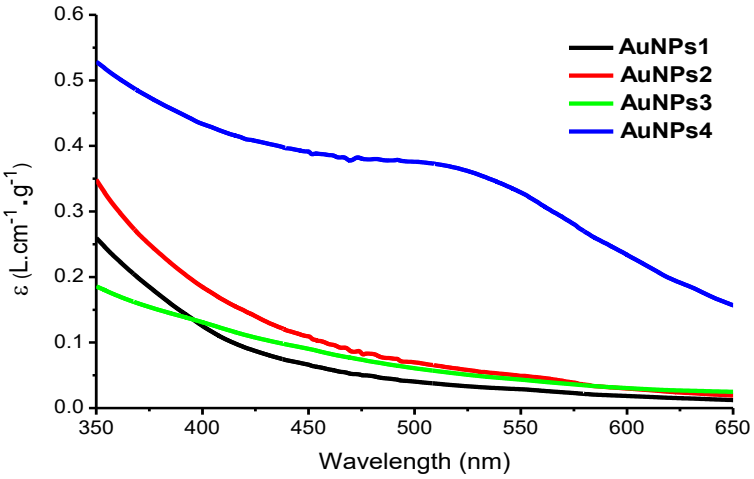

Figure 56. UV-Vis spectra of **AuNPs1-4** recorded in water at 20°C in the 350-650 nm region.

Another important feature of AuNPs is chirality, which may derive from several factors [122,123]: a chiral arrangement of metal atoms in the core; the binding of thiolates on the gold surface to form chirally arranged staples; the chirality of the monolayer of passivating organic molecules. Pseudopeptide oligomers, binding to the gold core, may influence the whole NP to assume a diverse organisation.

ECD (electronic circular dichroism) analysis of **AuNPs1-4** was performed in water solution (Figure 57), both in the far-UV region (190-250 nm) and in UV-Vis region (300-700 nm) where chiroptical signals are expected to arise from the chirality of the gold surface (chiral staples).

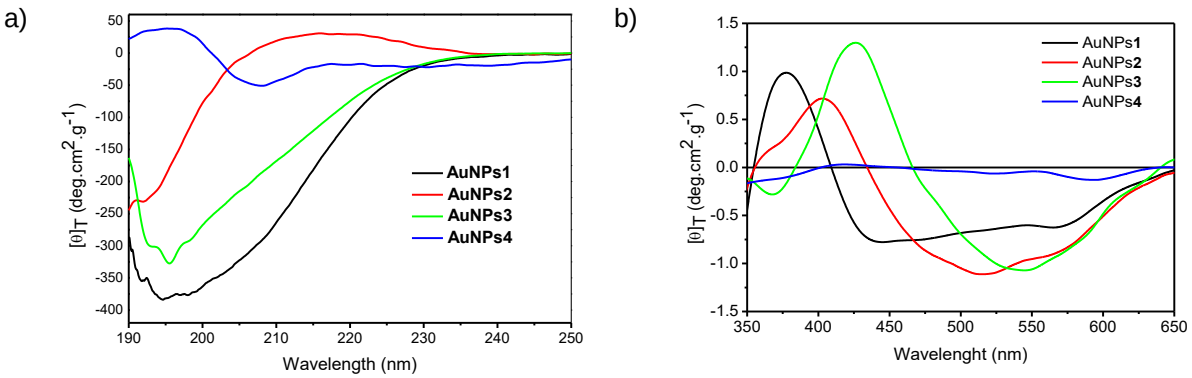

Figure 57. ECD spectra of **AuNPs1-4** recorded in water at 20 °C: (a) far-UV ECD spectra indicating the foldamer chirality; (b) UV-Vis ECD spectra indicating the chirality of the gold surface.

In Figure 57a the ECD spectra in the far-UV region are reported for **AuNPs1-4**. The spectra of **AuNPs1** and **AuNPs3** show only a deep minimum at 195 nm, which is usually associated to a random coil conformation, while **AuNPs2** shows a deep minimum at 191 nm and a weak maximum at 215 nm. All these spectra closely recall those of unordered peptides, whose ECD

[122] Alhassen, H.; Antony, V.; Ghanem, A.; Yajadda, M. M. A.; Han, Z. J.; Ostrikov, K., Organic/Hybrid Nanoparticles and Single-Walled Carbon Nanotubes: Preparation Methods and Chiral Applications. *Chirality* **2014,** *26* (11), 683-691.

[123] Okamoto, H.; Narushima, T.; Nishiyama, Y.; Imura, K., Local optical responses of plasmon resonances visualised by near-field optical imaging. *Physical Chemistry Chemical Physics* **2015,** *17* (9), 6192-6206.

response entails a strong negative band near 197 nm and a weak band at approximately 220 nm, that may be a negative shoulder on the short-wavelength band. In contrast, the spectrum of **AuNPs4** outlines the typical conformation of a 3_{10} helix, displaying a maximum at 195 nm, a deep minimum at 208 nm and a shoulder at 227 nm.

In Figure 57b the chiroptical signals associated with the gold surface are reported. The signals associated with **AuNPs1-3** show a variation of the molar ellipticity with a maximum ranging between 360 and 430 nm, while **AuNPs4** shows a steadier trend.

This outcome suggests that only an unordered conformation may influence the chirality of the whole AuNP, while the well-built secondary structure **36** does not communicate with the AuNPs. This is a remarkable effect that confirms previous observations on AuNPs passivated with short oligopeptides based on Aib-L-Ala repeating units (Aib = amino isobutyric acid) [119]. These NPs presented relevant ECD signals in the 300-650 nm wavelength region only for short peptides. These signals vanished when the sequences were long enough to assume a folded conformation.

3.2.6. Effect of Gold Nanoparticols on Cell Viability

The cytotoxic acute effect of the different AuNPs developed in this study was evaluated in HeLa cells, a human cell line from cervical cancer. After incubation at different nanoparticle concentrations, cell viability was assessed by MTS assay. In this test the MTS compound is reduced by living cells into a coloured formazan product soluble in tissue culture medium. So, the quantity of formazan, whose absorbance was measured at 490 nm, is directly proportional to the number of living cells in culture. As shown in Figure 58, all four **AuNPs** used are not toxic for human HeLa cells up the high dose of 200 µg/mL.

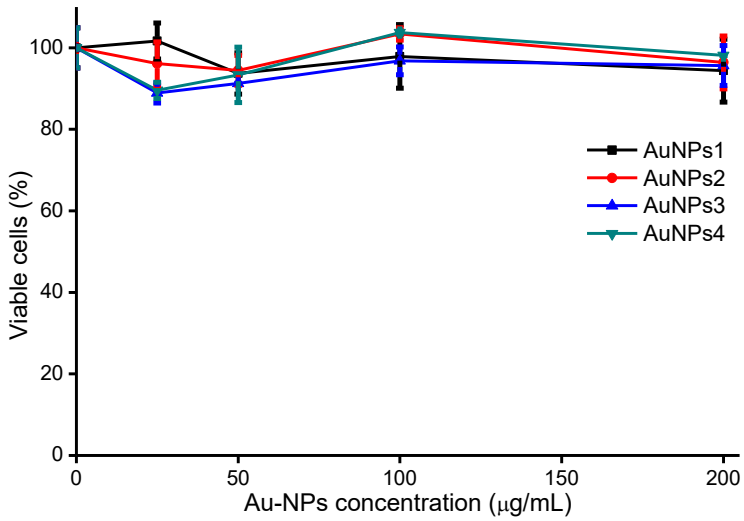

Figure 58. Cell viability evaluated in HeLa cells by MTS assay, after incubation for 24h with different concentrations of NPs. The percentage of alive cells was calculated with respect to control cells (no NPs). Values are means ± SE (N = 2).

We also determined the ability of **AuNPs** to induce the production of ROS. To this aim, HeLa cells were incubated with **AuNPs1-4** for three hours and the produced ROS were measured using Carboxy-H2DCFDA probe. This non-fluorescent molecule is converted to a green-fluorescent form by ROS, as they remove the acetate groups.

As shown in Figure 59, in spite of their lack of cytotoxicity, all **AuNPs** can induce ROS production. **AuNPs1** is the least active, while **AuNPs3** induces the strongest ROS production.

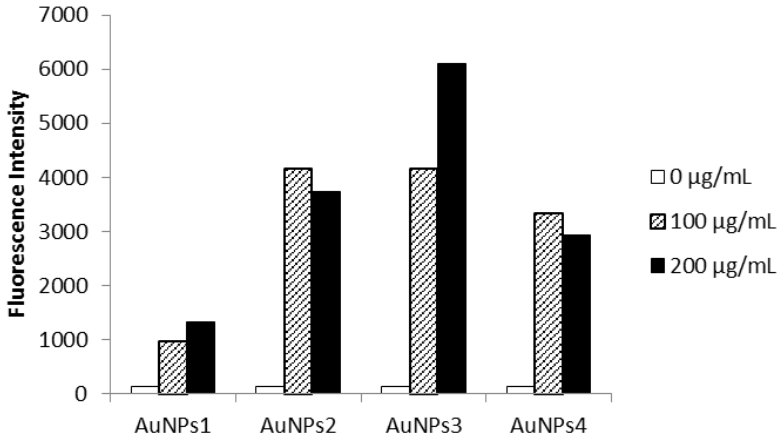

Figure 59. Fluorescence intensity of HeLa cells, seeded the day before the experiment and incubated with different concentrations of **AuNPs** (up to 200 µg/mL) for 3 h at 37 °C. 20 minutes before the end of the incubation, cells were incubated with 25 µM Carboxy-H_2DCFDA (Invitrogen); cells were then washed with PBS, treated with trypsin-EDTA and centrifuged; finally they were directly analyzed by cytofluorimetry.

3.3. Gel

In 1861 Graham gave the first definition of gel as “the softness of the gelatinous colloid partakes of fluidity” [124]. In 1926 Lloyd wrote “only one rule seems to hold for all gels and that is that they must be built up from two components, one which is a liquid at the temperature under consideration and the other which, the gelling substance proper, often spoken of as the gelator, is a solid.” [125]. Finally in 1974 Flory gave a definition of gel as “a continuous structure that is permanent on the analytical time scale and is solid-like in its rheological behavior” [126]. Gels can be classified in different ways depending upon their origin, constitution, the type of cross-linking that creates their 3D network and the medium (Figure 60) [127,128,129,130].

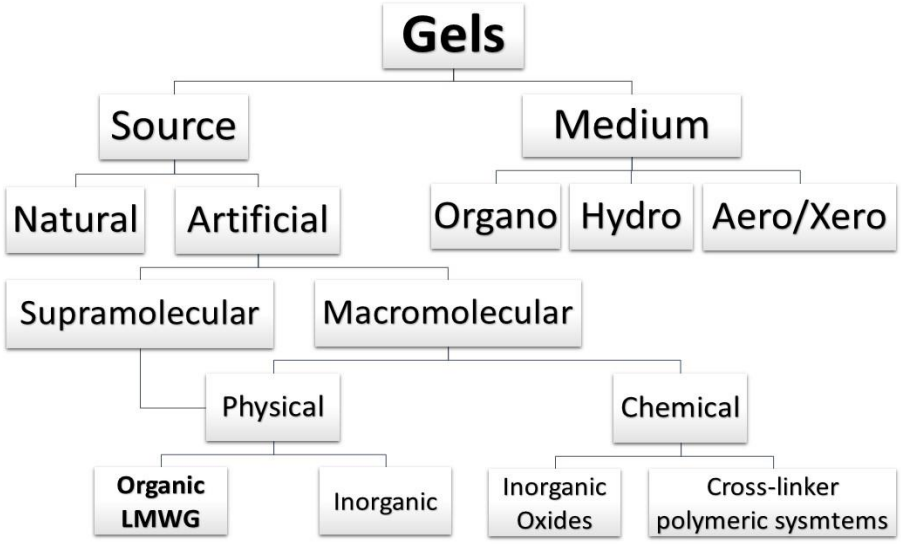

Figure 60. Classification of gels

Most of the naturally occurring gelators are macromolecular and they form gels by physical cross-linking (usually H-bonding). Such macromolecules include gelatin, collagen, agar, starch and gellan gum. Gels derived from synthetic compounds can be subdivided on the basis of their constitution into macromolecular (polymer) and molecular. The formation of gels from

[124] Graham, T., Liquid Diffusion Applied to Analysis. *Philosophical Transactions of the Royal Society of London* **1861,** *151*, 183-224.
[125] D. Jordan Lloyd, in Colloid Chemistry, ed. J. Alexander, The Chemical Catalog Co, New York, **1926**, vol. 1, pp. 767–782.
[126] Flory, P. J., Introductory lecture. *Faraday Discussions of the Chemical Society* **1974,** *57* (0), 7-18.
[127] Estroff, L. A.; Hamilton, A. D., Water Gelation by Small Organic Molecules. *Chemical Reviews* **2004,** *104* (3), 1201-1218.
[128] Sangeetha, N. M.; Maitra, U., Supramolecular gels: Functions and uses. *Chemical Society Reviews* **2005,** *34* (10), 821-836.
[129] Tomasini, C.; Castellucci, N., Peptides and peptidomimetics that behave as low molecular weight gelators. *Chemical Society Reviews* **2013,** *42* (1), 156-172.
[130] Yu, G.; Yan, X.; Han, C.; Huang, F., Characterization of supramolecular gels. *Chemical Society Reviews* **2013,** *42* (16), 6697-6722.

macromolecular compounds can either results from chemical cross-linking or physical interactions. When the gels are formed by strong chemical bonds, they cannot be redissolved and are thermally irreversible, whereas gels formed by weak noncovalent interactions (physical entanglements) are reversible. Gels derived from low molecular weight compounds are supramolecular in the strictest sense in that they are formed through self-aggregation of the small gelator molecules to form entangled Self-Assembled Fibrillar Networks through a combination of non-covalent interactions like H-bonding, π–π stacking, donor–acceptor interactions, metal coordination, solvophobic forces (hydrophobic forces for gels in water) and van der Waals interactions. Since these networks involve weak interactions, they can be readily transformed to a fluid (sol) by heating and are generally thermally reversible.

Based on medium the hydrogel is define as a gel made of a LMWG and water, instead, organogel as a gel made in any kind of organic solvent. Xerogel is a solid formed after evaporation of the solvent in a hydrogel or an organogel by drying with unhindered shrinkage. Xerogels usually retain high porosity (15–50%) and enormous surface area (150–900 m^2/g), along with very small pore size (1–10 nm), conversely aerogel is a solid formed when solvent removal occurs under supercritical conditions; the network does not shrink and a highly porous, low-density material is produced. Aerogels are materials with exceptional properties including very low density, high specific surface areas, and excellent thermal insulation properties.

Gels prepared with a low molecular weight compound are usually obtained by heating of ultrasound irradiation of the gelator in an appropriate solvent followed by cooling the resulting isotropic supersaturated solution to room temperature. When the hot solution is cooled, the molecules start to condense and three situations are possible (Figure 61):

1) a highly ordered aggregation giving rise to crystals i.e., crystallization
2) a random aggregation resulting in an amorphous precipitate or
3) an aggregation process intermediate between these two, yielding a gel.

The process of gelation involves self-association of the gelator molecules to form long, polymer-like fibrous aggregates, which get entangled during the aggregation process forming a matrix that traps the solvent mainly by surface tension. This process prevents the flow of solvent under gravity and the mass appears like a solid.

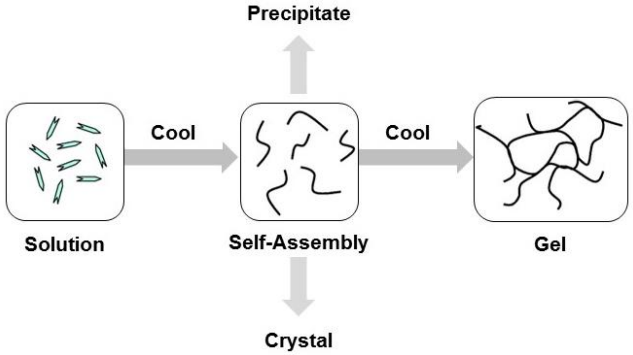

Figure 61. Schematic representation of mechanism of gelation.

3.3.1. Fmoc-Based Low Molecular Weight Gelator

Several authors reported dipeptides that are good gelators, when they contain an aromatic protecting group, such as fluorenyl-9-methoxycarbonyl. Indeed the self-assembly of Fmoc–dipeptides is driven by hydrogen bonding and π–π interactions, between π electrons in the aromatic fluorenyl rings. Fmoc-FF (Figure 62) is an important low molecular weight hydrogelator.

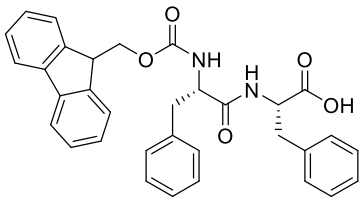

Fmoc-L-Phe-L-Phe-OH
Fmoc-FF

Figure 62. Molecular structure of Fmoc-FF.

Gazit and co-workers [131] discovered that the dissolution of Fmoc-Phe-Phe in aqueous solution resulted in the formation of a rigid material with macroscopic characteristics of a gel. Although the hydrogel contained less than 1% peptide material, it kept its 3D spacious volume exceptionally well. This self-assembled gel was stable across a broad range of temperatures, over a wide pH range. Gelation can be induced by either lowering the pH of an aqueous solution of Fmoc-Phe-Phe or by the addition of water to a solution of Fmoc-Phe-Phe in a solvent such as DMSO. Ulijn and co-worker [132] studied the influence of pH in the hydrogel formation. In fact, the self-assembly of Fmoc-FF occurs during the apparent pK_{a1} transition. When the Fmoc-FF$^-$ molecules are neutralized, they self-assemble to form supramolecular structures, which maintains the sample's pH constant. If the pH decrease under the apparent pK_{a2}, a precipitate is formed (Figure 63).

[131] Mahler, A.; Reches, M.; Rechter, M.; Cohen, S.; Gazit, E., Rigid, Self-Assembled Hydrogel Composed of a Modified Aromatic Dipeptide. *Advanced Materials* **2006,** *18* (11), 1365-1370.
[132] Tang, C.; Smith, A. M.; Collins, R. F.; Ulijn, R. V.; Saiani, A., Fmoc-Diphenylalanine Self-Assembly Mechanism Induces Apparent pKa Shifts. *Langmuir* **2009,** *25* (16), 9447-9453.

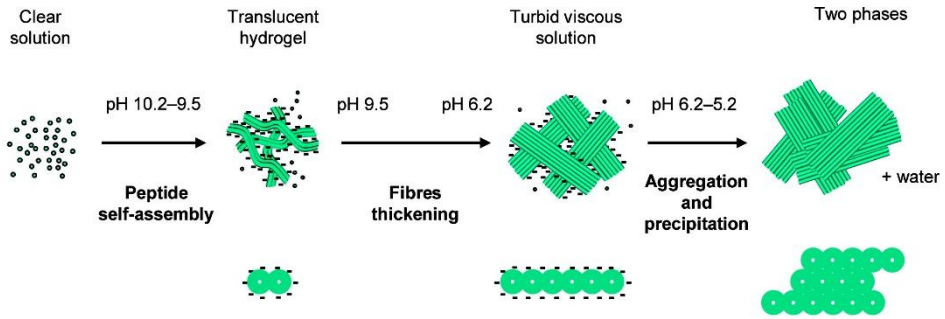

Figure 63. The self-assembly mechanism of Fmoc-FF from high to low pH.

3.3.2. Synthesis of New Gelators

The continue search of new compounds that are able to gelate solvents is a hot topic in research. We have analyzed and compared the effect of the substituents modification of the L-Phe-D-Oxd core and its replacement with the isosteric L-Phe-pGlu core, by preparing a small library of thirteen compounds shown in Figure 64. In particular, we are interested in the preparation of hydrogelators able to form reversible gels containing the phosphate buffered saline, that is a buffer solution commonly used in biological research. In biomedicine, there is significant interest in exploiting self-assembly to construct mimics of the ECM for cell-culture applications [133].

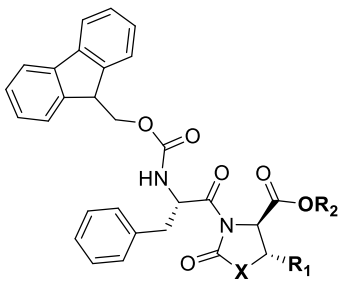

X=O, $\mathbf{R_1}$=CH_3, $\mathbf{R_2}$=Bn, H
X=CH_2, $\mathbf{R_1}$=H, $\mathbf{R_2}$=Bn, H

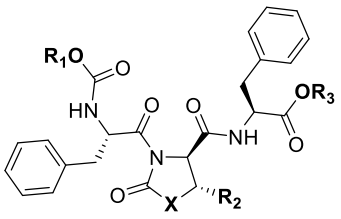

$\mathbf{R_1}$=9-Fluorenylmethyl, **X**=O, $\mathbf{R_2}$=CH_3, $\mathbf{R_3}$=Bn, H
$\mathbf{R_1}$=*tert*-Buthyl, **X**=O, $\mathbf{R_2}$=CH_3, $\mathbf{R_3}$=Bn, H
$\mathbf{R_1}$=Benzyl, **X**=O, $\mathbf{R_2}$=CH_3, $\mathbf{R_3}$=Bn
$\mathbf{R_1}$=9-Fluorenylmethyl, **X**=CH_2, $\mathbf{R_2}$=H, $\mathbf{R_3}$=Bn, H

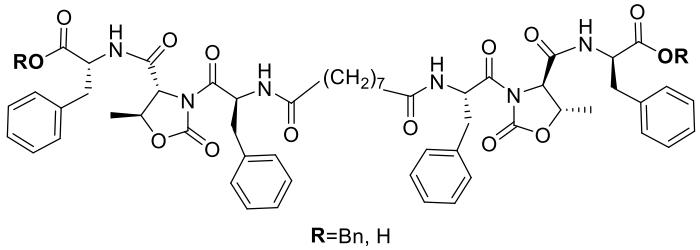

R=Bn, H

Figure 64. Small library of investigated compound.

[133] Milli, L.; Castellucci, N.; Tomasini, C., Turning Around the L-Phe-D-Oxd Moiety for a Versatile Low-Molecular-Weight Gelator. *European Journal of Organic Chemistry* **2014,** *2014* (27), 5954-5961.

Compounds **37a-41a** were selected randomly (Scheme 9), introducing the most common protective groups, azelaic acid and an additional L-Phe moiety. They were prepared by standard coupling reactions and all contain a benzyl ester, as aromatic rings generally favour compounds gelation properties. Four additional candidates were prepared by hydrogenolysis of **37a**, **38a**, **39a** and **41a**. The synthetic details are listed in Scheme 9.

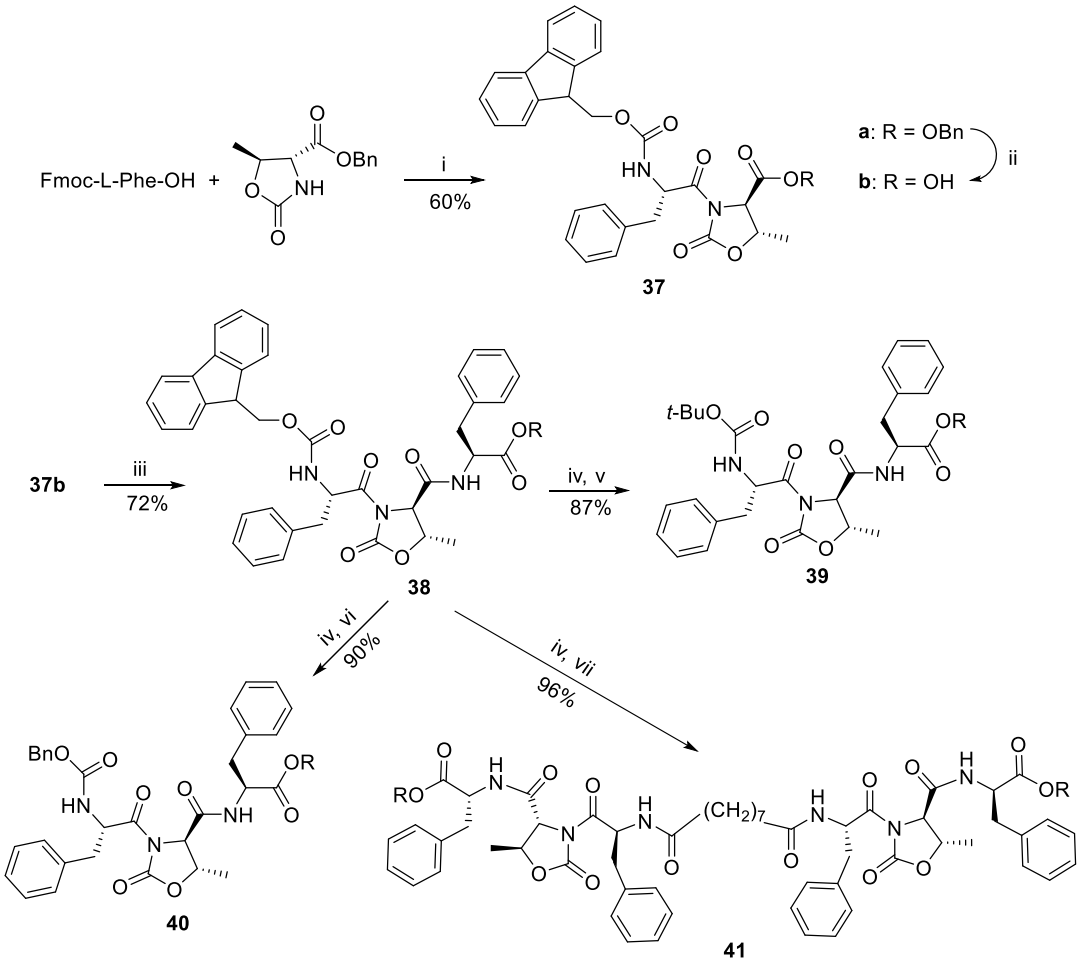

Scheme 9. Reagents and Conditions: (i) HBTU (1.1 equiv.), TEA (2.0 equiv.), dry acetonitrile, r.t., 50 min; (ii) H_2, Pd/C (10% w/w), MeOH, r.t., 4 h; (iii) HCl.H_2N-L-Phe-OBn (1.0 equiv.), HBTU (1.1 equiv.), TEA (3.0 equiv.), dry acetonitrile, r.t., 50 min; (iv) pyperidine 20%v/v in DCM, r.t., 30 min; (v) Boc_2O (1.0 equiv.), NaOH 1 M (1.1 equiv.), t-BuOH, r.t., 16 h; (vi) CbzCl (1.1 equiv.), NaOH 3M (1.1 equiv.), acetone, 0 °C, 3 h; (vii) azelaic acid (0.5 equiv.), HBTU (1.1 equiv.), TEA (2.0 equiv.), dry acetonitrile, r.t., 50 min.

To further extend our library to possible efficient gelators, the Oxd moiety has been replaced with the pyroglutamic moiety. This choice was due to the similar conformational behavior of the two groups. In Scheme 10, the synthesis of the esters **42-43a** and the corresponding acids **42-43b** is described.

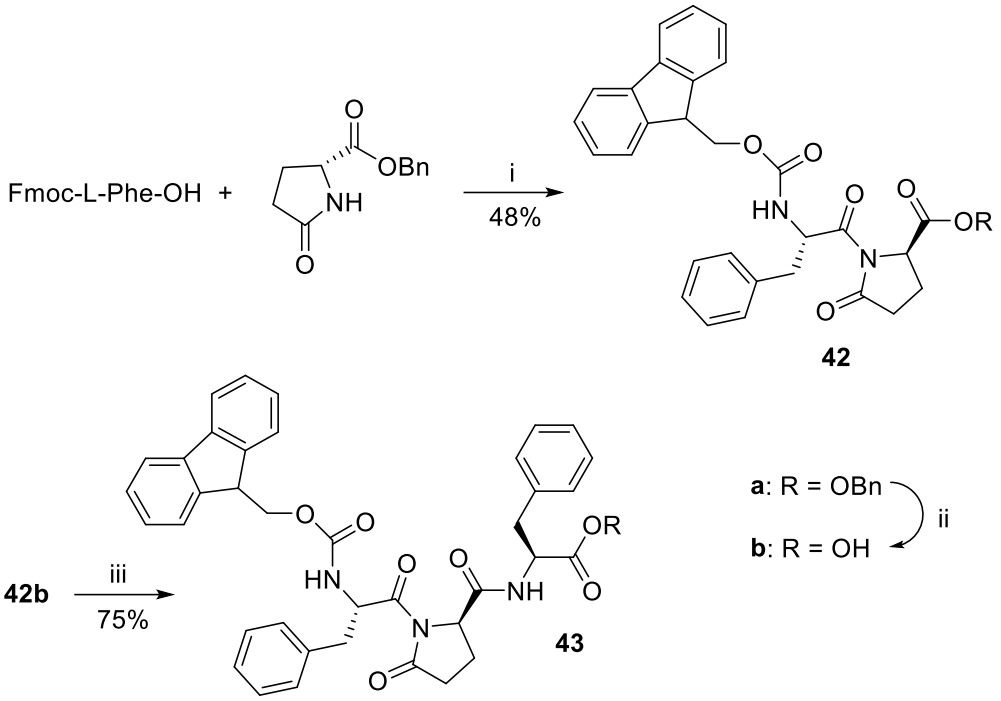

Scheme 10. Reagents and Conditions: (i) HBTU (1.1 equiv.), DBU (2.5 equiv.), dry acetonitrile, r.t., 50 min; (ii) H_2, Pd/C (10% w/w) MeOH, r.t., 4 h; (iii) HCl.H_2N-L-Phe-OBn (1.0 equiv.), HBTU (1.1 equiv.), TEA (3.0 equiv.), dry acetonitrile, r.t., 50 min.

3.3.3. Gelation Studies

The propensity of compounds **37a-43a** to form organogels was checked with a variety of organic solvents and solvent mixtures. The general method adopted to form gels was to place one compound in a small test tube (8 mm in diameter) and dissolve it in a suitable solvent. Sonication (15 minutes, 305 W) was used to speed dissolution, by breaking intermolecular interactions, then the tubes were left stand still overnight. The most common diagnostic test of gelation is tube inversion [134]. In this test, a sample tube containing the mixture of compound and solvent was inverted to ascertain if the sample would flow under its own weight. A gel was assumed to be a sample that had a yield stress that prevented it from flowing down the tube. A sol was taken to be a sample that flowed down the tube. When a partial gel is formed, the compound sticks on the test tube bottom, while little solvent (<20%) flows down.

The results of gelation tests of compound **37a-43a** are reported in Table 15, together with the gels melting points (Tgel).

[134] Takahashi, A.; Sakai, M.; Kato, T., Melting Temperature of Thermally Reversible Gel. VI. Effect of Branching on the Sol-Gel Transition of Polyethylene Gels. *Polym J* **1980,** *12* (5), 335-341.

Table 15. Gelation properties of compounds **37a-43a** in selected solvents (10 mM concentration). The gels melting points (Tgel) are reported in brackets.

Solvent	37a (Tgel)	38a (Tgel)	39a (Tgel)	40a (Tgel)	41a (Tgel)	42a (Tgel)	43a (Tgel)
EtOAc/cHex 1:1	S	S	S	P	P	S	P
EtOAc/DCM 1:1	S	S	S	S	P	S	P
EtOAc	S	S	S	P	P	S	P
DCM	S	S	S	S	P	S	S
MeCN	S	P	S	S	G (82°C)[a]	S	P
DCM/EtOH 1:1	S	S	S	S	P	S	P
Toluene	S	S	G (50°C)[b]	P	P	S	S
Toluene/DCM 1:1	S	S	S	P	P	S	P
Toluene/EtOH 1:1	S	S	S	P	P	S	P
TFE (500µL)	S	S	S	P	P	S	P
MTBE	P	S	G (56°C)[a]	P	P	S	P
EtOH	P	S	G (40°C)[b]	P	P	P	P
$CHCl_3$	S	S	S	S	PG	S	S

G = gel; PG = partial gel; S = solution; P = precipitate; (a) solvent evaporation; (b) thermoreversible gel.

The best outcomes were obtained with compounds **39a** and **41a** which do not contain any aromatic protective group at the nitrogen. In particular, **41a** forms a strong gel with acetonitrile. This gel is so stable that it reaches the solvent boiling point (82 °C) without melting. Compound **39a** forms stable thermoreversible gels with toluene and ethanol, while the gel formed with methyl *t*-butyl ether reaches the solvent boiling point (56 °C) without melting (Figure 65).

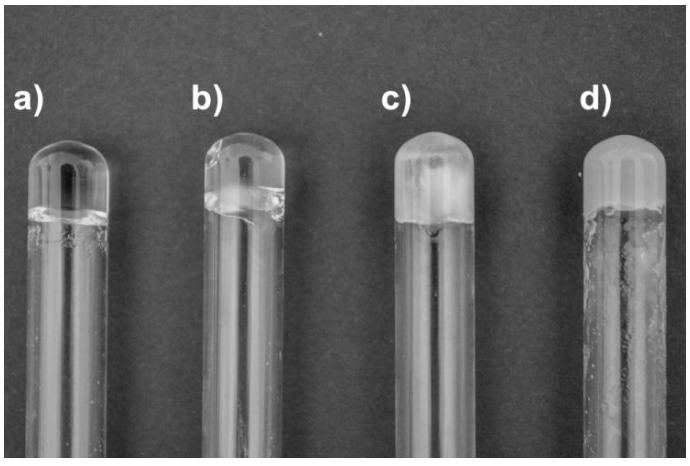

Figure 65. Photographs of organogels reported in Table 1: (a) **39a** in toluene; (b) **39a** in MTBE; (c) **39a** in EtOH; (d) **41a** in CH_3CN. All the organogels have been obtained after sonication (15 minutes, 305 W), then the tubes were left stand still overnight.

Then compounds **37b-43b** were tested as hydrogelators of ethanol, methanol, water and some mixtures of these solvents in 10 mM concentration. The results are shown in Table 16, together with the gels melting points (Tgel).

Table 16. Gelation properties of compounds **37b-43b** in selected solvents (10 mM concentration). The gels melting points (Tgel) are reported in brackets.

Solvent	37b (Tgel)	38b (Tgel)	39b (Tgel)	41b (Tgel)	42b (Tgel)	43b (Tgel)
EtOH	PG	S	S	PG	P	P
H_2O/EtOH 3:7	S	S	S	G (79°C)[a]	S	P
H_2O/EtOH 1:1	S	S	S	PG	PG	P
H_2O/EtOH 7:3	P	PG	S	PG	G (58°C)[b]	P
H_2O/EtOH 9:1	P	P	S	P	G (66°C)[c]	P
MeOH	P	P	S	PG	PG	P
H_2O/MeOH 3:7	P	PG	S	PG	PG	P
H_2O/MeOH 1:1	S	PG	S	PG	G (60°C)[b]	P
H_2O/MeOH 7:3	PG	P	S	P	G (76°C)[b]	P
H_2O/MeOH 9:1	P	P	S	P	G (82°C)[c]	P
H_2O	P	P	P	P	P	P

G = gel; PG = partial gel; S = solution; P = precipitate; (a) solvent evaporation; (b) thermoreversible gel; (c) not thermoreversible gel

The best gelators are **41b**, which efficiently gelates only the H_2O/EtOH 3:7 mixture, and **42b**, that is more versatile (Figure 66a-c), as it forms thermoreversible gels with a wide variety of ethanol/water and methanol/water mixtures.

We also tested if **42b** can gelate the phosphate buffered saline (PBS), that is a buffer solution commonly used in biological research. It is a water-based salt solution containing sodium hydrogen phosphate, sodium chloride, potassium chloride and potassium dihydrogen phosphate. The osmolarity and ion concentrations of the solutions match those of the human body (isotonic). In Table 17, the results for the gelation of PBS (1X) in the presence of various concentration of **42b** are shown.

Table 17. Gelation properties of various concentration of **42b** in PBS (1X).

Concentration (mM)	Concentration (w/w) %	Outcome	Tgel (°C)
10	0.5	Gel	25
20	1.0	Gel	25
30	1.5	Gel	58[a]
40	2.0	Gel	100[b]

(a) thermoreversible gel; (b) solvent evaporation.

A gel is formed at any concentration, and a strong and thermoreversible gel is formed with 30 mM concentration (1.5% w/w) (Figure 66d-e). This interesting result indicates that **42b** is an

excellent candidate for the preparation of novel materials that may be used for drug release, biological assays and tissue engeneering [135].

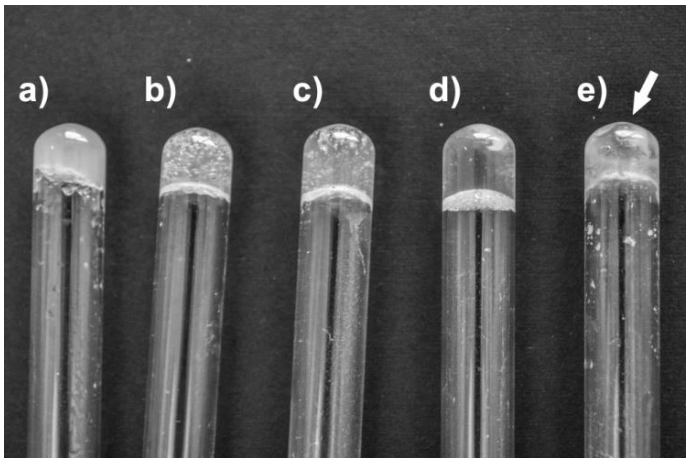

Figure 66. Photographs of selected hydrogels reported in Tables 2 and 3: (a) **41b** in H_2O/EtOH 3:7; (b) **42b** in H_2O/EtOH 7:3; (c) **42b** in H_2O/EtOH 9:1; (d) **42b** (1.5% w/w) in PBS 1X; (e) **42b** (1.5% w/w) in PBS 1X after melting and cooling (the arrow indicated the dropped ball trapped in the gel). The hydrogels have been obtained after sonication (15 minutes, 305 W), then the tubes were left stand still overnight.

3.3.4. Studies on the Relationship between Molecular Structure and Gelation Behaviour

The results shown in Table 15, 16 and 17 suggest that the correlation between gelation behaviour and molecular structure is not straightforward. While both bolamphiphilic **41a** and **41b** gelate selected solvents, as we could foresee by our previous results, the best hydrogelator Fmoc-L-Phe-D-pGlu-OH **42b** is totally different from the best organogelator Boc-L-Phe-D-Oxd-L-Phe-OBn **39a**.

To rationalize the gelation behaviour of **37a-43a**, we checked their conformational preferences by comparing their IR and ^{1}H NMR spectra. Selected signals are reported in Table 18.

[135] Yang, Z.; Liang, G.; Ma, M.; Gao, Y.; Xu, B., In Vitro and In Vivo Enzymatic Formation of Supramolecular Hydrogels Based on Self-Assembled Nanofibers of a β-Amino Acid Derivative. *Small* **2007,** *3* (4), 558-562.

Table 18. Selected ^{1}H NMR and IR signals of compounds **37a-43a**. The ^{1}H NMR spectra have been recorded on 3 mM solutions in $CDCl_3$ and the IR spectra have been recorded on 3 mM solutions in dichloromethane.

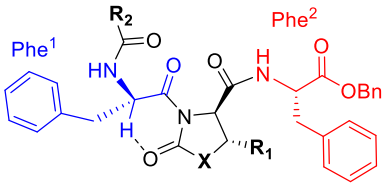

Oxd: X = O; $\mathbf{R_1}$ = CH_3
pGlu: X = CH_2; $\mathbf{R_1}$ = H
$\mathbf{R_2}$ = Fmoc, Boc, Cbz, azelaic acid

Compound	^{1}H NMR (ppm)				IR (cm^{-1})	
	CHα-Phe^1	NH-Phe^1	CHα-Phe^2	NH-Phe^2	NH stretching band	
37a	5.90	5.41	-	-	3428	-
38a	5.65	5.41	4.76	7.20	3419	3351 (weak)
39a	5.59	5.04	4.75	7.14	3432	3350 (weak)
40a	5.70	5.28	4.77	7.22	3427	3351 (weak)
41a	5.66	5.97	4.72	7.65	3435 (weak)	3325
42a	5.88	5.47	-	-	3429	-
43a	5.78	5.45	4.77	6.69	3421	-

The results shown in Table 18 could not help us to have a deeper understanding of the correlation between molecular structure and gelation propensities of compounds **37a-43a**. The very deshielded ^{1}H NMR signal of CHα-Phe1 indicates that in all the compounds a C-H•••O = C hydrogen bond with the endocyclic C = O is formed.

Moreover **41a** contains a N-H•••O = C hydrogen bond, as suggested by the strong stretching band at 3325 cm^{-1}, together with a very deshielded signal of NH-Phe^2 at 7.65 ppm. In contrast, the spectra of **39a** do not suggest that a stable N-H•••O = C hydrogen bond is formed, owing to the weak 3350 cm^{-1} stretching band and to the poorly deshielded signal of NH-Phe^2 at 7.14 ppm. All the spectra of the other compounds show similar signals. ROESY experiments performed on these compounds do not display any interesting cross peak. The analysis of the IR and ^{1}H NMR spectra of acids **37b-43b** do not furnish any more useful result.

As the analysis of gelators preferential conformation does not help, a possible rationalization of these outcomes takes into consideration the hydrophobicity of the molecules expressed in LogP (octanol/water partition coefficient), that is calculated as a sum of fragment-based contributions and correction factors. This method is very robust and is able to process practically all organic, and most organometallic molecules. Table 19 shows the estimated hydrophobicity for compounds **37-43**.

Table 19. Estimated hydrophobicity of compounds **37-43**.

Compound	Log *P*[a]	Compound	Log *P*[a]
37a	7.756	**37a**	4.089
38a	8.503	**38a**	4.986
39a	6.489	**39a**	2.822
40a	6.899	**-**	-
41a	8.535	**41a**	1.372
42a	7.406	**42a**	**3.738**
43a	8.265	**43a**	4.636

(a) Predicted hydrofobicities calculated using an online prediction program[136].

Among compounds **37a-43a**, **39a** has the smaller value, thus it is the less hydrophobic compound among the tested ones. This property reduces its solubility in organic solvents and favours gel formation, as the kinetics of assembly are known to have an effect on the properties of the gels prepared with LMWG. Gels formed from **39a** are obtained after self assembly into fibrils that are clearly visible on SEM analysis of the xerogels (Figure 67).

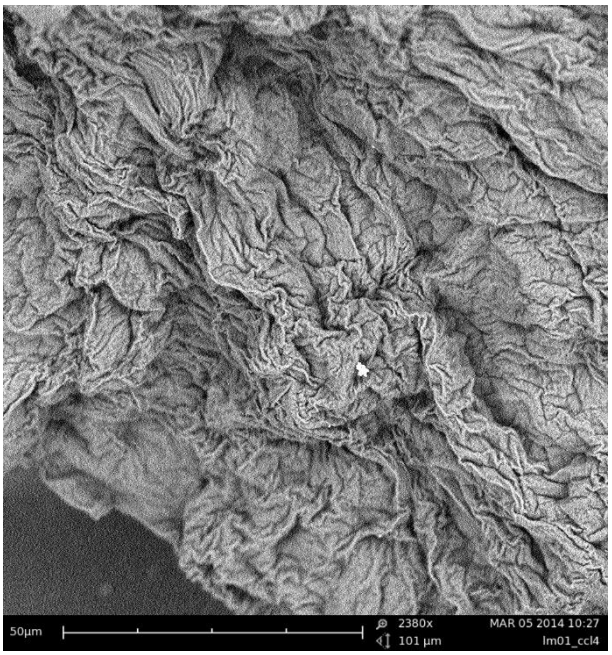

Figure 67. SEM image of Xerogel obtained from **39a**.

The Log *P* value of **43b** is between 3 and 4, that indicates a moderate hydrophobicity, as at the low end (log *P* < 2.6) syneresis occurs. Thus both for organogels and for hydrogels, an intermediate value of log *P* (about 6.5 for organogels and 3.5 for hydrogels) is a good starting point for the design of new LMWG. Compounds **41a** and **41b** are bolamphiphilic pseudopeptides and have extreme Log *P* values, as **41a** is very hydrophobic, while **41b** is very hydrophilic. They are both able to form gels only in selected conditions, suggesting that

[136] http://www.molinspiration.com

for these family of molecules the self-aggregation process proceeds in a different way, that is not fully described by Log *P* values [137].

3.3.5. Synthesis of Fmoc-Gelators

In literature many examples of Fmoc-FF and their modification as hydrogelators have been reported [137,138]. As we described that the Fmoc-L-Phe-D-pGlu-OH is a good gelator for mixtures of water and alcohol or for a PBS solution, we have then prepared four new gelators containing Oxd or pGlu and tyrosine or tryptophan as aromatic units (Figure 68) [139].

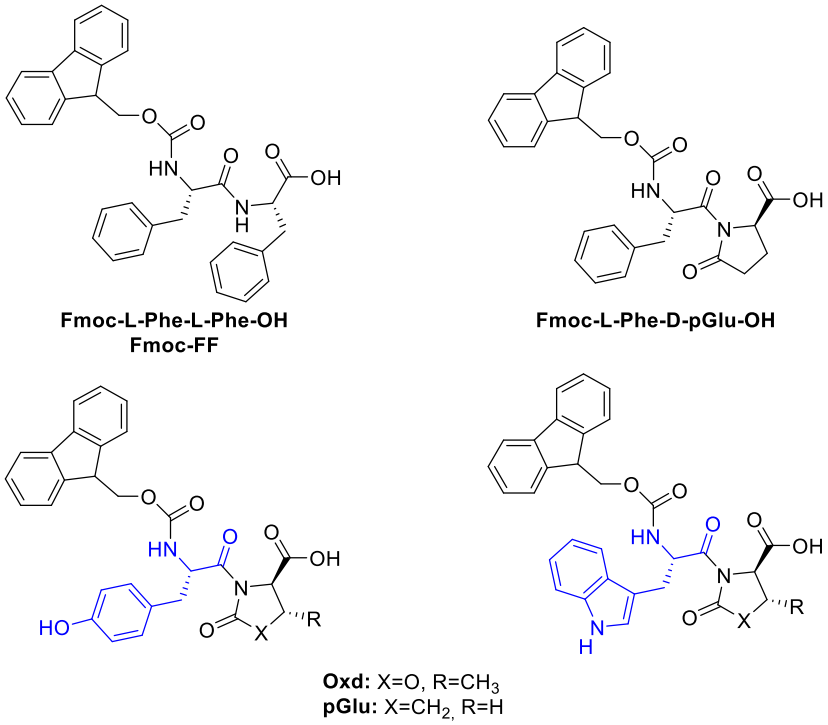

Figure 68. Chemical structures of the compounds described in this work.

Compound **45**, **47**, **49** and **51** were prepared by standard coupling reactions between Fmoc-Tyr(t-Bu) or Fmoc-Trp with Oxd or pGlu units (**44**, **46**, **48** and **50**). The benzyl protective groups have been removed by hydrogenolysis, but the compounds **45** and **47** required also the removal of the tyrosine-Boc protecting group by reaction with trifluoroacetic acid in dichloromethane (Scheme 11). The simplicity in the preparation of these compounds is therefore an important point in favour of these new kind of gelators.

[137] Adams, D. J.; Mullen, L. M.; Berta, M.; Chen, L.; Frith, W. J., Relationship between molecular structure, gelation behaviour and gel properties of Fmoc-dipeptides. *Soft Matter* **2010,** *6* (9), 1971-1980.
[138] Raeburn, J.; Zamith Cardoso, A.; Adams, D. J., The importance of the self-assembly process to control mechanical properties of low molecular weight hydrogels. *Chemical Society Reviews* **2013,** *42* (12), 5143-5156.
[139] Zanna, N.; Merlettini, A.; Tatulli, G.; Milli, L.; Focarete, M. L.; Tomasini, C., Hydrogelation Induced by Fmoc-Protected Peptidomimetics. *Langmuir* **2015,** *31* (44), 12240-12250.

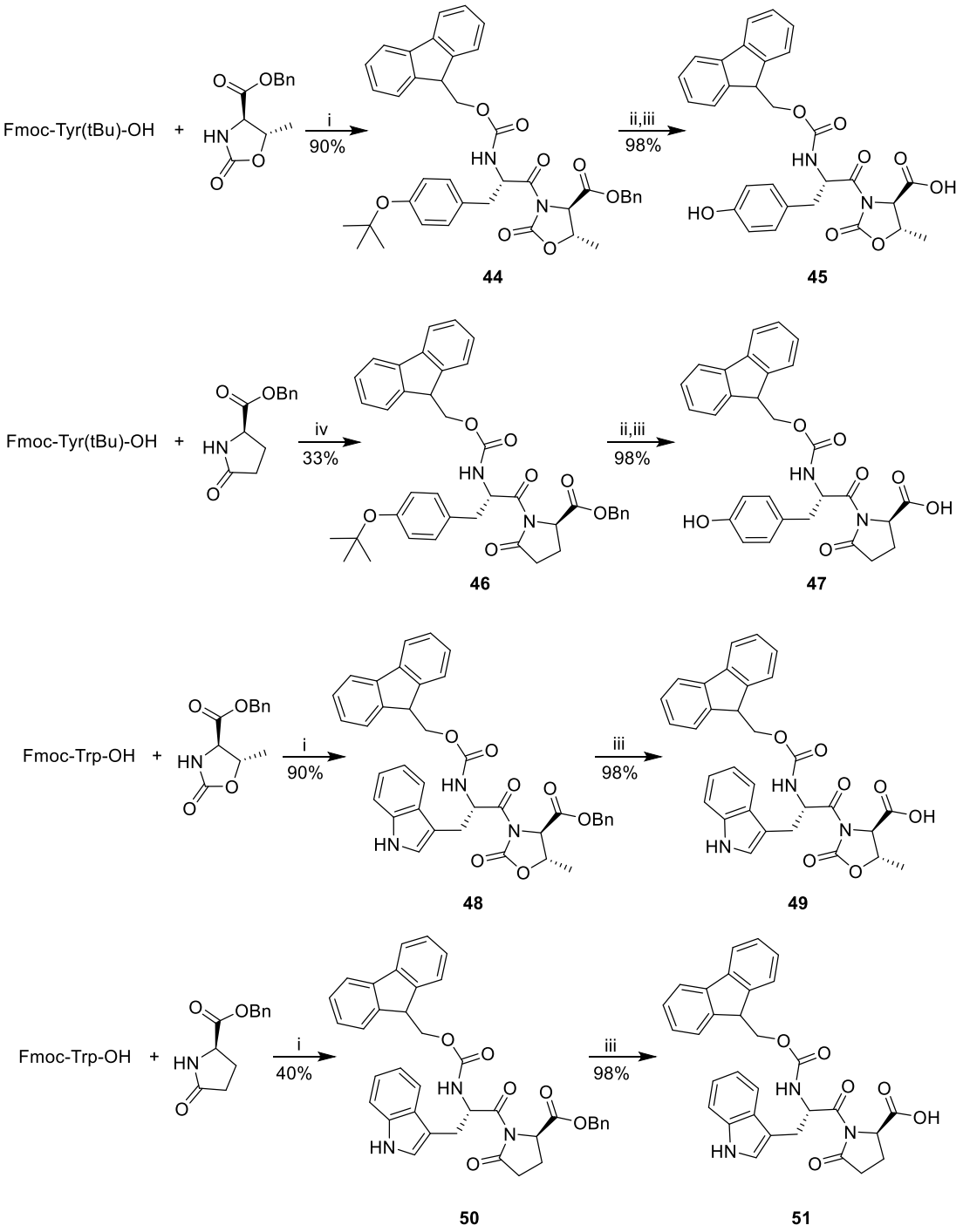

Scheme 11. Reagents and Conditions: (i) HATU (1.1 equiv.), DIEA (2.5 equiv.), dry acetonitrile, r.t., 2h; (ii) TFA (18 equiv.), dry DCM, r.t., 4h; (iii) H_2 (1atm), Pd/C (10%$_{w/w}$), MeOH, r.t., 4h; (iv) HBTU (1.1 equiv.), DBU (2.2 equiv.), dry acetonitrile, r.t., 2h.

We previously demonstrated that for this class of peptidomimetics, good LMWGs have a log *P* ranging between 3.5 and 3.8. To check if these peptidomimetics are good candidates to promote hydrogelation, we calculated their log *P* values and we measured their apparent pK_a values (Table 20) to try to rationalize this outcome. Moreover we have measured the pK_a values of unprotected D-Oxd and D-pGlu.

Table 20. Calculated log P values and measured pK_a values of compounds **45**, **47**, **49** and **51** (1% w/w).

Molecule		pKa	Log P
Fmoc-L-Tyr-D-Oxd-OH	**45**	5.4	3.61
Fmoc-L-Tyr-D-pGlu-OH	**47**	4.9	3.26
Fmoc-L-Trp-D-Oxd-OH	**49**	6.9	4.24
Fmoc-L-Trp-D-pGlu-OH	**51**	6.0	3.89

At a first glance, the best LMWG appears to be Fmoc-L-Tyr-D-Oxd-OH **45**, as its log *P* perfectly fits within the 3.5-3.8 range, while **47**, **49** and **51** have slightly smaller or slightly bigger log *P* values. We measured also their apparent pK_a: in Figure 69a-d we reported the titration curve of 1% w/w of **45**, **47**, **49** and **51**. The pK_a values appear to be higher than what expected for a C-terminus peptide, if compared to the pK_a values of free D-Oxd and D-pGlu (pK_a = 2.2 and 2.9 respectively, see Figures 69e and 2f), as it has been already observed for other small peptides. During the back titration, we could notice that the molecules tend to precipitate, so the pH of the solution is no more HA concentration dependent since, after reaching the gelator maximum concentration in solution given by its solubility, it remains constant for all the titration, hence reaching the same concentration of $[A^-]$ and [HA] at higher pH values.

As the pK_a shift is probably due to the high hydrophobicity and hence poor solubility of our gelators, this effect can explain the perfect correlation that we obtained between pK_a and log *P* (Figure 70): higher hydrophobicity means both lower water solubility and higher pK_a. To further confirm this outcome, we have measured the pK_a values of Fmoc-L-Tyr-D-Oxd-OH **45** in three different concentrations (Table 21, Figures 69a, 69g and 69h). We can observe that on lowering the gelator concentration, the pK_a decreases. Ideally, if we could carry out the pK_a measure at a gelator concentration under the limit of its solubility, we will probably obtain the exact pK_a of our gelators. Moreover in Figure 70 we reported a correlation between pK_a and calculated log *P*, showing an apparent linear relationship.

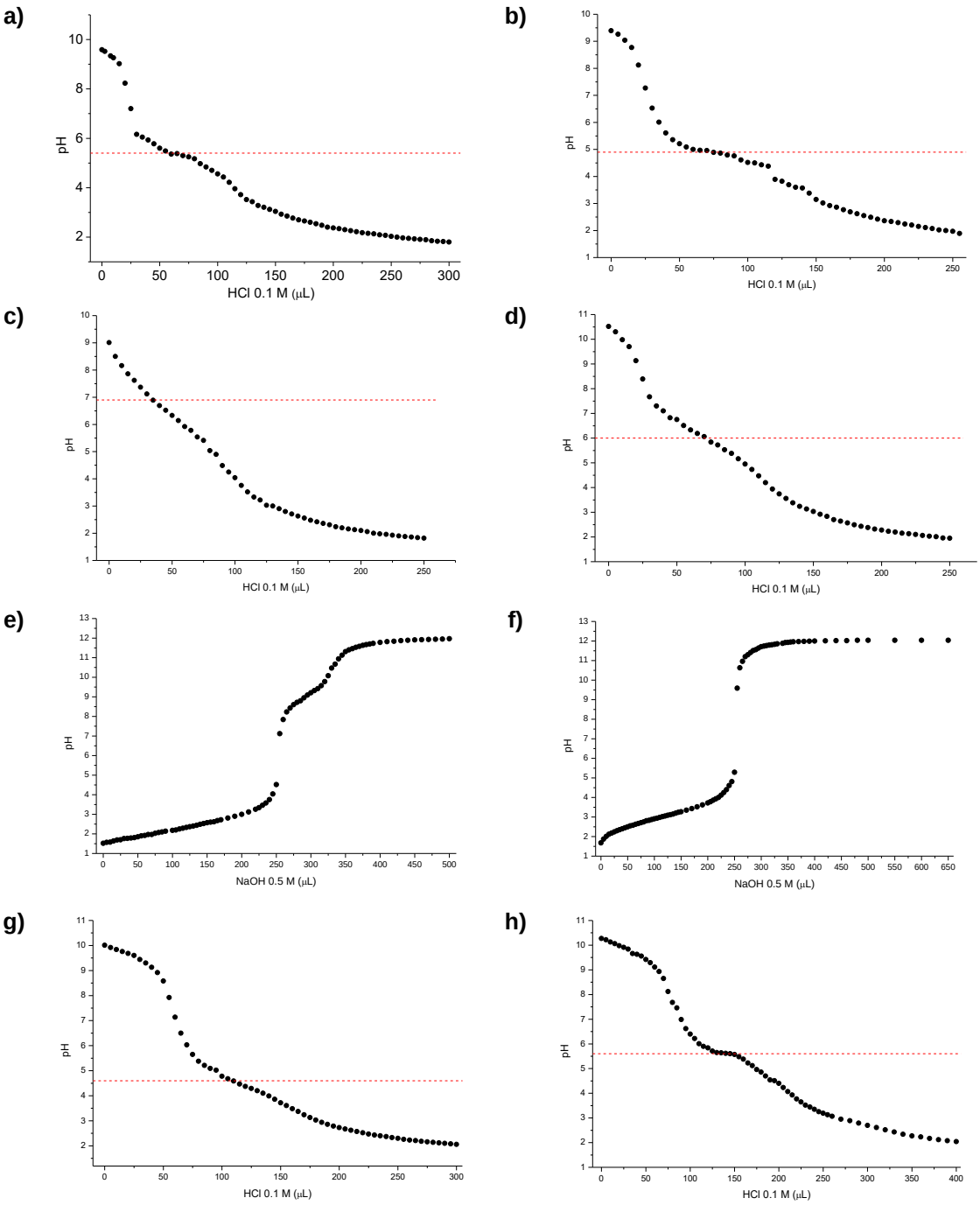

Figure 69. (a) Titration curve (µL of 0.1M HCl added versus pH) of Fmoc-L-Tyr-D-Oxd-OH **45** (1.0% w/w); (b) Titration curve (µL of 0.1M HCl added versus pH) of Fmoc-L-Tyr-D-pGlu-OH **47** (1.0% w/w); (c) Titration curve (µL of 0.1M HCl added versus pH) of Fmoc-L-Trp-D-Oxd-OH **49** (1.0% w/w; (d) Titration curve (µL of 0.1M HCl added versus pH) of Fmoc-L-Trp-D-pGlu-OH **51** (1.0% w/w); (e) Titration curve (µL of 0.1M HCl added versus pH) of H-D-Oxd-OH(0.15 mM); (f) Titration curve (µL of 0.1M HCl added versus pH) of H-D-pGlu-OH (0.15 mM); (g) Titration curve (µL of 0.1M HCl added versus pH) of Fmoc-L-Tyr-D-Oxd-OH **45** (0.5% w/w); (h) Titration curve (µL of 0.1M HCl added versus pH) of Fmoc-L-Tyr-D-Oxd-OH **45** (2.0% w/w).

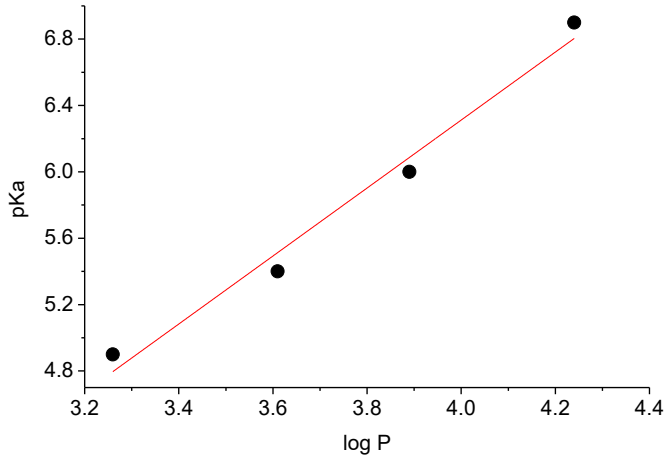

Figure 70. Correlation between calculated log *P* and experimental apparent pK_a for compounds **45**, **47**, **49** and **51** (1.0% w/w).

Table 21. Measured pK_a values of Fmoc-L-Tyr-D-Oxd-OH **45** in three different concentration.

Concentration of 45 (% w/w)	pK_a
0.5	4.6
1.0	5.4
2.0	5.6

3.3.6. Hydrogels Formation

After these preliminary analyses of the properties of the gelators **45**, **47**, **49** and **51**, their tendency to gelate water has been tested employing the general method adopted: the samples together with the liquid were placed in a small test tube. Sonication (15 minutes, 305 W) was used to speed up the dissolution, by breaking intermolecular interactions, then the tubes were left stand still overnight.

Unfortunately, we could never obtain a gel, thus we decided to apply a modified method recently described by Adams et al., where the gelators are dissolved in a basic aqueous solution, then glucono-δ-lactone is added to slowly decrease the solution pH [140]. In fact all compounds **45**, **47**, **49** and **51** are totally soluble at pH ≈ 10, while they are totally insoluble at pH ≈ 3, as reported above. If the pH slowly decreases, the pK_a value is reached and the molecules get organized into fibers that in turn trap the water molecules, yielding a hydrogel [141]. To check the gelation efficiency of our molecules, we have submitted to this test also the well described Fmoc-FF as a comparison.

We also tested the gelation behavior of **45**, **47**, **49** and **51** by decreasing the solution pH value with HCl 1M instead of GdL. Under these conditions, the gelation process occurs

[140] Adams, D. J.; Butler, M. F.; Frith, W. J.; Kirkland, M.; Mullen, L.; Sanderson, P., A new method for maintaining homogeneity during liquid-hydrogel transitions using low molecular weight hydrogelators. *Soft Matter* **2009,** *5* (9), 1856-1862.

[141] Frisch, H.; Besenius, P., pH-Switchable Self-Assembled Materials. *Macromolecular Rapid Communications* **2015,** *36* (4), 346-363.

instantaneously, producing a non-homogeneous gel, with white particulate suspended in the gel. This outcome is not surprising, because we noticed that, on gelator titration with HCl, the pH rapidly decreases from pH ≈ 10 and the stirred solution becomes progressively cloudy until pH ≈ 6. On further addition of HCl, the solution becomes more viscous and a white precipitate or a hydrogel forms, depending on the pH variation rate. The GdL pH variation method, thanks to the slow process of gelation rate-limited by the hydrolysis of GdL, allows the gelator to self-assembly, yielding homogeneous hydrogels. The final pH of the hydrogels is about 4.5, which is lower than the values of the measured pK_a of our gelators (Table 1).

The gelation behavior of compounds **45**, **47**, **49** and **51** and of Fmoc-FF has been tested in a concentration ranging between 0.5% to 2.0% w/w. The results are shown in Table 22, together with the gels melting points (Tgel). The Tgel is the temperature at which the ball falls down, but we could observe different behaviors among our samples: hydrogels obtained with Fmoc-L-Tyr-D-Oxd-OH **45** melt and are totally thermoreversible. In contrast, hydrogels obtained with **47**, **49** and **51** are not thermoreversible. In some cases the gelator melts, then precipitate on cooling, while with in other cases a solution is never obtained, as the gelator shrinks, water is ejected and syneresis occurs. Fmoc-FF leads to the formation of opaque hydrogels that are thermoreversible only in concentration ≥ 1% (w/w).

Table 22. Gelation properties of compounds **45**, **47**, **49** and **51** in water as a function of an increasing amount of gelator (expressed in % w/w). The gels melting points (Tgel) are reported in brackets. The gelation properties of Fmoc-FF have been tested in the same conditions for comparison.

Compound		**0.5% w/w** (Tgel, °C)	**1.0% w/w** (Tgel, °C)	**1.5% w/w** (Tgel, °C)	**2.0% w/w** (Tgel, °C)
Fmoc-L-Tyr-D-Oxd-OH	**45**	G [a,d] (55-85)	G [b,d] (58-100)	G [b,d] (59-100)	G [b,d] (66-100)
Fmoc-L-Tyr-D-pGlu-OH	**47**	G [b,e] (47-70)	G [c,e] (53-72)	G [c,e] (57-75)	G [c,e] (62-82)
Fmoc-L-Trp-D-Oxd-OH	**49**	G [a,f] (44-100)	G [b,f] (55-100)	G [c,f] (59-100)	G [c,f] (62-100)
Fmoc-L-Trp-D-pGlu-OH	**51**	PG	G [c,f] (43-100)	G [c,f] (52-100)	G [c,f] (78-100)
Fmoc-FF		G [c,f] (38-100)	G [c,d] (48-100)	G [c,d] (60-100)	G [c,d] (62-100)

G = gel; PG = partial gel. (a) transparent gel; (b) opalescent gel; (c) opaque gel; (d) thermoreversible gel; (e) not thermoreversible gel, the gelator melts then precipitate on cooling; (f) not thermoreversible gel, syneresis occurs on heating.

An interesting correlation may be found between the calculated log *P* of the gelators and the hydrogel behavior. Fmoc-L-Tyr-D-Oxd-OH **45** has a log *P* value (3.61) that nicely falls between 3.5 and 3.8 and forms thermoreversible hydrogels, while Fmoc-L-Tyr-D-pGlu-OH **47** has a lower log *P* value (3.26) and its hydrogels are not thermoreversible, with the formation of a precipitate on cooling. Finally the more hydrophobic **49** (log *P* = 4.24) and **51** (log *P* = 3.89) get organized in stable networks that do not break on melting, the hydrogels are not thermoreversible and syneresis occurs.

3.3.7. Hydrogel Characterization

The most common diagnostic test of gelation is tube inversion [134]. In this test, a sample tube containing the hydrogel is turned upside down to ascertain if the sample would flow under its own weight. A gel is assumed to be a sample that had a yield stress that prevented it from flowing down the tube, while a sol is taken to be a sample that flowed down the tube. When a partial gel is formed, the compound sticks on the test tube bottom, while little solvent (<20%) flows down.

As depicted in Figure 71, the gels formed by compounds **45** and **49** (Figure 71a and 71c) at low gelator concentration are rather transparent. This property can be very useful for applications in the field of 3D cell culture, since most of the cells counting methods consist of spectrophotometric analyses, therefore the optical transparency is an indispensable requirement for reliable measurements [142].

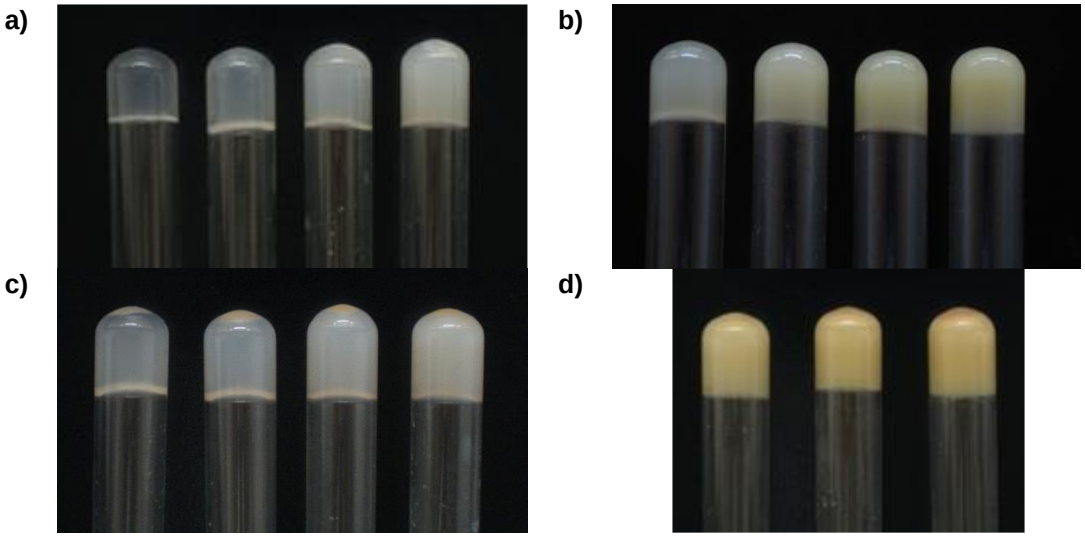

Figure 71. Photographs of hydrogels obtained with compounds **45**, **47**, **49** and **51** in different concentrations in water (% w/w): (A) Fmoc-L-Tyr-D-Oxd-OH **45**, from left to right: 0.5, 1.0, 1.5, 2.0; (B) Fmoc-L-Tyr-D-pGlu-OH **47**, from left to right: 0.5, 1.0, 1.5, 2.0; (C) Fmoc-L-Trp-D-Oxd-OH **49**, from left to right: 0.5, 1.0, 1.5, 2.0; (D) Fmoc-L-Trp-D-pGlu-OH **51**, from left to right: 1.0, 1.5, 2.0.

To quantify the transparency of our samples, spectroscopic techniques were used to study the influence of the gelator on the gel optical properties [143,144]. UV-visible analysis of the most transparent gel samples have been performed by measuring the % transmittance of the

[142] Wang, H.; Yang, Z.; Adams, D. J., Controlling peptidebased hydrogelation. *Materials Today* **2012,** *15* (11), 500-507.

[143] Orbach, R.; Mironi-Harpaz, I.; Adler-Abramovich, L.; Mossou, E.; Mitchell, E. P.; Forsyth, V. T.; Gazit, E.; Seliktar, D., The Rheological and Structural Properties of Fmoc-Peptide-Based Hydrogels: The Effect of Aromatic Molecular Architecture on Self-Assembly and Physical Characteristics. *Langmuir* **2012,** *28* (4), 2015-2022.

[144] Raeburn, J.; Mendoza-Cuenca, C.; Cattoz, B. N.; Little, M. A.; Terry, A. E.; Zamith Cardoso, A.; Griffiths, P. C.; Adams, D. J., The effect of solvent choice on the gelation and final hydrogel properties of Fmoc-diphenylalanine. *Soft Matter* **2015,** *11* (5), 927-935.

samples recorded at a wavelength of 600 nm, with MilliQ water used as reference (T = 100%). A gel sample obtained in the same conditions with Fmoc-FF has been analyzed for comparison (Table 23 and Figure 72). Gels obtained with LMWGs **45** and **49** at 0.5% w/w concentration possess high transparency, as we could measure a transmittance of 25.6% and 32.1% respectively. In contrast, gels obtained with Fmoc-FF showed a low transparency (T = 0.17%).

Table 23. % Transmittance of some selected gel samples obtained with **45**, **49** and Fmoc-FF for comparison.

Gelator		% w/w	T (%)
Fmoc-L-Tyr-D-Oxd-OH	**45**	0.5	25.6 ± 0.3
		1.0	6.0 ± 0.1
Fmoc-L-Trp-D-Oxd-OH	**49**	0.5	32.1 ± 0.2
		1.0	11.8 ± 0.2
Fmoc-FF		0.5	0.17 ± 0.02

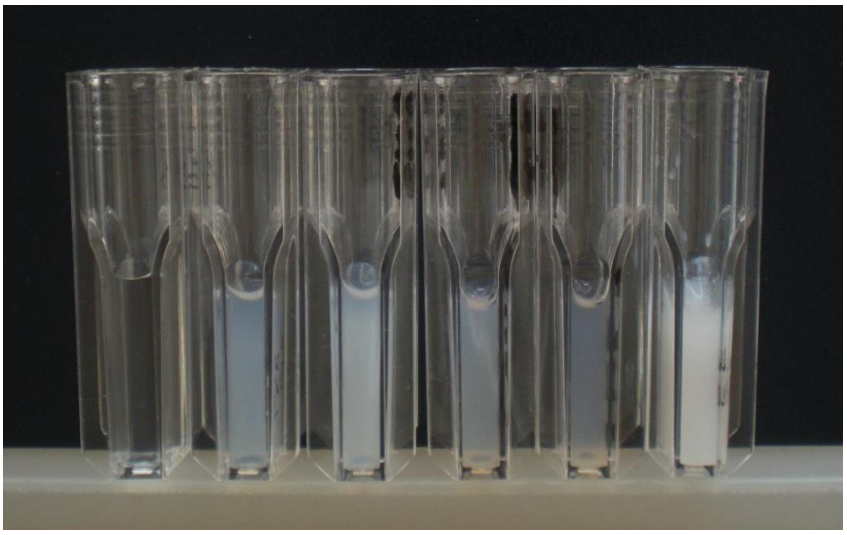

Figure 72. Picture of gels obtained in cuvettes for visible analysis. The analyses were performed on the gel about 20 hours after the gelation begun. From left to right: deionized water, gel obtained with: Fmoc-L-Tyr-D-Oxd-OH **45** (0.5% w/w), Fmoc-L-Tyr-D-Oxd-OH **45** (1.0% w/w), Fmoc-L-Trp-D-Oxd-OH **49** (0.5% w/w), Fmoc-L-Trp-D-Oxd-OH **49** (1.0% w/w), Fmoc-FF (0.5% w/w).

Another interesting piece of information was obtained by recording the ECD spectra of the hydrogels obtained with a 0.5% w/w concentration of **45**, **49** and Fmoc-FF (Figure 73). It should be noted that these measurements were carried out at low concentration, because at higher concentration strong absorption and light scattering arising from the structures forming on gelation precluded good data collection. Nevertheless the system still formed a gel.

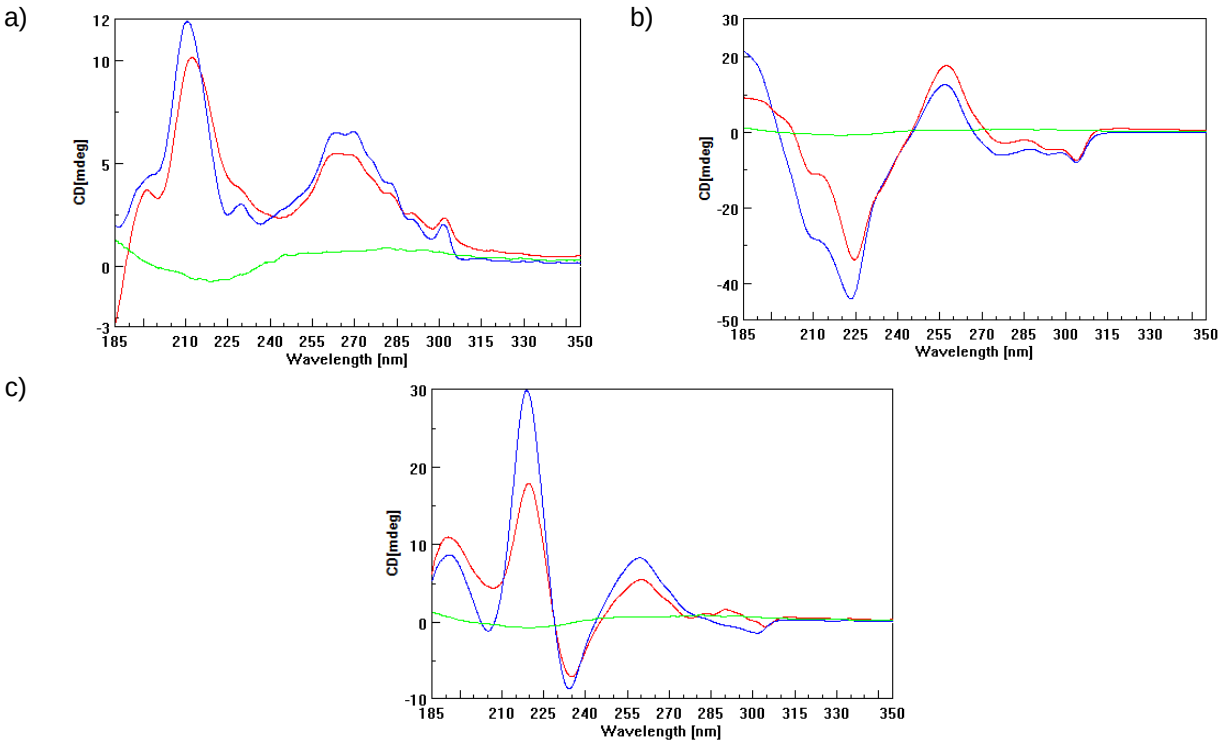

Figure 73. (a) ECD spectra of Fmoc-L-Tyr-D-Oxd-OH **45** in 0.5% w/w concentration in water; (b) ECD spectra of Fmoc-L-Trp-D-Oxd-OH **49** in 0.5% w/w concentration in water; (c) ECD spectra of Fmoc-FF in 0.5% w/w concentration in water. In all the spectra the green line is the ECD of pure GdL, the blu line is the ECD of gelator and GdL before the gelation occurs, the red line is the ECD of the hydrogel.

In all the spectra we can notice that CD signals of the molecules before and after gelation are quite similar, thus showing that the molecules get organized in a preferred conformation that is suitable for the formation of fibers that in turn end up with the gel formation. GdL by itself does not give significant contribution to CD spectrum, however one cannot exclude a contribution to CD spectrum when it is trapped in the gel structure.

The CD signals are quite different from one molecule to the other and are all affected by the broad band due to the aromatic chromophore contributions in region about 210 nm [145].

Our spectrum of Fmoc-FF hydrogel is very similar to the spectrum already reported for this system [146]. The authors attribute the presence of the negative band located at 218 nm to the formation of a β-sheet structure and use as a control sample the ECD spectrum of the non-gelling Fmoc-FF, that shows two positive peaks at 307 nm and below 214 nm.

If we analyze the spectra of **45** and **49**, we can notice that **49** has a spectrum that resembles the Fmoc-FF spectrum, with a minimum at 235 nm and a maximum at 260 nm, even though **49** contains the D-pGlu moiety. In contrast the CD spectrum of **45** is all positive and resemble the Fmoc-FF spectrum, even though it efficiently forms gels. In any case, due to the aromatic

[145] Brahms, S.; Brahms, J., Determination of protein secondary structure in solution by vacuum ultraviolet circular dichroism. *Journal of Molecular Biology* **1980,** *138* (2), 149-178.
[146] Smith, A. M.; Williams, R. J.; Tang, C.; Coppo, P.; Collins, R. F.; Turner, M. L.; Saiani, A.; Ulijn, R. V., Fmoc-Diphenylalanine Self Assembles to a Hydrogel via a Novel Architecture Based on π–π Interlocked β-Sheets. *Advanced Materials* **2008,** *20* (1), 37-41.

contributions and the presence of D and L configuration residues, one cannot easily associate spectral shapes with secondary structures. Noticeable the high wavelength band (about 300 nm) due to the Fmoc group shows opposite sign for Fmoc-L-Tyr-D-Oxd-OH **45** and Fmoc-FF suggesting that this group has a different orientation in the two cases [147].

3.3.8. Rheological Properties

Rheology studies have been carried out to evaluate the viscoelastic properties of the obtained gels in terms of storage modulus, crossover point (defined as the strain value, in the amplitude sweep curves, at which the G' and G'' curves intersected) and gelation kinetics. The strength of each gel was evaluated by taking into account the G' values obtained at gelator concentration at 2% and 1% w/w (Table 24).

Table 24. Storage modulus (G'), linear viscoelastic region (LVE) and crossover point of compounds **45**, **47**, **49** and **51** at 2% w/w and 1% w/w. Results of Fmoc-FF at 2% w/w and 1% w/w are also shown.

Compound		Concemtration (% w/w)	G' [a] (Pa)	LVE [a] (γ %)	Crossover Point [a] (γ %)
Fmoc-L-Tyr-D-Oxd-OH	**45**	2	52600	1	11
		1	6000	2	15
Fmoc-L-Tyr-D-pGlu-OH	**47**	2	30000	1	5
		1	12000	3	9
Fmoc-L-Trp-D-Oxd-OH	**49**	2	31600	1	6
		1	7000	3	9
Fmoc-L-Trp-D-pGlu-OH	**51**	2	36000	1	5
		1	3000	2	33
Fmoc-FF		2	100000	0.18	4
		1	10000	1	9

(a) The analyses were performed on the gels about 20 hours after the gelation begun.

For each gel, at fixed gelator concentration of 2% w/w, a constant G' value at strain within 1% (linear viscoelastic behavior) was found. Results of the amplitude sweep experiments for compounds **45**, **47**, **49** and **51** at 2% w/w concentration (Figure 74a-d) showed that the elastic response component (G') was approximately an order of magnitude larger than the viscous component (G''), indicating a "solid-like" attitude of the gels. Measurements of the moduli as a function of frequency (Figure 75) pointed out that both G' and G'' were almost independent from the frequency in the range from 0.1 to 100 rad.s^{-1} (with G' always greater than G'') confirming the 'solid-like' rheological behavior for the analyzed gels. To check the efficiency of our molecules, we evaluated also the strength of the gel obtained from Fmoc-FF as a comparison (Figure 76). A similar behavior was also found for the gels obtained from compounds **45**, **47**, **49** and **51** and Fmoc-FF at 1% w/w (Table 25 and Figure 77).

[147] Morris, K. L.; Chen, L.; Rodger, A.; Adams, D. J.; Serpell, L. C., Structural determinants in a library of low molecular weight gelators. *Soft Matter* **2015,** *11* (6), 1174-1181.

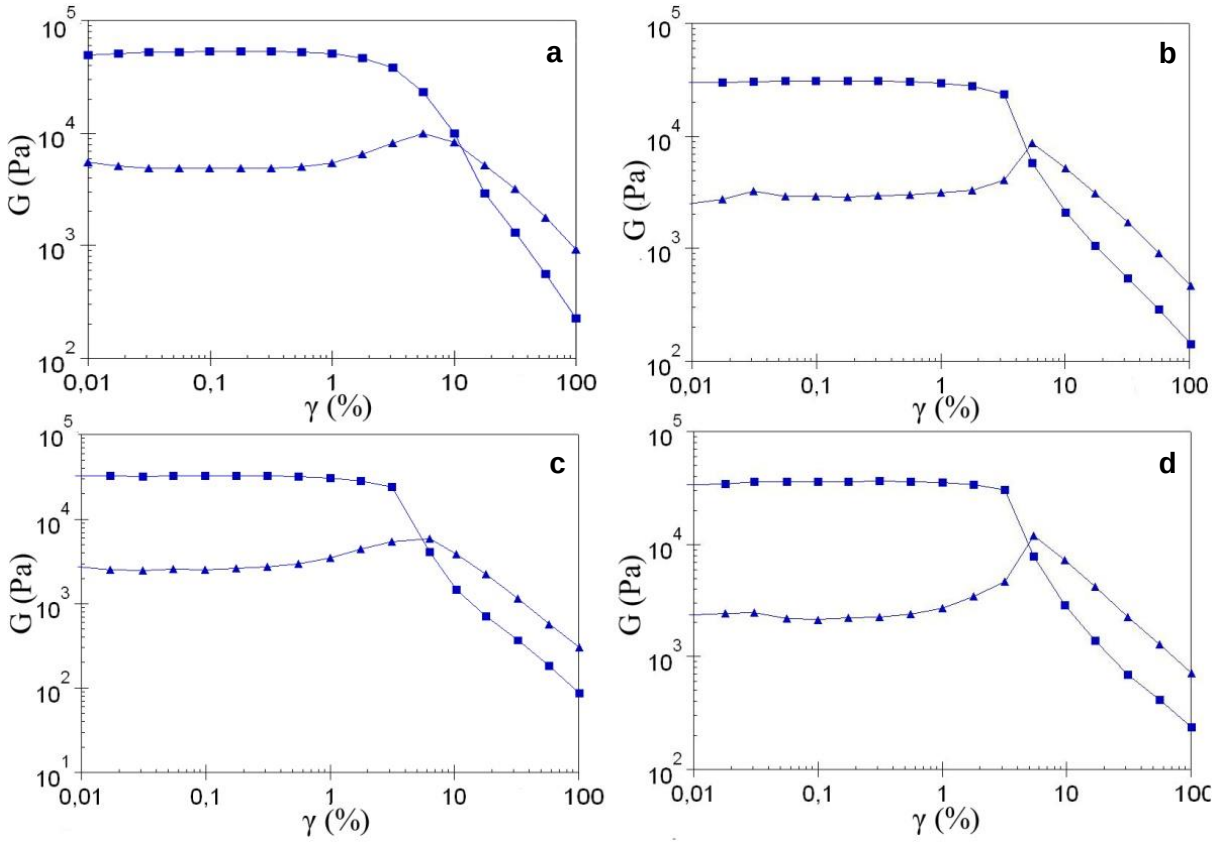

Figure 74. Strain dependence of storage modulus (square) and loss modulus (triangle) at 2% w/w gelator concentration of: (a) Fmoc-L-Tyr-D-Oxd-OH **45**, (b) Fmoc-L-Tyr-D-pGlu-OH **47**, (c) Fmoc-L-Trp-D-Oxd-OH **49**, (d) Fmoc-L-Trp-D-pGlu-OH **51**. The analyses on the gels were performed about 20 hours after the gelation begun.

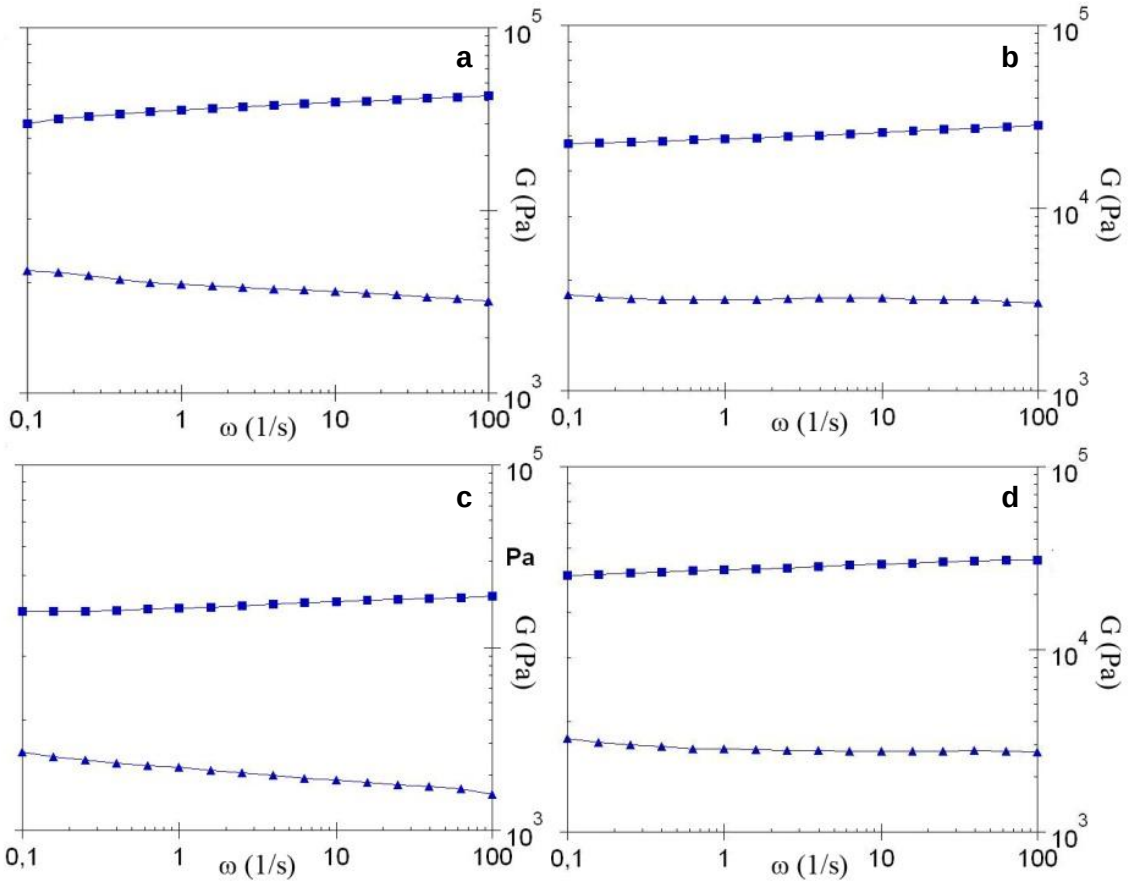

Figure 75. Frequency dependence of storage modulus (square) and loss modulus (triangle) at 2% w/w gelator concentration of: (a) Fmoc-L-Tyr-D-Oxd-OH **45**, (b) Fmoc-L-Tyr-D-pGlu-OH **47**, (c) Fmoc-L-Trp-D-Oxd-OH **49**, (d) Fmoc-L-Trp-D-pGlu-OH **51**. The analyses were performed on the gel about 20 hours after the gelation begun.

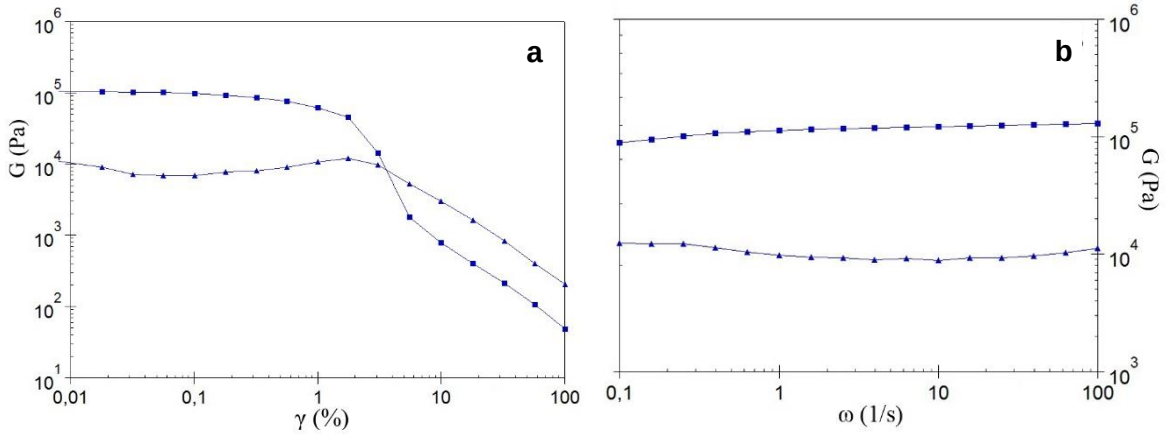

Figure 76. Strain dependence (a) and frequency dependence (b) of storage modulus (square) and loss modulus (triangle) for gels obtained starting from Fmoc-FF at 2% w/w. The analyses were performed on the gel about 20 hours after the gelation begun.

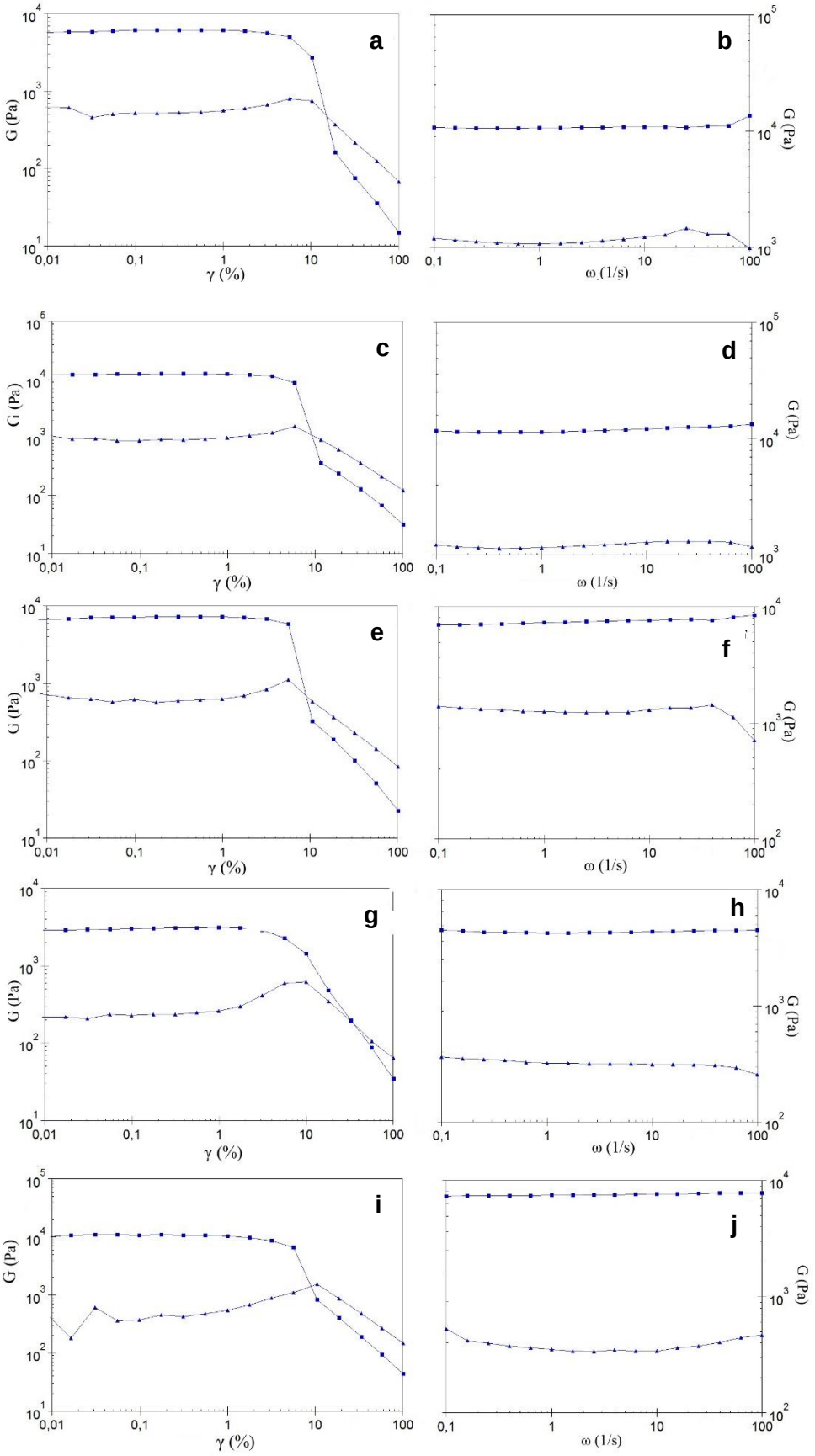

Figure 77. Strain dependence and frequency dependence of storage modulus (square) and loss modulus (triangle) at 1% w/w gelator concentration of: (a, b) Fmoc-L-Tyr-D-Oxd-OH **45**; (c, d) Fmoc-L-Tyr-D-pGlu-OH **47**; (e, f) Fmoc-L-Trp-D-Oxd-OH **39**; (g, h) Fmoc-L-Trp-D-pGlu-OH **51**; (i,j) Fmoc-FF. The analyses were performed on the gel about 20 hours after the gelation begun.

If we compare the gels obtained from our compounds **45**, **47**, **49** and **51** at fixed gelator concentration of 2% w/w, we can gather that those obtained from compound **45** show the highest G' value indicating that it is the stiffest gel even though weaker than what obtained from Fmoc-FF at the same concentration. Compounds **47** and **39** at 2% w/w produce gels characterized by similar G' values, lower than that of compound **45**, whereas compound **51** leads to gels showing an intermediate G' value.

It is worth mentioning that the crossover point of compound **45** is reached at higher strain (11%) than the other gels, all ranging between 4 and 6%. Since this parameter represents the deformation value at which the solid gel-like character of the material (G’ > G’’) changes to the “liquid-state” (G’’ > G’), comparison of the crossover point values suggests that compound **45**, besides being the strongest gel among the synthesized ones (higher G’), is characterized by a greater resistance to deformation. Interestingly, Fmoc-FF shows the lowest strain value at the crossover point (4%) (Figure 77), indicating that all the gels obtained from gelators synthesized in this work maintained the elastic, “solid-like” behavior also at deformations at which the Fmoc-FF gel lose its stability, assuming a viscous, “liquid like” character.

The kinetic behavior of the gels obtained from the compounds **45**, **47**, **49** and **51** at 2% w/w concentration was monitored through time sweep experiments (Figure 78). It is worth noticing that the slight decrease of G’ at the end of the gelation process, observed in the obtained curves, might be related to syneresis due to long standing of the material under stress conditions, whereas the sharp gradient and the little dip in G’ and G’’ in data set B was attributed to slippage. The obtained curves show a similar kinetics behavior and it appears that the hydrogel formation is a one-step process. Both storage and loss modulus increase reaching a constant G' and G'' values at different times, quoted in Table 25.

Boc-L-Tyr-D-Oxd-OH **45** possess the lowest gelation time suggesting that the fast hydrogel formation is related to the highest storage modulus value (Table 25). Interestingly gel obtained from LMWG **45** show G’ values of one order of magnitude higher compared to G’’ values even from the beginning of the gelification process. Furthermore at the beginning of the gelation process, it shows an increase of both moduli steeper than the other gelators.

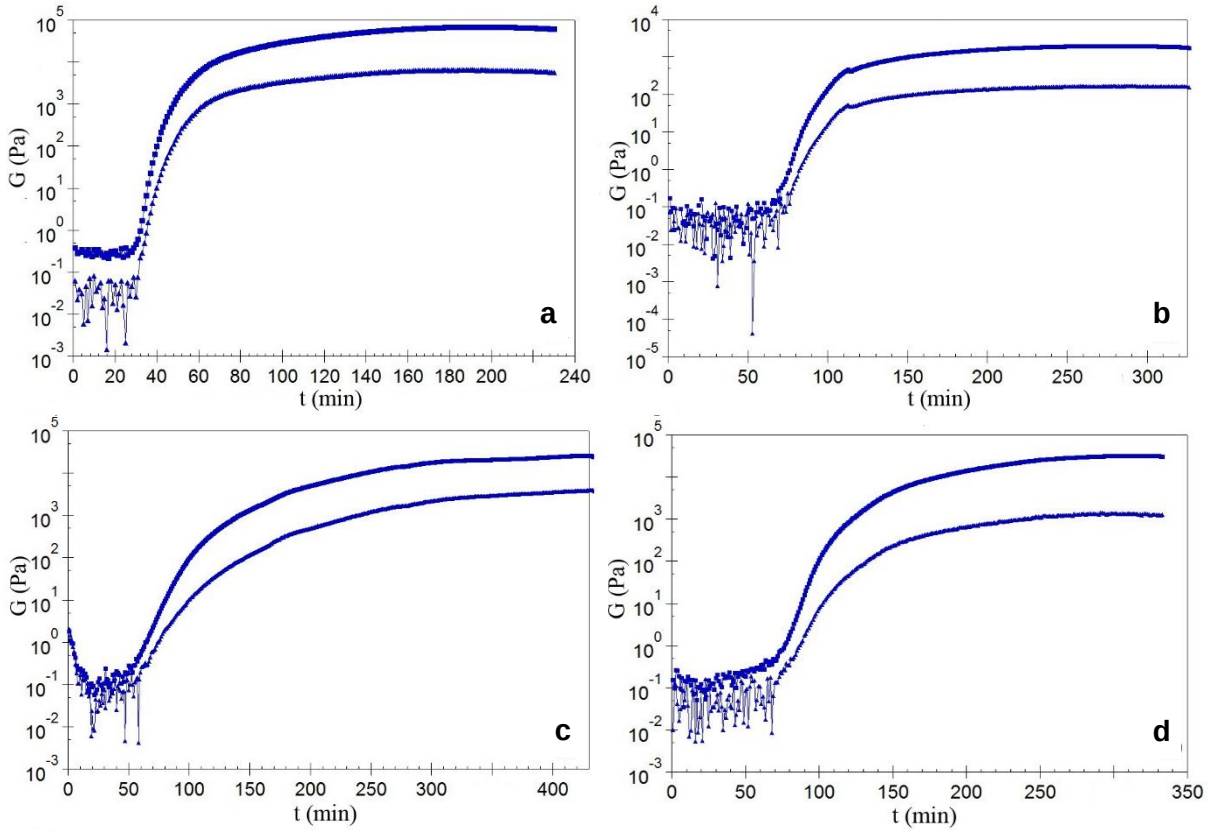

Figure 78. Time dependence of storage modulus and loss modulus for gels obtained starting from (a) Fmoc-L-Tyr-D-Oxd-OH **45**, (b) Fmoc-L-Tyr-D-pGlu-OH **47** and (c) Fmoc-L-Trp-D-Oxd-OH **49** (d) Fmoc-L-Trp-D-pGlu-OH **51** at fixed gelator concentration of 2% w/w.

As Fmoc-L-Tyr-D-Oxd-OH **45** is the most promising gelator among the synthesized ones, the effect of the concentration on its gel viscoelastic properties and the kinetics of the gel formation was studied by means of amplitude sweep (Figure 79a) and time sweep (Figure 79b) experiments respectively. The comparison between the amplitude sweep curves in Figure 79a pointed out that the decrease of the gelator concentration from 2% to 1% w/w causes both a shift in the LVE range limit towards higher values (from 1% to 2%) and a decrease of the G' values (Table 24). In addition, parallel to the LVE trend, the crossover point of the gels obtained from LMWG **45** increased with the decrease of concentration from 11% for 2% w/w gel to 15% for 1% w/w gel) (Table 24).

To better understand the influence of the gelator concentration not only on gels properties in terms of stiffness, but also on the gel formation, the gelation process for compound **45** was monitored through time sweep experiments (Figure 79b). Kinetics studies demonstrated that the decrease of the gelator concentration led to the increase of the gelation time (Table 25), i.e. the time needed to reach a constant G' values (the plateau value was considered reached when the difference between five consecutive acquired G' values was within 0.3%).

Table 25. Gelation time of compounds **45** at 2% w/w and 1% w/w and for compounds **47**, **49** and **51** at 2% w/w.

Compound		Concemtration (% w/w)	Gelation time (min) [a]
Fmoc-L-Tyr-D-Oxd-OH	**45**	2	196
		1	325
Fmoc-L-Tyr-D-pGlu-OH	**47**	2	300
Fmoc-L-Trp-D-Oxd-OH	**49**	2	430
Fmoc-L-Trp-D-pGlu-OH	**51**	2	321

[a] Gelation time values are quoted as the time needed to reach a constant G' value (the plateau was considered reached when the difference between five consecutive acquired G' values was within 0.3%).

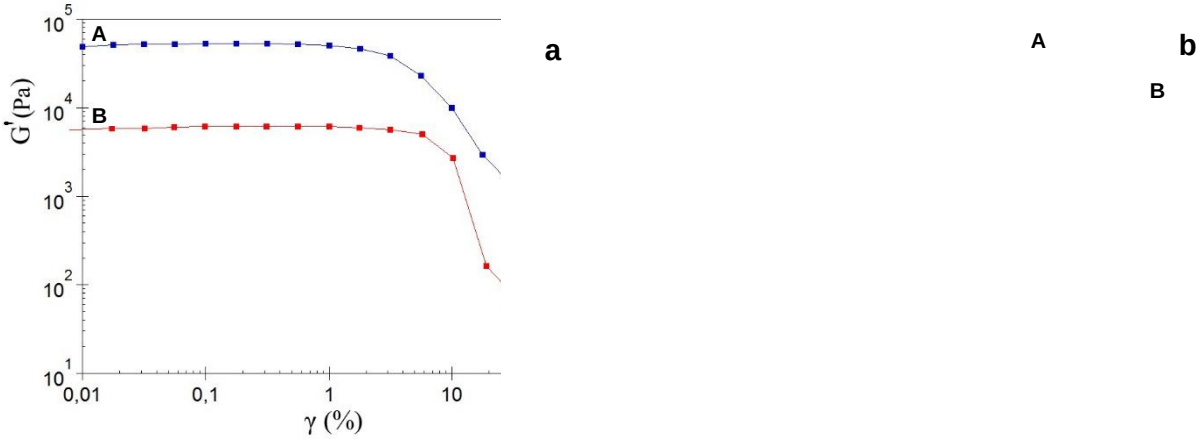

Figure 79. Effect of the concentration on (a) storage modulus and (b) gel formation kinetics for Fmoc-L-Tyr-D-Oxd-OH **45** at (A) 2% w/w (B) 1% w/w. The analyses were performed about 20 hours after the gelation begun.

In order to gain further insights on the kind of network formed for gel obtained from LMWG **45**, the storage moduli of the obtained gels at different concentration of 2% w/w, 1,5% w/w and 1% w/w was plotted against gelator concentration (Figure 80). The storage moduli scaled with the gelator concentration with an exponent of 3. This scaling is in agreement with the Mackintosh theory proposed for densely crosslinked gels [148].

[148] Wu, H.; Morbidelli, M., A Model Relating Structure of Colloidal Gels to Their Elastic Properties. *Langmuir* **2001,** *17* (4), 1030-1036.

a)

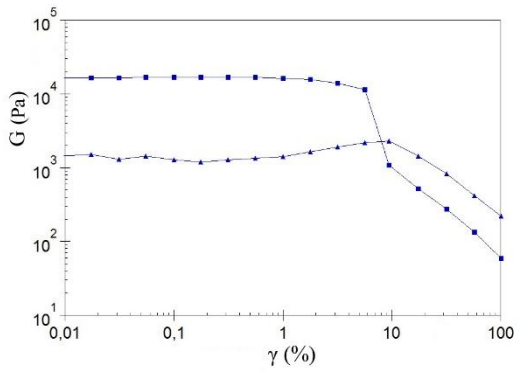

b)

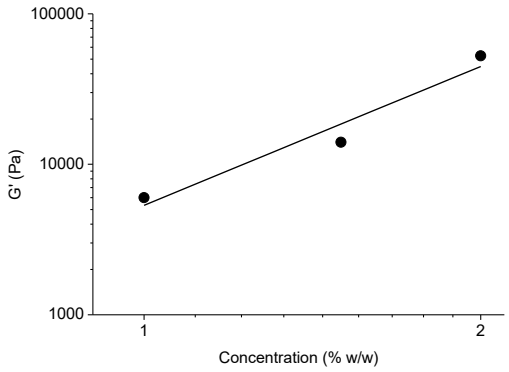

Figure 80. (a) Strain dependence of storage modulus (square) and loss modulus (triangle) for gels obtained starting from Fmoc-L-Tyr-D-Oxd-OH **45** at 1.5% w/w. The analyses were performed on the gel about 20 hours after the gelation begun. (b) Storage moduli (G') vs gelator concentration for gels obtained from compound **45** at 2% w/w, 1.5% w/w and 1% w/w. The solid line represents the fit to data points. Equation of the fit to data point: $G' = C^3$, $R^2 = 0.95$.

Thermal behavior of gels obtained starting from LMWGs **45** and **49** and Fmoc-FF at 1% w/w gelator concentration were characterized by performing an 'ad-hoc' rheological temperature sweep experiment and the results are shown in Figure 81 [149].

[149] Draper, E. R.; Morris, K. L.; Little, M. A.; Raeburn, J.; Colquhoun, C.; Cross, E. R.; McDonald, T. O.; Serpell, L. C.; Adams, D. J., Hydrogels formed from Fmoc amino acids. *CrystEngComm* **2015,** *17* (42), 8047-8057.

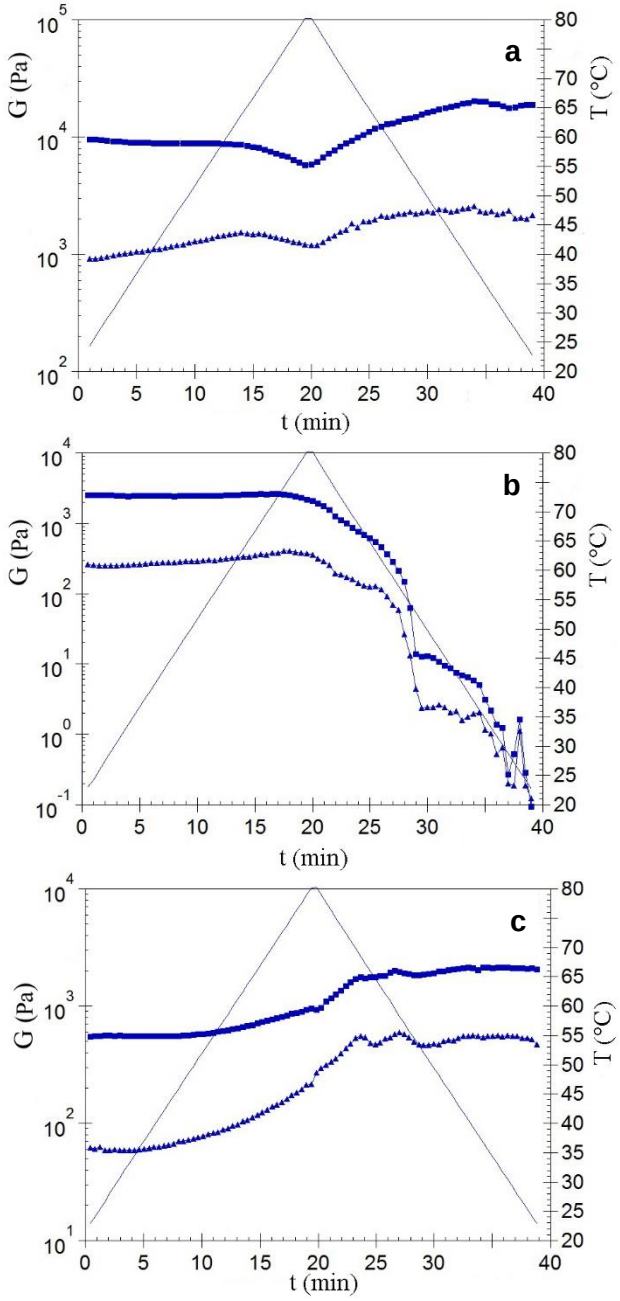

Figure 81. Temperature dependence of G' (squares) and G'' (triangles) for gels obtained from: (a) Fmoc-L-Tyr-D-Oxd-OH **45**, (b) Fmoc-L-Trp-D-Oxd-OH **49** and (c) Fmoc-FF, all at 1% w/w gelator concentration. Continuous line represents the heating and cooling ramp.

For the gel obtained from Fmoc-L-Tyr-D-Oxd-OH **45** (Figure 81a), G' remained almost constant from 23 °C up to about 65 °C while G'' increased in the same temperature range. At higher temperatures, both G' and G'' values started to slightly decrease without displaying a crossover point. This behavior might be attributed to a slight loss of network stability, while maintaining the gel-like structure. During the cooling cycle, from 80°C to 23°C, both G' and G'' increased reaching higher values compared to the starting ones, a behavior that can be related to water evaporation from gel network. A similar behavior can be found for the gel obtained from Fmoc-FF (Figure 81c), with G' almost independent from temperature from 23 °C

to around 55°C and G'' values that started to increase in the same temperature range. From 55 °C to 80 °C and even during cooling down to 23 °C, both G' and G'' increased reaching higher values compared to the starting ones, showing a behavior similar to that of LMWG **45.** In contrast, the curve obtained for the Fmoc-L-Trp-D-Oxd-OH **49** gel reported in Figure 81b shows an almost independent temperature behavior of both G' and G'' values from 23 °C to around 70 °C, followed by a decrease of G' and G'' from 70 °C to 23 °C. This outcome can be related to the loss of stability of the molecular network that is not recovered during the cooling cycle, typical of a non-thermoreversible gel.

Thus, comparing the rheological thermal behavior of the three gelators shown in Figure 81 we can conclude that while gels obtained from Fmoc-L-Tyr-D-Oxd-OH **45** and from Fmoc-FF in 1% w/w concentration create networks able to resist to the applied temperature ramp, the gels obtained from Fmoc-L-Trp-D-Oxd-OH **49** possess a molecular network less stable to temperature. This outcome confirms the rheological results obtained at room temperature, showing that gels obtained from gelator **45** are the strongest among the synthesized ones.

3.4. Water Remediation

3.4.1. Graphene Oxide

Since the Geim and Novoselov's [150] seminal report on the electronic properties of monolayer graphene in 2004, interest in graphene and related materials has quickly increased [151]. At the outset, much of the interest focused on the material's unique electronic features, particularly its high carrier mobility and lack of a band gap. Since that time, however, the scope of applications that graphene has been used for has grown significantly, largely as a result of its unique structure and properties [152].

One of the materials that has played a prominent role in the development of graphene and its derivatives is graphene oxide [153],[154],[155,156,157,158]. As the nomenclature indicates, graphene oxide and graphene are both carbon nanomaterials and, in their pristine, isolated forms, true monolayers. Beyond these basic similarities, graphene oxide and graphene are very different. While graphene is composed of only sp^2 hybridized carbon atoms, graphene oxide has a carbon structure that is interrupted by a range of oxygen functional groups (imparting a substantial degree of sp^3 hybridization).

Understanding the structure of graphene oxide is important and crucial prior to any subsequent chemical modifications of the material. Graphene oxide is primarily composed of carbon, oxygen and hydrogen atoms. Usually graphene oxide has a carbon/oxygen ratio ranging between 1.5 and 2.5. Several structures have been proposed over the years, such as the Hofmann, Ruess, Scholz–Boehm, Nakajima–Matsuo, Lerf–Klinowski, Dékány and Ajayan models (Figure 82).

---

[150] Novoselov, K. S.; Geim, A. K.; Morozov, S. V.; Jiang, D.; Zhang, Y.; Dubonos, S. V.; Grigorieva, I. V.; Firsov, A. A., Electric Field Effect in Atomically Thin Carbon Films. *Science* **2004,** *306* (5696), 666-669.

[151] Dreyer, D. R.; Ruoff, R. S.; Bielawski, C. W., From Conception to Realization: An Historial Account of Graphene and Some Perspectives for Its Future. *Angewandte Chemie International Edition* **2010,** *49* (49), 9336-9344.

[152] Zhu, Y.; Murali, S.; Cai, W.; Li, X.; Suk, J. W.; Potts, J. R.; Ruoff, R. S., Graphene and Graphene Oxide: Synthesis, Properties, and Applications. *Advanced Materials* **2010,** *22* (35), 3906-3924.

[153] Rao, C. N. R.; Sood, A. K., *Graphene: Synthesis, Properties, and Phenomena*. **2012**.

[154] Jiang, D. E.; Chen, Z., *Graphene Chemistry: Theoretical Perspectives*. **2013**.

[155] Dreyer, D. R.; Park, S.; Bielawski, C. W.; Ruoff, R. S., The chemistry of graphene oxide. *Chemical Society Reviews* **2010,** *39* (1), 228-240.

[156] Chua, C. K.; Pumera, M., Chemical reduction of graphene oxide: a synthetic chemistry viewpoint. *Chemical Society Reviews* **2014,** *43* (1), 291-312.

[157] Dreyer, D. R.; Todd, A. D.; Bielawski, C. W., Harnessing the chemistry of graphene oxide. *Chemical Society Reviews* **2014,** *43* (15), 5288-5301.

[158] Eigler, S.; Hirsch, A., Chemistry with Graphene and Graphene Oxide—Challenges for Synthetic Chemists. *Angewandte Chemie International Edition* **2014,** *53* (30), 7720-7738.

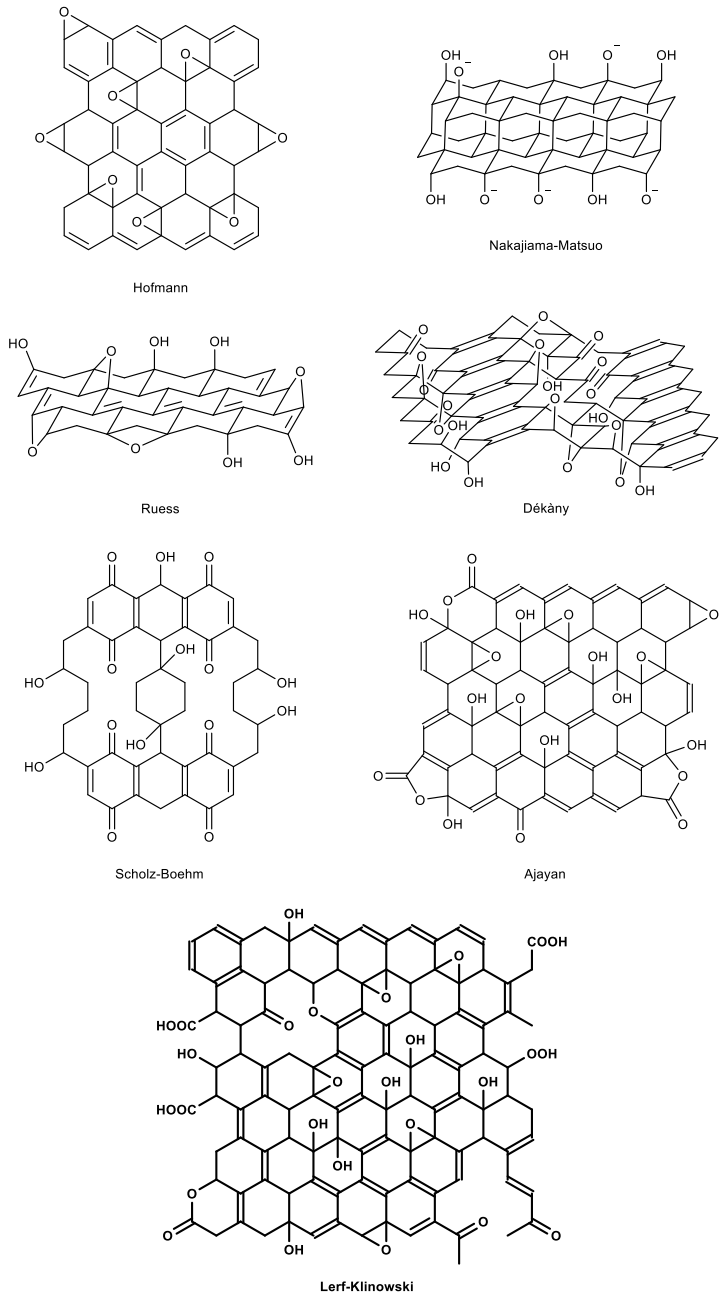

Figure 82. Proposed Structures of Graphene Oxide.

The model of GO that better represents the realistic structure of GO is attributed to Lerf and Klinowski. [159] In this model graphene oxide is consists of an aromatic region with unoxidised benzene rings and another region with aliphatic six-membered rings. Oxygen functionalities such as 1,2-epoxides and hydroxyl groups populated the basal-plane while the edge-plane contained mostly carboxyl and hydroxyl groups. A recent observation of graphene oxide using

[159] Lerf, A.; He, H.; Forster, M.; Klinowski, J., Structure of Graphite Oxide Revisited. *The Journal of Physical Chemistry B* **1998,** *102* (23), 4477-4482.

high-resolution TEM indicated the presence of such features on the graphene oxide sheets, in support of the Lerf–Klinowski model [160].

3.4.2. Applications of Graphene Oxide

After Geim and Novoselov's [150] seminal work, the interest on graphene and graphene oxide rapidly increased. In these last decades the scientists discovered many applications in the field of food, environment, catalysis, drug deliveries, sensor, water purification, etc. [161].
For instance, multiple crosslinking molecules were selected to drive the self-assembly of 3D graphene based macrostructures. So multivalent ions, biomolecules, monomers (unconverted), polymers and other small organic molecules have been successfully studied for the auxiliary gelation of graphene or GO. Rare-earth metallic ions of Eu^{3+} and La^{3+} can also act as cross-linkers: reversible gel–sol transition of the La^{3+} cross-linked GO hydrogel can be realized by control of EDTA and GdL (Figure 83) [162]. GO-based supramolecular hydrogels can be formed also in the presence of selected amino acids (arginine, tryptophan or histidine) or nucleosides (adenosine, guanosine or cytidine) [163].

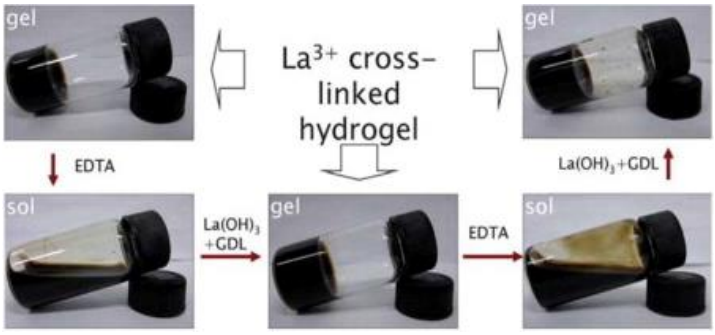

Figure 83. Reversible gel-sol transition of the La^{3+} cross-linked GO hydrogel.

3.4.3. Water Purification

Nowadays global population growth has intensified, with an estimated population increase from 7 to 10 billion by 2050. One significant consequence of this trend is the increasing scarcity of fresh water, which represents only 0.5% of Earth's overall water resources [164].

---

[160] Erickson, K.; Erni, R.; Lee, Z.; Alem, N.; Gannett, W.; Zettl, A., Determination of the Local Chemical Structure of Graphene Oxide and Reduced Graphene Oxide. *Advanced Materials* **2010,** *22* (40), 4467-4472.
[161] Fang, Q.; Shen, Y.; Chen, B., Synthesis, decoration and properties of three-dimensional graphene-based macrostructures: A review. Chemical Engineering Journal 2015, 264, 753-771.
[162] Huang, H.; Chen, P.; Zhang, X.; Lu, Y.; Zhan, W., Edge-to-Edge Assembled Graphene Oxide Aerogels with Outstanding Mechanical Performance and Superhigh Chemical Activity. *Small* **2013,** *9* (8), 1397-1404.
[163] Adhikari, B.; Biswas, A.; Banerjee, A., Graphene Oxide-Based Supramolecular Hydrogels for Making Nanohybrid Systems with Au Nanoparticles. *Langmuir* **2012,** *28* (2), 1460-1469.
[164] Qadir, M.; Sharma, B. R.; Bruggeman, A.; Choukr-Allah, R.; Karajeh, F., Non-conventional water resources and opportunities for water augmentation to achieve food security in water scarce countries. *Agricultural Water Management* **2007,** *87* (1), 2-22.

For many decades, drinking water treatment plant operations have been limited to removing natural organic matter and microbial contaminants (bacteria, viruses, and protozoa) by a combination of conventional chemical coagulation and disinfection processes. However, rapid industrialization, widespread utilization of antibiotics and other pharmaceuticals, expanded use of chemical products in agriculture, and other human activities have caused the introduction of many new synthetic organic and inorganic contaminants (i.e., dyes, pesticides, heavy metals, etc.) to drinking water treatment systems. Many of these emerging contaminants and the products they form, when in contact with organic matter, pose serious threats to human health. Additionally, disinfection using ozone or ultraviolet light is expensive, while chemical disinfection using chlorine may often produce carcinogenic byproducts [165]. Adsorbent materials may be a possible solution to these problems and have the potential to remove problematic byproducts downstream of chemical disinfection. Traditional adsorbents, such as activated carbon and polymers, are simple to implement and maintain, but are not always efficient enough to remove all biological and chemical contaminants. With increasing interest in nanotechnology, many types of metallic and carbon-based nanomaterials have emerged [166,167]. Initial interest in these nanomaterials was for application in the electronics industry, due to their exceptional thermal and electrical properties. However, properties like high surface area, ease of chemical or physical modification, tuning of properties for particular applications, excellent capacity for microbial disinfection and removal of both organic and inorganic contaminants determinate that carbon-based nanomaterials and their respective nanocomposites offer many possibilities for novel applications in water treatment [168].

The most common organic compounds of concern include natural organic matter, such as humic substances, proteins, lipids, carbohydrates and synthetic organic compounds, such as dyes, pharmaceuticals and pesticides. Many of these synthetic compounds, due to their recalcitrant molecular structures, are left largely untreated by conventional chemical and biological waste treatment processes, and have become significant issues in water treatment. So carbon-based nanomaterials have been shown to be a promising solution for the removal of these contaminants through adsorption [169,170]. The main physicochemical properties affecting removal of organic chemicals are pore size (micro and meso) and presence of

[165] Chowdhury, S.; Rodriguez, M. J.; Sadiq, R., Disinfection byproducts in Canadian provinces: Associated cancer risks and medical expenses. *Journal of Hazardous Materials* **2011,** *187* (1–3), 574-584.

[166] Smith, S. C.; Rodrigues, D. F., Carbon-based nanomaterials for removal of chemical and biological contaminants from water: A review of mechanisms and applications. Carbon 2015, 91, 122-143.

[167] Sundramoorthy, A. K.; Gunasekaran, S., Applications of graphene in quality assurance and safety of food. TrAC Trends in Analytical Chemistry 2014, 60, 36-53.

[168] Kyzas, G. Z.; Deliyanni, E. A.; Matis, K. A., Graphene oxide and its application as an adsorbent for wastewater treatment. Journal of Chemical Technology & Biotechnology 2014, 89 (2), 196-205.

[169] Gao, Y.; Li, Y.; Zhang, L.; Huang, H.; Hu, J.; Shah, S. M.; Su, X., Adsorption and removal of tetracycline antibiotics from aqueous solution by graphene oxide. *Journal of Colloid and Interface Science* **2012,** *368* (1), 540-546.

[170] Lapworth, D. J.; Baran, N.; Stuart, M. E.; Ward, R. S., Emerging organic contaminants in groundwater: A review of sources, fate and occurrence. *Environmental Pollution* **2012,** *163*, 287-303.

surface charges in functionalized nanomaterials. Typically, organic compounds with higher molecular weights will adsorb on the outer surface of the nanomaterial, while smaller molecules will adsorb inside the micropores. The presence of aromatic rings in these contaminants will also affect their removal by carbon nanomaterials. In general, the carbon-based nanomaterials in pure form cannot be directly applied for water treatment due to their extremely small size, which makes their recovery from water treatment systems difficult. Researchers have, therefore, been searching for mechanisms to incorporate these nanomaterials into membranes, to embed them into polymeric beads, or to modify these nanomaterials with magnetic metal oxides to facilitate their recovery from water.

3.4.4. Gelator and Hydrogel Preparation

Previously we reported the use of the peptide based hydrogelator Fmoc-L-Phe-D-pGlu-OH (Figure 84) for the formation of hydrogels in PBS solution. Unfortunately this molecule could not efficiently freeze pure water, due to its low solubility, so we used as gelation trigger a pH slow variation induced by the hydrolysis of glucono-δ-lactone, reported by Adams and co-workers [171].

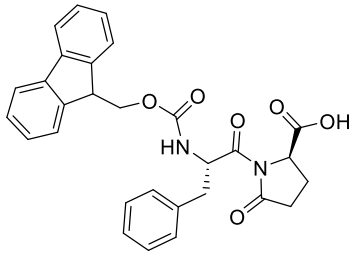

Figure 84. Chemical structure of the gelator Fmoc-L-Phe-D-pGlu-OH, described in this work.

We prepared hydrogels and composite GO-hydrogels based on Fmoc-L-Phe-D-pGlu-OH and we investigates their application for water remediation. Methylene Blue, a cationic dye, and Eosin Y, an anionic dye, were used as model pollutants.

Fmoc-L-Phe-D-pGlu-OH was synthesized by standard reactions. To prepare the hydrogels, Fmoc-L-Phe-D-pGlu-OH was added to water, together with NaOH, which is required to dissolve the peptide, that is insoluble at pH ≈ 4, while it is soluble at pH ≈ 10. Then GdL was added to slowly decrease the solution pH. When the pK_a value of the molecule was reached, the molecule precipitated getting organized into fibers that in turn trap the water molecules, yielding a hydrogel. The composite GO-hydrogel was obtained following the same method, but replacing water with a GO suspension in water (1 mg/mL). The sonication of basic solutions (both peptide in water and peptide and GO in water) for 15 minutes before and after GdL addition favours the formation of homogeneous hydrogels, that is crucial to avoid the

[171] Raeburn, J.; Pont, G.; Chen, L.; Cesbron, Y.; Levy, R.; Adams, D. J., Fmoc-diphenylalanine hydrogels: understanding the variability in reported mechanical properties. *Soft Matter* **2012,** *8* (4), 1168-1174.

formation of preferential paths in the gel, which could reduce its efficiency for pollutants adsorption. Using this technique, we prepared four hydrogels **A**, **B**, **C** and **D**, using Fmoc-L-Phe-D-pGlu-OH in 1% or 2% w/w concentration and pure water or GO/water suspension. The most common diagnostic test of gelation is tube inversion. In this test, a sample tube containing the hydrogel is turned upside down to ascertain if the sample would flow under its own weight. The photograph of the four test tubes upside down, containing the hydrogels **A**-**D** formed using this technique, is shown in Figure 85.

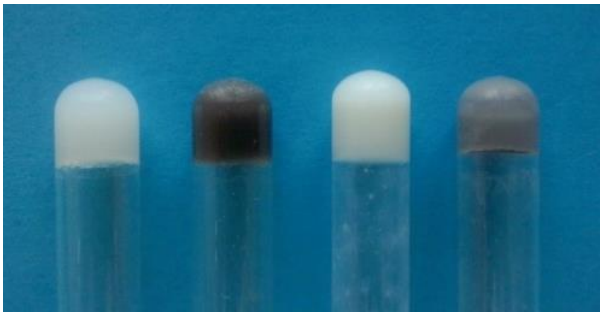

Figure 85. Photographs of hydrogels **A**-**D** prepared with Fmoc-L-Phe-D-pGlu-OH at different concentration. From left to right: **A**, 1% gelator/water; **B**, 1% gelator/GO/water; **C**, 2% gelator/water; **D**, 2% gelator/GO/water.

3.4.5. Hydrogel Properties

The first analysis useful to understand the strength of the hydrogel is the measurement of its melting point (T_{gel}), that is the range of temperatures while the gel decomposes. T_{gel} was determined by heating the test tubes (diameter: 8 mm) containing the gel with a glass ball (diameter: 5 mm, weight: 165 mg) on the top of it (Table 26).

Table 26. T_{gel} of hydrogels **A**-**D** in water or GO/water, as a function of an increasing amounts of gelator (expressed in % w/w).

Hydrogel	**Gelator Concentration** (w/w)	**Presence of GO** (1mg/mL)	**T_{gel}** (°C)
A	1	no	57-74[a]
B	1	yes	50-75[a]
C	2	no	56-79[a]
D	2	yes	61-85[a]

(a) The gel is not thermoreversible and syneresis occurs on heating.

In any case the hydrogel is not thermoreversible so, after heating, syneresis occurs and water is ejected. Furthermore, the T_{gel} of all the hydrogels always ranges between 50 and 85 °C, with very little variations, thus suggesting that the presence of GO does not strongly affect the fibers formation that ends in the final hydrogel.

Rheological studies have been carried out on hydrogels **A**, **B**, **C** and **D**. Strain sweep and gelation kinetics experiments have been performed to study the strength and the gelation

behavior of the hydrogels. The strength of the hydrogels **A**, **B**, **C** and **D** was evaluated in terms of storage modulus and linear viscoelastic region (G' and LVE, Table 27 and Figure 86).

Table 27. Storage modulus, linear viscoelastic region and gelation time of hydrogels **A**-**D**.

Hydrogel	G' (Pa)	LVE (γ %)	Gelation time (min)
A	5000	1.5	450
B	4000	3	450
C	6000	1	400
D	4000	3	400

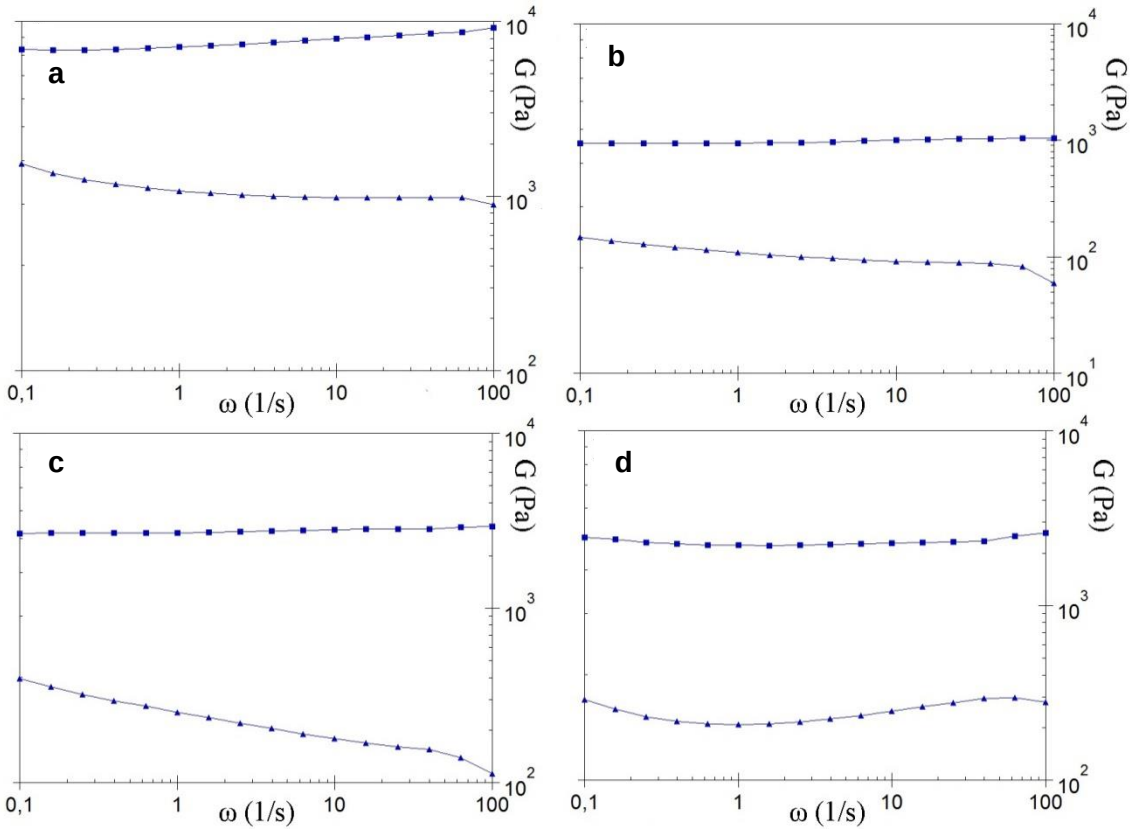

Figure 86. Frequency dependence of storage modulus (square) and loss modulus (triangle) for hydrogelator obtained at 2% w/w (a-b) and 1% w/w (c-d) gelator concentration without GO (a-c) and with GO (b-d) .

Hydrogel **C**, obtained from the gelator at 2% w/w concentration, was characterized by the highest storage modulus among the analyzed samples, with values of almost 6000 Pa, and LVE region of 1% (Figure 87a, Table 27). The addition of GO to this hydrogel (**D**) led to a lower storage modulus value (around 4000 Pa) and a more extended LVE region, up to 3% (Figure 87a, Table 27). Considering the hydrogels **A** and **B,** obtained starting from 1% w/w gelator concentration with and without the presence of GO, **A** was characterized by a storage modulus of 5000 Pa and LVE region of 1.5% while the GO loaded **B** by a storage modulus of

4000 Pa and LVE region of 3% (Figure 87b, Table 27). Hydrogels were also characterized by means of frequency sweep experiments (Figure 86) showing that for all the studied hydrogels both the storage and loss moduli were almost independent from the applied frequency, indicating the “solid-like” rheological behavior of the analyzed hydrogels in the range from 0.1 to 100 $rad \cdot s^{-1}$.

Although the introduction of GO in the hydrogels is not crucial for the modification of their properties, pure hydrogels **A** and **C** are slightly stronger compared to GO-loaded hydrogels **B** and **D**. The presence of GO might cause a partial loss of the 3D non-covalent interactions in the gel network, which are essential in order to obtain a solid and strong gel. To further investigate this aspect, gelation kinetics experiments have been performed. The gelation behavior was investigated in terms of both total gelation time and starting point of the gelation process, i.e. the first point at which the storage modulus and loss modulus start to significantly differentiate and increase. Figures 87c and 87d show that the gelation kinetics always follows a one-step mechanism. Comparing the gelation behavior of hydrogels **C** and **D** (2% w/w gelator concentration with and without GO), we could notice that the gelation mechanism is triggered earlier for hydrogel **C** than for the GO loaded sample **D** (around 50 minutes and 100 minutes respectively), while the total gelation time is about 400 minutes for both samples (Figure 87c, Table 27). A similar behavior was found for hydrogels **A** and **B** (1% w/w gelator concentration with and without GO), as the gelation process started earlier for hydrogel **A** compared to the GO loaded hydrogel **B** (around 100 minutes and 150 minutes respectively). In this case, for both hydrogels the total gelation time was about 450 minutes (Figure 87d, Table 27).

These results suggest that for both gelator concentrations GO interferes with the formation of the non-covalent interactions between the dipeptides that lead to the gel formation, slows down the gelation process and leads at the formation of a weaker hydrogel compared to the plain one, thus confirming the results obtained with the strain sweep experiments.

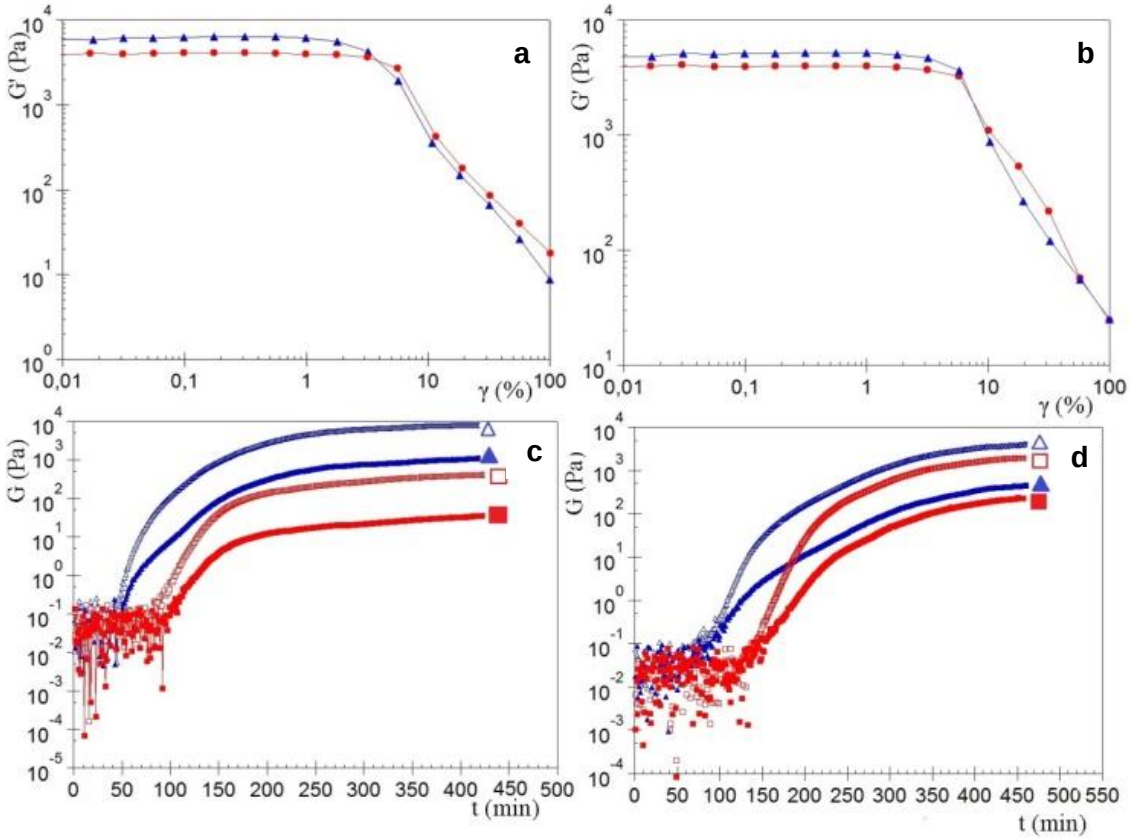

Figure 87. Strain dependence of storage modulus of hydrogel obtained starting from 2% w/w (a) and 1% w/w (b) of gelator concentration loaded with GO (●) and without GO (▲). The analyses were performed about 20 hours after the gelation begun. Time dependence of storage modulus (Δ, □) and loss modulus (▲, ■) for hydrogel obtained starting from Fmoc-L-Phe-D-pGlu-OH at 2% w/w (c) and 1% w/w (d) of gelator concentration loaded with GO (■,□) and without GO (▲, Δ).

The SEM analysis of the Xerogel obtained drying a sample of 1% w/w of gelator (Figura 88) and the SEM analysis of Aerogel obtained lyophilizing a sample of 1% w/w of gelator (Figure 89) shows the formation of locally oriented long strips that cross on the lasrge scale, thus forming a network.

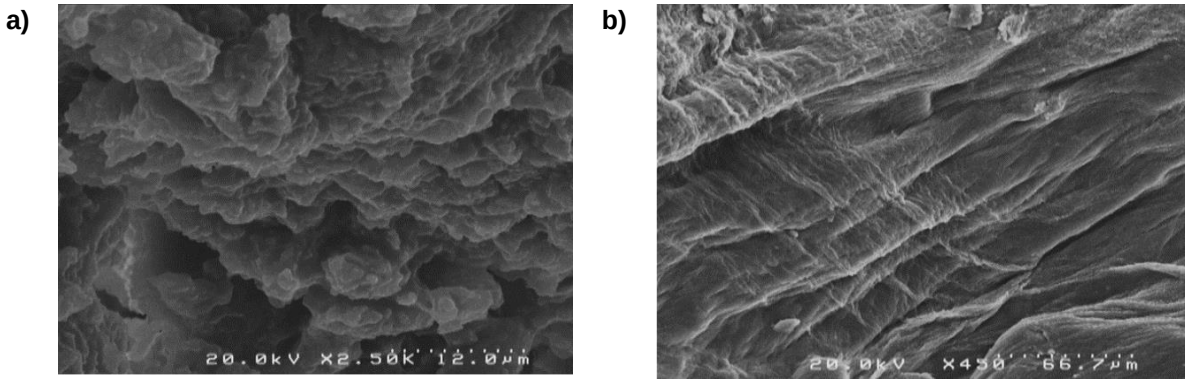

Figure 88. SEM images of xerogels obtained from Fmoc-L-Phe-D-pGlu-OH hydrogels at 1% concentration without GO (a) and with GO (b).

a) b)

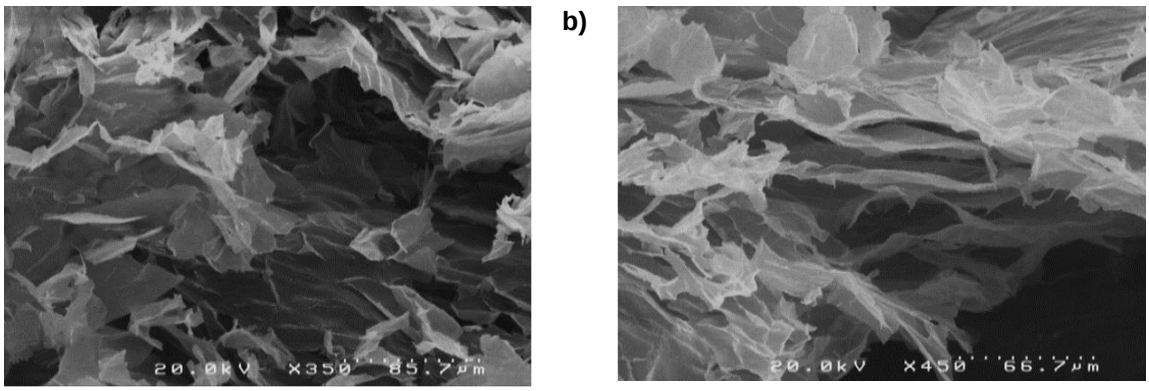

Figure 89. SEM images of aerogels obtained from Fmoc-L-Phe-D-pGlu-OH hydrogels at 1% concentration without GO (a) and with GO (b).

3.4.6. Water Purification

Hydrogels **A**-**D** were then prepared to check their efficacy to trap pollutants. For a preliminary screening, we chose methylene blue as model pollutant molecule: it is a cationic aromatic heterocycle that strongly absorbs visible light at 664 nm (Figure 90). The removal of MB is *per se* an extremely interesting topic because it founds many industrial applications as dye and staining in the textile and paper industry due to its vivid color. It is estimated that ca. 30% of synthetic dyes are lost during manufacturing or are released into the environment as wastewater from industries. High doses of MB are toxic and the large amounts of MB discharged annually deteriorate the water quality and represents risk to aquatic life. Therefore, efficient devices for removing MB from wastewaters are technologically interesting. In addition MB is commonly used as a general model pollutant.

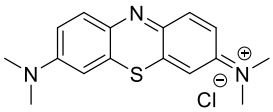

Figure 90. Chemical Structure of Methylene Blue.

We prepared hydrogels **A**-**D** into glass columns for flash chromatography (internal diameter 1.0 cm, equipped with a glass frit) to obtain a device where the dye aqueous solution could freely flow after interaction with hydrogels (Figure 91).

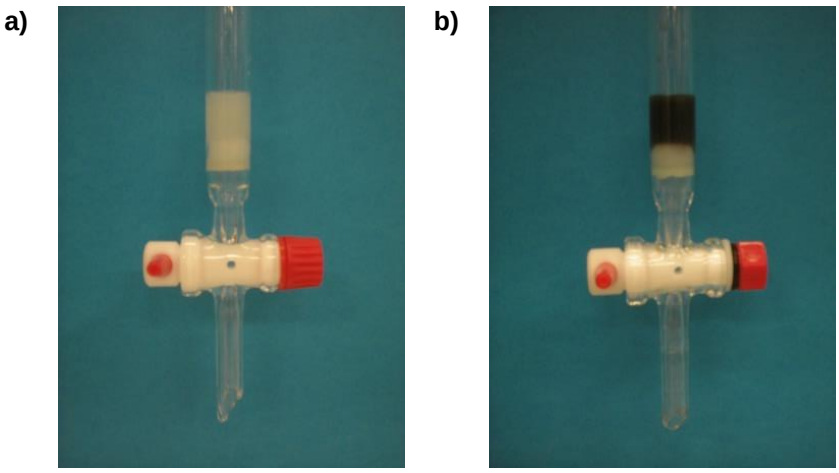

Figure 91. Photograph of glass column packed with hydrogel (a) and GO-composite hydrogel (b).

After addition of water (50 mL) containing MB (2 mg), the liquid flowed very slowly though hydrogels **A** and **B** (24 days and 16 days respectively). The elution through hydrogels **C** and **D** resulted so slow that it was impossible to carry out any measurement. We collected small portions of eluted water from hydrogels **A** and **B** and we measured the amount of MB contained in each portion by UV-Vis spectroscopy. Table 28 reports the total amount of dye retained by the hydrogels: in any case the amount of retained dye is very high, although the elution time is generally quite long.

Table 28. Amount of MB adsorbed from Hydrogels **A**-**B**, after elution of a solution of MB (2 mg) in water (50 mL).

Hydrogel	Dye Retained by Gel (%)	Time (h)
A	94	576
B	94	384

To better understand these results, we analyzed by UV-Vis spectroscopy the amount of dye present in each portions of eluted solutions. The results are reported in Figure 92.

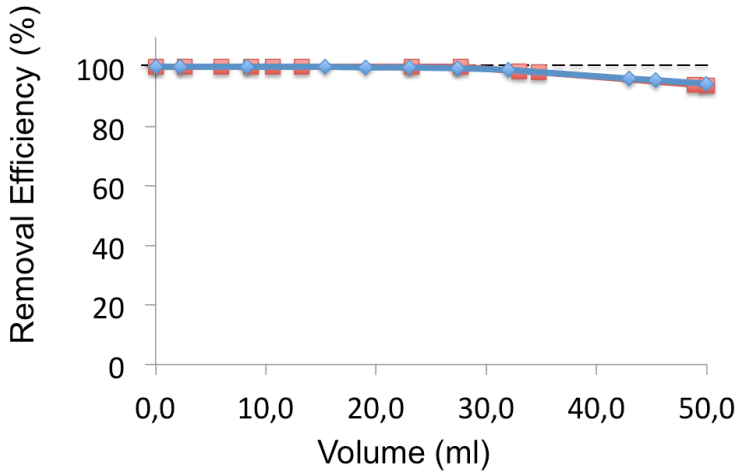

Figure 92. (A) Removal efficiency of the pure hydrogel **A** (red) and of the GO doped hydrogel **B** (blu).

Both hydrogels **A** and **B** are able to clean completely the first 30 mL of MB solution. They have an extremely good performance also for the other 20 mL, as 94% of the total dye is retained by the gel. This outcome means that Fmoc-L-Phe-D-pGlu-OH hydrogel itself is able to capture the MB both by π-π interactions due to the aromatic Phe and Fmoc moieties and via hydrogen bond and electrostatic interactions due to its hydrophilic functional groups.

After these satisfactory results, we prepared some devices that could be easily used outside a chemical laboratory. To cut the costs and to eliminate the column glass frit that is probably responsible for the slow elution, the glass column was replaced by a medical-grade disposable hypodermic plastic syringe (internal diameter 14 mm). To reduce the times, we also used smaller volume solutions and therefore more concentrated solutions (2 mg/5 mL and 2 mg/10 mL) to minimize elution times. Figure 93 shows the preparation and application of a purification column.

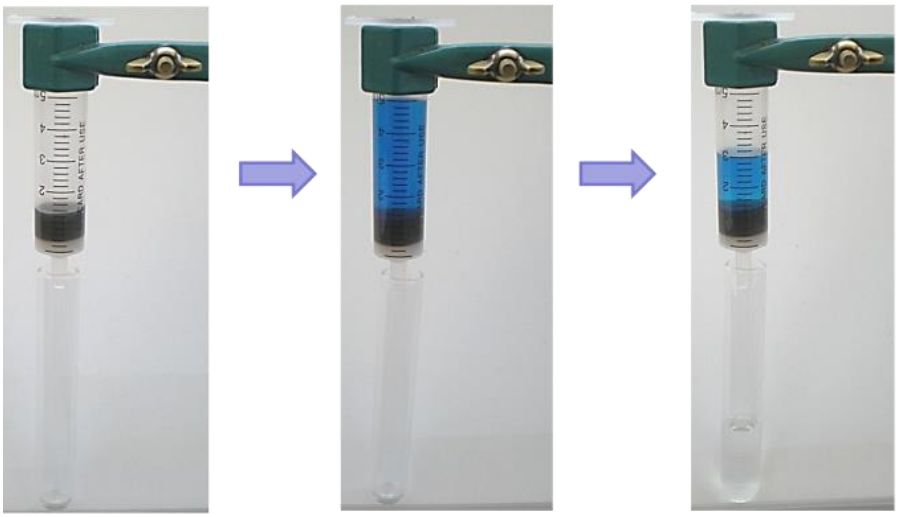

Figure 93. Photograph of the preparation of a device for water remediation.

In addition to MB, that is a cationic water pollutant, we checked the ability of these hydrogels to trap Eosin Y, an anionic water pollutant (Figure 94), to compare the adsorption capacity of hydrogels **A**-**C** and the GO–doped hydrogels **B**-**D** towards different types of model pollutants with opposite charges.

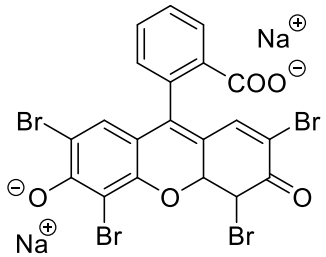

Figure 94. Chemical Structure of Eosin Y (EY).

Table 29 shows the results obtained when aqueous solutions of MB or EY in different concentration (2 mg/5 mL or 2 mg/10 mL) are eluted through our disposable syringes equipped with hydrogels **A**-**D**. In any case we notice that much shorter elution times are found for hydrogels **A** and **B**, but a too fast elution time causes a poor dye retention for both MB and EY. Interestingly hydrogel **B** is far more efficient than **A**, suggesting that for very fast filtration GO may help pollutants trapping, as it increases the active area able to trap the dyes. In contrast excellent results have been obtained with both hydrogels **C** and **D** that efficiently trap all the MB pollutant in reasonable times.

A similar outcome was observed for EY: hydrogels **C** and **D** efficiently trap most of the pollutant, in contrast with the results obtained with **A** and **B**. Here the presence of GO does not help to fully trap the dye because EY molecules not easily interact with the negatively charged GO, because it is an anionic pollutant.

Table 29. Adsorption of Dyes MB and EY form Hydrogels **A**-**D** using Disposable Plastic Syringes.

Entry	**Hydrogel**	**Dye** (2 mg)	**Solution** (mL)	**Detained Dye** (%)	**Elution Time** (h)
1	**A**	MB	5	11	0.5
2	**B**	MB	5	80	24
3	**A**	MB	10	40	8
4	**B**	MB	10	82	24
5	**C**	MB	5	100	103
6	**D**	MB	5	100	120
7	**C**	MB	10	100	96
8	**D**	MB	10	100	72
9	**A**	EY	5	22	5
10	**B**	EY	5	29	24
11	**A**	EY	10	83	26
12	**B**	EY	10	17	4
13	**C**	EY	5	95	27
14	**D**	EY	5	94	48
15	**C**	EY	10	90	75
16	**D**	EY	10	87	75

3.5. Biomineralization

The word biomineralization indicates processes in which organisms form minerals [172,173,174]. These processes are distinguished from abiotic mineralization by the control exerted by organisms over the mineral formation. The product of a biomineralization process is defined as “biomineral”, that indicates not only a mineral produced by organisms, but also to the fact that almost all of these mineralized products are composite materials comprised of both a mineral and a organic component. Furthermore, having formed under controlled conditions, biomineral phases often have properties such as shape, size, crystallinity, isotopic and trace element compositions quite unlike its inorganically formed counterpart.

Calcium carbonate is commonly found in many forms [175,176], for example as limestone, as the calcareous exoskeleton of marine animals, and as boiler scales. It has many applications: coating pigment for premium quality paper products in paper industry, fillers in rubber and paints in polymer applications, and calcium-based antacid tablets in healthcare. Calcium carbonate has also received considerable attention in the field of biomaterials and biomineralization since calcium carbonate is one of the most abundant biological minerals formed by living organisms. There are three polymorphs of anhydrous calcium carbonate: aragonite, vaterite and calcite, listed here in order of increasing thermodynamic stability. All three polymorphs can occur at the same time in some types of mollusks and marine algae. Aragonite (λ-$CaCO_3$) and calcite (β-$CaCO_3$) are more thermodynamically stable structures and they most commonly occur in nature. Vaterite, also known as μ-$CaCO_3$, less commonly occurs in nature because it is the least thermodynamically stable polymorph (Figure 95).

[172] Mann, S., *Biomineralization: Principles and Concepts in Bioinorganic Materials Chemistry*. Oxford University Press, New York. **2001**.
[173] Falini, G.; Fermani, S., The strategic role of adsorption phenomena in biomineralization. *Crystal Research and Technology* **2013,** *48* (10), 864-876.
[174] De Yoreo, J. J.; Vekilov, P. G., *Biomineralization*. Mineral Soc. Am., Washington, DC: 2003.
[175] Brečević, L.; Kralj, D., On calcium carbonates: From fundamental research to application. *Croatica Chemica Acta* **2007,** *80* (3-4), 467-484.
[176] Cölfen, H., Precipitation of carbonates: recent progress in controlled production of complex shapes. *Current Opinion in Colloid & Interface Science* **2003,** *8* (1), 23-31.

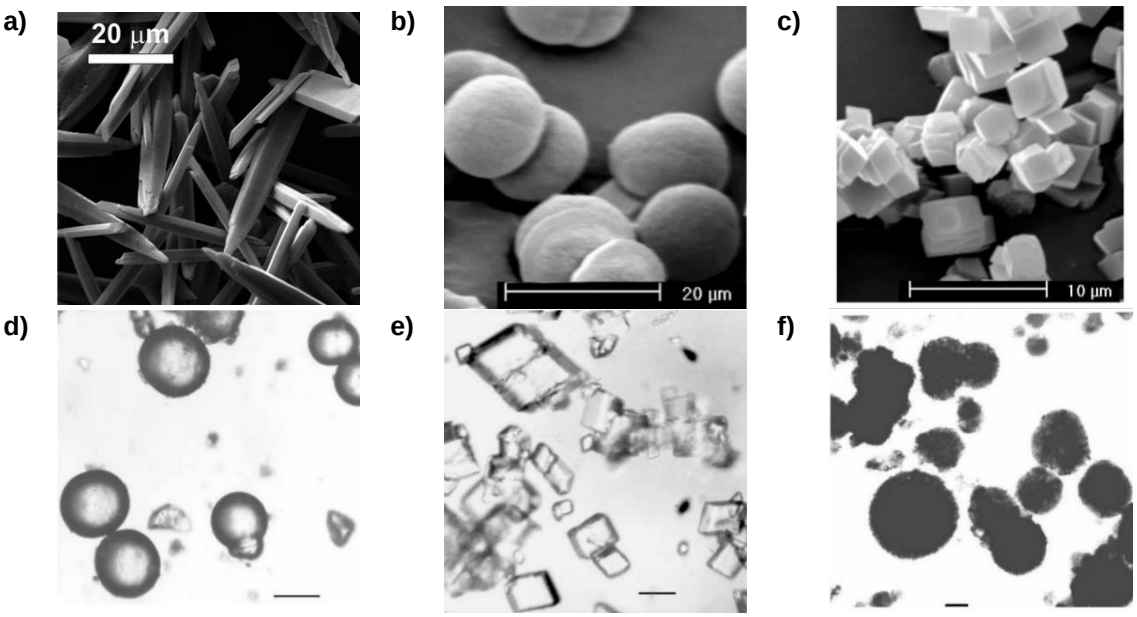

Figure 95. a) SEM image of aragonite; b) SEM image of vaterite; c) SEM image of calcite; d) Optical microscopy image of monohydratecalcite with scale bar 20 μm; e) Optical microscopy image of esahydratecalcite with scale bar 20 μm; f) Optical microscopy image of amorphous calcium carbonate with scale bar 100 μm.

The biomineralization strategies enable to have control over mineral size, shape, orientation, phase, texture and location. In biomineralization processes, the physiological environment imposes temperature and pressure. Thus, the control must occur through the change of the ionic reactants concentration and/or the use of additives, which can be either inorganic species or biological (macro)-molecules [176]. The process of crystal grows in the biomineralization is influenced by additives as small peptides [177,178], ions, soluble biopolymers [179], soluble synthetic polymers or templates [180].

In biomineralization process, it is important to discuss some of the practical aspects of crystal growth in gels. As in solution crystallization, the key for gel growth is to trigger nucleation and then allow for slow, controlled growth of the crystals. For precipitation reactions involving two components A and B (in case of $CaCO_3$ are Ca^{2+} and CO_3^{2-}), there are two typical methods for introducing A and B to the gel: single and double diffusion geometries (Figure 96). In a single diffusion set-up, one component is embedded in the gel and the other one is introduced either via a solution layered on top of the gel (Figure 96a) or as a gas phase above the gel (Figure 96b). In this geometry, the crystals are usually found near the solution/gel or vapor/gel

[177] Babu Mukkamala, S.; Powell, A. K., Biomimetic assembly of calcite microtrumpets: crystal tectonics in action. *Chemical Communications* **2004,** (8), 918-919.
[178] Gungormus, M.; Fong, H.; Kim, I. W.; Evans, J. S.; Tamerler, C.; Sarikaya, M., Regulation of in vitro Calcium Phosphate Mineralization by Combinatorially Selected Hydroxyapatite-Binding Peptides. *Biomacromolecules* **2008,** *9* (3), 966-973.
[179] Falini, G.; Gazzano, M.; Ripamonti, A., Control of the architectural assembly of octacalcium phosphate crystals in denatured collagenous matrices. *Journal of Materials Chemistry* **2000,** *10* (2), 535-538.
[180] Sone, E. D.; Zubarev, E. R.; Stupp, S. I., Supramolecular Templating of Single and Double Nanohelices of Cadmium Sulfide. *Small* **2005,** *1* (7), 694-697.

interface. Often a dense band of precipitate will be located at this interface, with larger, single crystals further down the gel column. When double diffusion is used, reservoirs containing solutions of the two reagents are physically separated on two sides of a gel column, in a U-tube or straight-tube configuration (Figure 96c), allowing diffusion of the two components into the gel from opposite ends. During the experiment, gradients of pH and concentration (supersaturation) that change with time develop along the length of the gel column, allowing access to a spectrum of conditions in one experimental set up. Generally, a band of crystals is observed to form near the center of the gel, but the exact location of crystallization depends on the gradients created along the length of the gel. Both single and double diffusion methods can be used to grow poorly soluble crystals, such as those of interest in modeling biomineralization, from two (or more) soluble reagents. In our case, we have used a single diffusion geometry with a vapor phase reactant (Figure 96b).

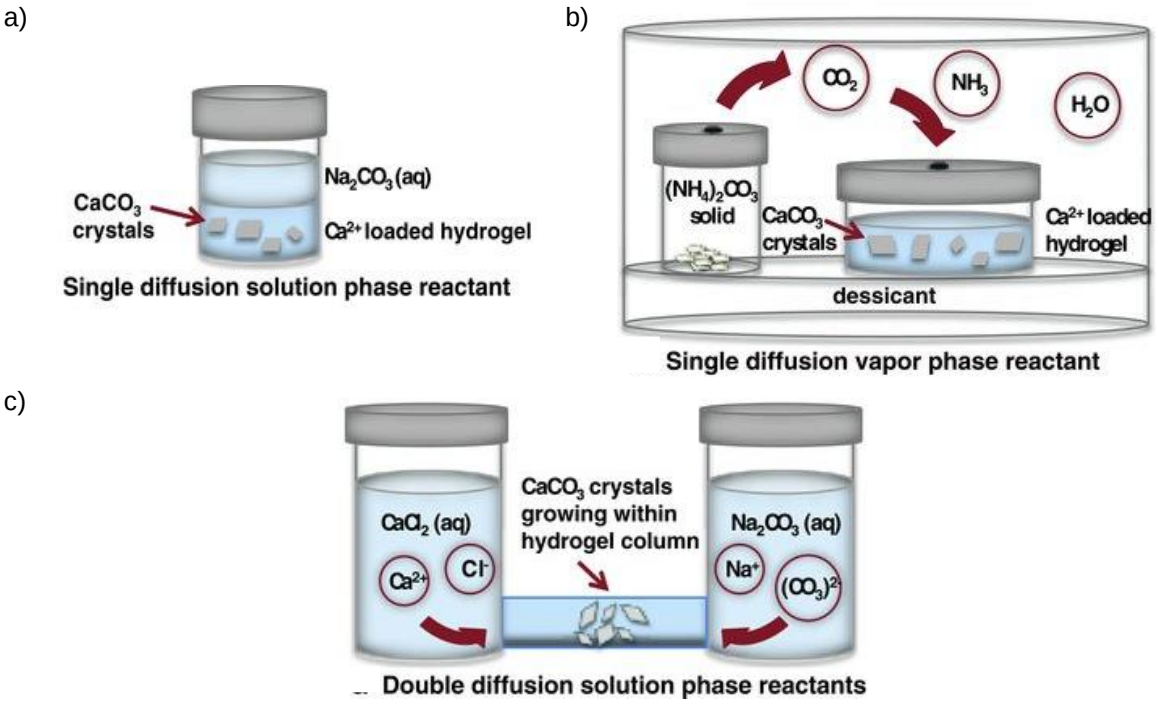

Figure 96. Schematic representation of experimental approaches used to grow calcium carbonate crystals in hydrogels: a) in the solution-based single diffusion set-up, the solution phase reactant diffuses into the gel; b) in the vapor phase single diffusion set-up, the vapor phase reactant diffuses within the sealed atmosphere of a desiccator, and reaches the hydrogel through a small hole in the lid; c) in the solution-based double diffusion system, aqueous solutions of the two reactants diffuse into opposite ends the gel and meet in the middle.

Historically, the use of gel matrices for single crystal growth has been employed as a means to control the purity, morphology and optical quality of the resulting crystals. More recently, crystal growth in gels has emerged as a popular platform for modeling biomineralization processes [181]. The increasing number of gel-like matrices identified in association with

[181] Asenath-Smith, E.; Li, H.; Keene, E. C.; Seh, Z. W.; Estroff, L. A., Crystal Growth of Calcium Carbonate in Hydrogels as a Model of Biomineralization. *Advanced Functional Materials* **2012,** *22* (14), 2891-2914.

mineralization by biological organisms motivates this interest. In matrix-mediated biomineralization, the mineralization environment is characterized by the presence of an extracellular matrix, which is a three-dimensional macromolecular assembly of proteins, polysaccharides and/or glycoproteins that mediates mineral formation. These matrices are often fibrous, porous, and hydrated networks that both provide the structural framework upon which inorganic minerals grow and serve as a source of chemical functionalities to direct nucleation and growth of the crystals. Physical gels are the most commonly encountered class of hydrogels in biomineralization systems. They are often composed of biopolymers or of polysaccharides such as agarose, pectin and cellulose, as well as proteins such as collagen, gelatin and silk fibroin.

3.5.1. Peptide Amphiphilic Low Molecular Weight Gelator

Peptide amphiphiles are a class of molecules consisting of a hydrophobic nonpeptidic tail covalently conjugated to a peptide sequence [182]. These molecules consist of three segments:

1) a hydrophobic sequence, which is commonly an alkyl tail that drives aggregation through hydrophobic collapse;
2) a β-sheet-forming peptide that promotes nanofibre formation;
3) a peptide segment that contains ionizable side chains and often an amino acid sequence of interest for biological signaling.

A particular kind of amphiphilic peptides are bolaamphiphiles (two-headed amphiphiles). They are named after the “bola”, which is a South American weapon made of two balls connected by a string. As with conventional amphiphiles, the chemical functionality of the headgroups and linking group can be varied to change the aggregation properties. Some groups have reported the design and synthesis of hydrogelators and/or organogelators that have this skeleton. Tomasini and co-worker have reported the hydrogel formed by two units of Phe-D-Oxd bind with azelaic acid (Figure 97). They also replaced the D-Oxd moiety with a D-Pro unit (Figure 97), to if the presence of the Oxd moiety was essential for the formation of gels.

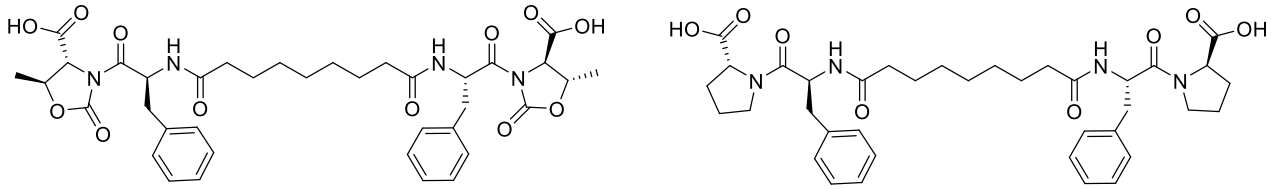

Figure 97. Molecular structures of bolaamphiphilic compounds **52** and **53**.

The hyrogelator $CH_2(C_3H_6CO\text{-}L\text{-}Phe\text{-}D\text{-}Oxd\text{-}OH)_2$ **52**, it is an efficient and biocompatible low molecular weight gelator that has been used as “Trojan horse” for drug delivery [183].

[182] Greenfield, M. A.; Hoffman, J. R.; Olvera de la Cruz, M.; Stupp, S. I., Tunable Mechanics of Peptide Nanofiber Gels. *Langmuir* **2010,** *26* (5), 3641-3647.

Compound $CH_2(C_3H_6CO\text{-L-Phe-D-Pro-OH})_2$ **53** has the same structure, but the D-Oxd moiety has been replaced with a D-Pro moiety, to check if the presence of the Oxd moiety is essential for the existence of the properties of the supramolecular material .

Molecules **52** and **53** are long chain derivatives and belong to the family of bolaamphiphiles. Synthetic bolaamphiphiles try to reproduce the unusual architecture of monolayered membranes found in archaebacteria but commonly do not use the same building blocks, which are difficult to synthesize. The synthesis of these molecules has been previously described by Tomasini and o-worker [184] and may be obtained easily in multigram scale (Scheme 12).

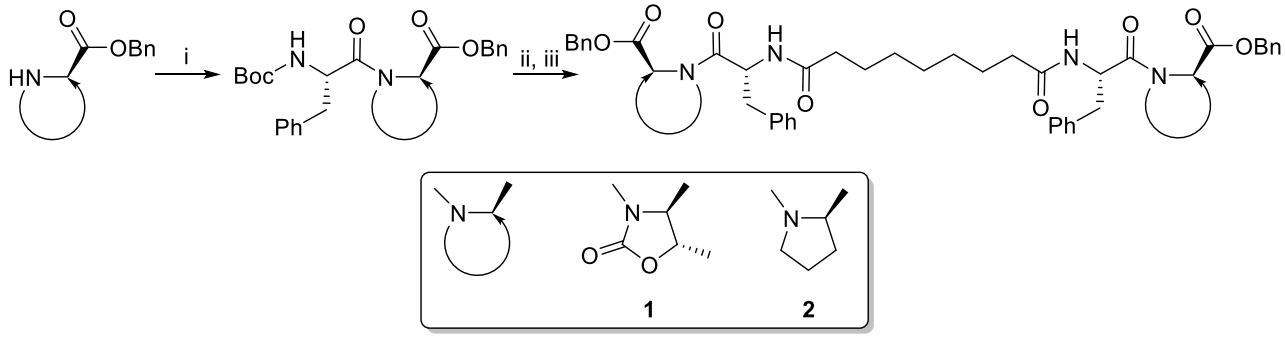

Scheme 12. Reagents and conditions: (i) Boc-L-Phe-OH (1 equiv.), HBTU (1.1 equiv.), DBU (2.1 equiv.), dry acetonitrile, r.t., 50 min; (ii) TFA (18 equiv.), dry dichloromethane, r.t., 4h; (iii) azelaic acid (1 equiv.), HBTU (1.1 equiv.), DIEA (3 equiv.), dry acetonitrile, r.t., 50 min.

The study on the self assembly capability of molecules **52** and **53** showed that while molecule **53** does not form gel in any concentration, molecule **52** forms a gel in 10 mM concentration and a highly viscous sol in 5 mM concentration (Figure 98).

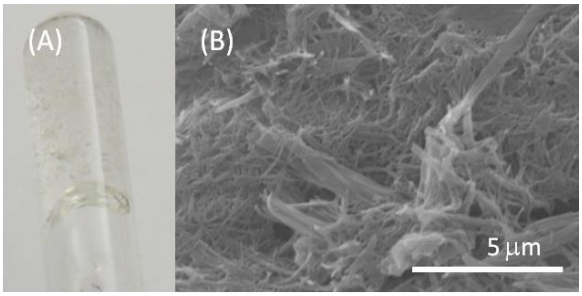

Figure 98. (A) Photograph of hydrogel obtained from a 10 mM solution of molecule **52** in a 10 mM $CaCl_2$ solution in 9:1 (*v*/*v*) mixture of H_2O/EtOH; (B) scanning electron microscopy picture of the corresponding xerogel.

The assembly of molecule **53** was investigated by dynamic light scattering. This molecule assembled in big structures having a diameter ranging from 100 nm to about 1 μm in 1 mM

[183] Castellucci, N.; Sartor, G.; Calonghi, N.; Parolin, C.; Falini, G.; Tomasini, C., A peptidic hydrogel that may behave as a "Trojan Horse". *Beilstein Journal of Organic Chemistry* **2013,** *9*, 417-424.
[184] Castellucci, N.; Angelici, G.; Falini, G.; Monari, M.; Tomasini, C., L-Phe-D-Oxd: A Privileged Scaffold for the Formation of Supramolecular Materials. *European Journal of Organic Chemistry* **2011,** *2011* (16), 3082-3088.

solution (Figure 99a). The concentration of these species increased, by increasing the molecule **53** concentration. Indeed, upon 0.45 μm filtration, only particles having a size of about 100 nm were observed from the 1 mM and the 5 mM solution (Figure 99), while from the 10 mM solution small particles of about 1 nm were observed. This information suggests that in 10 mM concentration the 100 nm particles aggregate to form bigger structures, that are removed by 0.45 μm filtration, thus leaving in solution only single molecules, having a size of about 1 nm (Figure 99b). Beside the characterization on molecule **53** aggregation as function of its concentration, molecule **53** solutions were used for the $CaCO_3$ precipitation experiments without applying any filtration procedure.

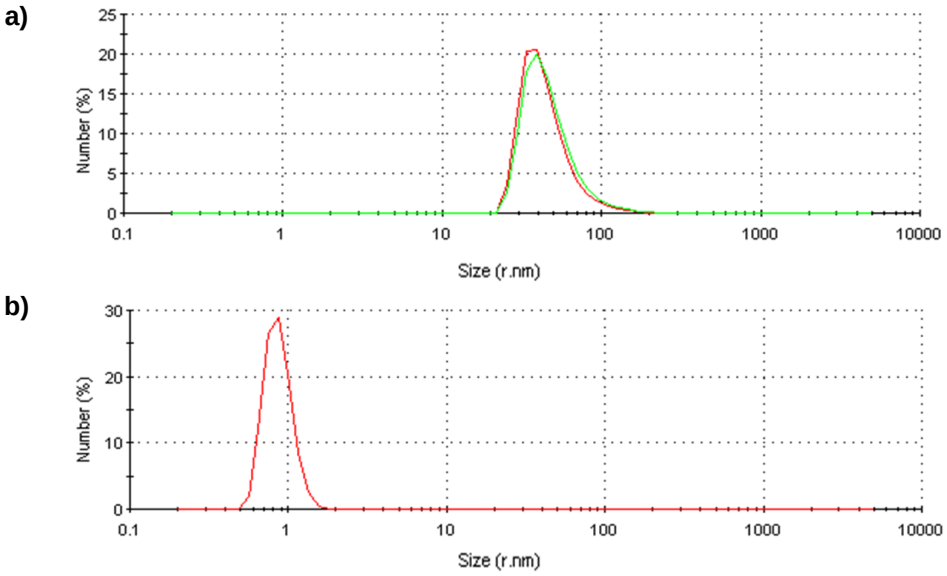

Figure 99. SDS profiles of size distribution numbers of the molecule **53** particles solution after 450 nm filtration. (a) 1 mM solution [red] and 5 mM solution [green]; (b) 10 mM solution.

3.5.2. $CaCO_3$ Precipitation Experiments

The precipitation experiments of $CaCO_3$ were made by the vapour diffusion method described above. In this method, vapours of $CO_{2(g)}$ and $NH_{3(g)}$ from $(NH_4)_2CO_{3(s)}$ diffuse into a $CaCl_2$ solution, optionally containing additives. A first set of crystallization experiments was carried by precipitating $CaCO_3$ in a 9/1 (*v*/*v*) H_2O/EtOH mixture, an optimal solvent for molecules **52** and **53** that also efficiently dissolves $CaCl_2$ with a final concentration 10 or 100 mM.

The presence of EtOH causes a reduction of the solubility of $CaCO_3$. This implies that nucleation and growth processes occur at lower values of supersaturation than that in pure water. The presence of EtOH also causes a reduction of the hydration sphere of the ions. In this process, the solvation enthalpy does not change significantly, while it is significantly reduced to the perturbation of the ion on the structure of the solvent. Thus, the reduction of the sphere of hydration in the presence of EtOH is mainly due to an entropic factor. This

facilities the crystal nucleation and growth process, as the ion incorporation into the crystalline structure requires de-solvation.

In agreement with the above considerations, both from 10 mM $CaCl_2$ and 100 mM $CaCl_2$ in 9/1 (*v*/*v*) H_2O/EtOH mixture, the precipitation of calcite, the most stable $CaCO_3$ polymorph, was exclusively observed (Figure 100).

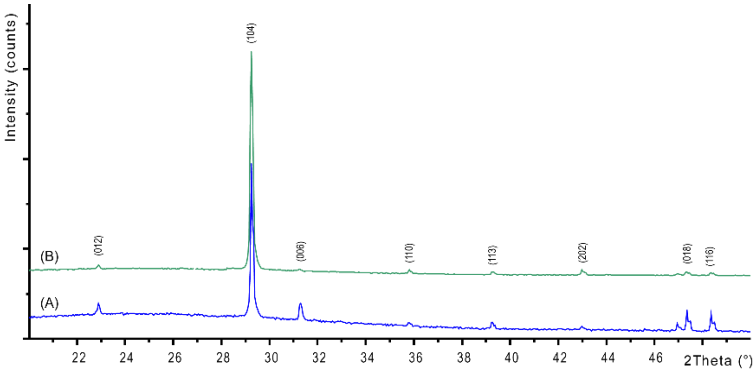

Figure 100. XRD patterns of calcium carbonate precipitates from a 9:1 (v/v) water/ethanol mixture containing 10 mM (A) or 100 mM (B) $CaCl_2$. The Miller indexes of calcite are reported.

The induced nucleation of $CaCO_3$ causes a decrease in the average size of the crystals and an increase in density of precipitation, because the crystal nuclei number increased. The Ca^{2+} mass balance determined the stop of the growth and the average size of the crystals.

Calcite precipitated forming perfect rhombohedra that showed only {10.4} faces and the size of the crystals was from 10 μm to 100 μm and from 5 μm to 50 μm the 10 mM $CaCl_2$ (low supersaturation) and the 100 mM $CaCl_2$ (high supersaturation) solution, respectively (Figure 101).

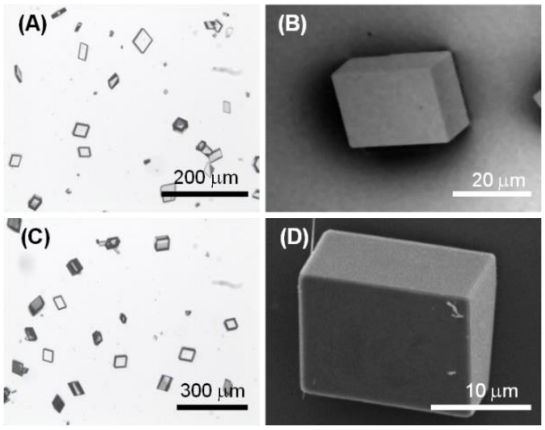

Figure 101. Optical and scanning electron microscopy pictures of calcite crystals precipitated from the 9/1 (*v*/*v*) H_2O/EtOH mixture from a 10 mm (A, B) or 100 mM (C, D) $CaCl_2$ solution. These pictures are representative of the entire population of crystals.

The effect of molecules **52** and **53** on the $CaCO_3$ precipitation was studied in several conditions, all having a 10 mM $CaCl_2$ in 9:1 H_2O/EtOH mixture. Several concentrations of both molecules have been analyzed: 1 mM, 5 mM or 10 mM. For molecule **53**, the study was also carried out in 100 mM $CaCl_2$ solution, as molecule **52** is not soluble in 100 mM $CaCl_2$ solution.

The X-ray diffraction analysis of all the samples showed diffraction patterns in which only peaks associable to calcite were observed (Figure 102).

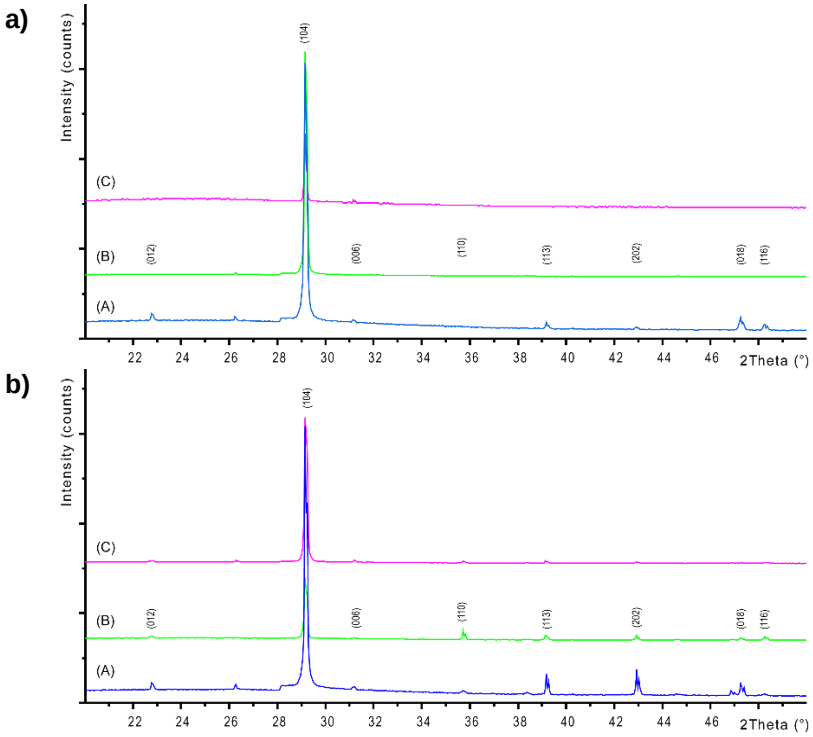

Figure 102. a) XRD patterns of calcium carbonate precipitates from a 9:1 (v/v) water/ethanol mixture containing 10 mM ($CaCl_2$ in the presence of 1 mM (A), 5 mM (B) or 10 mM (C) of molecule **52**. The Miller indexes of calcite are reported. b) XRD patterns of calcium carbonate precipitates from a 9:1 (v/v) water/ethanol mixture containing 10 mM ($CaCl_2$ in the presence of 1 mM (A), 5 mM (B) or 10 mM (C) of molecule **53**. The Miller indexes of calcite are reported.

Molecule **52** has the aptitude to form fibrous structures that can generate hydrogels. At a concentration of 1 mM the molecule does not make gels. In this condition, with a Ca^{2+}/molecule **52** molar ratio = 10, the effect on the nucleation and growth of $CaCO_3$ must be attributed to the molecule in its non supramolecular assemblies. The images at the optical microscope (Figure 103A) of the precipitated particles show that they are single crystals and no aggregates, having an average size of about 40 μm, similar to that of the crystals precipitated in the absence of molecule **52**. From these images the co-presence of an amorphous precipitate, probably due to the partial precipitation of molecule **52**, is also observed. The amorphous state was deduced from the observation that the material does not present any crystalline morphology and that under an optical microscope with cross-polar it does not show any birefringence effect. The SEM images (Figure 103B and 103C) provide more details on the shape and morphology of the crystals. Almost perfect rhombohedral crystals were observed. However, the crystals in addition to the {10.4} faces showed the minimum areas of interaction that suggest a partial adsorption of the molecule **52** on the crystal.

Molecule **52** forms a highly viscous sol at a 5 mM, with a Ca^{2+}/molecule **52** molar ratio = 2. Here, the molecule **52** effect on the nucleation and growth of $CaCO_3$ is driven by the presence

of supramolecular assemblies in solution. Optical microscopy images (Figure 104A) of the precipitated particles in this condition show that they are single crystals and no aggregates having an average size of about 30 μm, smaller than that of the crystals precipitated in the absence of molecule **52**. This effect may be due to an inhibition of the growth process, which involves the adsorption of the assembled molecule **52** on the crystals. The crystals show a not homogeneous diffusion of visible light, with dark areas in the central region of the faces, where the adsorption is supposed to occur. The SEM image in Figure 104B shows an aggregate of molecule **52** forming needle-like units located on $CaCO_3$ a crystal face. In the SEM Figure 104C, an aggregate of molecule **52** is partially entrapped into $CaCO_3$ crystal. Thus, it can act as a site for the heterogeneous nucleation of crystals of $CaCO_3$ and became completely entrapped into the crystals (dark areas on the crystals in the optical microscope images). It is also noted that the rhombohedral morphology of the crystals was altered. The crystals in addition to faces {10.4}, {18.0} faces were shown, probably due to the interaction of molecule **52** with these crystalline planes.

At 10 mM concentration, molecule **52** forms gels. In this condition, Ca^{2+}/molecule **52** molar ratio = 1, the effect on the nucleation and growth of $CaCO_3$ is due to the presence of fibrous structures from the molecule **52** (Figure 98B). Here, the crystal growth occurs in the confined space generated three dimensional fibrous network making the gel. In the gel, the ion diffusion is slower than in solution and convection is absent. This determines a slower process of crystal growth. The images at the optical microscope (Figure 105A) of the precipitated particles show that they are single crystals, not aggregates and having an average size of about 50 μm, bigger than that of the crystals precipitated in the absence of molecule **52**. This effect may be due to an inhibition of the nucleation process. The crystals do not scatter light. This indicates that the gel fibres are entrapped into the crystalline structure. A similar observation has been reported for the growth of calcite in agarose gel. The SEM image (Figure 105B) show the co-precipitation of $CaCO_3$ crystals of varying shapes. These are probably due to structural reorganization of the gel regions occurred during the process of crystallization. The other SEM image (Figure 105C) illustrates how the $CaCO_3$ crystals have almost completely lost the rhombohedral morphology. In them, the {10.4} faces are little exposed and more extended appear {kh.0} faces, indicating molecule **52** interaction on these family of crystallographic planes. The FT-IR spectra (Figure 106) conformed the above observations, in the them absorption bands due to the molecule **52** and calcite are observed. The relative intensity of the absorption bands due to molecule **52** increases with its concentration in solution. Unfortunately, the co-presence of calcite crystals and of an amorphous precipitate containing molecules **52** does not allow a quantification of molecule **52** entrapped in the crystals.

The molecule **53**, as described above, does not form gel, but generates supramolecular assemblies (≈ 100 nm) that aggregate in bigger particles.

Figure 103D and Figure 103E illustrates the optical and electron microscope images of the precipitate obtained in the presence of 1 mM molecule **53 (**Ca^{2+}/molecule **53** molar ratio = 10). The optical microscope images (Figure 103E) of the precipitated particles show that they are single crystals (Figure 106), not aggregated and having an average size of about 40 μm, similar to that of the crystals precipitated in the absence of molecule **53**. The SEM images (Figure 103E and 103F) show that the rhombohedral crystals morphology was not significantly altered. However, the crystals showed on the {10.4} faces zones of interaction with the molecule characterized by a considerable roughness. This interaction appears as a surface phenomenon in the faces {10.4} suggesting that molecule **53** affected the crystal growth process without specifically interacting with some crystalline planes. This not specific interaction generated in some crystals the appearance of {kh.0} faces together with the rhombohedral {10.4} faces.

Figure 104D and Figure 104E shows the optical and electron microscope images of the precipitate obtained in the presence of 5 mM molecule **53** (Ca^{2+}/molecule **53** molar ratio = 2). The optical microscope images (Figure 104D) show single crystal particles, not aggregated and having an average size of about 40 μm, as those precipitated in the absence of molecule **53**. SEM images (Figure 104D and 104E) showed that in the rhombohedral crystals, on {10.4} faces, presented zones characterized by a considerable roughness. Moreover, in some crystals cavities of sub-micrometer dimensions (Figure 104E) were also observed on the same faces. These cavities appeared as dark regions under the optical microscope. This crystallization condition also caused the formation of shapeless aggregates (Figure 104E), probably due to precipitation of molecule **53**.

The optical and electron microscope images of the precipitate obtained in the presence 10 mM molecule **53** (Ca^{2+}/molecule **53** molar ratio = 1) are illustrated in Figure 105D and Figure 105E. The optical microscopy image (Figure 105D) shows that crystals are aggregated and each crystal has average size of about 20 μm. SEM images (Figure 105E and 105F) show that in the faces {10.4} cavities along the direction parallel to the rhombohedral axis were present. These cavities had a spherical shape. The shape of the cavity, coupled to the DLS observation listed above, suggested that in these conditions molecule **53** form aggregates of 100 nm supramolecular assemblies, that act as template for the crystal nucleation and growth. This outcome has been reported for liposomes, and other spherical particles, that efficiently sculpture calcite crystals. The above observation are in agreement with the FT-IR spectra of the samples (Figure 107). The intensity of the absorption bands due to molecule **53** increases with its concentration in solution, with respect to those due to $CaCO_3$. Unfortunately, as observed for molecule **52**, the co-presence of calcite crystals and of an amorphous precipitate does not allow a quantification of the molecule **53** entrapped in the crystals.

The influence of molecule **53** on the precipitation of $CaCO_3$ was also studied using a 100 mM $CaCl_2$ solution. The increase in Ca^{2+} concentration caused a higher starting $CaCO_3$

supersaturation and a decrease of Ca^{2+}/molecule **53** molar ratio. Figure 108 shows SEM images of the crystals obtained in the presence of different concentrations of molecule **53**. At a concentration of 1 mM (Figure 108A, 108B and 108C) rhombohedral crystals formed, which sometimes aggregated. In this condition molecule **53** seems do not interact with crystals (Ca^{2+}/molecule **53** molar ratio = 0.01). With the increase of the concentration of molecule **53** (10 mM, Ca^{2+}/molecule **53** molar ratio = 0.1) calcite crystals showed {hk.0} faces together with the rhombohedral {10.4} faces. This observation suggested that the capability of molecule **53** to act as crystal growth modifier is also affected by the starting conditions of supersaturation.

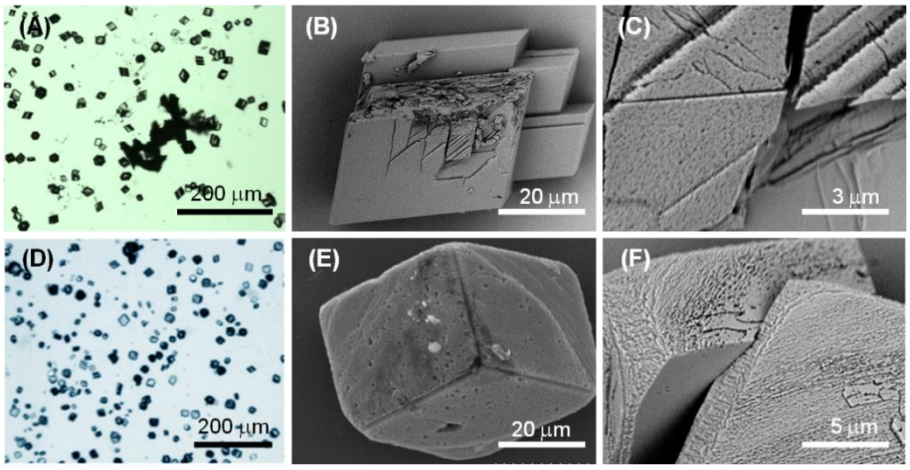

Figure 103. Optical (A, D) and scanning electron microscopy (B, C, E, F) pictures of calcite crystals precipitated from the 9/1 (v/v) H_2O/EtOH mixture in the presence of 1 mM molecule **52** (A-C) or molecule **53** (D-F). These pictures are representative of the entire population of crystals.

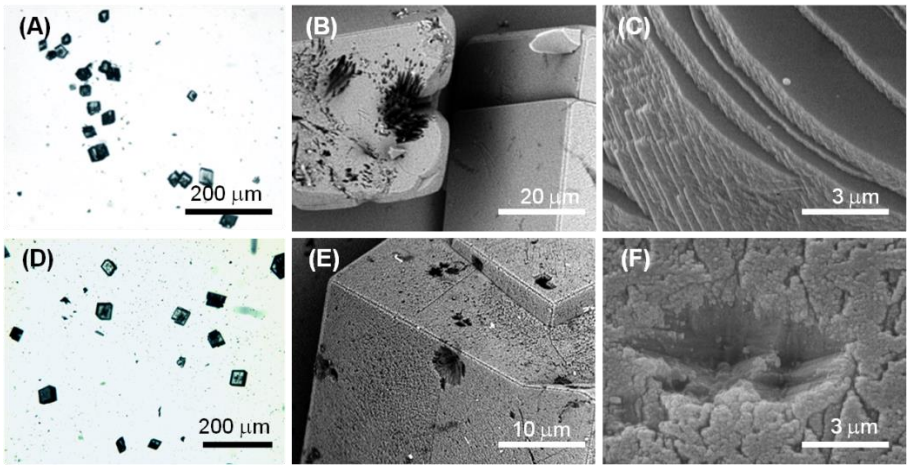

Figure 104. Optical (A, D) and scanning electron microscopy (B, C, E, F) pictures of calcite crystals precipitated from the 9/1 (*v*/*v*) H_2O/EtOH mixture in the presence of 5 mM molecule **52** (A-C) or molecule **53** (D-F). These pictures are representative of the entire population of crystals.

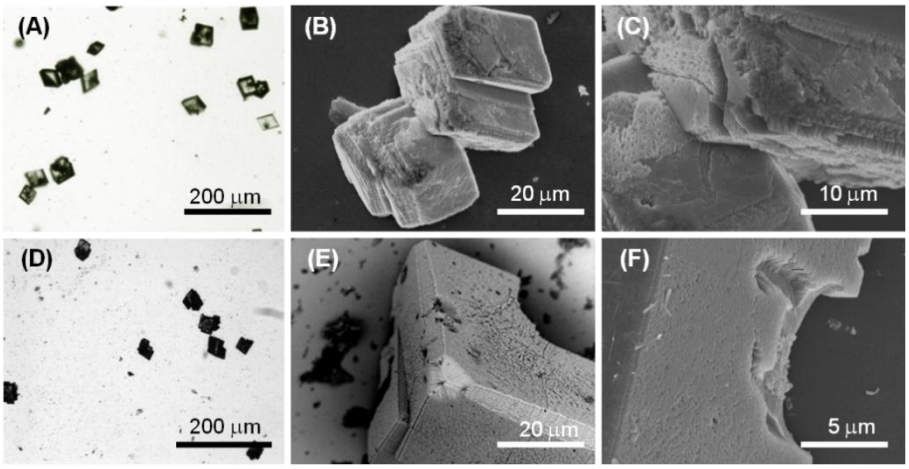

Figure 105. Optical (A, D) and scanning electron microscopy (B, C, E, F) pictures of calcite crystals precipitated from the 9/1 (v/*v*) H_2O/EtOH mixture in the presence of 10 mM molecule **52** (A-C) or molecule **52** (D-F). These pictures are representative of the entire population of crystals.

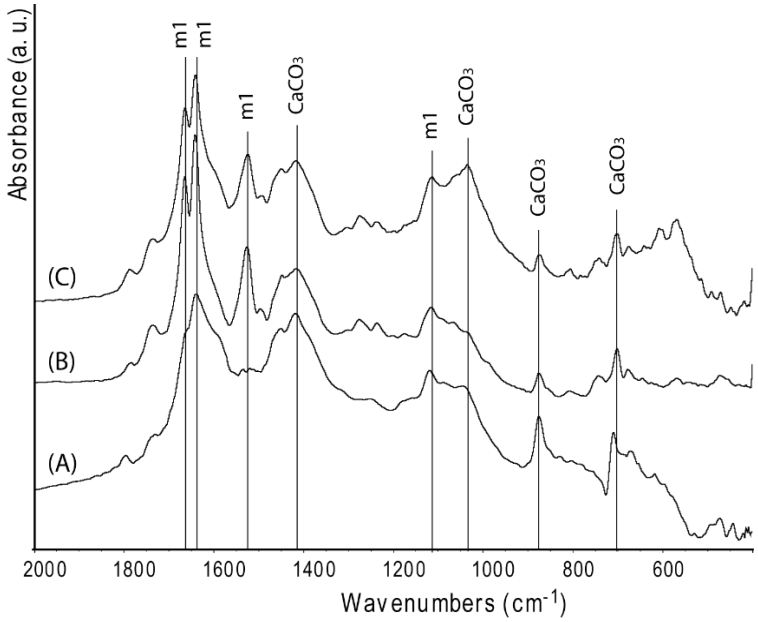

Figure 106. FTIR spectra of calcium carbonate precipitates from a 9:1 (v/v) water/ethanol mixture containing 10 mM ($CaCl_2$ in the presence of 1 mM (A), 5 mM (B) or 10 mM (C) of molecule **52**. The absorption bands due to molecule **52** (m1) and calcite ($CaCO_3$) are indicated.

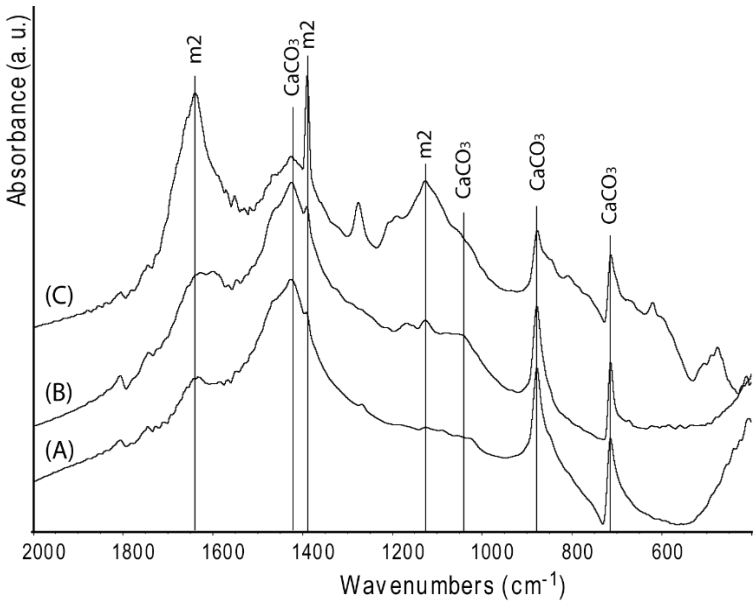

Figure 107. FTIR spectra of calcium carbonate precipitates from a 9:1 (v/v) water/ethanol mixture containing 10 mM ($CaCl_2$ in the presence of 1 mM (A), 5 mM (B) or 10 mM (C) of molecule **53**. The absorption bands due to molecule **53** (m2) and calcite ($CaCO_3$) are indicated.

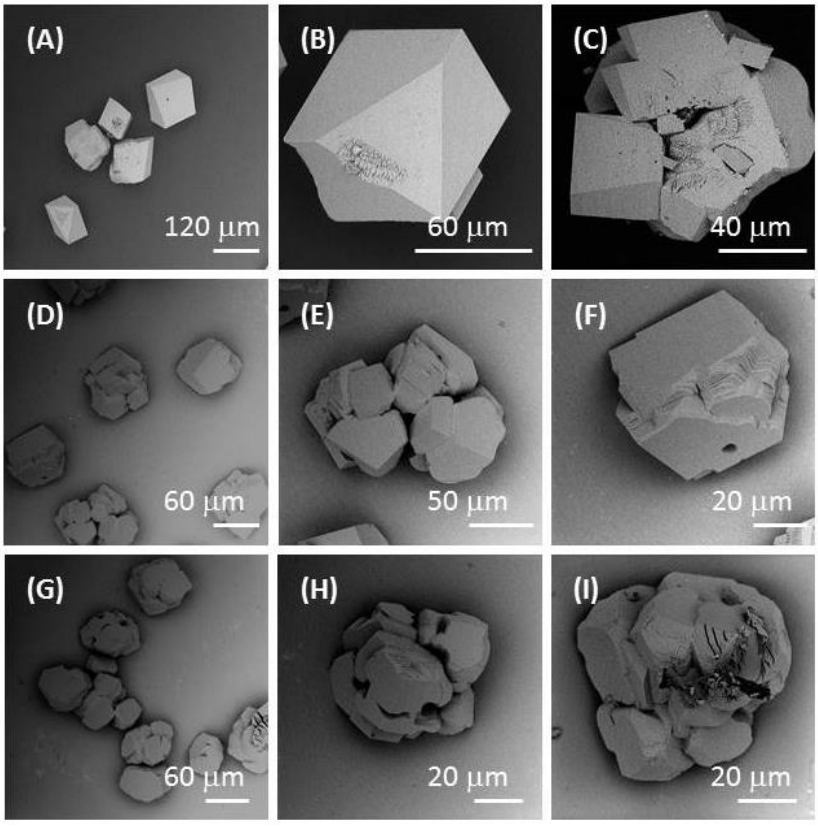

Figure 108. SEM images of calcium carbonate precipitates obtained from a 100 mM $CaCl_2$ solution in the presence of 1 mM (A-C), 5 mM (D-F) or 10 mM (G-I) of molecule **53**.

A clear view on the effect of the foldamers, molecule **52** and molecule **53**, on the precipitation of $CaCO_3$ appears from the study of Table 30. The assembly of these molecules, which have the same ionizable carboxylic groups, change as function of their sterochemistry. In the case of molecule **53** the assembly state is a function of the concentration. The molecules **52** and **53**

should interact with the crystallizing calcite in their assembled form, since the assembly was studied in the same conditions of Ca^{2+} concentration and pH of $CaCO_3$ precipitation. Thus, it is their physical state that governs the interactions. The diverse physical states should bring at a different space distribution of the interacting ionizable carboxylic groups. As a consequence a diverse interaction with $CaCO_3$ is expected. This concept was deeply investigated for example by using self assembled monolayers, and liposomes as counterpart of foldamers. The reported observations also agree with the behaviour of some biomineralization proteins that are assumed to adopt an ordered conformation, and geometry of ionizable functional groups, to interact with biominerals.

Table 30. Summary of the assembly state of molecule **52** and **53** in the 10 mM $CaCl_2$ solution and their capability to act as calcite shape and morphology modifiers.

	molecule **1**				molecule **2**			
			$CaCO_3$ precipitation				$CaCO_3$ precipitation	
conc (mM)	Ca^{2+}/mol. molar ratio	physical state	polymorph / size (µm)	shape / morphology	Ca^{2+}/mol molar ratio	physical state	polymorph / size (µm)	shape / morphology
0	-	-	calcite / 40	rhomb. / {10.4}	-	-	calcite / 40	rhomb. / {10.4}
1	10	solution	calcite / 40	rhomb. / {10.4}	10	supram. aggregates	calcite / 40	rhomb. / {10.4}
5	2	highly viscous sol	calcite / 30	rhomb. / {10.4} - {hk.0}	2	supram. aggregates	calcite / 40	rhomb. / {10.4} /cavities
10	1.0	gel	calcite / 50	rhomb. / {10.4} - {hk.0}	1.0	supram. aggregates	calcite / 20	rhomb. / {10.4} - {hk.0} / cavities

4. Conclusions

This thesis describes the synthesis, the conformational analysis and the applications of pseudopetide foldamers containing the 4-carboxy-5-methyl-oxazolidin-2-one moiety or the pyroglutamic acid unit. These molecules mimic a proline group and have been applied to the formation of oligomers that in solution may easily adopt a stable secondary structure. These pseudoprolines block the peptide bond always in the *trans* conformation, because the nitrogen atom of the ring is adjacent to both an exocyclic and an endocyclic carbonyl group, forcing them to a strict *trans* conformation. This remarkable property induces a constrain in the pseudopeptide chain that may help the formation of supramolecular materials.

Following a simple methodology we have efficiently prepared a variety of foldamers, whose proprieties may be changed choosing different amino acids, thus providing several secondary structures.

We have prepared foldamers containing the 1,2,3-triazole unit that efficiently mimics a peptide bond: when it is introduced in the L-Ala-D-Oxd-Tri unit, this system folds in a β-turn secondary structure.

Another class of oligomers, containing the L-Ala-D-Oxd moiety, are versatile backbones for the investigation of the electron transfer mechanism, as they can modulate the distance between the donor and the acceptor units. The same class of oligomers may also be used for decoration of gold nano particles, that mimic the shape of globular protein and may be used for drug delivery applications.

If an aromatic amino acid (Phe, Tyr or Trp) is introduced in the foldamer backbone, the properties of the foldamer will change drastically, as the β-sheet conformation is favoured, thus providing the formation of nanofibres that may trap water or organic solvents, with the formation of hydrogel or organogels. Physical gels are very versatile materials, as we could obtain both organogels and hydrolegs that were used for several applications: we prepared matrices for cells encapsulation that may be useful in the field of regenerative medicine. Other interesting applications are the use of hydrogels as pollutant adsorbent for the water remediation and as matrices in biomineralization processes. Finally a rheological study has been carried out on the most promising gels, that demonstrated that these gels are well built solids with interesting viscoelastic and thermoreversible properties.

5. Experimental Section

(4S,5S)-4-(Hydroxymethyl)-5-methyloxazolidin-2-one (D-1)
D-Thr-OMe (2.1 g, 12.6 mmol) was stirred in THF (15 mL) at room temperature until it was fully dissolved. Then triphosgene (3.9 g, 13.2 mmol) was added and the reaction was stirred and refluxed for 1 hour in an apparatus equipped with refrigerator and a trap containing $CaCl_2$ and NaOH. Then the mixture was cooled to room temperature and the solvent was removed in vacuo. The (4S,5S)-4-(carboxymethyl)-5-methyloxazolidin-2-one was obtained in 86% yield (1.72 g) and directly transformed in **D1**. Solid $NaBH_4$ (1.64 g, 11 mmol) was added to a stirred solution of (4S,5S)-4-(carboxymethyl)-5-methyloxazolidin-2-one (1.59 g, 10 mmol) in dry ethanol at 0 °C. After 5 minutes, the mixture was heated at room temperature and stirred for 1.5 hour, then a saturated aqueous solution of NH_4Cl (2.5 mL) was added and the mixture was stirred for additional 45 minutes. Then the mixture was filtered to eliminated the inorganic salts and concentrated in vacuo, leading to the formation of a waxy solid in 82% yield (1.08 g).
$[\alpha]_D^{20}$ = - 58.8 (c = 1.5, $CHCl_3$); IR (CH_2Cl_2, 3 Mm): υ 3611, 3452, 3280, 1760 cm^{-1}; ^1H NMR ($CDCl_3$, 400 MHz): δ 1.44 (3H, d, *J* = 7.2 Hz, Oxd-CH_3), 3.49-3.60 (2H, m, CHN-Oxd + CHNCHH), 3.65-3.79 (1H, m, CHN-CHH), 4.51 (1H, quintet, *J* = 5.6 Hz, CHO-Oxd), 6.73 (1H, bs, NH); ^{13}C NMR ($CDCl_3$, 100 MHz): δ 20.3, 60.9, 62.8, 75.6, 160.3. Anal. Calcd. for $C_5H_9NO_3$: C, 45.80; H, 6.92; N, 10.68. Found: C, 45.78; H, 6.91; N, 10.70.

[(4S,5S)-5-Methyl-2-oxooxazolidin-4-yl]methyl methylparatoluensulfonate (D-2)
To a stirred solution of **D-1** (1.6 g, 12.6 mmol) and dimethylaminopyridine (0.13 g, 1.1 mmol) in pyridine (12 mL) was added tosyl chloride (3.4 g, 17.7 mmol) at 0 °C and stirring was maintained for 18 hours at room temperature.
After the end of the reaction, checked by TLC, CH_2Cl_2 (50 mL) was added and the mixture was washed with brine (3 x 30mL). The organic phase was dried over sodium sulfate and concentrated under low pressure. The product was obtained pure after silica gel chromatography (cyclohexane/ethyl acetate 80:20 → cyclohexane/ethyl acetate 10:90 as eluant) in 74% overall yield as a white solid (2.66 g).
M.p. = 95-98 °C; $[\alpha]_D^{20}$ = - 32.2 (c = 1.5, $CHCl_3$); IR (CH_2Cl_2, 3 Mm): υ 3441, 1767, 1365 cm^{-1}; ^1H NMR ($CDCl_3$, 400 MHz): δ 1.38 (3H, d, *J* = 6.0 Hz, Oxd-CH_3), 2.43 (3H, s, Ar-CH_3), 3.64 (1H, dt, *J* = 5.6, 5.3 Hz CHN-Oxd), 3.96 (2H, dd, *J* = 5.3, Hz, CH_2-Ts), 4.37 (1H, quintet, *J* = 5.6 Hz, CHO-Oxd), 6,40 (1H, bs, NH), 7.24 (2H, d, *J* = 8.4 Hz, Ar), 7.75 (2H, d, *J* = 8.4 Hz, Ar); ^{13}C NMR ($CDCl_3$, 100 MHz): δ 20.4, 21.7, 57.6, 69.4, 75.3, 127.8, 128.1, 130.0 130.3, 132.0, 145.5, 158.7. Anal. Calcd. for $C_{12}H_{15}NO_5S$: C, 50.52; H, 5.30; N, 4.91. Found: C, 50.55; H, 5.28; N, 4.94.

(4S,5S)- 4-(Azidomethyl)-5-methyloxazolidin-2-one (D-3)
To a stirred solution of compound **D-2** (2.63 g, 9.2 mmol) in dry DMF (15 mL), sodium azide (0.66 g, 10.2 mmol) was added. The mixture was stirred under microwave at 150W for 25 minutes. After the end of the reaction, checked by TLC, ethyl acetate (40 mL) was added to the mixture and the organic phase was washed with water and with a 1M aqueous solution of HCl. The organic layer was isolated, dried over sodium sulfate and concentrated under low pressure. The product was obtained pure without any further purification in 79% yield (1.14 g) as a yellow oil.
$[\alpha]_D^{20}$ = - 37.5 (c 0.9, $CHCl_3$); IR (CH_2Cl_2, 3 Mm): v 3440, 2120, 1764 cm^{-1}; ^1H NMR ($CDCl_3$, 400 MHz): δ 1.44 (3H, d, *J* = 6.4 Hz, Oxd-CH_3), 3.44 (2H, ABX, J_{AB} = 12.4 Hz, J_{AX} = 5.2 Hz, J_{BX} = 5.6 Hz, CH_2-N_3), 3.55 (1H, dd, *J* = 5.2, 12.0 Hz, CHN), 4.44 (1H, dq, *J* = 0.8, 6.8 Hz), 6.87 (1H, bs, NH); ^{13}C NMR ($CDCl_3$, 100 MHz): δ 20.4, 53.5, 58.4, 76.3, 159.2. Anal. Calcd. for $C_5H_8N_4O_2$: C, 38.46; H, 5.16; N, 35.88. Found: C, 38.42; H, 5.19; N, 35.85.

D-Oxd-Tri-COOBn (D-4)
To a stirred solution of benzyl propiolate (0.25 g, 1.6 mmol) in dry acetonitrile (10 mL), diisopropylethylamine (3.2 mmol, 0.56 mL), lutidine (3.2 mmol, 0.37 mL), CuI (0.16 mmol, 0.03 g) and azide **D-3** (1.6 mmol, 0.25 g) were added in this order at room temperature. Stirring

was maintained for about 2 hours at room temperature, then, after checking the reaction by TLC, the acetonitrile was removed under reduced pressure, replaced with ethyl acetate and washed twice with brine (3 x 30 mL). The organic layer was isolated, dried over sodium sulfate and concentrated under reduced pressure. The product was obtained pure after silica gel chromatography (cyclohexane/ethyl acetate 30:70 → ethyl acetate 100% as eluant) in 78% yield (0.39 g) as a white solid.
M.p. = 165-166 °C; $[\alpha]_D^{20}$ = - 52.0 (c 1.2, $CHCl_3$); IR (CH_2Cl_2, 3 Mm): v 3436, 3284, 1765 cm^{-1}; ^1H NMR ($CDCl_3$, 400 MHz): δ 1.36 (3H, d, *J* = 6.4 Hz, $CHCH_3$), 3.95 (1H, m, CHN), 4.41-4.55 (3H, m, CHO + CH_2CH), 5.38 (2H, AB, *J* = 12.8 Hz, CH_2Ph), 7.03 (1H, bs, NH), 7.25-7.47 (5H, m, Ph), 8.11 (1H, s, CH-triazole); ^{13}C NMR ($CDCl_3$, 100 MHz): δ 20.2, 53.1, 58.5, 67.0, 75.7, 128.6, 128.7, 129.0, 135.2, 158.4, 160.3. Anal. Calcd. for $C_{15}H_{16}N_4O_4$: C, 56.96; H, 5.10; N, 17.71. Found: C, 56.91; H, 5.14; N, 17.65.

Boc-L-Ala-D-Oxd-Tri-COOBn (5)
A stirred solution of Boc-L-Ala-OH (0.09 g, 0.47 mmol) and HBTU (0.20 g, 0.52 mmol) in dry acetonitrile (20 mL) was stirred under nitrogen atmosphere for 10 minutes at room temperature. Then D-Oxd-Tri-OBn **D-4** (0.150 g, 0.474 mmol) and DBU (0.141 mL, 0.948 mmol) in dry acetonitrile (10 mL) were added at room temperature. The solution was stirred for 2 hours under nitrogen atmosphere, then acetonitrile was removed under reduced pressure and replaced with ethyl acetate. The mixture was washed with brine (1 x 30 mL), 1 N aqueous HCl (1 x 30 mL), and with a concentrated solution of $NaHCO_3$ (1 x 30 mL), dried over sodium sulphate and concentrated in vacuo. The product was obtained pure after silica gel chromatography (cyclohexane/ethyl acetate 30:70 → ethyl acetate 100% as eluant) as a white solid in 95% yield (0.22 g).
M.p. = 155-156 °C; $[\alpha]_D^{20}$ = - 26.9; (c = 1.4, $CHCl_3$); IR ($CHCl_3$, 3 mM): v 3440, 1789, 1704 cm^{-1}; ^1H NMR ($CDCl_3$, 400 MHz): δ 1.40 (3H, d, *J* = 7.6 Hz, $CHCH_3$), 1.42 (9H, s, t-Bu), 1.43 (3H, d, *J* = 6.0 Hz, $CHCH_3$), 4.44 (1H, q, *J* = 3.6 Hz, CHN), 4.75-4.80 (2H, m, CH_2CH), 4.84 (1H, dq, *J* = 3.4, 5.6 Hz, CHO), 5.05 (1H, bs, NH), 5.27 (q, 1H, *J* = 6.8 Hz, CHAla), 5.41 (2H, AB, *J* = 13.6 Hz, CH_2Ph), 7.28-7.49 (5H, m, Ph), 8.78 (1H, s, CH-triazole); ^{13}C NMR ($CDCl_3$, 100 MHz): δ 16.6, 20.5, 28.2, 49.2, 49.6, 59.7, 66.8, 73.5, 80.5, 128.3, 128.4, 128.5, 129.6, 135.5, 140.6, 151.3, 155.6, 160.2, 175.2. Anal. Calcd. for $C_{23}H_{29}N_5O_7$: C, 56.67; H, 6.00; N, 14.37. Found: C, 56.70; H, 5.97; N, 14.35.

Boc-L-Ala-D-Oxd-Tri-COOH (6)
Compound **5** (0.3 g, 0.61 mmol) was dissolved in MeOH (30 mL) under nitrogen. Pd/C (30 mg, 10% w/w) was added under nitrogen. Vacuum was created inside the flask using the vacuum line. The flask was then filled with hydrogen using a balloon (1 atm). The solution was stirred for4 hours under a hydrogen atmosphere. The product was obtained pure as an oil in 98% yield (0.24 g), after filtration through filter paper and concentration in vacuo.
M.p. = 194 °C (dec.); $[\alpha]_D^{20}$ = - 21.9 (c = 0.91, $CHCl_3$); IR 3440, 1789, 1709, 1705, 1700 cm^{-1}; ^1H NMR (CD_3OD, 400 MHz): δ 1.34 (3H, d, *J* = 6.0 Hz, $CHCH_3$), 1.36 (3H, d, *J* = 6.8 Hz, $CHCH_3$), 1.43 (9H, s, t-Bu), 4.51-4.58 (1H, m, CHN), 4.69-4.80 (3H, m, CH_2CH + CHO), 5.16-5.28 (m, 1H, CH-Ala), 8.60 (1H, s, CH-triazole); ^{13}C NMR (CD_3OD, 100 MHz): δ 16.0, 19.2, 27.3, 49.2, 66.7, 74.2, 79.1, 128.8, 142.6, 152.1, 156.4, 174.7. Anal. Calcd. for $C_{16}H_{23}N_5O_7$: C, 48.36; H, 5.83; N, 17.62. Found: C, 48.40; H, 5.85; N, 17.59.

Boc-(L-Ala-D-Oxd-Tri-CO)$_2$OBn (7)
A solution of **5** (0.14 g, 0.287 mmol) and TFA (0.14 mL, 1.80 mmol) in dry methylene chloride (20 mL) was stirred at room temperature for 4 hours, then the volatiles were removed under reduced pressure and CF_3COO^- H_3N^+-L-Ala-D-Oxd-Tri-COOBn was obtained pure without further purification as a waxy solid. ^1H NMR (CD_3OD, 400 MHz): δ 1.40 (3H, d, *J* = 6.4 Hz, $CHCH_3$), 1.53 (3H, d, *J* = 6.8 Hz, $CHCH_3$), 4.62-4.67 (1H, m, CH-Ala), 4.74-5.05 (4H, m, CH_2CH + CHO + CHN), 5.37 (2H, s, CH_2Ph), 7.29-7.40 (5H, m, Ph), 8.66 (1H, s, CH-triazole).
A solution of **6** (0.11 g, 0.287 mmol) and HATU (0.12 g, 0.32 mmol) in dry acetonitrile (20 mL) was stirred under nitrogen atmosphere for 10 minutes at room temperature. Then a mixture of the previously obtained CF_3COO^- H_3N^+-L-Ala-D-Oxd-Tri-COOBn (0.143 g, 0.287 mmol) and DIEA (0.17 mL, 1.02 mmol) in dry acetonitrile (10 mL) was added dropwise at room

temperature. The solution was stirred for 50 minutes under nitrogen atmosphere, then acetonitrile was removed under reduced pressure and replaced with ethyl acetate. The mixture was washed with brine (1 x 30 mL), 1 N aqueous HCl (1 x 30 mL), and with a concentrated solution of $NaHCO_3$ (1 x 30 mL), dried over sodium sulphate and concentrated in vacuo. The product was obtained pure after silica gel chromatography (c-Hex/ethyl acetate 30:70 → ethyl acetate 100% as eluant) in 70% overall yield (0.16 g), as a white solid.
M.p. = 164 °C; $[\alpha]_D^{20}$ = + 48.5 (c = 1.0, $CHCl_3$); IR ($CHCl_3$, 3 mM): v 3414, 1790, 1711, 1676 cm^{-1}; ^1H NMR ($CDCl_3$, 400 MHz): δ 1.37-1.48 (18H, m, $CHCH_3$ Ala + 2 x $CHCH_3$ Oxd + t-Bu), 1.59 (3H, d, *J* = 7.2 Hz, $CHCH_3$ Ala), 4.40-4.50 (2H, m, 2 x CHN), 4.74-4.89 (6H, m, 2 x CH_2CH + 2 x CHO), 5.21-5.31 (1H, m, CH-Ala), 5.41 (2H, s, CH_2Ph), 5.52-5.61 (1H, m, CH-Ala), 7.28-7.54 (6H, m, Ph + NH), 8.47 (1H, s, CH-triazole), 8.78 (1H, s, CH-triazole). ^{13}C NMR ($CDCl_3$, 100 MHz): δ 16.5, 20.6, 28.2, 28.3, 29.7, 30.9, 37.5, 48.2, 48.7, 49.3, 59.2, 59.7, 73.4, 73.7, 74.0, 80.4, 127.5, 128.2, 128.4, 129.7, 135.5, 140.6, 142.7, 151.3, 159.7, 160.2, 173.6, 175.0. Anal. Calcd. for $C_{34}H_{42}N_{10}O_{11}$: C, 53.26; H, 5.52; N, 18.27. Found: C, 53.29; H, 5.50; N, 18.31.

Boc-(L-Ala-D-Oxd-Tri-CO)$_2$-OH (8)
For the synthetic procedure from **7** (0.77 g, 0.100 mmol), see the preparation of **6** given above (99% yield, 0.099 mmol, 0.67 g).
M.p. = 200 °C; $[\alpha]_D^{20}$ = + 20.5 (c = 1.0, CH_2Cl_2); IR (CH_2Cl_2, 3 mM): v 3446, 3412, 1790, 1718, 1670 cm^{-1}; ^1H NMR (CD_3OD, 400 MHz): δ 1.34-1.45 (18H, m, $CHCH_3$ Ala + 2 x $CHCH_3$ Oxd + t-Bu), 1.50 (3H, d, *J* = 6.4 Hz, $CHCH_3$ Ala), 4.54-4.67 (2H, m, 2 x CHN), 4.74-4.95 (6H, m, 2 x CH_2CH + 2 x CHO), 5.20 (m, 1H, CH-Ala), 5.59 (m, 1H, CH-Ala), 8.47 (1H, s, CH-triazole), 8.78 (1H, s, CH-triazole); ^{13}C NMR (CD_3OD, 100 MHz): δ 15.5, 15.6, 16.2, 27.3, 48.5, 49.2, 49.6, 51.2, 51.5, 52.4, 58.4, 59.6, 74.4, 75.9, 79.3, 127.8, 129.6, 142.2, 152.0, 152.1, 152.1, 156.4, 160.39, 160.5, 173.0, 173.2, 174.7. Anal. Calcd. for $C_{27}H_{36}N_{10}O_{11}$: C, 47.93; H, 5.36; N, 20.70. Found: C, 47.88; H, 5.41; N, 20.74.

Boc-(L-Ala-D-Oxd-Tri-CO)$_3$-OBn (9)
A solution of **5** (0.049 g, 0.100 mmol) and TFA (0.14 mL, 1.80 mmol) in dry methylene chloride (20 mL) was stirred at room temperature for 4 hours, then the volatiles were removed under reduced pressure and CF_3COO^- H_3N^+-L-Ala-D-Oxd-Tri-COOBn was obtained pure without further purification as a waxy solid.
A solution of **8** (0.068 g, 0.100 mmol) and HATU (0.042 g, 0.11 mmol) in dry acetonitrile (20 mL) was stirred under nitrogen atmosphere for 10 minutes at room temperature. Then a mixture of the previously obtained CF_3COO^- H_3N^+-L-Ala-D-Oxd-Tri-COOBn and DIEA (0.04 mL, 0.3 mmol) in dry acetonitrile (10 mL) was added dropwise at room temperature. The solution was stirred for 50 minutes under nitrogen atmosphere, then acetonitrile was removed under reduced pressure and replaced with ethyl acetate. The mixture was washed with brine (1 x 30 mL), 1 N aqueous HCl (1 x 30 mL), and with a concentrated solution of $NaHCO_3$ (1 x 30 mL), dried over sodium sulphate and concentrated in vacuo. The product was obtained pure after silica gel chromatography (c-Hex/ethyl acetate 10:90 → ethyl acetate 100% as eluant) in 51% yield (54 mg), as a white solid.
M.p. = 194 °C; $[\alpha]_D^{20}$ = + 69.0 (c = 0.97, CH_2Cl_2); IR (CH_2Cl_2, 3 mM): v 3446, 3412, 1790, 1718, 1670 cm^{-1}; ^1H NMR ($CDCl_3$, 400 MHz): δ 1.38 (3H, d, *J* = 7.0 Hz, CH_3 Ala), 1.38 (3H, d, *J* = 7.0 Hz, CH_3 Oxd), 1.39 (9H, s, t-Bu), 1.43 (3H, d, *J* = 6.8 Hz, CH_3 Oxd), 1.46 (3H, d, *J* = 7.2 Hz, CH_3 Oxd), 4.41-4.52 (3H, m, 3 x CHN), 4.65-4.90 (9H, m, 3 x CHO + 3 x CH_2CH), 5.17 (1H, d, *J* = 6.4 Hz, NH), 5.28 (1H, q, *J* = 6.4 Hz, CH Ala), 4.32-5.42 (2H, m, CH_2Ph), 5.52 (1H, m, CH Ala), 5.56 (1H, m, CH Ala), 7.29-7.39 (3H, m, Ph), 7.41-7.49 (2H, m, Ph), 7.57 (1H, d, *J* = 5.6 Hz, NH), 7.62 (1H, d, *J* = 5.6 Hz, NH), 8.50 (1H, s, CH-triazole), 8.64 (1H, s, CH-triazole), 8.75 (1H, s, CH-triazole); ^{13}C NMR ($CDCl_3$, 100 MHz): δ 16.2, 16.6, 20.6, 28.2, 48.6, 48.8, 49.5, 59.6, 59.7, 59.8, 66.8, 73.9, 80.4, 127.8, 128.3, 128.5, 129.8, 135.5, 142.6, 151.3, 151.5, 155.9, 159.8, 173.6, 177.8. Anal. Calcd. for $C_{45}H_{55}N_{15}O_{15}$: C, 51.67; H, 5.30; N, 20.09. Found: C, 51.72; H, 5.28; N, 20.11.

Boc-(L-Ala-D-Oxd-Tri-CO)$_3$-OH (10)
For the synthetic procedure from **9** (0.05 mmol, 52 mg), see the preparation of **6** given above (99% yield, 0.049 mmol, 47 mg).
M.p. = 206 °C; $[\alpha]_D^{20}$ = + 120.0; (c = 0.90, CH_2Cl_2); IR (CH_2Cl_2, 3 mM): ν 3687, 3600, 3411, 1790, 1713, 1674, 1606, 1575, 1505 cm^{-1}; ^{1}H NMR ($CDCl_3$, 400 MHz): δ 1.22-1.62 (27H, m, 3 x CH_3 Ala + 3 x CH_3 Oxd + t-Bu), 4.50-4.68 (3H, m, 3 x CHN), 4.69-4.99 (9H, m, 3 x CHO + 3 x CH_2CH), 5.14-5.28 (1H, m, CH-Ala), 5.57-5.70 (2H, m, 2 x CH-Ala), 8.68 (1H, s, CH-triazole), 8.74 (1H, s, CH-triazole), 8.77 (1H, s, CH-triazole); ^{13}C NMR ($CDCl_3$, 100 MHz): δ 15.7, 19.0, 27.3, 36.0, 37.6, 49.3, 59.6, 66.7, 74.1, 74.4, 79.2, 127.9, 142.2, 152.0, 156.5, 160.6, 173.4, 174.7. Anal. Calcd. for $C_{38}H_{49}N_{15}O_{15}$: C, 47.75; H, 5.17; N, 21.98. Found: C, 47.70; H, 5.15; N, 22.02.

L-Oxd-Tri-COOBn (L-4)
For the synthetic procedure from **L-3** (1.6 mmol, 0.25 g), see the preparation of **D-4** given above (78% yield, 1.25 mmol, 0.39 g).
M.p. = 167 °C; $[\alpha]_D^{20}$ = + 53.0 (c 1.6, $CHCl_3$); IR (CH_2Cl_2, 3 Mm): ν 3436, 3284, 1765 cm^{-1}; ^{1}H NMR ($CDCl_3$, 400 MHz): δ 1.38 (3H, d, *J* = 6.4 Hz, $CHCH_3$), 3.95 (1H, m, CHN), 4.41-4.55 (3H, m, CHO + CH_2CH), 5.31 (2H, AB, *J* = 12.8 Hz, CH_2Ph), 7.03 (1H, bs, NH), 7.25-7.47 (5H, m, Ph), 8.26 (1H, s, CH-triazole); ^{13}C NMR ($CDCl_3$, 100 MHz): δ 20.2, 53.1, 58.5, 67.0, 75.7, 128.6, 128.7, 129.0, 135.2, 158.4, 160.3. Anal. Calcd. for $C_{15}H_{16}N_4O_4$: C, 56.96; H, 5.10; N, 17.71. Found: C, 56.91; H, 5.14; N, 17.65.

Boc-L-Ala-L-Oxd-Tri-COOBn (11)
For the synthetic procedure from **L-4** (1.2 mmol, 0.38 g), see the preparation of **5** given above (71% yield, 0.85 mmol, 0.41 g).
M.p. = 117-118 °C; $[\alpha]_D^{20}$ = - 38.0 (c 0.8, CH_3OH); IR (CH_2Cl_2, 3 Mm): υ 3436, 1780, 1740, 1708 cm^{-1}; ^{1}H NMR ($CDCl_3$, 400 MHz): δ 1.38 (3H, d, *J* = 6.8 Hz, $CHCH_3$), 1.48 (12H, m, CH_3-Ala + t-Bu), 4.38 (1H, m, CHN), 4.65 (1H, d, *J* = 3.6, 6.4 Hz, CHO), 4.80 (2H, m, CH_2CH), 5.13 (1H, m, NH-Boc), 5.25 (1H, m, CH-Ala), 5.40 (2H, s, CH_2Ph), 7.25-7.43 (5H, m, Ph), 8.10 (1H, s, CH-triazole). ^{13}C NMR ($CDCl_3$, 100 MHz): δ 15.2, 18.1, 20.2, 28.3, 49.6, 59.6, 67.1, 74.2, 128.5, 128.6, 135.1, 140.2, 151.3, 160.0, 175.0. Anal. Calcd. for $C_{23}H_{29}N_5O_7$: C, 56.67; H, 6.00; N, 14.37. Found: C, 56.65; H, 5.99; N, 14.40.

Boc-L-Ala-L-Oxd-Tri-COOH (12)
For the synthetic procedure from **11** (0.80 mmol, 0.32 g), see the preparation of **6** given above (99% yield, 0.79 mmol, 0.31 g).
M.p. = 180 °C (dec.); $[\alpha]_D^{20}$ = - 48.7 (c = 2.5, $CHCl_3$); IR (nujol): ν 3442, 3138, 1785, 1731, 1706, 1701, 1685 cm^{-1}; ^{1}H NMR (CD_3OD, 400 MHz): δ 1.32 (3H, d, *J* = 6.0 Hz, $CHCH_3$), 1.40 (9H, s, t-Bu), 1.43 (3H, d, *J* = 6.8 Hz, $CHCH_3$), 4.55-4.59 (1H, m, CHN), 4.70-4.82 (2H, m, CH_2CH), 4.93 (m, 1H, CHO), 5.10-5.16 (m, 1H, CH-Ala), 8.32 (1H, s, CH-triazole); ^{13}C NMR (CD_3OD, 100 MHz): δ 16.2, 18.9, 27.3, 29.3, 35.8, 49.7, 59.25 73.9, 74.2, 79.1, 129.1, 142.6, 152.1, 156.5, 174.7. Anal. Calcd. for $C_{16}H_{23}N_5O_7$: C, 48.36; H, 5.83; N, 17.62. Found: C, 48.39; H, 5.80; N, 17.57.

Boc-(L-Ala-L-Oxd-Tri-CO)$_2$-OBn (13)
A solution of **11** (0.14 g, 0.287 mmol) and TFA (0.14 mL, 1.80 mmol) in dry methylene chloride (20 mL) was stirred at room temperature for 4 hours, then the volatiles were removed under reduced pressure and CF_3COO^- H_3N^+-L-Ala-L-Oxd-Tri-COOBn was obtained pure without further purification as a waxy solid. ^{1}H NMR (CD_3OD, 400 MHz): δ 1.44 (3H, d, *J* = 6.4 Hz, $CHCH_3$), 1.52 (3H, d, *J* = 7.2 Hz, $CHCH_3$), 4.64 (1H, q, *J* = 3.8 Hz, CH-Ala), 4.73-4.81 (2H, m, CHHCH + CHN), 4.86-4.93 (1H, m, CHO), 4.98 (1H, dd, *J* = 4.0, 14.8 Hz, CHHCH), 5.35 (2H, AB, *J* = 13.2 Hz, CH_2Ph), 7.29-7.47 (5H, m, Ph), 8.64 (1H, s, CH-triazole). A solution of **12** (0.113 g, 0.287 mmol) and HATU (0.12 g, 0.32 mmol) in dry acetonitrile (20 mL) was stirred under nitrogen atmosphere for 10 minutes at room temperature. Then a mixture of the previously obtained CF_3COO^- H_3N^+-L-Ala-D-Oxd-Tri-COOBn and DIEA (0.17 mL, 1.02 mmol) in dry acetonitrile (10 mL) was added dropwise at room temperature. The solution was stirred for 50 minutes under nitrogen atmosphere, then acetonitrile was removed under reduced

pressure and replaced with ethyl acetate. The mixture was washed with brine (1 x 30 mL), 1 N aqueous HCl (1 x 30 mL), and with a concentrated solution of $NaHCO_3$ (1 x 30 mL), dried over sodium sulphate and concentrated in vacuo. The product was obtained pure after silica gel chromatography (c-Hex/ethyl acetate 30:70 → ethyl acetate 100% as eluant) in 70% overall yield (0.20 mmol, 0.15 g), as a white solid.
M.p. = 110 °C; $[\alpha]_D^{20}$ = - 60.5; IR ($CHCl_3$, 3 Mm): v 3438, 3434, 3410, 1674, 1791, 1743, 1710 cm^{-1}; ^1H NMR (CD_3OD, 400 MHz): δ 1.31 (3H, d, *J* = 7.2 Hz), 1.41 (9H, s, t-Bu), 1.43 (15H, m, CH_3-Oxd), 1.46 (3H, d, *J* = 8 Hz), 4.51-4.65 (3H, m, CHN-Oxd), 4.69-4.80 (4H, m, CHO-Oxd), 5.11 (1H, q, *J* = 6.8 Hz), 5.36 (2H, s), 5.55 (1H, q, *J* = 7.2 Hz), 7.27-7.47 (5H, m), 8.37 (1H, s, CH-triazole), 8.58 (1H, s, CH-triazole); ^{13}C (CD_3OD, 100 MHz): δ 17.6, 20.3, 28.7, 29.5, 38.9, 48.3, 49.0, 49.6, 50.3, 51.0, 53.9, 59.7, 60.6, 67.9, 75.8, 77.3, 80.6, 129.0, 129.6, 131.0, 137.0, 140.7, 143.4, 153.5, 157.9, 161.6, 174.5, 175.8. Anal. Calcd. for $C_{34}H_{42}N_{10}O_{11}$: C, 53.26; H, 5.52; N, 18.27. Found: C, 53.22; H, 5.48; N, 18.26.

Boc-(L-Ala-L-Oxd-Tri-CO)$_2$-OH (14)
For the synthetic procedure from **13** (0.20 mmol, 0.15 g), see the preparation of **6** given above (99% yield, 0.19 mmol, 0.13 g).
M.p. = 200 °C; $[\alpha]_D^{20}$ = - 60.9 (c = 1.0, CH_3OH); IR (nujol): v 3373, 3144, 1781, 1744, 1707, 1663, 1577, 1507 cm^{-1}; ^1H NMR (CD_3OD, 400 MHz): δ 1.26-1.51 (21H, m, 2 x $CHCH_3$-Ala + 2 x $CHCH_3$-Oxd + t-Bu), 4.52-4.82 (8H, m, 2 x CHN + 2 x CHO + 2 x CH_2CH) 5.11 (1H, q, *J* = 6.8 Hz, CH-Ala), 5.57 (1H, q, *J* = 6.8 Hz, CH-Ala), 8.28 (1H, s, CH-triazole), 8.40 (1H, s, CH-triazole); ^{13}C NMR (CD_3OD, 100 MHz): δ 16.2, 16.3, 19-0 27.3, 48.9, 49.6, 52.3, 52.4, 58.3, 58.4, 58.5, 59.6, 74.4, 75.9, 79.2, 127.1, 127.6, 129.2, 142.0, 142.2, 152.1, 156.5, 159.3, 160.4, 173.0, 173.0, 173.2, 174.4. Anal. Calcd. for $C_{27}H_{36}N_{10}O_{11}$: C, 47.93; H, 5.36; N, 20.70. Found: C, 47.94; H, 5.38; N, 20.73.

Boc-(L-Ala-L-Oxd-Tri-CO)$_3$-OBn (15)
For the synthetic procedure from **11** (0.15 mmol, 0.10 g), see the preparation of **9** given above (40% yield, 0.04 mmol, 42 mg).
M.p. = 108 °C; $[\alpha]_D^{20}$ = - 17.5; IR ($CHCl_3$, 3 Mm): v 3447, 3433, 3410, 1789, 1772, 1749, 1712, 1676 cm^{-1}; ^1H NMR: (CD_3OD): δ 1.31 (3H, d, *J* = 6,8 Hz, CH_3–Ala), 1.41 (9H, s, t-Bu), 1.48 (3H, d, *J* = 6 Hz, CH_3–Ala), 1.49 (3H, d, *J* = 7.6 Hz, CH_3–Ala), 4.50–4.60 (6H, m, 3 x CHO-Oxd + 3 x CHN-Oxd), 5.10 (1H, d, *J* = 6.8 Hz, CH-Ala), 5.36 (2H, s), 5.56 (1H, d, *J* = 6 Hz), 5.59 (1H, d, *J* = 7.6 Hz), 7.41-7.47 (2H, m), 7.28-7.40 (3H, m), 8.37 (1H, s, CH-triazole), 8.40 (1H, s, CH-triazole), 8.59 (1H, s, CH-triazole); ^{13}C NMR (CD_3OD, 100 MHz): δ 18.7, 21.4, 31.7, 49.4, 49.6, 49.8, 50.0, 50.3, 50.5, 50.7, 51.4, 52.1, 54.9, 60.9, 61.8, 69.0, 77.0, 78.4, 81.8, 130.1, 130.7, 131.9, 132.3, 138.2, 141.8, 144.7, 154.6, 159.0, 162.9, 175.6. Anal. Calcd. for $C_{45}H_{55}N_{15}O_{15}$: C, 51.67; H, 5.30; N, 20.09. Found: C, 51.66; H, 5.27; N, 20.05.

Boc-(L-Ala-L-Oxd-Tri-CO)$_3$-OH (16)
For the synthetic procedure from **15** (0.04 mmol, 42 mg), see the preparation of **6** given above (99% yield, 0.39 mmol, 38 mg).
M.p. = 155°C; $[\alpha]_D^{20}$ = -23.2 (c = 0.50, CH_3OH); IR (nujol): v 3335, 1748, 1735, 1684, 1653, 1617, 1577, 1559, 1507 cm^{-1}; ^1H NMR (CD_3OD, 400 MHz) δ 1.13-1.67 (27H, m, 3 x CH_3 Ala + 3 x CH_3 Oxd + t-Bu), 3.92-4.01 (3H, m, 3 x CHN), 4.54-4.68 (10H, m, 3 x CHO + 3 x CH_2CH + CH-Ala), 4.95-5.05 (2H, m, 2 x CH-Ala), 8.68 (1H, s, CH-triazole), 8.74 (1H, s, CH-triazole), 8.77 (1H, s, CH-triazole); ^{13}C NMR (CD_3OD, 100 MHz): δ 16.1, 19.0, 29.3, 36.0, 37.6, 51.5, 52.2, 52.3, 58.4, 58.5, 75.9, 126.5, 127.1, 142.2, 159.3, 160.6, 172.9. Anal. Calcd. for $C_{38}H_{49}N_{15}O_{15}$: C, 47.75; H, 5.17; N, 21.98. Found: C, 47.79; H, 5.19; N, 21.96.

2-(6-dodecyl-1,3,5,7-tetraoxo-6,7-dihydropyrrolo[3,4-f]isoindol-2(1H,3H,5H)-yl)acetic acid (17)
For the preparation and characterization see Ref 185.

[185] Zhou, Q.-Z.; Jia, M.-X.; Shao, X.-B.; Wu, L.-Z.; Jiang, X.-K.; Li, Z.-T.; Chen, G.-J., Self-assembly of a novel series of hetero-duplexes driven by donor–acceptor interaction. Tetrahedron **2005,** 61 (30), 7117-7124

Methyl 2-(6-dodecyl-1,3,5,7-tetraoxo-6,7-dihydropyrrolo[3,4-f]isoindol-2(1H,3H,5H)-yl)acetate (18)

$SOCl_2$ (500 µL, 6.85 mmol) was slowly added to a solution of **17** (50 mg, 0.11 mmol) in CH_3OH (5 mL). The mixture was stirred 24 h at room temperature, then it was concentrated in vacuo. The crude was purified by column chromatography (c-Hex/ethyl acetate 9:1 → 85:15 → 80:20) and the product **18** was obtained in 45% yield (0.05 mmol, 23 mg).

M.p. = 139-141°C; IR (CH_2Cl_2, 3 mM): v 2928, 2855, 1775, 1755, 1729 cm^{-1}; ^1H NMR (400 MHz, $CDCl_3$): δ 0.90 (t, 3H, *J* = 6.5 Hz, CH_3), 1.21-1.26 (m, 12H, 6 x CH_2), 1.29-1.34 (m, 4H, 2 x CH_2), 1.57 (s, 2H, CH_2), 1.65-1.70 (m, 2H, CH_2-CH_2N), 3.70 (t, 2H, *J* = 7.5 Hz, NCH_2), 3.80 (s, 3H, OCH_3), 4.50 (s, 2H, CH_2 Gly), 8.30 (s, 2H, 2 x Ar); ^{13}C NMR (100 MHz, $CDCl_3$): δ 14.1, 22.7, 26.8, 28.4, 29.1, 29.3, 29.4, 29.5, 29.6, 29.7, 31.9, 38.8, 39.1, 52.9, 118.5, 137.0, 137.5, 165.3, 166.1, 167.1. Anal. Calcd. for $C_{25}H_{32}N_2O_6$: C, 65.77; H, 7.07; N, 6.14. Found: C, 65.79; H, 7.09; N, 6.11.

5-(Heptyloxy)naphthalen-1-ol (19) and 1,5-bis(heptyloxy)naphthalene (20)

Potassium carbonate (1.5 g, 11 mmol), potassium iodide (0.83 g, 5 mmol) and n-heptyl bromide (786 µL, 5 mmol) were added to a stirred solution of 1,5-dihydroxynaphthalene (0.80 g, 5 mmol) in acetone (18 mL) at room temperature. The suspension was stirred at reflux for 10 h, then cooled to room temperature. The solid was filtered off, the solvent was concentrated under reduced pressure and replaced with ethyl acetate (30 mL). The homogenous mixture was washed with 1 N aqueous HCl (6 mL), water (6 mL), brine (6 mL), dried over sodium sulfate and concentrated in vacuo. The crude was purified by flash chromatography (c-Hex/ethyl acetate 6:1). The product **19** was obtained in 37% yield (1.85 mmol, 0.48 g) and the by-product **20** was obtained in 30% yield (1.5 mmol, 0.53 g).

19: M.p. = 83-85°C (dec.); IR (CH_2Cl_2, 3 mM): v 3580, 2994, 2957, 2932, 2872, 2859, 1598, 1517, 1464, 1415, 1386, 1354 cm^{-1}; ^1H NMR (400 MHz, $CDCl_3$): δ 0.88 (t, 3H, *J* = 6.3 Hz, CH_3), 1.27-133 (m, 4H, 2 CH_2), 1.38 (t, 2H, *J* = 7.0 Hz, CH_2), 1.49-1.58 (m, 4H, 2 CH_2), 1.85-1.93 (m, 2H, OCH_2CH_2), 4.10 (t, 2H, *J* = 6.3 Hz, OCH_2), 5.16 (bs, 1H, OH), 6.81 (t, 2H, *J* = 7.0 Hz, Ar), 7.27 (t, 1H, *J* = 8.0 Hz, Ar), 7.34 (t, 1H, *J* = 8.0 Hz, Ar), 7.68 (d, 1H, *J* = 8.5 Hz, Ar), 7.85 (d, 1H, *J* = 8.5 Hz, Ar); ^{13}C NMR (100 MHz, $CDCl_3$): δ 14.1, 22.6, 26.2, 29.1, 29.3, 31.8, 68.2, 105.2, 109.4, 113.3, 114.9, 125.0, 125.3, 127.1, 151.1, 154.8. Anal. Calcd. for $C_{17}H_{22}O_2$: C, 79.03; H, 8.58; N, 12.39. Found: C, 79.04; H, 8.61; N, 12.36.

20: for the characterization see Ref 186.

(S)-5-(heptyloxy)naphthalen-1-yl 2-((tert-butoxycarbonyl)amino)propanoate (21)

Into a solution of Boc-L-Ala-OH (0.33 g, 1.73 mmol) in CH_2Cl_2 (15 mL) were added consecutively N,N-dicyclohexylcarbodiimide (0.36 g, 1.73 mmol), **19** (0.41 g, 1.57 mmol) and 4-(dimethylamino)pyridine (18 mg, 0.15 mmol). The reaction was stirred at room temperature for 24 h. The final suspension was filtered and the solution was concentrated in vacuo. The crude was purified by column chromatography (c-Hex/ethyl acetate 95:5), and the product was obtained in 55% yield (0.95 mmol, 0.41 g).

M.p. = 76-77°C (dec.); $[\alpha]_D^{20}$ = -33,4 (c 0.12, CH_2Cl_2); IR (CH_2Cl_2, 3 mM): v 3439, 1763, 1714, 1600, 1581 cm^{-1}; ^1H NMR (400 MHz, $CDCl_3$): δ 0.89 (t, 3H, *J* = 6.9 Hz, CH_3), 1.30-1.35 (m, 4H, 2 x CH_2), 1.35-1.43 (m, 2H, CH_2), 1.47 (s, 9H, t-Boc), 1.50-1.55 (m, 4H, 2 x CH_2), 1.65 (d, 3H, *J* = 7.3 Hz, CH_3-Ala), 1.85-2.00 (m, 2H, CH_2-CH_2O), 4.10 (t, 2H, *J* = 6.3 Hz, OCH_2), 4.65-4.75 (m, 1H, CH-Ala), 5.10-5.15 (m, 1H, NH), 6.80 (d, 1H, *J* = 7.0 Hz, Ar), 7.25 (d, 1H, *J* = 6.2 Hz, Ar), 7.35-7.45 (m, 3H, 3 x Ar), 8.20 (d, 1H, *J* = 8.6 Hz, Ar); ^{13}C NMR (100 MHz, $CDCl_3$): δ 14.1, 18.7, 22.6, 26.2, 28.3, 29.1, 29.2, 31.8, 49.6, 68.3, 80.1, 105.2, 112.9, 118.4, 120.6, 124.4, 126.8, 127.1, 127.7, 146.1, 155.0, 155.2, 172.2. Anal. Calcd. for $C_{25}H_{35}NO_5$: C, 69.90; H, 8.21; N, 3.26. Found: C, 69.87; H, 8.22; N, 3.25.

---

[186] Zhao, X.; Jia, M.-X.; Jiang, X.-K.; Wu, L.-Z.; Li, Z.-T.; Chen, G.-J., Zipper-Featured δ-Peptide Foldamers Driven by Donor−Acceptor Interaction. Design, Synthesis, and Characterization. The Journal of Organic Chemistry **2004,** 69 (2), 270-279

Boc-L-Ala-D-Oxd-L-Ala-5-(heptyloxy)naphthalen-1-yl ester (22a)
Compound **21** (67.4 mg, 0.157 mmol) was dissolved in dry CH_2Cl_2 (1.5 mL) and then TFA (217 µL, 2.82 mmol) was added. The reaction mixture was stirred in a nitrogen atmosphere for 4 h at room temperature. The corresponding ammonium trifluoroacetate salt was obtained pure after solvent removal in vacuo.
A solution of Boc-L-Ala-D-Oxd-OH (48 mg, 0.157 mmol) and HATU (65.5 mg, 0.157 mmol) in dry CH_3CN was stirred in a nitrogen atmosphere for 10 min at room temperature, then a solution of the ammonium trifluoroacetate salt and DIEA (82.0 µL, 0.47 mmol) in dry CH_3CN was then added dropwise. The solution was stirred for 1 h in a nitrogen atmosphere, and then CH_3CN was removed under reduced pressure and replaced with ethyl acetate (30 mL). The mixture was washed with brine (1 × 30 mL), 1 N aqueous HCl (1 × 30 mL) and 5% (w/v) aqueous $NaHCO_3$ (1 × 30 mL), dried over sodium sulfate and concentrated in vacuo. The product was obtained pure after silica gel chromatography (6:4 c-Hex/ethyl acetate → 1:1 c-Hex/ethyl acetate as eluent) in 75% yield (0.118 mmol, 74.1 mg).
M.p. = 133-138°C; $[\alpha]_D^{20}$ = 14.7 (c 0.18, CH_2Cl_2); IR (CH_2Cl_2, 3 mM): ν 3444, 3369, 1789, 1722, 1698, 1602, 1509 cm^{-1}; ^1H NMR (400 MHz, $CDCl_3$): δ 0.90 (t, 3H, *J* = 6.4 Hz, CH_3), 1.31-1.35 (m, 4H, 2 x CH_2), 1.42 (s, 12H, t-Bu + CH_3-Ala), 1.56 (d, 5H, *J* = 6.2 Hz, CH_2 + CH_3-Oxd) 1.60-1.63 (m, 2H, CH_2), 1.79 (d, 3H, *J* = 7.3 Hz, CH_3-Ala), 1.92 (q, 2H, *J* = 7.4 Hz, CH_2-CH_2O), 4.15 (t, 2H, *J* = 6.2 Hz, OCH_2), 4.53 (d, 1H, *J* = 5.2 Hz, CHN-Oxd), 4.79 (q, 1H, *J* = 6.1 Hz, CHO-Oxd), 4.89 (q, 1H, *J* = 7.0 Hz, CH-Ala), 5.09-5.12 (m, 1H, NH), 5.20 (q, 1H, *J* = 6.7 CHα-Ala), 6.83 (d, 1H, *J* = 7.3 Hz, Ar), 7.24 (d, 1H, *J* = 7.6 Hz, Ar), 7.35-7.50 (m, 4H, 3 x Ar + NH), 8.19 (d, 1H, *J* = 8.5 Hz, Ar); ^{13}C NMR (100 MHz, $CDCl_3$): δ 14.1, 16.6, 17.0, 21.0, 22.6, 26.2, 28.3, 29.1, 29.2, 31.8, 31.9, 49.0, 49.4, 62.9, 68.3, 75.3, 80.5, 105.2, 112.9, 118.3, 120.6, 124.3, 126.8, 127.1, 127.7, 146.1, 151.8, 154.9, 167.6, 170.9, 174.3. Anal. Calcd. for $C_{33}H_{45}N_3O_9$: C, 63.17; H, 7.23; N, 6.69. Found: C, 63.21; H, 7.27; N, 6.70.

Dyad (23)
Compound **22a** (74.1 mg, 0.118 mmol) was dissolved in dry CH_2Cl_2 (1.2 mL), then TFA (164 µL, 2.12 mmol) was added. The reaction mixture was stirred under nitrogen atmosphere for 4 h at room temperature. The corresponding ammonium trifluoroacetate salt was obtained pure after solvent removal in vacuo. A solution of **17** (52.2 mg, 0.118 mmol) and HBTU (49 mg, 0.130 mmol) in dry DMF (1 mL) was stirred under nitrogen atmosphere for 10 min at room temperature, then a solution of the ammonium trifluoroacetate salt and DIEA (64.3 µL, 0.369 mmol) in dry DMF (1 mL) was added. The mixture was stirred for 2 h under nitrogen atmosphere, then CH_3CN was removed under reduced pressure and replaced with ethyl acetate (30 mL). The mixture was washed with brine (1 × 30 mL), 1 N aqueous HCl (1 × 30 mL), 5% (w/v) aqueous $NaHCO_3$ (1 × 30 mL), dried over sodium sulfate and concentrated in vacuo. The product was obtained pure after silica gel chromatography (6:4 Hex/ethyl acetate → 1:1 Hex/ethyl acetate as eluent) in 50% (0.059 mmol, 56.1 mg) yield.
M.p. = 178-183°C; $[\alpha]_D^{20}$ = 10.9 (c 0.29, CH_2Cl_2); IR (CH_2Cl_2, 3 mM): ν 3427, 3342, 1788, 1773, 1727, 1684 cm^{-1}; ^1H NMR (400 MHz, $CDCl_3$): δ 0.83-0.91 (m, 6H, 2 x CH_3), 1.23 (bs, 18H, 9 x CH_2), 1.29-1.35 (m, 8H, 4 x CH_2), 1.50 (d, 3H, *J* = 6.7 Hz, CH_3-Ala), 1.53 (d, 3H, *J* = 6.9 Hz, CH_3-Ala), 1.61 (d, 3H, *J* = 6.2 Hz, CH_3-Oxd), 1.62-1.65 (m, 2H, CH_2-CH_2N), 1.88-1.96 (m, 2H, CH_2-CH_2O), 3.63 (t, 2H, *J* = 7.4 Hz, NCH_2), 4.06-4.16 (m, 3H, OCH_2 + CHH-Gly), 4.50 (d, 1H, *J* = 3.5 Hz, CHN-Oxd), 4.51 (d, 1H, *J* = 26.6 Hz, CHH-Gly), 4.78 (t, 1H, *J* = 6.5 Hz, CHO-Oxd), 4.85 (t, 1H, *J* = 6.9 Hz, CHα-Ala), 5.08 (t, 1H, *J* = 6.3 Hz, CHα-Ala), 6.70 (d, 1H, *J* = 7.5 Hz, Ar), 6.85 (d, 1H, *J* = 5.6 Hz, NH), 7.00 (d, 1H, *J* = 7.5, Ar), 7.10 (d, 1H, *J* = 8.2 Hz, Ar), 7.20-7.25 (m, 2H, 2 x Ar), 7.45 (d, 1H, *J* = 7.5 Hz, NH), 7.80 (s, 2H, 2 x Ar) 8.00 (d, 1H, *J* = 8.4 Hz, Ar); ^{13}C NMR (100 MHz, $CDCl_3$): δ 14.1, 15.8, 16.9, 20.6, 22.6, 22.7, 26.2, 26.9, 28.4, 29.1, 29.2, 29.3, 29.5, 29.6, 29.7, 31.8, 31.9, 38.6, 40.6, 48.4, 50.1, 63.7, 68.2, 75.5, 105.0, 112.5, 118.3, 118.5, 120.2, 124.3, 126.6, 126.9, 127.2, 136.3, 136.6, 145.9, 152.4, 154.8, 165.6, 165.7, 166.4, 166.9, 170.4, 172.8. Anal. Calcd. for $C_{52}H_{65}N_5O_{12}$: C, 65.60; H, 6.88; N, 7.36. Found: C, 65.63; H, 6.90; N, 7.33.

Boc-(-L-Ala-D-Oxd-)$_2$-L-Ala-5-(heptyloxy)naphthalen-1-yl ester (22b)
Compound **21** (35.6 mg, 0.08 mmol) was dissolved in dry CH_2Cl_2 (0.1M, 0.8 mL) and then TFA (143 µL, 1.44 mmol) was added. The reaction mixture was stirred under nitrogen

atmosphere for 4 h at room temperature. The corresponding ammonium trifluoroacetate salt was obtained pure after solvent removal in vacuo.
A solution of Boc-(-L-Ala-D-Oxd-)$_2$-OH (48.3 mg, 0.08 mmol) and HATU (33.5 mg, 0.088 mmol) in dry CH_3CN was stirred under nitrogen atmosphere for 10 min at room temperature, then a solution of the ammonium trifluoroacetate salt and DIEA (41.8 µL, 0.24 mmol) in dry CH_3CN was added dropwise. The solution was stirred for 1 h under nitrogen atmosphere, then CH_3CN was removed under reduced pressure and replaced with ethyl acetate (30 mL). The mixture was washed with brine (1 × 30 mL), 1 N aqueous HCl (1 × 30 mL), 5% (w/v) aqueous $NaHCO_3$ (1 × 30 mL), dried over sodium sulfate and concentrated in vacuo. The product was obtained pure after silica gel chromatography (6:4 c-Hex/ethyl acetate → 1:1 c-Hex/ethyl acetate as eluent) in 58% (0.046 mmol, 38.3 mg) yield.
M.p. = 98-101°C; $[\alpha]_D^{20}$ 19.3 (c 0.23, CH_2Cl_2); IR (CH_2Cl_2, 3 mM): v 3441, 3360, 1790, 1721, 1696, 1600, 1533, 1509 cm^{-1}; ^{1}H NMR (400 MHz, $CDCl_3$): δ 0.88 (t, 3H, *J* = 6.5 Hz, CH_3), 1.23 (bs, 4H, 2 x CH_2), 1.29-1.32 (m, 4H, 2 x CH_2), 1.35-1.44 (m, 15H, t-Boc + CH_3-Ala + CH_3-Oxd), 1.48-1.55 (m, 6H, CH_3-Ala, CH_3-Oxd), 1.70 (d, 3H, *J* = 8.3 Hz, CH_3-Ala), 1.89 (q, 2H, *J* = 6.8 Hz, CH_2-CH_2O), 4.10 (t, 2H, *J* = 6.3, OCH_2), 4.42 (d, 1H, *J* = 4.7, CHN-Oxd), 4.50 (d, 1H, *J* = 5.0 Hz, CHN-Oxd), 4.62-4.67 (m, 1H, CHO-Oxd), 4.78 (q, 1H, *J* = 5.9 Hz, CHO-Oxd), 4.87 (q, 1H, *J* = 6.8 Hz, CHα-Ala), 5.10 (bs, 1H, NH), 5.21 (d, 1H, *J* = 6.8 Hz, CHα-Ala), 5.27-5.34 (m, 1H, CHα-Ala), 6.80 (d, 1H, *J* = 7.7 Hz, Ar), 7.21-7.23 (d, 1H, *J* = 7.6 Hz Ar), 7.35-7.43 (m, 4H, 3 x Ar + NH), 7.57 (d, 1H, *J* = 5.9 Hz, NH), 8.16 (d, 1H, *J* = 8.3 Hz, Ar); ^{13}C NMR (100 MHz, $CDCl_3$): δ 14.1, 15.5, 16.8, 21.0, 21.1, 22.6, 26.2, 28.2, 29.1, 29.2, 29.6, 29.7, 31.8, 48.9, 49.2, 62.4, 62.6, 68.3, 74.8, 75.3, 80.7, 105.2, 112.8, 118.4, 120.6, 124.4, 126.9, 127.0, 127.7, 146.1, 151.6, 151.7, 154.9, 167.7, 168.2, 171.0, 174.8. Anal. Calcd. for $C_{41}H_{55}N_5O_{13}$: C, 59.62; H, 6.71; N, 8.48. Found: C, 59.58; H, 6.73; N, 8.50.

Dyad (24)
Compound **22b** (38.0 mg, 0.046 mmol) was dissolved in dry CH_2Cl_2 (0.1M, 460 µL), and then TFA (63.9 µL, 0.829 mmol) was added. The reaction mixture was stirred in a nitrogen atmosphere for 4 h at room temperature. The corresponding ammonium trifluoracetate salt was obtained pure after solvent removal in vacuo. A solution of **17** (20.3 mg, 0.046 mmol) and HBTU (19.2 mg, 0.050 mmol) in dry DMF (1 mL) was stirred in a nitrogen atmosphere for 10 min at room temperature. A solution of the corresponding ammonium trifluoracetate salt and DIEA (24.0 µL, 0.138 mmol) in dry DMF (1 mL) was then added dropwise. The solution was stirred for 2 h in a nitrogen atmosphere, and then CH_3CN was removed under reduced pressure and replaced with ethyl acetate (30 mL). The mixture was washed with brine (1 × 30 mL), 1 N aqueous HCl (1 × 30 mL), 5% (w/v) aqueous $NaHCO_3$ (1 × 30 mL), dried over sodium sulfate and concentrated in vacuo. The product was obtained pure after silica gel chromatography (1:1 Hex/ethyl acetate → 2:8 Hex/ethyl acetate as eluent) in 45% (0.021 mmol, 23.8 mg) yield.
M.p. = 182-187°C; $[\alpha]_D^{20}$ = 9.4 (c 0.34, CH_2Cl_2); IR (CH_2Cl_2, 3 mM): v 3424, 3412, 3359, 3350, 3336, 1789, 1775, 1728, 1719, 1683 cm^{-1}; ^{1}H NMR (400 MHz, $CDCl_3$): δ 0.83-0.90 (m, 6H, CH_3), 1.14 (m, 2H, CH_2), 1.23 (bs, 12H, 6 x CH_2), 1.27-1.34 (m, 9H, 3 x CH_2 + CH_3-Ala), 1.35-1.39 (m, 3H, CH_3-Oxd), 1.40-1.45 (m, 6H, CH_3-Ala + CH_3-Oxd), 1.52 (m, 6H, 3 x CH_2), 1.65 (m, 3H, CH_3-Ala), 1.86-1.92 (m, 4H, CH_2-CH_2O + CH_2-CH_2N), 3.66-3.72 (m, 2H, NCH_2), 4.07-4.11 (m, 2H, OCH_2), 4.30-4.50 (m, 4H, 2 CHN-Oxd + CH_2-Gly), 4.62-4.68 (m, 1H, CHO-Oxd), 4.70-4.76 (m, 1H, CHO Oxd), 4.80-4.86 (m, 1H, CHα-Ala), 5.11-5.17 (m, 1H, CHα-Ala), 5.35-5.41 (m, 1H, CHα-Ala), 6.76-6.81 (m, 2H, Ar + NH), 7.17 (d, 1H, *J* = 7.3 Hz, Ar), 7.18-7.22 (m, 2H, Ar), 7.32-7.42 (m, 3H, Ar + 2 x NH), 8.12 (d, 1H, *J* = 7.8 Hz, Ar), 8.18 (s, 2H, 2 x Ar); ^{13}C NMR (100 MHz, $CDCl_3$): δ 14.1, 15.5, 16.9, 20.8, 22.6, 26.2, 26.9, 28.4, 29.1, 29.2, 29.3, 29.6, 31.6, 31.8, 31.9, 38.7, 40.5, 48.9, 49.1, 62.8, 68.3, 75.0, 75.4, 105.2, 112.7, 118.8, 118.3, 120.3, 124.3, 126.8, 126.9, 127.3, 127.5, 136.5, 136.9, 145.9, 151.7, 154.8, 165.3, 165.7, 166.0, 166.3, 167.6, 168.1, 171.1, 173.2. Anal. Calcd. for $C_{60}H_{75}N_7O_{16}$: C, 62.65; H, 6.57; N, 8.52. Found: C, 62.62; H, 6.63; N, 8.56.

Boc-(-L-Ala-D-Oxd-)$_3$-L-Ala-5-(heptyloxy)naphthalen-1-yl ester (22c)
Compound **21** (71.4 mg, 0.166 mmol) was dissolved in dry CH_2Cl_2 (1.6 mL), then TFA (231 µL, 2.99 mmol) was added. The mixture was stirred under nitrogen atmosphere for 4 h at

room temperature. The corresponding ammonium trifluoroacetate salt was obtained pure after solvent removal in vacuo. A solution of Boc-(-L-Ala-D-Oxd-)$_3$-OH (118.2 mg, 0.166 mmol) and HATU (33.5 mg, 0.088 mmol) in dry CH_3CN was stirred under nitrogen atmosphere for 10 min at room temperature, then a solution of the ammonium trifluoroacetate salt and DIEA (86.7 µL, 0.498 mmol) in dry CH_3CN was added dropwise. The mixture was stirred for 1 h in a nitrogen atmosphere, then CH_3CN was removed under reduced pressure and replaced with ethyl acetate (30 mL). The mixture was washed with brine (1 × 30 mL), 1 N aqueous HCl (1 × 30 mL), 5% (w/v) aqueous $NaHCO_3$ (1 × 30 mL), dried over sodium sulfate and concentrated in vacuo. The product was obtained pure after silica gel chromatography (6:4 c-Hex/ethyl acetate → 1:1 c-Hex/ethyl acetate as eluent) in 40% (0.066 mmol, 68.0 mg) yield.
M.p. = 140-144°C; $[\alpha]_D^{20}$ = -5.3 (c 0.3, CH_2Cl_2); IR (CH_2Cl_2, 3 mM): v 3402, 3351, 1790, 1694, 1600, 1535, 1509 cm^{-1}; ^1H NMR (400 MHz, $CDCl_3$): δ 0.90 (t, 3H, *J* = 6.9 Hz, CH_3), 1.24-1.27 (m, 2H, CH_2), 1.30-1.35 (m, 4H, 2 x CH_2), 1.36-1.57 (24H, t-Bu, CH_3-Oxd, 4 x CH_3-Ala), 1.71-1.75 (m, 3H, CH_3-Oxd), 1.77-1.82 (m, 5H, CH_2 + CH_3-Oxd), 1.87-1.95 (m, 2H, CH_2-CH_2O), 4.11 (t, 2H, *J* = 6.4 Hz, OCH_2), 4.38-4.40 (m, 1H, CHN-Oxd), 4.42-4.45 (m, 1H, CHN-Oxd), 4.50-4.54 (m, 1H, CHO-Oxd), 4.60-4.64 (m, 1H, CHO-Oxd), 4.65-4.70 (m, 1H, NH), 4.73-4.78 (m, 1H, CHα-Ala), 4.92 (q, 1H, J = 6.7, CHα-Ala), 5.17-5.24 (m, 2H, CHα-Ala), 5.32-5.40 (m, 2H, CHα-Ala), 6.80-6.84 (m, 1H, Ar), 7.21-7.23 (m, 1H, Ar), 7.37-7.44 (m, 3H, Ar), 7.50-7.54 (m, 2H, 2 x NH), 7.59-7.62 (m, 1H, NH), 8.19 (d, 1H, *J* = 8.2 Hz, Ar); ^{13}C NMR (100 MHz, $CDCl_3$): δ 14.0, 15.8, 16.9, 17.1, 20.5, 20.7, 22.6, 26.2, 28.2, 29.1, 29.2, 29.6, 31.8, 38.6, 48.9, 49.0, 49.3, 62.4, 62.6, 68.3, 74.9, 75.4, 80.5, 105.1, 112.5, 112.7, 118.4, 120.7, 124.2, 127.0, 127.6, 146.0, 151.7, 151.8, 154.9, 167.8, 168.1, 171.4, 171.5, 173.0, 174.2. Anal. Calcd. for $C_{49}H_{65}N_7O_{17}$: C, 57.47; H, 6.40; N, 9.57. Found: C, 57.50; H, 6.43; N, 9.61.

Dyad (25)
Compound **22c** (68.9 mg, 0.067 mmol) was dissolved in dry CH_2Cl_2 (0.5 mL), then TFA (93.0 µL, 1.2 mmol) was added. The reaction mixture was stirred under nitrogen atmosphere for 4 h at room temperature. The corresponding trifluoracetate salt was obtained pure after solvent removal in vacuo. A solution of **17** (29.6 mg, 0.067 mmol) and HBTU (28.1 mg, 0.0.074 mmol) in dry DMF (1 mL) was stirred under nitrogen atmosphere for 10 min at room temperature. A solution of the corresponding trifluoracetate salt and DIEA (64.3 µL, 0.20 mmol) in dry DMF (1 mL) was then added dropwise. The mixture was stirred for 2 h in a nitrogen atmosphere, then CH_3CN was removed under reduced pressure and replaced with ethyl acetate (30 mL). The mixture was washed with brine (1 × 30 mL), 1 N aqueous HCl (1 × 30 mL), and 5% (w/v) aqueous $NaHCO_3$ (1 × 30 mL), dried over sodium sulfate and concentrated in vacuo. The product was obtained pure after silica gel chromatography (1:1 Hex/ethyl acetate → 2:8 Hex/ethyl acetate as eluent) in 40% (0.027 mmol, 36.1 mg) yield.
M.p. = 90-98°C; $[\alpha]_D^{20}$ = -7.4 (c 0.4, CH_2Cl_2); IR (CH_2Cl_2, 3 mM): v 3418, 3412, 3366, 3353, 3344, 1787, 1774, 1727, 1687, 1683 cm^{-1}; ^1H NMR (400 MHz, $CDCl_3$): δ 0.85-0.90 (m, 6H, 2 x CH_3), 1.21-1.26 (m, 16H, 8 x CH_2), 1.28-1.33 (m, 11H, CH_3-Ala + 4 x CH_2), 1.35-1.45 (m, 8H, 2 x CH_3-Oxd + CH_2), 1.49-1.54 (m, 9H, 3 x CH_3-Ala), 1.65-1.72 (m, 3H, CH_3-Oxd), 1.87-1.94 (m, 4H, CH_2-CH_2O + CH_2-CH_2N), 3.67-3.75 (m, 3H, 3 x CHN-Oxd), 3.98-4.05 (m, 2H, CH_2-Gly), 4.07-4.13 (m, 4H, OCH_2 + NCH_2), 4.34-4.52 (m, 4H, 2 x CH-Ala + 2 x CHO-Oxd), 4.55-4.65 (m, 1H, CHα-Ala), 4.67-4.74 (m, 2H, CHα-Ala + CH Oxd), 4.87-4.95 (m, 1H, NH), 6.79 (d, 1H, *J* = 7.0 Hz, Ar), 7.18-7.24 (m, 3H, Ar + 2 x NH), 7.32-7.41 (m, 4H, 3 x Ar + NH), 8.17 (d, 1H, CH = 8.7 Hz, Ar), 8.22 (s, 2H, Ar); ^{13}C NMR (100 MHz, $CDCl_3$): δ 14.0, 17.6, 21.0, 22.6, 22.7, 26.2, 26.8, 28.4, 29.0, 29.1, 29.2, 29.3, 29.4, 29.5, 29.6, 30.9, 31.8, 31.9, 38.8, 40.7, 48.5, 48.8, 52.2, 61.9, 62.8, 68.3, 68.7, 75.4, 105.2, 112.6, 118.3, 118.4, 120.7, 124.3, 127.0, 127.5, 129.5, 136.9, 137.0, 137.3, 137.4, 145.9, 155.0, 159.3, 165.5, 165.6, 165.7, 166.0, 166.1, 166.2, 169.6, 171.3. Anal. Calcd. for $C_{68}H_{85}N_9O_{20}$: C, 60.57; H, 6.35; N, 9.35. Found: C, 60.60; H, 6.32; N, 9.37.

Boc-L-Ala-D-Oxd-OBn (26)
HBTU (3.71 g, 9.8 mmol) was added to a solution of Boc-(L-Ala)-OH (1.68 g, 8.9 mmol) and CH_3CN (40 mL) under nitrogen atmosphere. The mixture was left stirring for 10 minutes to activate the acid. A solution of D-Oxd-OBn (2.09 g, 8.9 mmol) and DBU (2.66 mL, 17.8 mmol) in dry acetonitrile (6 mL) was added dropwise. The progress of the reaction was followed by

TLC and after 1 hour the reaction went to completion. The mixture was concentrated in vacuo, it was partitioned between ethyl acetate (20 mL) with brine (20 mL), 1N aqueous HCl (20 mL) and saturated $NaHCO_3$ (20 mL). The extracted organic layer was dried (Na_2SO_4), filtered and concentrated in vacuo. The crude of the reaction was purified via flash chromatography (9:1 ciclohexane/AcOEt as eluent) to afford compound **26** as a white solid (2.86 g, 79% yield). For the characterization, see Ref. 50.

Boc-L-Ala-D-Oxd-OH (27)
For the synthesis and characterization see Ref. 50.

Boc-(L-Ala-D-Oxd)$_2$-OBn (28)
Trifluoroacetic acid (TFA) (1.69 mL, 22 mmol) was added in inert atmosphere to a solution of **26** (0.5 g, 1.23 mmol) in anhydrous dichloromethane (15 mL). The mixture was stirred at room temperature for 4 hours and concentrated in vacuo after a control via TLC. H-L-Ala-D-Oxd-OBn·CF_3CO_2H was obtained in quantitative yield without any further purification. HBTU (0.512 g, 1.35 mmol) was added to a solution of **27** (0.41 g, 1.23 mmol) and dry acetonitrile (30 mL) under nitrogen atmosphere. The mixture was left stirring for 10 minutes in order to activate the acid. A solution of the previously obtained H-L-Ala-D-Oxd-OBn·CF_3CO_2H and TEA (0.5 mL, 3.6 mmol) in dry acetonitrile (20 mL) was added dropwise. The progress of the reaction was followed by TLC and after 1 hour the reaction went to completion. The mixture was concentrated in vacuo, it was partitioned between ethyl acetate (20 mL) with brine (20 mL), HCl 1N (20 mL) and $NaHCO_3$ (20 mL). The extracted organic layer was dried (Na_2SO_4), filtered and concentrated in vacuo. The crude of the reaction was purified via flash chromatography (70:30 ciclohexane/AcOEt) to afford compound **3** as a white solid (0.65 g, 88% yield). For the characterization see Ref. 49.

Boc(L-Ala-D-Oxd)$_2$OH (29)
For the synthesis and characterization see Ref. 50.

Boc-(L-Ala-D-Oxd)$_4$-OBn (30)
Trifluoroacetic acid (TFA) (0.57 mL, 7.40 mmol) was added under nitrogen atmosphere to a solution of **28** (0.25 g, 0.41 mmol) in anhydrous dichloromethane (10 mL). The mixture was stirred at room temperature for 4 hours and concentrated in vacuo after a control via TLC. H-(L-Ala-D-Oxd)$_4$-OBn·CF_3CO_2H was obtained in quantitative. HBTU (0.17 g, 0.45 mmol) was added to a solution of **29** (0.21 g, 0.41 mmol) and dry acetonitrile (30 mL) under nitrogen atmosphere. The mixture was left stirring for 10 minutes in order to activate the acid. A solution of the previously obtained H-(L-Ala-D-Oxd)$_4$-OBn·CF_3CO_2H and TEA (0.17 mL, 1.23 mmol) in CH_3CN (20 mL) was added dropwise. The progress of the reaction was followed by TLC and after 1 hour the reaction went to completion. The mixture was concentrated in vacuo, it was partitioned between ethyl acetate (20 mL) and brine (20 mL), HCl 1N (20 mL) and $NaHCO_3$ (20 mL). The combined organic layers were dried (Na_2SO_4), filtered and concentrated in vacuo. The crude of the reaction was purified via flash chromatography (from 45:55 nHex/AcOEt to 100% AcOEt) to afford compound **30** as a white solid (0.29 g, 72% yield); For the characterization see Ref. 49.

Boc-(L-Ala-D-Oxd)$_4$-OH (31)
For the synthesis and characterization see Ref. 50.

Boc-(L-Ala-D-Oxd)$_8$-OBn (32)
Trifluoroacetic acid (TFA) (0.13 mL, 1.7 mmol) was added under nitrogen atmosphere to a solution of **30** (0.10 g, 0.10 mmol) in dry dichloromethane (20 mL). The mixture was stirred at room temperature for 4 hours and concentrated in vacuo after a control via TLC. H-(L-Ala-D-Oxd)$_4$-OBn·CF_3CO_2H was obtained in quantitative yield. HBTU (0.042 g, 0.11 mmol) was added to a solution of **31** (91 mg, 0.10 mmol) and dry acetonitrile (15 mL) under nitrogen atmosphere. The mixture was left stirring for 10 minutes in order to activate the acid. A solution of the previously obtained H-(L-Ala-D-Oxd)$_4$-OBn·CF_3CO_2H and TEA (0.042 mL, 0.30

mmol) in dry acetonitrile (20 mL) was added dropwise. After 1 hour the reaction went to completion. The mixture was concentrated in vacuo, it was partitioned between AcOEt (20 mL) with brine (20 mL), HCl 1N (20 mL) and $NaHCO_3$ (20 mL). The combined organic layers were dried (Na_2SO_4), filtered and concentrated in vacuo. The purification occurred with an ultrasound-assisted washing process using organic solvents as n-Hex, ether and pentane achieving product **32** as a white solid (0.14 g, 77% yield).
M.p. = 266-268 °C; $[\alpha]_D^{20}$ = - 148 (c = 0.26, CH_2Cl_2); IR (CH_2Cl_2 3 mM) ν = 3352, 3288, 1787, 1744, 1708, 1664 cm^{-1}; ^1H NMR (400 MHz $CDCl_3$): δ 1.32-1.62 (m, 48H, 8 x CH_3 Ala + 8 x CH_3 Oxd), 4.43-4.60 (m, 8H, 8 x CHO Oxd), 4.64-4.74 (m, 2H, 2 x CHN Oxd), 4.95-5.12 (m, 6H, 6 x CHN Oxd), 5.23 (s, 2H, CH_2 Ph), 5.72-6.10 (m, 8H, 8 x CH Ala), 7.14-7.20 (m, 1H, NH), 7.30-7.44 (m, 5H, 5 x CH Ph), 7.88-7.98 (m, 2H, 2 x NH), 8.11-8.19 (m, 1H, NH), 8.20-8.26 (m, 1H, NH), 8.28-8.47 (m, 4H, 4 x NH); ^{13}C NMR (100 MHz $CDCl_3$): δ 18.1, 21.0, 21.2, 28.4, 28.6, 28.7, 38.8, 46.1, 49.2, 53.6, 62.1, 75.0, 75.5, 128.1, 128.5, 128.9, 129.0, 133.4, 134.6, 151.8, 168.8, 170.1, 171.5, 172.2. $C_{76}H_{96}N_{16}O_{35}$ (1793.66): calcd. C, 50.89; H, 5.39; N, 12.49. Found: C, 50.96; H, 5.37; N, 12.43.

Trityl-mercapto-L-Ala-D-Oxd-OBn (33)
Trifluoroacetic acid (0.24 mL, 3.1 mmol) was added under nitrogen atmosphere to a solution of **26** (69 mg, 0.17 mmol) in dry dichloromethane (20 mL). The mixture was stirred at room temperature for 4 hours and concentrated in vacuo after a control via TLC. H-L-Ala-D-Oxd-OBn·CF_3CO_2H was obtained in quantitative yield. HBTU (71 mg, 0.187 mmol) was added to a solution of 3-tritylmercapto propionic acid (0.0571 g, 0.17 mmol) in dry acetonitrile (10 mL) under inert atmosphere. After 10 minutes, a solution of the previously obtained H-L-Ala-D-Oxd-OBn·CF_3CO_2H and TEA (0.071 mL, 0.51 mmol) in dry acetonitrile (10 mL) was added dropwise to the mixture. The progress of the reaction was controlled by TLC and after one hour the reaction went to completion. The mixture was concentrated in vacuo and it was partitioned between AcOEt (20 mL) with brine (20 mL), HCl 1N (20 mL) and $NaHCO_3$ (20 mL). The extracted organic layer was dried (Na_2SO_4), filtered and concentrated in vacuo. The reaction crude was purified by flash chromatography (from 90:10 to 80:20 cHex/AcOEt) to afford compound **33** as a white solid (56 mg, 52% overall yield); R_f = 0.72 (1:1 cHex /AcOEt).
M.p. = 98-102 °C; $[\alpha]_D^{20}$ = 11.1 (c = 0.19 in CH_2Cl_2); IR (CH_2Cl_2 3 mM) ν = 3419, 1789, 1752, 1711, 1670 cm^{-1}; ^1H NMR (400 MHz $CDCl_3$): δ 1.38 (d, J = 6.8 Hz, 3H, CH_3 Ala), 1.48 (d, J = 6.4 Hz, 3H, CH_3 Oxd), 1.97 (dd, J = 7.2 Hz, J = 13.7 Hz, 2H, CH_2), 2.49 (td, J = 2.2 Hz, J = 7.3 Hz, 2H, CH_2), 4.43 (d, *J* = 4.1 Hz, 1H, CHN Oxd), 4.53 (dq, J = 4.2 Hz, *J* = 6.4 Hz, 1H, CHO Oxd), 5.17 (s, 2H, O-CH_2-Ph), 5.52-5.60 (1H, m, CH Ala), 6.08 (d, *J* = 7.7 Hz, 1H, NH Ala), 7.16–7.44 (20H, m, 20 x CH Ph); ^{13}C NMR (100 MHz $CDCl_3$): δ 18.7, 21.2, 27.6, 35.5, 48.4, 62.0, 68.2, 73.9, 126.8, 128.0, 128.5, 128.8, 128.9, 129.7, 134.7, 144.8, 151.0, 167.4, 170.0, 173.4. $C_{37}H_{36}N_2O_6S$ (636.76): calcd. C, 69.79; H, 5.70; N, 4.40. Found: C, 69.87; H, 5,77; N, 4.49.

Trityl-mercapto-(L-Ala-D-Oxd)$_2$-OBn (34)
Trifluoroacetic acid (0.24 mL, 3.1 mmol) was added under nitrogen atmosphere to a solution of **28** (0.25 g, 0.41 mmol) in dry dichloromethane (20 mL). The mixture was stirred at room temperature for 4 hours and concentrated in vacuo after a control via TLC. H-(L-Ala-D-Oxd)$_2$-OBn·CF_3CO_2H was obtained in quantitative yield. HBTU (0.17 g, 0.45 mmol) was added to a solution of 3-tritylmercapto propionic acid (0.138 g, 0.36 mmol) and dry acetonitrile (30 mL) under inert atmosphere. The mixture was left stirring for 10 minutes in order to activate the acid. A solution of the previously obtained H-(L-Ala-D-Oxd)$_2$-OBn·CF_3CO_2H and TEA (0.17 mL, 1.22 mmol) in dry acetonitrile (20 mL) was added dropwise. The progress of the reaction was followed by TLC and after 1 hour the reaction went to completion. The mixture was concentrated in vacuo, it was partitioned between ethyl acetate (20 mL) with brine (20 mL), HCl 1N (20 mL) and $NaHCO_3$ (20 mL). The aqueous layer was extracted with ethyl acetate and the combined organic layers were dried (Na_2SO_4), filtered and concentrated in vacuo. The crude of the reaction was purified via flash chromatography (from 60:40 to 50:50 ciclohexane/AcOEt) to afford compound **34** as a white solid (0.22 g, 63% overall yield); Rf = 0.18 (1:1 cHex/AcOEt).

M.p. = 197-199 °C; $[\alpha]_D^{20}$ = - 4.8 (c = 0.25 in CH_2Cl_2); IR (CH_2Cl_2 3 mM) ν = 3436, 3347, 1791, 1721, 1674 cm^{-1}; ^1H NMR (400 MHz $CDCl_3$): δ 1.34 (d, *J* = 7.1 Hz, 3H, CH_3 Ala), 1.40 (d, *J* = 7.0 Hz, 3H, CH_3 Ala), 1.49 (d, *J* = 6.3 Hz, 3H, CH_3 Oxd), 1.51 (d, J = 6.4 Hz, 3H, CH_3 Oxd), 1.88-1.97 (m, 2H, CH_2), 2.03-2.12 (m, 2H, CH_2), 2.35-2.43 (m, 2H, CH_2), 2.47-2.56 (m, 2H, CH_2), 4.40 (d, *J* = 5.8 Hz, 1H, CHN Oxd), 4.45 (d, *J* = 4.3 Hz, 1H, CHN Oxd), 4.54-4.62 (m, 2H, CHO Oxd), 5.22 (s, 2H, O-CH_2-Ph), 5.24-5.27 (m, 1H, CH Ala), 5.54-5.58 (m, 1H, CH Ala), 5.92 (d, *J* = 5.1 Hz, 1H, NH Ala), 7.18 – 7.42 (21H, m, 20 x CH Ph + NH Ala); ^{13}C NMR (100 MHz $CDCl_3$): δ 16.1, 17.0, 21.1, 21.2, 27.4, 35.0, 48.6, 49.0, 62.2, 63.1, 68.0, 73.9, 75.5, 126.9, 128.0, 128.1, 128.4, 128.8, 128.9, 129.7, 134.9, 144.7, 151.4, 152.1, 166.6, 167.5, 171.9, 172.7, 173.7. $C_{45}H_{46}N_4O_{10}S$ (834.93): calcd. C, 64.73; H, 5.55; N, 6.71. Found: C, 64.85; H, 5.50; N, 6.60.

Trityl-mercapto-(L-Ala-D-Oxd)$_4$-OBn (35)

Trifluoroacetic acid (0.24 mL, 3.1 mmol) was added under nitrogen atmosphere to a solution of **30** (0.17 g, 0.17 mmol) in dry dichloromethane (20 mL). The mixture was stirred at room temperature for 4 hours and concentrated in vacuo after a control via TLC. H-(L-Ala-D-Oxd)$_4$-OBn·CF_3CO_2H was obtained in quantitative yield. HBTU (0.077 g, 0.2 mmol) was added to a solution 3-tritylmercapto propionic acid (0.057 g, 0.16 mmol) in dry acetonitrile (15 mL) under inert atmosphere. The mixture was left stirring for 10 minutes in order to activate the acid. A solution of the previously obtained H-(L-Ala-D-Oxd)$_4$-OBn·CF_3CO_2H and TEA (0.07 mL, 0.5 mmol) in dry acetonitrile (15 mL) was added dropwise. The progress of the reaction was followed by TLC and after 1 hour the reaction went to completion. The mixture was concentrated in vacuo, it was partitioned between AcOEt (20 mL) with brine (20 mL), HCl 1N (20 mL) and $NaHCO_3$ (20 mL). The aqueous layer was extracted with AcOEt and the organic layer were dried (Na_2SO_4), filtered and concentrated in vacuo. The crude of the reaction was purified via flash chromatography (from 50:50 to 10:90 cHex/AcOEt) to afford compound **35** as a white solid (0.13 g, 62% yield); Rf = 0.65 (100% AcOEt).

M.p. = 138-142 °C; $[\alpha]_D^{20}$ = - 20.8 (c = 1.0 in CH_2Cl_2); IR (CH_2Cl_2 3 mM) ν = 3355, 3299,1790, 1743, 1714, 1670 cm^{-1}; ^1H NMR (400 MHz $CDCl_3$): δ 1.35-1.57 (m, 24H, 4 x CH_3 Ala + 4 x CH_3 Oxd), 2.10-2.48 (m, 4H, 2 x CH_2), 4.42-4.60 (m, 6H, 3 x CHN Oxd + 3 x CHO Oxd), 4.65-4.73 (m, 2H, CHN Oxd + CHO Oxd), 5.23 (s, 2H, O-CH_2-Ph), 5.32-5.40 (m, 1H, CH Ala), 5.42-5.49 (m, 1H, CH Ala), 5.60-5.68 (m, 1H, CH Ala), 5.88 (1H, bs, NH), 5.98-6.05 (m, 1H, CH Ala), 7.16 (1H, d, *J* = 6.7 Hz, NH), 7.18-7.45 (m, 20H, 20 x CH Ph), 7.57 (1H, s, NH), 7.75 (1H, s, NH); ^{13}C NMR (100 MHz $CDCl_3$): δ 18.6, 19.3, 20.6, 20.9, 21.0, 21.2, 21.4, 27.4, 28.1, 29.8, 34.7, 34.8, 38.8, 49.0, 49.1, 61.9, 62.3, 62.4, 66.6, 67.1, 68.1, 68.3, 74.0, 74.1, 74.7, 75.0, 126.6, 126.9, 127.4, 128.0, 128.1, 128.2, 128.4, 128.5, 128.8, 128.9, 129.0, 129.7, 129.8, 134.7, 144.6, 145.0, 147.0, 151.4, 151.7, 151.9, 152.1, 167.4, 167.9, 168.2, 168.6, 172.2, 172.3, 172.8. $C_{61}H_{66}N_8O_{18}S$ (1231.28): calcd. C, 59.50; H, 5.40; N, 9.10. Found: C, 59.63; H, 5.31; N, 9.24.

Trityl-mercapto-(L-Ala-D-Oxd)$_8$-OBn (36)

Trifluoroacetic acid (TFA) (0.077 mL, 1 mmol) was added under inert atmosphere to a solution of **32** (0.100 g, 0.056 mmol) in dry dichloromethane (20 mL). The mixture was stirred at room temperature for 4 hours and concentrated in vacuo after a control via TLC. The product H-(L-Ala-D-Oxd)$_8$-OBn·CF_3CO_2H was obtained in quantitative yield. HATU (0.024 g, 0.063 mmol) was added to a solution of 3-tritylmercapto propionic acid (0.0195 g, 0.056 mmol) and dry acetonitrile (15 mL) under inert atmosphere. The mixture was left stirring at room temperature for 10 minutes, and then a solution of the previously obtained H-(L-Ala-D-Oxd)$_8$-OBn·CF_3CO_2H and TEA (0.023 mL, 0.164 mmol) in dry acetonitrile (20 mL) was added dropwise. The progress of the reaction was followed by TLC and after 1 hour the reaction went to completion. The mixture was concentrated in vacuo, it was partitioned between AcOEt (20 mL) with brine (20 mL), 1N HCl (20 mL) and $NaHCO_3$ (20 mL). The combined organic layer was dried (Na_2SO_4), filtered and concentrated in vacuo. The purification occurred with an ultrasound-assisted washing process using organic solvents as n-Hex, ether and pentane achieving product **32** as a white solid (60 mg, overall 53% yield).

M.p. = 273-275°C; $[\alpha]_D$ = -114 (c = 0.61 in CH_2Cl_2); IR (CH_2Cl_2 3 mM) ν = 3461, 3394, 1785, 1715, 1662 cm^{-1}; ^1H NMR (400 MHz $CDCl_3$): δ 1.32-1.62 (m, 48H, 8 x CH_3 Ala + 8 x CH_3 Oxd), 2.20-2.60 (m, 4H, CH_2), 4.52 (bs, 8H, 8 x CHO Oxd), 4.60-4.64 (m, 1H, CHN Oxd), 4.70-4.78 (m, 2H, 2 x CHN Oxd), 4.95-5.10 (m, 5H, 5 x CHN Oxd), 5.06-5.12 (m, 1H, CHO Oxd) 5.22 (s, 2H, O-CH_2-Ph), 5.70-6.05 (m, 8H, 8x CH Ala), 7.00-7.45 (m, 20H, 20 x CH Ph), 7.90-8.00 (m, 2H, 2 x NH), 8.20-8.30 (m, 2H, 2 x NH), 8.30-8.45 (m, 4H, 4 x NH); ^{13}C NMR (100 MHz $CDCl_3$): δ 18.1, 19.1, 21.0, 21.2, 21.4, 28.4, 31.1, 49.2, 62.1, 74.4, 75.1, 126.8, 127.4, 128.0, 128.6, 128.9, 129.7, 134.9, 144.9, 151.0, 151.9, 168.8, 171.4, 172.0, 172.3. $C_{93}H_{106}N_{16}O_{34}S$ (2023.99): calcd. C, 55.19; H, 5.28; N, 11.07. Found: C, 55.11; H, 5.21; N, 11.01.

General synthesis of AuNPs

Compound **33**, **34**, **35** or **36** (0.026 mmol) was dissolved in a mixture of Milli-Q water, MeOH and CH_2Cl_2. A solution of $HAuCl_4$ (0.040 g, 0.11 mmol) in water was added and the mixture was left stirring for 20 minutes, in order to permit the polymerisation. A solution of $NaBH_4$ (0.020 g, 0.53 mmol) dissolved in water was then added to the mixture very rapidly. A brown solution was obtained and after two hours the reaction went to completion. The reaction was quenched by addition of 0.1 M HCl (1 mL). The solvent was removed under reduced pressure to dryness and the dark residue was dissolved in Milli-Q water (4 mL). Subsequently, the so-obtained solution was filtered through a 45 ym microfilter, the nanoparticles precipitated by adding a large amount of CH_3CN and **AuNPs** finally isolated by centrifugation or filtration.

Fmoc-L-Phe-D-Oxd-OBn (37a)

To a stirred solution of Fmoc-L-Phe-OH (1 mmol, 0.39 g) and HBTU (1.1 mmol, 0.42 g) in dry acetonitrile (10 mL) under inert atmosphere, D-Oxd-OBn (1 mmol, 0.24 g) in dry acetonitrile (5 mL) was added at room temperature, followed by a solution of triethylamine (2.2 mmol, 0.30 mL). The solution was stirred for 40 minutes under inert atmosphere, then acetonitrile was removed under reduced pressure and replaced with ethyl acetate. The mixture was washed with brine, 1 N aqueous HCl (3 x 30 mL) and with 5% aqueous $NaHCO_3$ (1 x 30 mL), dried over sodium sulphate and concentrated in vacuo. The product was obtained pure after silica gel chromatography (cyclohexane/ethyl acetate 9:1 → 7:3 as eluant) in 60% yield (0.6 mmol, 0.36 g).

M.p. = 153-156 °C; $[\alpha]_D^{20}$ = 25.1 (c = 0.26 in CH_2Cl_2); IR (CH_2Cl_2, 3 mM) v = 3428, 1752, 1727, 1701, 1605 cm^{-1}; ^1H NMR (400 MHz, $CDCl_3$): δ 1.42 (d, *J* = 6.4 Hz, 3H, Me-Oxd), 3.00 (dd, *J* = 8.0, 12.4 Hz, 1H, CHβ-Phe), 3.16 (dd, *J* = 4.0, 12.4 Hz, 1H, CHβ-Phe), 4.06-4.44 (m, 4H, O-CH-CH_2-fluorene + CHN-Oxd), 4.52 (dq, *J* = 4.8, 6.4 Hz, CHO-Oxd), 5.16 (s, 2H, OCH_2Ph), 5.42 (d, *J* = 8.4 Hz, 1H, NH), 5.87 (dt, *J* = 6.0, 8.4 Hz, 1H, CHα-Phe), 7.11-7.80 (m, 18 H, 2 x Phe + fluorene); ^{13}C NMR (100 MHz, $CDCl_3$): δ 21.1, 29.7, 38.9, 47.1, 54.2, 61.8, 67.0, 68.1, 73.6, 119.9, 125.1, 127.0, 127.2, 127.6, 128.5, 128.9, 129.5, 134.5, 135.4, 141.2, 143.8, 151.1, 155.2, 167.3, 172.1. Elemental analysis calcd (%) for $C_{36}H_{32}N_2O_7$: C, 71.51; H, 5.33; N, 4.63; found: C, 71.48; H, 5.37; N, 4.60.

Fmoc-L-Phe-D-Oxd-OH (37b)

Compound **37a** (0.36 g, 0.6 mmol) was dissolved in MeOH (30 mL) under nitrogen. Pd/C (35 mg, 10% w/w) was added under nitrogen. Vacuum was created inside the flask using the vacuum line. The flask was then filled with hydrogen using a balloon (1 atm). The solution was stirred for 4 hours under a hydrogen atmosphere. The product was obtained pure as an oil in 98% yield (0.59 mmol, 0.30 g), after filtration through filter paper and concentration in vacuo.

M.p. = 221-223 °C; $[\alpha]_D^{20}$ = 31.6 (c = 0.1 in DMF); IR (nujol) v = 3322, 1783, 1719, 1690, 1559 cm^{-1}; ^1H NMR (400 MHz, CD_3OD): δ 1.45 (d, *J* = 6.4 Hz, 3H, Me-Oxd), 2.80 (dd, *J* = 9.6, 14.0 Hz, 1H, CHβ-Phe), 3.17 (dd, *J* = 4.0, 14.0 Hz, 1H, CHβ-Phe), 4.01-4.30 (m, 3H, O-CH-CH_2-fluorene + O-CH-CH_2-fluorene), 4.38-4.45 (m, 1H, CHN-Oxd), 4.68 (dq, *J* = 6.0, 6.4 Hz, CHO-Oxd), 5.71-5.80 (m, 1H, CHα-Phe), 7.05-7.85 (m, 13 H, Phe + fluorene); ^{13}C NMR (100 MHz, $CDCl_3$): δ 19.8, 22.7, 37.8, 54.7, 62.1, 66.6, 74.7, 119.4, 124.8, 126.7, 127.2, 127.9, 128.7, 129.1, 136.8, 141.0, 143.7, 170.3, 172.3. Elemental analysis calcd (%) for $C_{29}H_{26}N_2O_7$: C, 67.70; H, 5.09; N, 5.44; found: C, 67.73; H, 5.10; N, 5.47.

Fmoc-L-Phe-D-Oxd-L-Phe-OBn (38a)
To a stirred solution of Fmoc-L-Phe-D-Oxd-OH **37b** (1 mmol, 0.52 g) and HBTU (1.1 mmol, 0.42 g) in dry acetonitrile (10 mL) under inert atmosphere, a mixture of HCl.H_2N-L-Phe-OBn (1 mmol, 0.29 g) and triethylamine (3.1 equiv., 0.43 mL) in dry acetonitrile (5 mL) was added at room temperature. The solution was stirred for 40 minutes under inert atmosphere, then acetonitrile was removed under reduced pressure and replaced with ethyl acetate. The mixture was washed with brine, 1 N aqueous HCl (3 x 30 mL) and with 5% aqueous $NaHCO_3$ (1 x 30 mL), dried over sodium sulphate and concentrated in vacuo. The product was obtained pure after silica gel chromatography (dichloromethane/ethyl acetate 99:1 → 97:3 as eluant) in 72% yield (0.72 mmol, 0.48 g).
M.p. = 150 °C; $[\alpha]_D^{20}$ = 24.8 (c = 0.1 in CH_2Cl_2); IR (CH_2Cl_2, 3 mM) v = 3419, 3350, 1792, 1788, 1704, 1683 cm^{-1}; ^{1}H NMR (400 MHz, $CDCl_3$): δ 1.29 (d, *J* = 6.4 Hz, 3H, Me-Oxd), 2.93-3.24 (m, 4H, 2 x CH_2β-Phe), 4.07-4.37 (m, 4H, O-CH-CH_2-fluorene + O-CH-CH_2-fluorene + CHN-Oxd), 4.53 (dq, *J* = 5.2, 6.4 Hz, CHO-Oxd), 4.75 (q, *J* = 6.0 Hz, CHα-Phe), 5.03 (AB, *J* = 10.8 Hz, 2H, OCH_2Ph), 5.36 (bs, 1H, NH), 5.65 (bs, 1H, CHα-Phe), 6.92-7.82 (m, 24 H, 3 x Phe + fluorene + NH); ^{13}C NMR (100 MHz, $CDCl_3$): δ 20.8, 29.7, 37.3, 46.9, 54.0, 54.4, 62.6, 67.1, 67.4, 74.9, 120.0, 125.0, 127.1, 127.4, 127.7, 128.3, 128.4, 128.5, 128.8, 129.2, 129.4, 135.0, 135.2, 141.2, 143.4, 151.5, 166.8, 170.1, 172.6. Elemental analysis calcd (%) for $C_{45}H_{41}N_3O_8$: C, 71.89; H, 5.50; N, 5.59; found: C, 71.93; H, 5.53; N, 5.55.

Fmoc-L-Phe-D-Oxd-L-Phe-OH (38b)
For the synthetic procedure from **38a**, see the preparation of **37b** given above, yield: 99%.
M.p. = 155 °C; $[\alpha]_D^{20}$ = 41.5 (c = 0.1 in MeOH); IR (nujol) v = 3351, 1776, 1727, 1691, 1663, 1529 cm^{-1}; ^{1}H NMR (400 MHz, CD_3OD): δ 1.25 (d, *J* = 6.8 Hz, 3H, Me-Oxd), 2.79 (dd, *J* = 10.0, 13.6 Hz, 1H, CHβ-Phe), 2.89 (dd, *J* = 9.6, 13.6 Hz, 1H, CHβ-Phe), 3.04-3.30 (m, 2H, CH_2β-Phe), 3.80-4.38 (m, 5H, O-CH-CH_2-fluorene + O-CH-CH_2-fluorene + CHN-Oxd + CHO-Oxd), 4.51-4.61 (m, 1H, CHα-Phe), 5.68-5.76 (m, 1H, CHα-Phe), 7.09-7.80 (m, 18 H, 2 x Phe + fluorene); ^{13}C NMR (100 MHz, CD_3OD): δ 19.4, 37.1, 37.3, 37.7, 53.8, 54.7, 61.3, 62.5, 66.6, 71.1, 74.9, 76.9, 119.4, 124.8, 124.9, 126.7, 127.3, 128.0, 128.9, 129.2, 136.7, 137.1, 141.0, 143.7, 152.3, 156.6, 168.4, 172.2, 173.0. Elemental analysis calcd (%) for $C_{38}H_{34}N_3O_8$: C, 69.08; H, 5.19; N, 6.36; found: C, 69.06; H, 5.21; N, 6.38.

Boc-L-Phe-D-Oxd-L-Phe-OBn (39a)
Fmoc-L-Phe-D-Oxd-L-Phe-OBn **38a** (0.5 mmol, 0.38 g) was added to a solution of pyperidine (4 mmol, 0.4 mL) in dichloromethane (2 mL) and the mixture was stirred for 30 minutes at room temperature then concentrated in vacuo. The product was dissolved in tert-butanol (3 mL), then Boc_2O (0.6 mmol, 0.13 g) and NaOH 1M (0.6 mmol, 0.6 mL) were added at 0 °C and the mixture was stirred for 3 hours at 0 °C. Then ethyl acetate (30 mL) was added to the mixture, that was washed with brine, 1 N aqueous HCl (3 x 30 mL) and with 5% aqueous $NaHCO_3$ (1 x 30 mL), dried over sodium sulphate and concentrated in vacuo. The product was obtained pure after silica gel chromatography (dichloromethane → dichloromethane/ethyl acetate 95:5 as eluant) in 87% yield (0.44 mmol, 0.27 g).
M.p. = 196-198 °C; $[\alpha]_D^{20}$ = 31.1 (c = 0.1 in CH_2Cl_2); IR (CH_2Cl_2, 3 mM) v = 3432, 3350, 1788, 1740, 1700, 1684 cm^{-1}; ^{1}H NMR (400 MHz, $CDCl_3$): δ 1.26 (d, *J* = 6.4 Hz, 3H, Me-Oxd), 1.33 (s, 9H, O-tBu), 2.80-2.92 (m, 1H, CHβ-Phe), 3.01-3.21 (m, 3H, CHβ-Phe + CH_2β-Phe), 4.21 (bs, 1H, CHN-Oxd), 4.53 (dq, *J* = 5.2, 6.4 Hz, CHO-Oxd), 4.75 (q, *J* = 6.8 Hz, CHα-Phe), 4.98-5.17 (m, 3H, NH + OCH_2Ph), 5.59 (bs, 1H, CHα-Phe), 6.94-7.44 (m, 16 H, 3 x Phe + NH); ^{13}C NMR (100 MHz, $CDCl_3$): 20.7, 28.2, 37.3, 54.1, 62.6, 67.2, 74.7, 80.5, 127.2, 128.5, 128.7, 129.2, 129.4, 135.2, 135.5, 136.0, 151.5, 166.9, 170.5, 172.8. Elemental analysis calcd (%) for $C_{35}H_{39}N_3O_8$: C, 66.76; H, 6.24; N, 6.67; found: C, 66.80; H, 6.28; N, 6.71.

Boc-L-Phe-D-Oxd-L-Phe-OH (39b)
For the synthetic procedure from **39a**, see the preparation of **37b** given above, yield: 98%.
M.p. = 227-230 °C; $[\alpha]_D^{20}$ = 21.9 (c = 1.0 in MeOH); IR (nujol) v = 3322, 1779, 1717, 1693, 1653 cm^{-1}; ^{1}H NMR (400 MHz, CD_3OD): δ 1.02-1.26 (m, 12H, Me-Oxd + t-Bu), 2.46-2.67 (m, 1H, CHβ-Phe), 2.69-2.83 (m, 1H, CHβ-Phe), 2.83-2.97 (m, 1H, CHβ-Phe), 3.04-3.20 (m, 1H, CHβ-Phe), 3.69-4.78 (m, 1H, CHN-Oxd), 4.08-4.18 (m, 1H, CHO-Oxd), 4.45-4.61 (m, 1H,

CHα-Phe), 5.45-5.56 (m, 1H, CHα-Phe), 6.98-7.18 (m, 10 H, 2 x Phe); ^{13}C NMR (100 MHz, CD_3OD): δ 19.4, 26.8, 27.2, 37.3, 38.1, 54.1, 62.4, 74.8, 79.1, 126.4, 127.9, 128.0, 129.0, 129.2, 136.6, 137.1, 152.3, 156.0, 168.5, 172.4. Elemental analysis calcd (%) for $C_{28}H_{33}N_3O_8$: C, 62.33; H, 6.16; N, 7.79; found: C, 62.37; H, 6.13; N, 7.82.

Cbz-L-Phe-D-Oxd-L-Phe-OBn (40a)
Fmoc-L-Phe-D-Oxd-L-Phe-OBn **38a** (0.5 mmol, 0.38 g) was added to a solution of pyperidine (4 mmol, 0.4 mL) in dichloromethane (2 mL) and the mixture was stirred for 30 minutes at room temperature then concentrated in vacuo. The product was dissolved in acetone (5 mL) and NaOH 1M (0.6 mmol, 0.6 mL), then CbzCl (0.6 mmol, 0.10 g) in acetone (2 mL) was added dropwise at 0 °C and the mixture was stirred for 3 hours at 0 °C. Then acetone was removed in vacuo and ethyl acetate (30 mL) was added to the mixture, that was washed with brine, 1 N aqueous HCl (3 x 30 mL) and with 5% aqueous $NaHCO_3$ (1 x 30 mL), dried over sodium sulphate and concentrated in vacuo. The product was obtained pure after silica gel chromatography (dichloromethane → dichloromethane/ethyl acetate 95:5 as eluant) in 90% yield (0.45 mmol, 0.30 g).
M.p. = 197-199 °C; $[\alpha]_D^{20}$ = 20.6 (c = 0.2 in CH_2Cl_2); IR (CH_2Cl_2, 3 mM) ν = 3427, 3351, 1789, 1704, 1605 cm^{-1}; ^{1}H NMR (400 MHz, $CDCl_3$): δ 1.29 (d, *J* = 6.4 Hz, 3H, Me-Oxd), 2.90 (dd, *J* = 8.8, 13.6 Hz, 1H, CHβ-Phe), 3.02 (dd, *J* = 7.2, 13.6 Hz, 1H, CHβ-Phe), 3.11-3.20 (m, 2H, CH_2β-Phe), 4.27 (bs, 1H, CHN-Oxd), 4.54 (dq, *J* = 5.6, 6.4 Hz, 1H, CHO-Oxd), 4.77 (dt, *J* = 6.0, 8.0 Hz, 1H, CHα-Phe), 4.83-5.14 (m, 4H, 2 x OCH_2Ph), 5.70 (m, 1H, CHα-Phe), 6.96-7.38 (m, 21 H, 4 x Phe + NH); ^{13}C NMR (100 MHz, $CDCl_3$): 20.9, 37.3, 37.8, 53.3, 54.3, 62.5, 67.3, 74.9, 127.0, 127.4, 128.0, 128.1, 128.3, 128.5, 128.6, 128.8, 129.2, 129.4, 135.3, 135.6, 151.5, 156.2, 166.9, 170.2, 170.6, 170.7, 172.8. Elemental analysis calcd (%) for $C_{38}H_{37}N_3O_8$: C, 68.77; H, 5.62; N, 6.33; found: C, 68.74; H, 5.66; N, 6.38.

CH_2-[$(CH_2)_3$-CO-L-Phe-D-Oxd-L-Phe-OBn]$_2$ (41a)
Fmoc-L-Phe-D-Oxd-L-Phe-OBn **38a** (0.5 mmol, 0.38 g) was added to a solution of pyperidine (4 mmol, 0.4 mL) in dichloromethane (2 mL) and the mixture was stirred for 30 minutes at room temperature then concentrated in vacuo. The residue was dissolved in dry acetonitrile (5 mL) and was added to a stirred solution of azelaic acid (0.25 mmol, 50 mg) and HBTU (0.55 mmol, 0.21 g) in dry acetonitrile (10 mL) at room temperature and under inert atmosphere, followed by a solution of triethylamine (2.0 mmol, 0.28 mL). The final solution was stirred for 40 minutes under inert atmosphere, then acetonitrile was removed under reduced pressure and replaced with ethyl acetate. The mixture was washed with brine, 1 N aqueous HCl (3 x 30 mL) and with 5% aqueous $NaHCO_3$ (1 x 30 mL), dried over sodium sulphate and concentrated in vacuo. The product was sonicated in ethyl ether (3 x 10 mL) for 10 minutes each, then filtered and dried in vacuo. It was obtained pure in 96% yield (0.26 mmol, 0.61 g).
M.p. = 227-229 °C; $[\alpha]_D^{20}$ = 49.9 (c = 0.4 in CH_2Cl_2); IR (CH_2Cl_2, 3 mM) ν = 3435, 3325, 1787, 1743, 1716, 1677, 1660 cm^{-1}; ^{1}H NMR (400 MHz, $CDCl_3$): δ 1.01-1.09 (m, 6H, 3 x CH_2 azelaic acid), 1.27 (d, *J* = 6.4 Hz, 6H, 2 x Me-Oxd), 1.33-1.43 (m, 4H, 2 x CH_2 azelaic acid), 1.92-2.02 (m, 4H, 2 x CH_2 azelaic acid), 2.89 (dd, *J* = 9.2, 13.2 Hz, 2H, 2 x CHβ-Phe), 3.07 (dd, *J* = 8.0, 13.2 Hz, 2H, 2 x CHβ-Phe), 3.11-3.21 (m, 4H, 2 x CH_2β-Phe), 4.30 (d, *J* = 5.2 Hz, 2H, 2 x CHN-Oxd), 4.50 (dq, *J* = 5.2, 6.4 Hz, 2H, 2 x CHO-Oxd), 4.72 (dt, *J* = 6.4, 7.6 Hz, 2H, 2 x CHα-Phe), 5.03 (AB, *J* = 12.4 Hz, 4H, 2 x OCH_2Ph), 5.62-5.70 (m, 2H, 2 x CHα-Phe), 5.97 (d, *J* = 4.4 Hz, 2H, 2 x NH), 7.04-7.34 (m, 30 H, 6 x Phe), 7.65 (d, *J* = 7.6 Hz, 2H, 2 x NH); ^{13}C NMR (100 MHz, $CDCl_3$): 20.9, 24.5, 28.6, 29.6, 35.3, 36.4, 36.9, 53.4, 54.2, 59.8, 62.3, 66.9, 75.1, 126.7, 127.4, 128.1, 128.3, 128.4, 128.8, 129.1, 135.2, 136.6, 151.6, 167.3, 170.7, 172.5, 173.8. Elemental analysis calcd (%) for $C_{69}H_{74}N_6O_{14}$: C, 68.41; H, 6.16; N, 6.94; found: C, 68.38; H, 6.14; N, 6.97.

CH_2-[$(CH_2)_3$-CO-L-Phe-D-Oxd-L-Phe-OH]$_2$ (41b)
For the synthetic procedure from **41a**, see the preparation of **37b** given above, yield: 97%.
M.p. = 233 °C; $[\alpha]_D^{20}$ = 49.9 (c = 0.4 in CH_2Cl_2); IR (nujol) ν = 3292, 1784, 1718, 1654, 1603, 1545 cm^{-1}; ^{1}H NMR (400 MHz, DMSO-d_6): δ 0.86-1.08 (m, 6H, 3 x CH_2 azelaic acid), 1.14-1.43 (m, 10H, 2 x Me-Oxd + 2 x CH_2 azelaic acid), 1.87-2.02 (m, 4H, 2 x CH_2 azelaic acid), 2.56-2.71 (m, 2H, 2 x CHβ-Phe), 2.71-2.89 (m, 2H, 2 x CHβ-Phe), 2.89-3.12 (m, 4H, 2 x

CH_2β-Phe), 3.88 (d, *J* = 4.4 Hz, 2H, 2 x CHN-Oxd), 4.26-4.33 (m, 2H, 2 x CHα-Phe), 4.51 (dq, *J* = 4.4, 5.6 Hz, 2H, 2 x CHO-Oxd), 5.65-5.75 (m, 2H, 2 x CHα-Phe), 7.09-7.25 (m, 20 H, 4 x Phe), 8.00 (bs, 2H, 2 x NH), 8.13 (d, *J* = 7.6 Hz, 2H, 2 x NH); ^{13}C NMR (100 MHz, DMSO-*d*$_6$): 21.2, 21.3, 25.5, 28.7, 35.5, 37.8, 52.8, 53.8, 55.3, 60.2, 62.3, 74.8, 75.1, 77.2, 126.7, 126.8, 128.5, 128.6, 129.6, 137.8, 138.2, 152.6, 158.2, 170.1, 172.3, 172.5, 172.7, 173.7. Elemental analysis calcd (%) for $C_{55}H_{62}N_6O_{14}$: C, 64.07; H, 6.06; N, 8.15; found: C, 64.12; H, 6.10; N, 8.18.

Fmoc-L-Phe-D-pGlu-OBn (42a)

To a stirred solution of Fmoc-L-Phe-OH (1 mmol,0.39 g) and HBTU (1.1 mmol, 0.42 g) in dry acetonitrile (10 mL) under inert atmosphere, D-pGlu-OBn (1 mmol,0.22 g) in dry acetonitrile (5 mL) was added at room temperature, followed by a solution of DBU (2.5 mmol, 0.37 mL). The solution was stirred for 2 hours under inert atmosphere, then acetonitrile was removed under reduced pressure and replaced with ethyl acetate. The mixture was washed with brine, 1 N aqueous HCl (3 x 30 mL) and with 5% aqueous $NaHCO_3$ (1 x 30 mL), dried over sodium sulphate and concentrated in vacuo. The product was obtained pure after silica gel chromatography (cyclohexane/ethyl acetate 8:2 → 7:3 as eluant) in 48% yield (0.48 mmol, 0.28 g).

M.p. = 83-84 °C; $[\alpha]_D^{20}$ = 63.9 (c = 0.18 in $CHCl_3$); IR (CH_2Cl_2, 3 mM) v = 3429, 1794, 1755, 1711, 1605 cm^{-1}; ^{1}H NMR (400 MHz, $CDCl_3$): δ 2.00-2.11 (m, 1H, CHβ-pGlu), 2.16-2.31 (m, 1H, CHβ-pGlu), 2.43-2.56 (m, 1H, CHγ-pGlu), 2.63-2.80 (m, 1H, CHγ-pGlu), 2.94 (dd, *J* = 7.6, 13.6 Hz, 1H, CHβ-Phe), 3.16 (dd, *J* = 7.6, 13.6 Hz, 1H, CHβ-Phe), 4.12-4.27 (m, 2H, O-CH-CH_2-fluorene), 4.34-4.41 (m, 1H, O-CH-CH_2-fluorene), 4.64 (m, 1H, CHα-pGlu), 5.14 (s, 2H, OCH_2Ph), 5.47 (d, *J* = 8.4 Hz, 1H, NH), 5.85 (dt, *J* = 6.4, 8.4 Hz, 1H, CHα-Phe), 7.11-7.76 (m, 18 H, Phe + fluorene); ^{13}C NMR (100 MHz, $CDCl_3$): δ 21.6, 29.7, 31.6, 39.0, 47.1, 53.4, 55.3, 58.2, 66.9, 67.5, 119.9, 125.2, 127.0, 127.6, 128.2, 128.4, 128.5, 128.6, 129.5, 135.0, 135.8, 141.2, 143.9, 155.1, 170.2, 172.6, 173.8. Elemental analysis calcd (%) for $C_{36}H_{32}N_2O_6$: C, 73.45; H, 5.48; N, 4.76; found: C, 73.48; H, 5.51; N, 4.73.

Fmoc-L-Phe-D-pGlu-OH (42b)

For the synthetic procedure from **42a**, see the preparation of **37b** given above, yield: 99%.

M.p. = 197-200 °C; $[\alpha]_D^{20}$ = 34.7 (c = 0.15 in $CHCl_3$); IR (nujol) v = 1735, 1714, 1695, 1538 cm^{-1}; ^{1}H NMR (400 MHz, DMSO-*d6*): δ 1.96 (d, *J* = 9.2, 10.4 Hz, 1H, CHβ-pGlu), 2.26-2.40 (m, 1H, CHβ-pGlu), 2.49-2.72 (m, 3H, CH_2γ-pGlu + CHβ-Phe), 3.02 (dd, *J* = 1.1, 13.2 Hz, 1H, CHβ-Phe), 4.01-4.15 (m, 3H, O-CH-CH_2-fluorene), 4.52 (dd, *J* = 1.8, 9.6 Hz, 1H, CHα-pGlu), 5.40 (dd, *J* = 9.6, 10.8 Hz, 1H, CHα-Phe), 7.12-7.87 (m, 13 H, Phe + fluorene); ^{13}C NMR (100 MHz, DMSO-*d6*): δ 21.7, 32.1, 37.2, 46.9, 56.7, 58.6, 66.1, 120.5, 125.7, 126.8, 127.5, 128.0, 128.5, 128.6, 129.6, 138.3, 141.0, 144.1, 144.2, 156.1, 172.7, 173.5, 175.6. Elemental analysis calcd (%) for $C_{29}H_{26}N_2O_6$: C, 69.87; H, 5.26; N, 5.62; found: C, 69.90; H, 5.30; N, 5.59.

Fmoc-L-Phe-D-pGlu-L-Phe-OBn (43a)

For the synthetic procedure from **42b**, see the preparation of **38a** given above, (dichloromethane/ethyl acetate 98:2 → 90:10 as eluant) yield: 75%.

M.p. = 210-213 °C; $[\alpha]_D^{20}$ = 39.6 (c = 0.2 in CH_2Cl_2); IR (CH_2Cl_2, 3 mM) v = 3421, 1749, 1695, 1605 cm^{-1}; ^{1}H NMR (400 MHz, $CDCl_3$): δ 1.94-2.13 (m, 2H, CH_2β-pGlu), 2.25-2.40 (m, 1H, CHα-pGlu), 2.55-2.73 (m, 1H, CHα-pGlu), 2.91 (dd, *J* = 8.0, 13.6 Hz, 1H, CHβ-Phe), 3.00 (dd, *J* = 6.4, 13.6 Hz, 1H, CHβ-Phe), 3.08-3.18 (m, 2H, CH_2β-Phe), 4.06-4.25 (m, 2H, O-CH-CH_2-fluorene), 4.29-4.37 (m, 1H, O-CH-CH_2-fluorene), 4.52-4.56 (m, 1H, pGlu), 4.77 (dq, *J* = 6.4, 6.4 Hz, 1H, CHα-Phe), 5.05 (AB, *J* = 12.0 Hz, 2H, OCH_2Ph), 5.42 (d, *J* = 6.4 Hz, 1H, NH), 5.78 (dt, *J* = 6.0, 6.4 Hz, 1H, CHα-Phe), 6.67 (d, *J* = 7.6 Hz, 1H, NH), 6.94-7.75 (m, 23 H, 3 x Phe + fluorene); ^{13}C NMR ($CDCl_3$): δ 22.7, 29.7, 37.4, 38.2, 47.0, 53.4, 55.2, 59.1, 67.1, 67.3, 77.1, 119.9, 125.1, 127.0, 127.1, 127.6, 128.5, 129.2, 129.4, 134.9, 135.6, 135.9, 141.2, 143.7, 155.7, 169.3, 170.9, 173.0, 174.5. Elemental analysis calcd (%) for $C_{45}H_{41}N_3O_7$: C, 73.45; H, 5.62; N, 5.71; found: C, 73.49; H, 5.68; N, 5.73.

Fmoc-L-Phe-D-pGlu-L-Phe-OH (43b)
For the synthetic procedure from **43a**, see the preparation of **37b** given above, yield: 98%.
M.p. = 199-201 °C; $[\alpha]_D^{20}$ = 45 (c = 0.2 in CH_2Cl_2); IR (nujol) v = 3326, 1733, 1694, 1650, 1548 cm^{-1}; ^1H NMR (400 MHz, DMSO-*d6*): δ 1.54-1.64 (m, 1H, CHβ-pGlu), 2.06-2.19 (m, 1H, CHβ-pGlu), 2.30-2.43 (m, 1H, CHα-pGlu), 2.43-2.57 (m, 1H, CHα-pGlu), 2.73 (dd, *J* = 8.8, 13.6 Hz, 1H, CHβ-Phe), 2.92 (dd, *J* = 10.0, 14.0 Hz, 1H, CHβ-Phe), 3.12 (dd, *J* = 3.6, 13.6 Hz, 1H, CHβ-Phe), 3.22 (dd, *J* = 4.8, 14.0 Hz, 1H, CHβ-Phe), 4.03-4.12 (m, 2H, O-CH-CH_2-fluorene), 4.18-4.27 (m, 1H, O-CH-CH_2-fluorene), 4.54-4.60 (m, 1H, pGlu), 4.65-4.72 (m, 1H, CHα-Phe), 5.66-5.74 (m, 1H, CHα-Phe), 7.06-7.77 (m, 20 H, 2 x Phe + fluorene + 2 x NH), ; ^{13}C NMR (DMSO-*d6*): δ 19.0, 23.0, 32.7, 37.5, 37.9, 46.9, 53.3, 56.4, 56.5, 59.0, 66.0, 120.4, 125.7, 126.8, 127.5, 128.0, 128.5, 129.6, 129.7, 137.8, 138.3, 140.1, 141.1, 144.1, 155.9, 170.3, 173.0, 173.2, 175.9. Elemental analysis calcd (%) for $C_{38}H_{35}N_3O_7$: C, 70.68; H, 5.46; N, 6.51; found: C, 70.65; H, 5.48; N, 6.54.

Fmoc-L-Tyr(O-tert-Bu)-D-Oxd-OBn (44)
To a stirred solution of Fmoc-Tyr(O-tert-Bu)-OH (0.64 mmol, 294 mg) and HATU (0.70 mmol, 267 mg), in dry acetonitrile (15 mL), under inert atmosphere, D-Oxd-OBn (0.64 mmol, 150 mg) in dry acetonitrile (7 mL) was added at room temperature, followed by a solution of N,N-diisopropylethylamine (1.6 mmol, 272 µL). The solution was stirred for 2 hours under inert atmosphere, then acetonitrile was removed under reduced pressure and replaced with dichloromethane (30 mL). The mixture was washed with brine (30 mL), 1 N aqueous HCl (30 mL) and with saturated aqueous $NaHCO_3$ (30 mL), dried over sodium sulphate and concentrated in vacuo. The product was obtained pure after silica gel chromatography (dichloromethane → dichloromethane/ethyl acetate 98:2) in 90% of yield (0.576 mmol, 389 mg).
M.p. = 89-90 °C; $[\alpha]_D^{20}$ = 31.5 (c = 0.20 in CH_2Cl_2); IR (CH_2Cl_2 3 mM) v = 3429, 1793, 1755, 1712, 1608, 1506 cm^{-1}; ^1H NMR (400 MHz $CDCl_3$): δ 1.29 (s, 9H, CH_3 tert-Bu), 1.47 (d, J = 6.2 Hz, 3H, CH_3 Oxd), 2.95 (dd, J = 7.5, J = 13.3 Hz, 1H, CH_2β-Tyr), 3.15 (dd, J = 5.4 Hz, J = 13.7 Hz , 1H, CH_2β-Tyr), 4.15-4.21 (m, 1H, O-CH-CH_2-Fluorene), 4.23-4.29 (m, 1H, O-CH-CH_2-Fluorene), 4.38 (s, 2H, CHN Oxd + O-CH-CH2-Fluorene), 4.52-4.58 (m, 1H, CHO Oxd), 5.19 (s, 2H, O-CH_2-Ph), 5.42 (d, J = 8.4 Hz, 1H, NH Tyr), 5.82-5.89 (m, 1H, CHα-Tyr), 6.89 (d, J = 7.4 Hz, 2H, CH Ar Tyr), 7.08 (d, J = 7.4 Hz, 2H, CH Ar Tyr), 7.28-7.34 (m, 7H, 2 CH Fluorene + 5 CH Ph), 7.40 (t, J = 7.4 Hz, 2H, CH Fluorene), 7.56 (d, J = 7.1 Hz, 2H, CH Fluorene), 7.76 (d, J = 7.1 Hz, 2H, CH Fluorene); ^{13}C NMR (100 MHz $CDCl_3$): δ 21.3, 28.9, 38.4, 47.2, 54.5, 62.0, 67.1, 68.2, 73.8, 78.5, 120.0, 124.2, 125.2, 125.3, 127.2, 127.8, 128.4, 128.8, 130.0, 130.2, 134.6, 141.4, 144.0, 151.2, 154.7, 155.3, 167.4, 172,3.

Fmoc-L-Tyr-D-Oxd-OH (45)
To a stirred solution of **44** (0.576 mmol, 389 mg) in dry dichloromethane (6 mL), under inert atmosphere, trifluoroacetic acid (10.4 mmol, 800 µL) was added at room temperature. The solution was stirred for 4 hours under inert atmosphere, then the mixture was washed with water (3 x 5 mL), dried over sodium sulphate and concentrated in vacuo. The white solid obtained (356 mg) was dissolved in methanol (10 mL) under inert atmosphere. Pd/C (10% w/w, 39 mg) was added under inert atmosphere. Vacuum was created inside the flask using the vacuum line. The flask was then filled with hydrogen using a balloon (1 atm). The solution was stirred for 4 hours under a hydrogen atmosphere. The product was obtained pure after filtration through Celite filter and concentrated in vacuo in 98% yield (0.563 mmol 299 mg).
M.p. = 192-195 °C; $[\alpha]_D^{20}$ = 9.5 (c = 0.13 in CH_3OH); ATR-IR v = 3326, 1781, 1691, 1535, 1513 cm^{-1}; ^1H NMR (400 MHz CD_3OD): δ = 1.45 (d, *J* = 6.3 Hz, 3H, CH_3 Oxd), 2.76 (dd, J = 9.6 Hz, J = 13.5 Hz 1H, CH_2β-Tyr,), 3.07 (dd, J = 4.7 Hz, J = 13.7 Hz, 1H, CH_2β-Tyr), 4.12-4.20 (m, 2H, O-CH-CH_2-Fluorene), 4.25-4.29 (m, 1H, O-CH-CH_2-Fluorene), 4.40 (d, J = 3.6 Hz 1H, CHN Oxd,), 4.65-4.73 (m, 1H, CHO Oxd), 5.73 (dd, J = 4.8 Hz, J = 9.6 Hz, 1H, CHα-Tyr), 6.70 (d, J = 8.3 Hz, 2H, CH Ar Tyr), 7.14 (d, J = 8.5 Hz, 2H, CH Ar Tyr), 7.29 (q, J = 7.8 Hz, 2H, CH Fluorene), 7.38 (t, J = 7.4 Hz, 2H, CH Fluorene), 7.52-7.57 (m, 1H, NH Tyr), 7.60 (d, J = 7.5 Hz, 2H, CH Fluorene), 7.78 (d, J = 7.4 Hz, 2H, CH Fluorene). ^{13}C NMR (100 MHz CD_3OD): δ = 21.2, 38.6, 48.2, 56.3, 68.0, 76.1, 116.2, 120.8, 126.2, 126.3, 128.1, 128.7, 131.2, 131.6, 142.4, 145.1, 145.2, 153.8, 157.3, 158.0, 174.1.

Fmoc-L-Tyr(O-tert-Bu)-D-pGlu-OBn (46)
To a stirred solution of Fmoc-Tyr(O-tert-Bu)-OH (0.91 mmol, 418 mg) and HBTU (1.00 mmol, 379 mg), in dry acetonitrile (15 mL), under inert atmosphere, D-pGlu-OBn (0.91 mmol, 199.5 mg) in dry acetonitrile (10 mL) was added at room temperature, followed by a solution of 1,8-Diazabicyclo[5.4.0]undec-7-ene (2 mmol, 298 µL). The solution was stirred for 2 hours under inert atmosphere, then acetonitrile was removed under reduced pressure and replaced with dichloromethane (30 mL). The mixture was washed with brine (30 mL), 1 N aqueous HCl (30 mL) and with saturated aqueous $NaHCO_3$ (30 mL), dried over sodium sulphate and concentrated in vacuo. The product was obtained pure after silica gel chromatography (dichloromethane → dichloromethane/ethyl acetate 96:4) in 33% of yield (0.302 mmol, 200 mg).
M.p. = 68-70 °C; $[\alpha]_D^{20}$ = 16.5 (c = 0.20 in CH_2Cl_2); IR (CH_2Cl_2 3 mM) ν 3429, 1752, 1701, 1608, 1506 cm^{-1}; ^1H NMR (400 MHz $CDCl_3$): δ = 1.28 (s, 9H, CH_3 tert-Bu), 2.03-2.11 (m, 1H, CH_2β-pGlu), 2.18-2.31 (m, 1H, CH_2β-pGlu), 2.44-2.54 (m, 1H, CH_2γ-pGlu), 2.66-2.78 (m, 1H, CH_2γ-pGlu), 2.91 (dd, J = 7.5 Hz, J = 13.3 Hz, 1H, CH_2β-Tyr), 3.12 (dd, J = 4.9 Hz, J = 13.7 Hz, 1H, CH_2β-Tyr), 4.14-4.20 (m, 1H, O-CH-CH_2-Fluorene), 4.22-4.28 (m, 1H, O-CH-CH_2-Fluorene), 4.33-4.40 (m, 1H, O-CH-CH_2-Fluorene), 4.65 (d, J = 9.1 Hz, 1H, CHα-pGlu), 5.17 (s, 2H, O-CH_2-Ph), 5.49 (d, J = 8.6 Hz, 1H, NH Tyr), 5.82-5.89 (m, 1H, CHα-Tyr), 6.87 (d, J = 7.9 Hz, 2H, CH Ar Tyr), 7.05 (d, J = 7.8 Hz, 2H, CH Ar Tyr), 7.27-7.34 (m, 7H, 5 CH Ph + 2 CH Fluorene), 7.40 (t, J = 7.2 Hz, 2H, CH Fluorene), 7.57 (d, J = 7.0 Hz, 2H, CH Fluorene), 7.76 (d, J = 7.5 Hz, 2H, CH Fluorene). ^{13}C NMR (100 MHz $CDCl_3$): δ = 21.8, 28.9, 31.8, 38.7, 47.2, 55.5, 58.3, 67.0, 67.6, 78.5, 120.0, 124.1, 125.2, 125.3, 127.2, 127.8, 128.4, 128.7, 128.8, 130.1, 130.6, 135.1, 141.4, 144.0, 154.6, 155.3, 170.4, 172.9, 173.9.

Fmoc-L-Tyr-D-pGlu-OH (47)
To a stirred solution of **46** (0.302 mmol, 200 mg) in dry dichloromethane (6 mL), under inert atmosphere, trifluoroacetic acid (5.45 mmol, 420 µL) was added at room temperature. The solution was stirred for 4 hours under inert atmosphere, then the mixture was washed with water (3 x 5 mL), dried over sodium sulphate and concentrated in vacuo. The white solid obtained (183 mg) was dissolved in methanol (10 mL) under inert atmosphere. Pd/C (10% w/w, 20 mg) was added under inert atmosphere. Vacuum was created inside the flask using the vacuum line. The flask was then filled with hydrogen using a balloon (1 atm). The solution was stirred for 4 hours under a hydrogen atmosphere. The product was obtained pure after filtration through Celite filter and concentrated in vacuo in 98% yield (0.30 mmol 155 mg).
M.p. = 121-124 °C; $[\alpha]_D^{20}$ = 25.4 (c = 0.12 in CH_3OH); ATR-IR ν = 3302, 2921, 2852, 1690, 1613, 1514, 1448 cm^{-1}; ^1H NMR (400 MHz CD_3OD): δ = 2.07-2.15 (m, 1H, CH_2β-pGlu), 2.30-2.41 (m, 1H, CH_2β-pGlu), 2.52-2.62 (m, 1H, CH_2γ-pGlu), 2.64-2.81 (m, 2H, CH_2γ-pGlu + CH_2β-Tyr), 3.07 (dd, J = 4.2 Hz, J = 13.4 Hz, 1H, CH_2β-Tyr), 4.10-4.17 (m, 2H, O-CH-CH_2-Fluorene + O-CH-CH_2-Fluorene),4.22-4.31 (m, 1H, O-CH-CH_2-Fluorene), 4.59-4.68 (m, 1H, CHα-pGlu), 5.66 (dd, J = 4.0 Hz, J = 9.6 Hz, 1H, CHα-Tyr), 6.69 (d, J = 8.3 Hz, 2H, CH Ar Tyr), 7.14 (d, J = 8.4 Hz, 2H, CH Ar Tyr), 7.25-7.32 (m, 2H, CH Fluorene), 7.34-7.40 (m, 2H, CH Fluorene), 7.52 (d, J = 7.9 Hz, 1H, NH Tyr), 7.58 (dd, J = 4.2 Hz, J = 7.3 Hz, 2H, CH Fluorene), 7.77 (d, J = 7.4 Hz, 2H, CH Fluorene); ^{13}C NMR (100 MHz CD_3OD): δ = 22.9, 32.8, 38.5, 48.1, 57.7, 60.2, 68.0, 116.0, 120.8, 126.3, 126.4, 128.2, 128.7, 129.1, 131.6, 131.7, 142.5, 145.2, 145.3, 157.3, 158.1, 174.7, 176.8.

Fmoc-L-Trp-D-Oxd-OBn (48)
To a stirred solution of Fmoc-Trp-OH (0.43 mmol,183 mg) and HATU (0.47 mmol, 180 mg), in dry acetonitrile (10 mL), under inert atmosphere, D-Oxd-OBn (0.43 mmol, 101 mg) in dry acetonitrile (5 mL) was added at room temperature, followed by a solution of N,N-diisopropylethylamine (1.1 mmol, 183 µL). The solution was stirred for 2 hours under inert atmosphere, then acetonitrile was removed under reduced pressure and replaced with dichloromethane (30 mL). The mixture was washed with brine (30 mL), 1 N aqueous HCl (30 mL) and with saturated aqueous $NaHCO_3$ (30 mL), dried over sodium sulphate and concentrated in vacuo. The product was obtained pure after silica gel chromatography

(dichloromethane → dichloromethane/ethyl acetate 94:6) in 90% of yield (0.387 mmol, 249 mg).
M.p. = 172-174 °C; $[\alpha]_D^{20}$ = 14.2 (c = 0.19 in CH_2Cl_2); IR (CH_2Cl_2 3 mM) v = 3467, 3430, 2980, 2855, 1793, 1756, 1712, 1606, 1507 cm^{-1}; ^1H NMR (400 MHz $CDCl_3$): δ = 1.14 (d, *J* = 5.3 Hz, 3H, CH_3 Oxd), 3.28-3.40 (m, 2H, CH_2β-Trp), 4.12 (s, 1H, O-CH-CH_2-Fluorene), 4.15-4.24 (m, 1H, O-CH-CH_2-Fluorene), 4.27-4.34 (m, 1H, CHN Oxd), 4.42 (s, 2H, CHO Oxd + O-CH-CH_2-Fluorene), 5.16 (s, 2H, O-CH_2-Ph), 5.58 (d, J = 7.6 Hz, 1H, NH Trp), 5.94-6.00 (m, 1H, CHα-Trp), 7.06-7.12 (m, 2H, CH Ar Trp), 7.14-7.20 (m, 1H, CH Ar Trp), 7.28-7.36 (m, 8H, 5 CH Ph + 2 CH Fluorene + CH Ar Trp), 7.40 (t, J = 6.8 Hz, 2H, CH Fluorene), 7.56 (t, J = 6.9 Hz, 3H, 2 CH Fluorene + CH Ar Trp), 7.77 (d, J = 7.2 Hz, 2H, CH Fluorene) 8.08 (s, 1H, NH Indole). ^{13}C NMR (100 MHz $CDCl_3$): δ = 20.7, 29.8, 47.2, 53.8, 61.9, 67.1, 68.0, 73.6, 108.9, 111.6,118.2, 119.8, 120.0, 122.2, 124.1, 125.2, 125.3, 125.4, 127.2, 127.5, 127.7, 128.4, 128.7, 134.6, 136.0, 141.3, 143.9, 144.0, 151.3, 155.5, 167.6, 172.8.

Fmoc-L-Trp-D-Oxd-OH (49)
To a stirred solution of **48** (0.387 mmol, 249 mg) in methanol (10 mL) under inert atmosphere, then Pd/C (10% w/w, 25 mg) was added under inert atmosphere. Vacuum was created inside the flask using the vacuum line. The flask was then filled with hydrogen using a balloon (1 atm). The solution was stirred for 4 hours under a hydrogen atmosphere. The product was obtained pure after filtration through Celite filter and concentrated in vacuo in 98% yield (0.383 mmol 212 mg).
M.p. = 220-223 °C; $[\alpha]_D^{20}$ = 5.2 (c = 0.18 in CH_3OH); ATR-IR v = 3404, 3315, 1783, 1715, 1688, 1535, 1450 cm^{-1}; ^1H NMR (100 MHz CD_3OD): δ = 1.13 (d, *J* = 6.4 Hz, 3H, CH_3 Oxd), 3.16 (dd, J = 8.2 Hz, J = 14.1 Hz, 1H, CH_2β-Trp), 3.28 (d, J = 6.5 Hz, 1H, CH_2β-Trp), 4.12-4.18 (m, 2H, CHN Oxd + O-CH-CH_2-Fluorene), 4.20-4.29 (m, 2H, O-CH-CH_2-Fluorene), 4.54-4.60 (m, 1H, CHO Oxd), 5.90 (t, J = 7.2 Hz, 1H, CHα-Trp), 7.00 (t, J = 7.3 Hz, 1H, CH Ar Trp), 7.08 (t, J = 7.4, 1H, CH Ar Trp), 7.16 (s, 1H, NH Indole), 7.19-7.30 (m, 2H, CH Fluorene), 7.31-7.39 (m, 3H, 2 CH Fluorene + CH Ar Trp), 7.51 (t, J = 8.4, 1H, NH Trp), 7.59 (d, J = 7.3, 2H, CH Fluorene), 7.64 (d, J = 8.0, 1H, CH Ar Trp), 7.71-7.79 (m, 3H, 2 CH Fluorene + CH Ar Trp); ^{13}C NMR (100 MHz CD_3OD): δ = 20.9, 29.7, 47.9, 55.2, 63.3, 68.1, 75.6, 110.8, 112.3, 119.5, 119.9, 120.8, 122.4, 125.4, 126.3, 126.4, 128.2, 128.7, 137.9, 142.5, 145.2, 145.3, 153.5, 158.0, 171.6, 174.6.

Fmoc-L-Trp-D-pGlu-OBn (50)
To a stirred solution of Fmoc-Trp-OH (0.46 mmol,183 mg) and HATU (0.47 mmol, 180 mg), in dry acetonitrile (10 mL), under inert atmosphere, D-pGlu-OBn (0.46 mmol, 101 mg) in dry acetonitrile (5 mL) was added at room temperature, followed by a solution of N,N-diisopropylethylamine (1.15 mmol, 196 µL). The solution was stirred for 2 hours under inert atmosphere, then acetonitrile was removed under reduced pressure and replaced with dichloromethane (30 mL). The mixture was washed with brine (30 mL), 1 N aqueous HCl (30 mL) and with saturated aqueous $NaHCO_3$ (30 mL), dried over sodium sulphate and concentrated in vacuo. The product was obtained pure after silica gel chromatography (dichloromethane → dichloromethane/ethyl acetate 92:8) in 40% of yield (0.184 mmol, 115 mg).
M.p. = 82-84 °C; $[\alpha]_D^{20}$ = 46.7 (c = 0.18 in CH_2Cl_2); IR (CH_2Cl_2 3 mM) v = 3468, 3430, 1752, 1701, 1606, 1505 cm^{-1}. ^1H NMR (400 MHz $CDCl_3$): δ = 1.92-2.00 (m, 2H, CH_2β-pGlu), 2.35-2.45 (m, 1H, CH_2γ-pGlu), 2.59-2.761 (m, 1H, CH2-γ pGlu), 3.32 (d, *J* = 5.6 Hz, 2H, CH_2β-Trp), 4.16-4.22 (m, 1H, O-CH-CH_2-Fluorene), 4.29.4.35 (m, 1H, O-CH-CH_2-Fluorene), 4.39-4.44 (m, 2H, O-CH-CH_2-Fluorene + CHα-pGlu), 5.14 (s, 2H, O-CH_2-Ph), 5.67 (d, J = 8.0 Hz, 1H, NH Trp), 5.89-5.96 (m, 1H, CHα-Trp), 7.00 (s, 1H, CH Ar Trp), 7.09 (t, J = 7.4 Hz, 1H, CH Ar Trp), 7.17 (t, J = 7.5 Hz, 1H, CH Ar Trp), 7.27-7.36 (m, 8H, CH Ph + 2 CH Fluorene + CH Ar Trp), 7.40 (t, J = 7.4 Hz, 2H, CH Fluorene), 7.49 (d, J = 7.4 HZ, 1H, CH Ar Trp), 7.56 (t, J = 7.3 Hz, 2H, CH Fluorene), 7.76 (d, J = 7.3 Hz, 2H, CH Fluorene), 8.06 (s, 1H, NH Indole); ^{13}C NMR (100 MHz $CDCl_3$): δ = 21.6, 28.8, 31.7, 47.3, 55.1, 58.5, 67.0, 67.5, 109.6, 111.5, 118.2, 119.7, 120.0, 122.2, 123.8, 125.3, 125.4, 127.2, 127.7, 128.3, 128.7, 135.1, 136.0, 141.4, 144.1, 155.5, 170.5, 173.0, 174.0.

Fmoc-L-Trp-D-pGlu-OH (51)
To a stirred solution of **50** (0.184 mmol, 115 mg) in methanol (11 mL) under inert atmosphere, then Pd/C (10% w/w, 12 mg) was added under inert atmosphere. Vacuum was created inside the flask using the vacuum line. The flask was then filled with hydrogen using a balloon (1 atm). The solution was stirred for 4 hours under a hydrogen atmosphere. The product was obtained pure after filtration through Celite filter and concentrated in vacuo in 98% yield (0.181 mmol 97 mg).
M.p. = 216-219 °C; $[\alpha]_D^{20}$ = 65.7 (c = 0.14 in CH_3OH); ATR-IR v = 3404, 3315, 1783, 1715, 1688, 1535 cm^{-1}. 1H NMR (400 MHz CD_3OD): δ = 1.97-2.06 (m, 1H, CH_2β-pGlu), 2.13-2.19 (m, 1H, CH_2β-pGlu), 2.25-2.55 (m, 1H, CH_2γ-pGlu), 2.60-2.72 (m, 1H, CH_2γ-pGlu), 3.09-3.26 (m, 1H, CH_2β-Trp), 3.27-3.34 (m, 1H, CH_2β-Trp), 4.11-4.22 (m, 2H, O-CH-CH_2-Fluorene), 4.24-4.30 (m, 1H, O-CH-CH_2-Fluorene), 4.38-4.42 (m, 1H, CHα-pGlu), 5.84-5.91 (m, 1H, CHα-Trp), 7.00 (t, J = 7.5, 1H, CH Ar Trp), 7.06-7.13 (m, 2H, CH Ar Trp), 7.21-7.30 (m, 3H, 2 CH Fluorene + NH Trp), 7.31-7.39 (m, 3H, 2 CH Fluorene + CH Ar Trp), 7.57 (d, J = 7.2 Hz, 2H, CH Fluorene), 7.65 (d, J = 7.9 Hz, 1H, CH Ar Trp), 7.77 (d, J = 7.4 Hz, 2H, CH Fluorene), 10.32 (s, 1H, NH Indole); ^{13}C NMR (100 MHz CD_3OD): δ = 22.6, 30.7, 31.8, 47.8, 56.6, 60.1, 68.0, 110.5, 112.2, 119.5, 119.8, 120.8, 122.3, 125.2, 126.3, 126.4, 128.1, 128.7, 137.9, 138.0, 141.4, 145.2, 158.0, 174.5, 174.9, 176.5

$CH_2(C_3H_6CO$-L-Phe-D-Oxd-OH$)_2$ (52)
For the synthesis and characterization see Ref. 184.

$CH_2(C_3H_6CO$-L-Phe-D-Pro-OH$)_2$ (53)
For the synthesis and characterization see Ref. 184.